THE EFFECTS OF CLIMATE CHANGE ON LAKE TAHOE IN THE 21st CENTURY: METEOROLOGY, HYDROLOGY, LOADING AND LAKE RESPONSE

Robert Coats (Co-PI)[1]
John Reuter (PI)[1]
Michael Dettinger[2]
John Riverson[3]
Goloka Sahoo[4]
Geoff Schladow[4]
Brent Wolfe[5]
Mariza Costa-Cabral[6]

June 30, 2010

Prepared by
[1] University of California, Davis, Tahoe Environmental Research Center and Department of Environmental Science & Policy, One Shields Avenue, Davis, CA 95616
[2] US Geological Survey and Scripps Institute of Oceanography, La Jolla, CA 92093
[3] Tetra Tech, Inc.; 10306 Eaton Place, Suite 340; Fairfax, VA 22030
[4] University of California, Davis, Tahoe Environmental Research Center and Department of Civil & Environmental Engineering, One Shields Avenue, Davis, CA 95616
[5] Northwest Hydraulic Consultants, 870 Emerald Bay Road, Suite 308, South Lake Tahoe, CA 96150
[6] Hydrology Futures, LLC, 4509 Interlake Ave N #300, Seattle WA 98103

Prepared for
Jonathan Long
Pacific Southwest Research Station, Tahoe Environmental Science Center, 291 Country Club Drive, Incline Village, NV 89451

Table of Contents

List of Figures

Appendix figures not listed.

List of Tables

Appendix tables not listed.

Abstract

The 21st Century global climate is expected to experience long-term changes in response to anthropogenic greenhouse gas emissions. Discussions on the potential impacts of climate change on water resources in the Lake Tahoe basin have only recently begun and our scientific understanding to date has focused on identifying existing impacts and trends in the historic data. Water resource managers need to know the potential effects of changing meteorologic conditions on a variety of topics such as expected future air temperature, amount and type of precipitation, stream discharge, sediment and nutrient loading characteristics, BMP performance, lake mixing and water quality response. In this study we examined all these topics using existing water resource models already developed for the Lake Tahoe TMDL. A sophisticated statistical downscaling methodology was applied to the model outputs of the of the Geophysical Fluid Dynamics Laboratory Model (GFDL) and the Parallel Climate Model (PCM) given the A2 and B1 emissions scenarios, to produce simulated data records at a 12 km grid scale in the Tahoe basin for the 21st Century (2000-2099).

The results show:

1) Upward trends in T_{max} and T_{min}, with trends for the GFDL > PCM, and trends for the A2 > B1,
2) No strong trends in annual precipitation amount, except for declining precipitation for the GFDL A2 case toward the end of the century,
3) A continuing shift from snowfall to rain, toward earlier snowmelt and runoff during the water year, for both scenarios,
4) A downward shift in the hydrologic flow-duration curve for the A2 scenario in the last third of the century,
5) Some increases in drought severity, especially toward the end of the century,
6) Dramatic increases in flood magnitude in the middle third of the century, especially with the B1 scenario,
7) Sediment and nutrient loading to Lake Tahoe should not increase, to any meaningful level, as a result of climate change and may actually decrease due to the estimated decline in water yield,
8) That while climate change will result in a modest decline in BMP performance for fine sediment particle load reductions (i.e. increase in average pollutant load), any diminished performance will be relatively small and load reduction should still be significant,
9) That by the middle of the 21st Century (after about 2050) Lake Tahoe could cease to mix to the bottom. This will in turn result in complete oxygen depletion in the deep waters and an increase in sediment release of nitrogen and phosphorus,
10) That annual loading of soluble reactive phosphorus under sustained conditions of lake stratification (no deep mixing) and anoxic sediments could be twice the current load from all other sources. Loading of ammonium under these conditions could increase the amount of biological available nitrogen that enters the lake by 25 percent. This effect on the Lake Tahoe's nutrient budgets could have a dramatic and long-lasting impact on the food web and trophic status of Lake Tahoe,
11) That the resulting annual Secchi depth in the later portion of the 21st Century could be in the range of 15-20 m as compared measured values of 21-22 m since 2000 and,
12) Climate change will drive the lake surface level down below the natural rim after 2086 for the GFDL A2 but not the GFDL B1 scenario.

1.0 INTRODUCTION

1.1 Emissions and Global Climate Models

The 21st Century global climate is expected to experience long-term human-induced changes in response to greenhouse gases that have been added to the atmosphere by human activities. Several decades of warming and a variety of hydrologic and landscape responses have already occurred and are expected to accelerate in the 21st Century until greenhouse-gas emissions are brought under control and even reversed (IPCC 2007).

How these global-scale climate and landscape changes will play out in the Tahoe basin is highly uncertain, but current numerical models of the global climate system provide a number of plausible scenarios that can be investigated and evaluated to determine likely points of particular vulnerability in the basin's hydrologic characteristics, nutrient and sediment loading, and lake response. Given widespread concerns about the approaching climate changes, such assessments are being performed in local to regional resource systems worldwide--assessment strategies and scenarios have emerged and are widely accepted as suitable for initial planning given current states of knowledge. Indeed, the State of California has recently completed the second in a biannual round of State-scale climate-change assessments using scenarios of the sort analyzed here, a new US national assessment of potential climate-change impacts is in planning stages and will be largely scenario based, and the next IPCC Assessment is expected to focus even more than in the past on regional scenarios of change and response.

These various assessment activities typically begin by identifying some workable number of climate-change projections generated as simulations by a variety of global climate models forced by selected scenarios of future economic development and resulting greenhouse-gas emissions. Simulations from current global models typically are made on very coarse spatial grids, with model grid points separated geographically by anywhere from 1º latitude and longitude to as much as 3º latitude and longitude. At this scale, the climate of the entire State of California is represented by less than 10 grid cells, and the Tahoe basin covers much less than any one grid cell. As a consequence, the second step in most local to regional assessments is to "downscale" global-model results to some finer grid or individual stations so as to preserve local climatic differences within a study area while representing the projected climate changes. The downscaled versions of the climate-change scenarios are then presented to various models or experts regarding the local systems to identify their vulnerabilities to the kinds of climate change encompassed by the scenario or ensemble of scenarios considered. Having identified key vulnerabilities to the climate changes investigated, options for adaptation of existing management systems or structures can—in principle—be identified and weighed, as can options for new management approaches.

1.2 Climate Change and Water Resources

A complete understanding the historic and likely future conditions of Lake Tahoe requires consideration of the input of water, nutrients, sediment and energy from the lake's watershed and from the atmosphere. Previous work on the historic trends in the Basin's hydroclimatology in the 20th Century indicated strong upward trends in air temperature (especially minimum daily temperature), a shift from snow to rain, a shift in snowmelt timing to earlier dates, increased rainfall intensity, increased interannual variability, and increase in the temperature of Lake Tahoe (Coats et al. 2006; Coats 2010). The latter investigation included a comparison with other areas in the vicinity of Lake Tahoe in order to relate these observations to large-scale regional climatic trends in the western USA and identify impacts and drivers. Sahoo and Schladow (2008) reported on an initial attempt to model changes in lake mixing based on coarse-scaled future meteorologic conditions.

Recent work on climate change impacts in the western U.S. has focused attention on the shift in snowmelt timing toward earlier dates (Aguado et al., 1992; Dettinger et al., 2004; Cayan et al., 2001; Dettinger and Cayan, 1995; Johnson et al., 1999; Stewart et al., 2005), the shift from snow to rain (Knowles et al., 2006; Regonda et al., 2005), the earlier onset of spring (Cayan et al., 2001); and the effect that these changes will have on water supply in California and throughout the western US (Hamlet et al., 2005; Barnett et al., 2008; Mote et al., 2005). Pierce et al. (2008) showed that about half of the observed decline in western U.S. springtime snowpack (1950-1999) results from climate changes forced by anthropogenic greenhouse gases (GHGs), ozone and aerosols. In 2007, the catastrophic Angora Fire in the Tahoe basin showed how legacy vegetation changes can interact with climate change to increase fire hazard, and provided a stunning illustration of the increasing risk of wildfire in the western U.S. (Westerling et al., 2006); Running, 2006; Brown et al., 2004).

Since continued change toward a warmer climate in the basin is inevitable (Hansen et al., 2009), we would like to know: 1) how fast will the air temperature in the basin increase; 2) how will the form, timing and annual amount of precipitation change? 3) how will the changes in temperature and precipitation affect drought? 4) how will changes in precipitation affect streamflow regimes, especially high- and low-flow frequency-magnitude relationships? The purpose of this paper is to begin answering these questions. Our approach is to downscale the output for the 21st century from two General Circulation Models (GCMs) and two emissions scenarios, and use the downscaled output to drive a distributed basin hydrology model. The output from the hydrology model is then used to derive streamflow and soil moisture at various time scales, for use in calculating flood frequency, flow duration, drought severity and shifts in snowmelt timing, for selected sub-basins and sites in the Tahoe basin.

1.3 Lake Tahoe: Concern with Climate Change

Lake Tahoe is world renowned for its natural beauty and cobalt-blue color. However, long-term monitoring shows that (1) Secchi depth transparency has declined by 10 m since 1968, (2) the rate of ^{14}C primary productivity continues to increase at about 5 percent per year, and (3) thick growths of attached algae cover portions of the once-pristine shoreline. Additionally, like many lakes world-wide, Lake Tahoe has been affected by non-native species that were either intentionally introduced or were part of a large pattern of regional invasion.

Lake clarity is driven by the influx of phosphorus, nitrogen but especially fine sediment particles <16 μm in diameter (Lahontan and NDEP 2010a; Sahoo et al. 2010). These pollutants come from land disturbance and urbanization (including roadways and road maintenance) and their transport to the lake is further exacerbated by an accompanying loss of natural landscape capable of treating runoff.

Fine sediment particles come primarily from the urban setting (72% of total), while 55% of the nitrogen enters Lake Tahoe via direct atmospheric deposition. Surface runoff from the urban and non-urban portions of the landscape account for 39% and 26% of the phosphorus load, respectively (Lahontan and NDEP 2010a). The Lake Clarity Model shows that the 30 m target can be achieved if nutrients and particles from all sources are reduced by 55 percent or with a 75 percent reduction from just urban sources. Based on a pollutant reduction opportunities analysis for the Tahoe basin, the *Clarity Challenge* (24 m Secchi depth within 15 years) can be met by a reduction of 32%, 14% and 4% for particles, P and N, respectively (Lahontan and NDEP 2010b). The results from paleolimnological research and an empirical Secchi depth versus particle relationship suggest that Lake Tahoe can improve once loading is reduced (Heyvaert 1997). A model simulation where all fine particles from urban source are set to zero results in a 31 m Secchi depth which resembles the hypothesized historic baseline.

Efforts to reduce nutrient and sediment input to Lake Tahoe have been the cornerstone of watershed management for decades. Perhaps the largest and best organized of these efforts has been the Environmental Improvement Program (EIP) that was developed by the Tahoe Regional Planning Agency (http://www.trpa.org/default.aspx?tabid=227). The EIP was highlighted during the 1997 Presidential Summit at Lake Tahoe in order to focus actions related to lake and watershed management. According to the TRPA, the EIP "encompasses hundreds of capital improvement, research, program support, and operation and maintenance projects in the Tahoe Basin, all designed to help restore Lake Tahoe's clarity and environment."

The Lake Tahoe Total Maximum Daily Load Program (TMDL) can be considered a science-based operational blueprint for implementation of the EIP. The Lake Tahoe TMDL (1) quantifies fine particle and nutrient loading from urban runoff, vegetated upland flow, atmospheric deposition, stream channel/shoreline erosion and groundwater, (2) uses a customized Lake Clarity Model to link pollutant loading to lake response, and (3) develops the framework for a plan to achieve an annual average Secchi depth of 30 m as required by existing regulations.

1.4 Goals and Objectives

While the Lake Tahoe TMDL considers climate change in a conceptual manner (Lahontan and NDEP 2010b), a more quantitative analysis was unavailable. Fully aware of this knowledge gap, we submitted, and were awarded, a grant from the Southern Nevada Public Lands Management Act (SNPLMA) Round 8 science projects to begin to evaluate the implications of climate change on hydrology, pollutant loading and the response of Lake Tahoe. While additional data evaluation and technical analysis is needed to tie climate change impacts directly into policy, the goal of this present study was to provide water resource agencies and decision-makers with a scientifically-justified assessment as to what extent climate change needs to be considered in ongoing efforts to protect Lake Tahoe.

The purpose of this research was to investigate the likely effects of climate change on Lake Tahoe, while assessing the implications of hydrologic changes associated with climate charge for (1) changes in loads of sediment and nutrients to Lake Tahoe, (2) design and effectiveness of Best Management Practices (BMPs) and (3) lake response to warming.

The results of our investigations have been used to address the following specific questions:

- What has been the historical change key meteorology/hydrology parameters such as air temperature, precipitation amount, form of precipitation (rain versus snow), snowpack characteristics, timing and duration of snowmelt, etc?
- What are expected changes to these parameters over the next 100 years based on output from general circulation models (GCM) that have been developed to evaluate climate change?
- How will the magnitude and frequency of runoff, both from the entire Lake Tahoe drainage basin and to water quality treatment projects (BMPs) respond to climate change in the 21st Century?
- How will the discharge of sediments and nutrients to Lake Tahoe respond to climate change?
- What is the expected impact of a change in hydraulic and pollutant loading on BMP treatment and project implementation?
- How would reduced mixing of the lake affect deep-water dissolved oxygen and nutrient release from bottom sediments?

1.5 Overview of Approach

To analyze the likely future impacts of climate change on hydrology and water quality at Lake Tahoe, four models (or suites of models) were used together. First, a General Circulation Model (GCM) of global climate was employed to generate future scenarios of climate variables, at appropriate time and spatial scales. To be applied at the scale of the Tahoe basin, the model output was downscaled using local records of temperature and precipitation.

Second, a watershed model was used to model or predict stream discharge and loads of nutrients and sediment in response to long-term climate trends. For development of the Total Maximum Daily Load (TMDL) allocations for the Tahoe Basin, Tetra Tech (2007) customized the Load Simulation Program in C++ (LSPC) model for Tahoe basin hydrology. This watershed model uses local weather data as the forcing factor, together with watershed characteristics (including existing land use coverage, elevation, slope, and soils) and measured stream discharge and water quality to generate existing condition loads for ammonia, nitrate, organic nitrogen, dissolved phosphorus, and organic phosphorus (Lahontan and NEP 2010a).

Third, the climate data and watershed outputs must be used to drive a lake hydrodynamic and clarity model. The UC Davis Dynamic Lake Model (DLM) coupled with the Water Quality Model (DLM-WQ) constitutes the Lake Clarity Model that was developed and used as part of the Total Maximum Daily Load (TMDL) program to meet regulatory water quality requirements (Sahoo et al. 2010). DLM-WQ is a complex system of sub-models including the hydrodynamic sub-model, ecological sub-model, water quality sub-model, particle sub-model and optical sub-model.

Fourth, the implications of climate change for the design of water quality BMPs must be analyzed. For the Lake Tahoe TMDL, the Pollutant Load Reduction Model was developed to analyze the reduction in pollutant loads associated with specific BMPs and sets of BMPs (nhc et al. 2009). It can be used to compare the effectiveness of a given BMP design with and without the increased magnitude and frequency of runoff that may result from climate change. Figure 1-1 is a flow chart showing the flow of information used in this project.

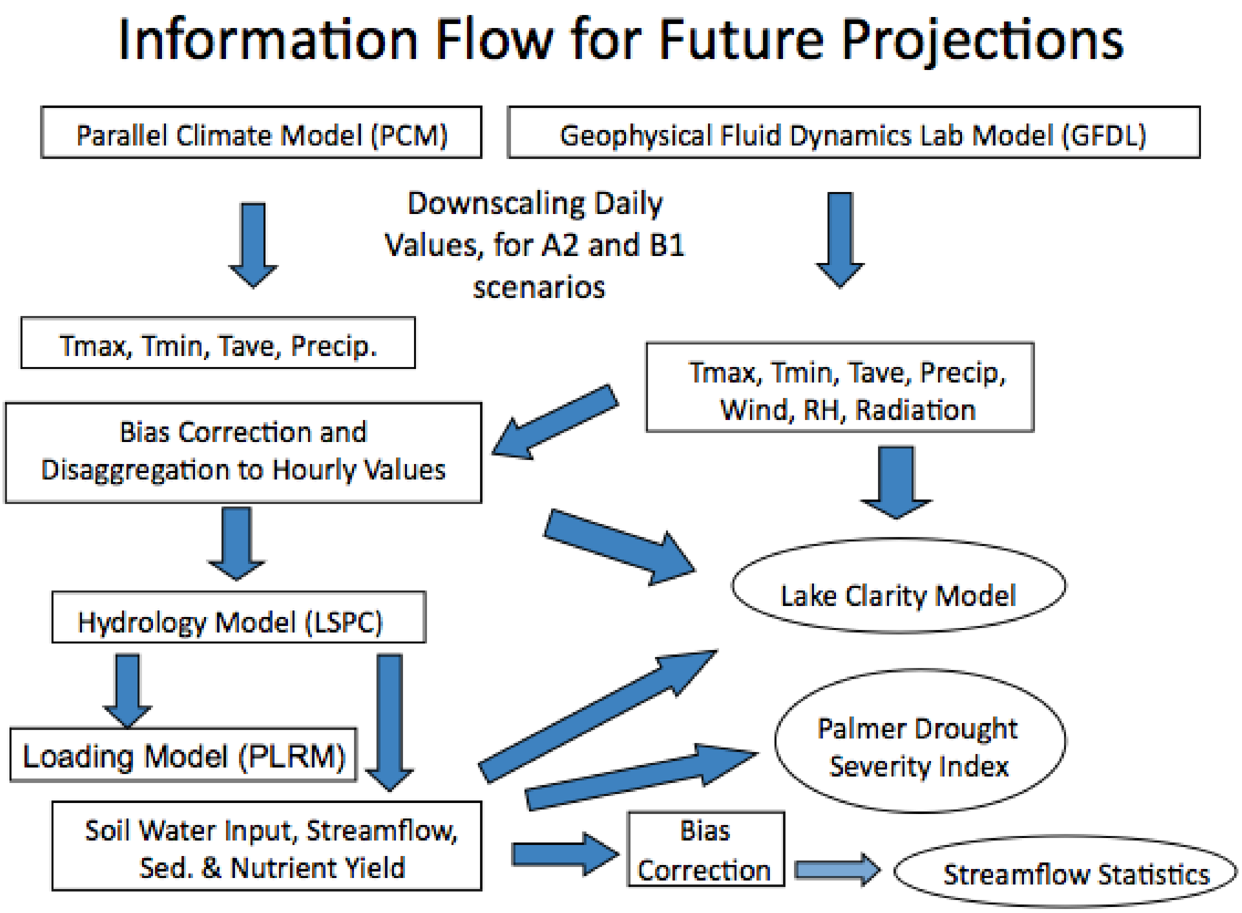

Figure 1-1. Summary of information flow used for modeling and analysis.

2.0 PROJECTIONS & DOWNSCALING OF CLIMATE CHANGE DATA FOR THE LAKE TAHOE BASIN

Author: Michael D. Dettinger Ph.D.

2.1 Selection of Global Climate Model and Emission Scenarios

In this study, the most attention was placed on simulations by NOAA's Geophysical Fluid Dynamics Laboratory (GFDL) - at Princeton University - global climate model (CM2.1) and its response to two greenhouse-gas emissions scenarios generated by the IPCC for its Special Report on Emissions Scenarios (Nakicenovic et al. 2000). The A2 emissions scenario is one that is based on assumptions of a very heterogeneous world economy with high population growth, moderate overall economic growth, and resulting emissions that accelerate throughout the 21st Century. Notably, even just a year ago, the A2 scenario was widely viewed as a reasonable "worst case" scenario, but recent evaluations have shown that in the past decade, emissions have actually exceeded the A2 trajectory; consequently, currently A2 is being viewed as more of a middle-of-the-road or business-as-usual scenario and other even more severe emissions scenarios are being evaluated in many studies just starting now (Figure 2-1). Climatic responses to a second emissions scenario labeled B1 were also evaluated as part of our study. The B1 scenario is based on assumptions of a greener future with lower population growth and technological moves towards service and information economies, with emissions that level off by end of century (Figure 2-1). The B1 scenario is considered to be an optimistic scenario that results in much less change and challenge than does the A2 scenario. It is noteworthy that 2004 through at least 2007, global CO_2 emissions from fossil fuels actually exceeded the IPCC/SRES trajectory for the A2 scenario (US Global Change Research Program 2009).

The GFDL climate model warms more in response to each unit of greenhouse gas added to the atmosphere than do most of the two-dozen climate models that were evaluated in the most recent Intergovernmental Panel on Climate Change Assessment (IPCC 2007). Simulations of temperature and precipitation from another climate model, the National Center for Atmospheric Research's Parallel Climate Model (PCM1), were also obtained and downscaled for the present study. The PCM1 model warms less than most of the other IPCC climate models. By considering climatic responses simulated under high-emissions A2 and low-emissions B1 scenarios by highly responsive GFDL and a minimally responsive PCM model, this study, when required, had the opportunity to evaluate potential impacts from the broad range of possibilities spanning the range of scenarios presented in the most recent IPCC global assessment. These same scenarios were also key components of the recent State of California climate-change assessments (Cayan et al., 2008, 2009).

2.2 Approaches to Downscaling

Downscaling is the process of transforming simulated climate variables from coarse-grid climate models to produce estimates of what climate variables would look like at higher resolution of spatial scale. Many different approaches to downscaling have been developed and used in assessment studies. Two broad categories of downscaling methods are statistical methods (which use a variety of statistical models or relations between coarse-grained historical observations and their higher resolution counterparts as a basis for inferences about the high-resolution implications of climate-model outputs) and dynamical methods (which apply climate models that have much finer grid spacings but over limited areas of the Earth to fill in detail over a desired area) (e.g., Wood et al. 2004). Dynamical methods will ultimately provide more physically consistent and flexible visions of the future but at present suffer from very high computation costs so that it is still rare to see dynamically downscaled products that span more than 20-30 years. Furthermore dynamically downscaled products still maintain, or even worsen, biases suffered by the global models, so that it is generally necessary to statistical correct even the dynamically downscaled products before they are suitable for use. Statistical downscaling is much less computationally burdensome and typically has bias corrections as an integral part. The statistical methods, however, make explicit or implicit assumptions that historical (statistical) relations between coarse-grained climatic variables and their high-resolution counterparts will not change in the future as the global climate changes.

2.3 Downscaling of Tahoe Basin Climate Data

In this study, a statistical method, called constructed analogs method (Hidalgo et al., 2008), was used to downscale daily global climate-model outputs from their original roughly 2º latitude-longitude grid spacings onto a 1/8º (roughly 12 km) grid. Figure 2-2 is a schematic of the method wherein, given a coarse-gridded depiction of some day’s climate (weather), the first step is to identify a set of days with coarse-gridded climate patterns in the historical record that are similar to the model pattern. The linear combination of the weather maps from these coarse-grained historical analogs that best fits the model pattern is determined by simple linear regressions. The constructed analog method then applies the same regression coefficients to the high-resolution maps of those historical analog days to obtain a high-resolution version of the original model weather. In order to test the method, daily historical climate datasets were coarsened to global-model grid spacings and then downscaled by constructed analogs, with results compared to the original, unmodified high-resolution fields. Figure 2-3 shows the correlations between daily “anomalized” temperatures and precipitation totals from the unmodified datasets and from the coarsened-and-then-downscaled results, where “anomalized” means “with long-term-mean seasonal cycles removed at each grid cell” so that no credit is given for knowing that winters are colder than summers or that high places are cooler than low, etc. High-resolution temperature variations are very well recovered in this experiment with anomaly correlations dipping no lower than 0.8 over most of the US, and remaining well about 0.9 over the Tahoe basin.

Precipitation is more difficult and at daily scale anomaly correlations are at best about 0.7 over the Tahoe basin. However, when the daily precipitation values are summed to form monthly totals and those monthly totals are compared, the anomaly correlations are quite high (>0.95). Thus the constructed analogs method can recapture high-resolution historical temperature and precipitation variations from a version of the historical record that has been re-gridded onto the coarse global-climate model grids with impressive skill.

Temperature trends in downscaled versions of the GFDL projections under A2 and B1 emission scenarios are shown in Figure 2-4. Temperatures rise by somewhat over 4ºC in the vicinity of the Tahoe basin by 2100 under the A2 emissions scenario and by about 2.5ºC under B1 emissions. Under both scenarios, the GFDL responds to greenhouse-gas emissions with drying trends of 10 to 20 cm/yr/century over the Sierra Nevada and Tahoe basin (Figure 2-4). Figure 2-5 shows projected temperatures and precipitation from the less-sensitive PCM1 model under the A2 emissions scenario. Under the A2 emissions, the GFDL model projects warming by over 4ºC in the vicinity of the Tahoe basin (Figure 2-4) whereas the PCM1 model projects only about 2ºC warming (Figure 2-5). Both models (PCM1 not shown) warm considerably less under the B1 emissions, so that although there is considerable uncertainty about the actual magnitudes of warming to be expected—as indicated by the model-to-model differences in Figure 2-5—less emissions (e.g., B1) is projected to result in less change in whichever model turns out to be closer to the real future. The PCM1 projections of future precipitation (Figure 2-5) yield less precipitation change than does the GFDL model (Figure 2-4), indeed very little change at all over the Tahoe basin.

Most climate-change assessments have focused entirely on projections of temperature and precipitation change. In this study, given the central role of surface heat balances in Lake Tahoe to its deep-mixing and turn over, its future water quality and clarity, and to the microclimate of the basin, several additional climate variables were also downscaled and assessed. These additional variables were surface-wind speeds, downward shortwave (solar) radiation fluxes and downward longwave (infrared) radiation fluxes at the surface, and were used primarily in the DLM - Lake Clarity Model. Because historical observations of these variables are much less common than those of temperature and precipitation, no entirely observationally based historical grids of these variables are available. Therefore the strategy used here was to draw instead upon the high-resolution regional-climate model output (called CARD10; Kanamitsu and Kanamaru 2007a,b) from a historical simulation of climate on a 10-km grid over California and Nevada that was closely constrained each day by observations and a global climate product called the NCAR/NCEP Reanalysis fields. This regional-model product is the best approximation available as to how climate variables like surface winds and radiative fluxes varied over the landscape at high geographic resolutions and on a daily basis from 1950-1999. The CARD10 variables were treated the same as the observationally based historical temperature and precipitation fields discussed earlier to test the applicability of the constructed analogs method to downscaled these variables from global-model outputs and to downscaled future variations of these variables. Notably, the GFDL outputs included these additional variables, but the PCM1 team did not save and share these variables, so that only the GFDL trends in these variables can be considered here. Also, problems with output for humidity saved from the GFDL projections prevented us from being able to downscale humidities for this study.

Figure 2-6 shows anomaly correlations between monthly means of historical CARD10 values of surface-wind speeds, downward shortwave insolation, and downward longwave radiation and coarsened-and-then-downscaled versions of the same. Downward longwave fluxes are very well downscaled (correlation > 0.95 over Tahoe basin), surface-wind speeds also are reasonably well recovered (> 0.9), and downward solar radiation somewhat less so (>0.75 or 0.8) at this monthly scale, giving some confidence in the downscaled projections shown in following figures. Notably, surface-wind speeds were not directly downscaled in this test, but rather southerly and westerly wind components were downscaled in parallel from global-model values and only then combined to calculate wind speeds, which were tested here.

Downward longwave radiation is projected to increase under both the A2 and B1 scenarios (Figure 2-7). This is the essence of the greenhouse effect; more greenhouse gas in the atmosphere results in more trapping of heat in the atmosphere, especially more trapping of longwave heat fluxes, and thus more warming and re-radiation downward of longwave heat towards the surface. Under the A2 scenario, more greenhouse gases are emitted and downward longwave fluxes increase more than under the B1 emissions. In the downscaled fields, downward longwave radiation increases about three times as rapidly under A2 as under B1 emissions.

Downward solar insolation changes much less (in watts/m2) than do longwave radiative fluxes in the GFDL projections. In the downscaling experiment here, solar insolation appears to decline slightly under A2 emissions (due to increased cloudiness) and may increase even less under B1 emissions (Figure 2-8). Similarly mean surface-wind speeds are projected to change by only a few percent on average over the Lake Tahoe basin, under the two emissions scenarios (Figure 2-9).

This downscaled model output provides us with a reasonable view of how meteorologic conditions will change in the Tahoe basin over the next 100 years under various, internationally accepted emission scenarios. Given that GCM model output is much too coarse for looking at localized or regional affects, it was imperative that this downscaling exercise be done prior to any further analysis. The product of the Tahoe basin downscaling is unique, with no other climate modeling results of this type available for this region. The modeled meteorologic conditions in the 21st Century allows us to (1) evaluate changes in basin hydrology under climate change – and compare this to past trends (Chapter 3), (2) use this meteorologic output to drive a series of management models customized for application in the Tahoe basin (i.e. LSPC^{++} Tahoe Watershed Model, Pollutant Load Reduction Model and the DLM Lake Clarity Model (Chapters 4, 5 and 6). Finally, this downscaled output is now available for use by others who wish to study the ecological (e.g. fire frequency, vegetation type) or economic (e.g. snow-dependent recreation) impacts of climate change in the Tahoe basin. This contribution is viewed as a significant product of this study.

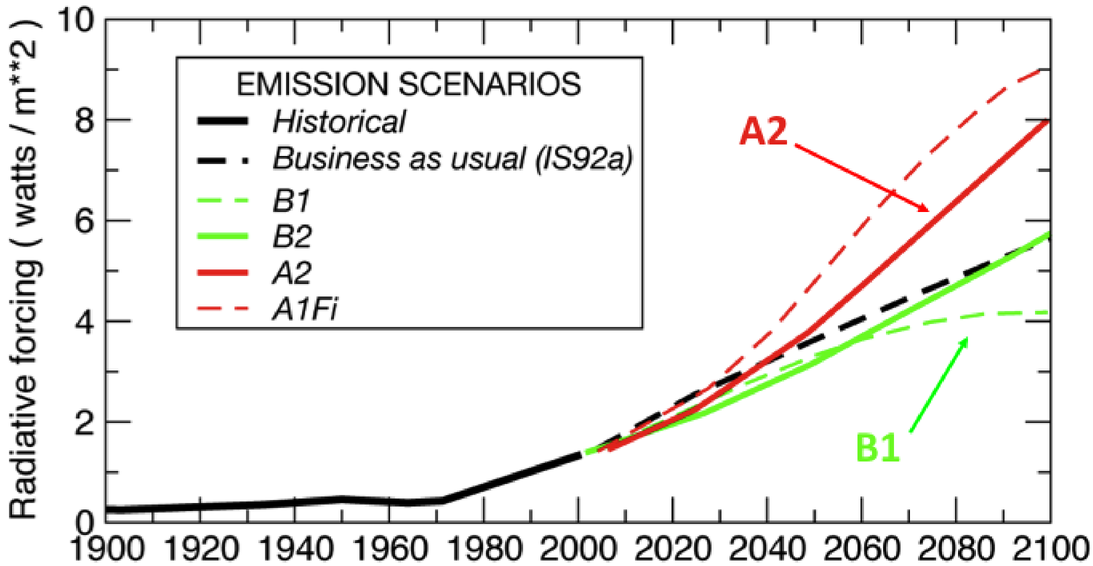

Figure 2-1. Changes in global anthropogenic greenhouse-gas radiative forcing of climate in the 20th Century and under several scenarios of future emissions.

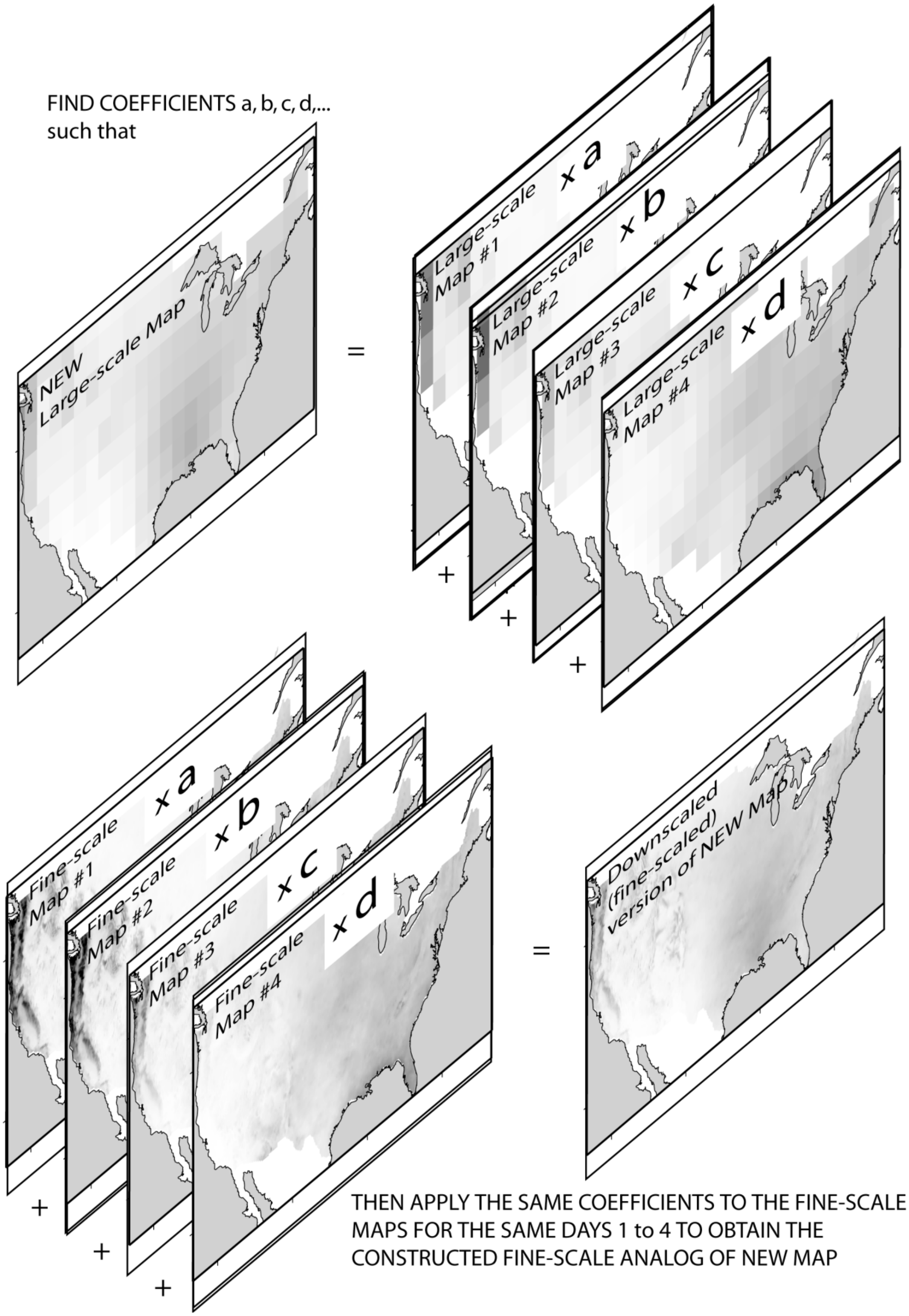

Figure 2-2. Schematic depiction of the two primary steps in downscaling climate model outputs by constructed-analogs method. More detailed description available at http://www.energy.ca.gov/2007publications/CEC-500-2007-123/CEC-500-2007-123.PDF

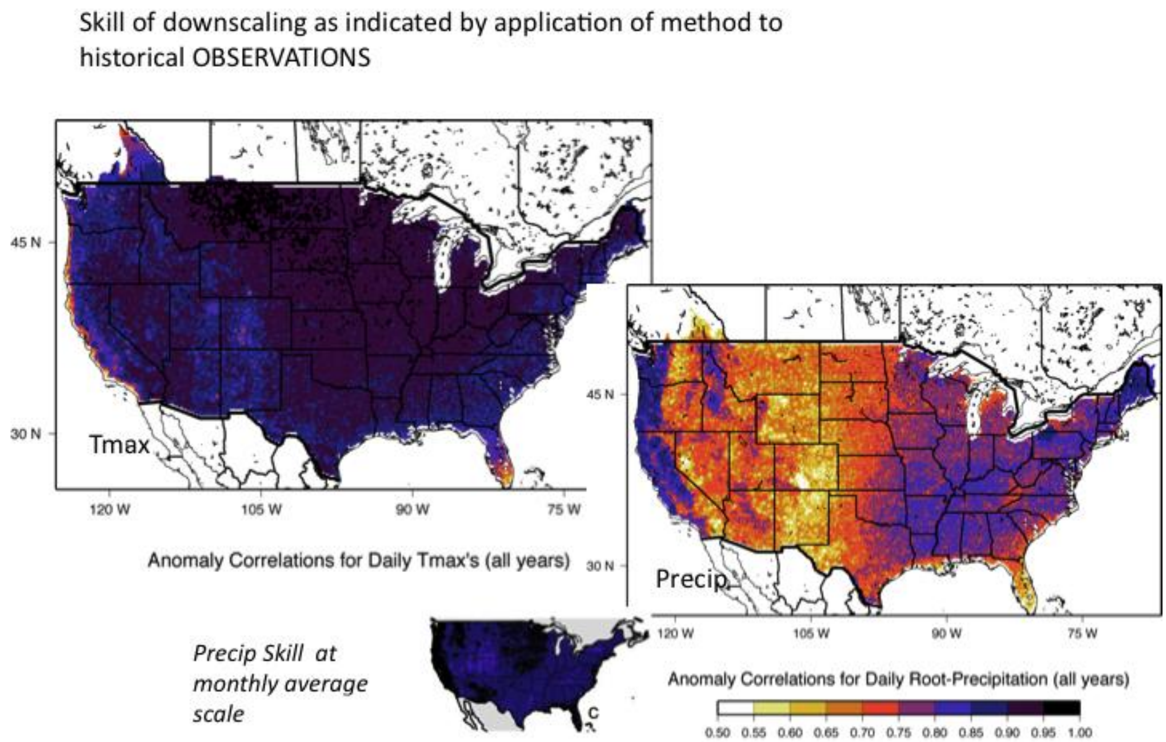

Figure 2-3. Anomaly correlations between gridded, observed daily temperatures and precipitation and versions of same obtained by aggregating high-resolution observations to global-climate model gridding and then downscaling back to original, 1/8º gridding by constructed-analogs method of Hidalgo et al. (2008); inset shows anomaly correlations for monthly precipitation totals. Anomaly correlations are correlations between variables that have had long-term mean seasonal cycles removed at each grid cell. Base period for all calculations is 1950-1999.

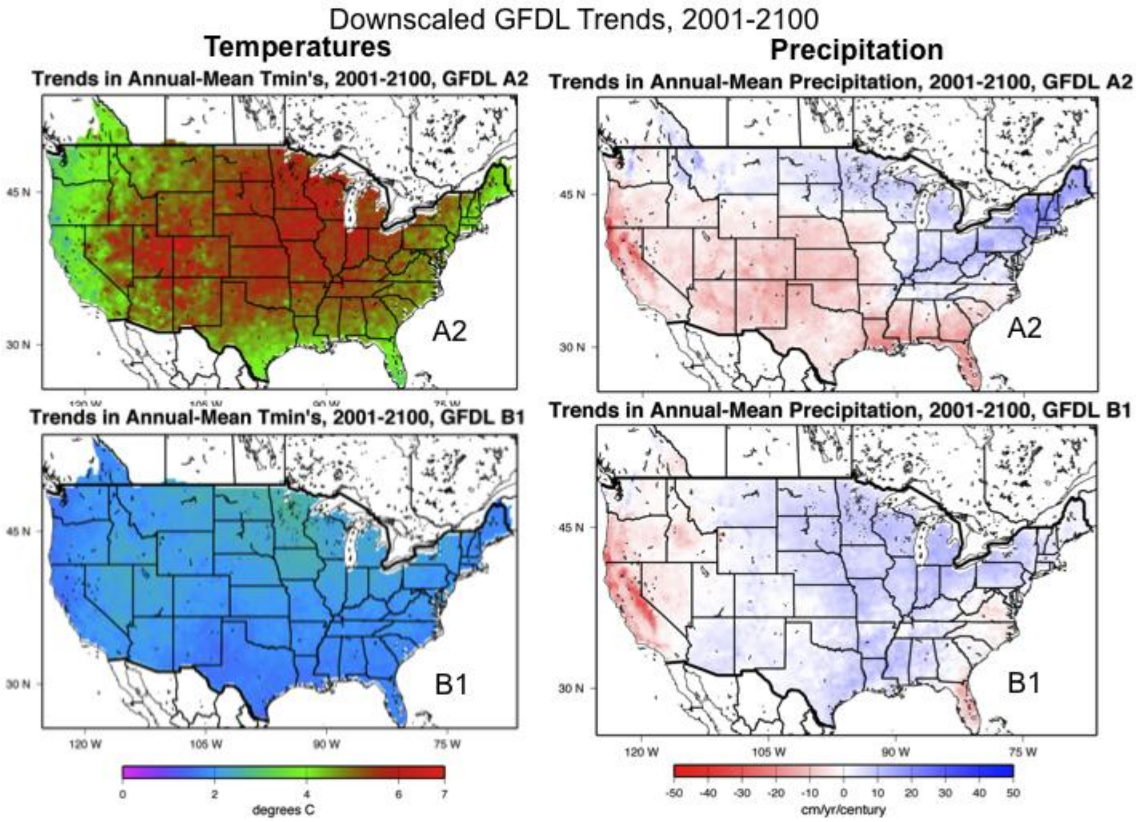

Figure 2-4. Downscaled temperature (left panels) and precipitation (precipitation) trends under A2 (top panels) and B1 (bottom panels) emission scenarios from the GFDL global climate model.

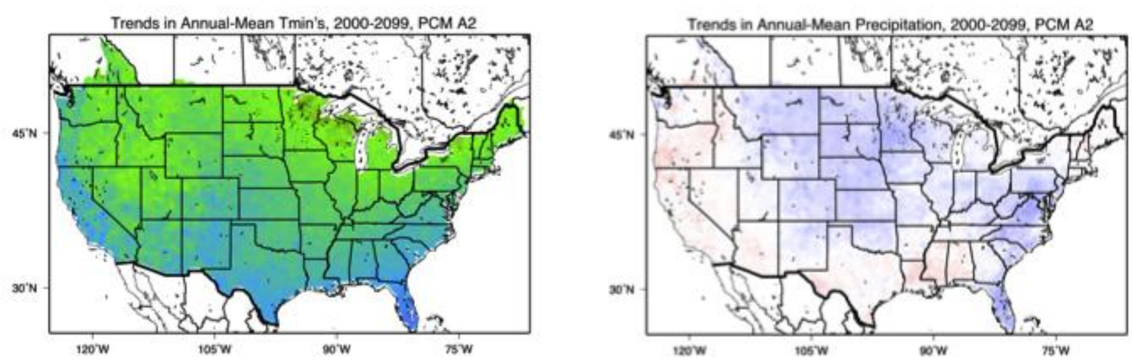

Figure 2-5. Same as Figure 2-4, except for projections by PCM1 climate model under A2 emissions scenario; same color bars as Figure 2-4.

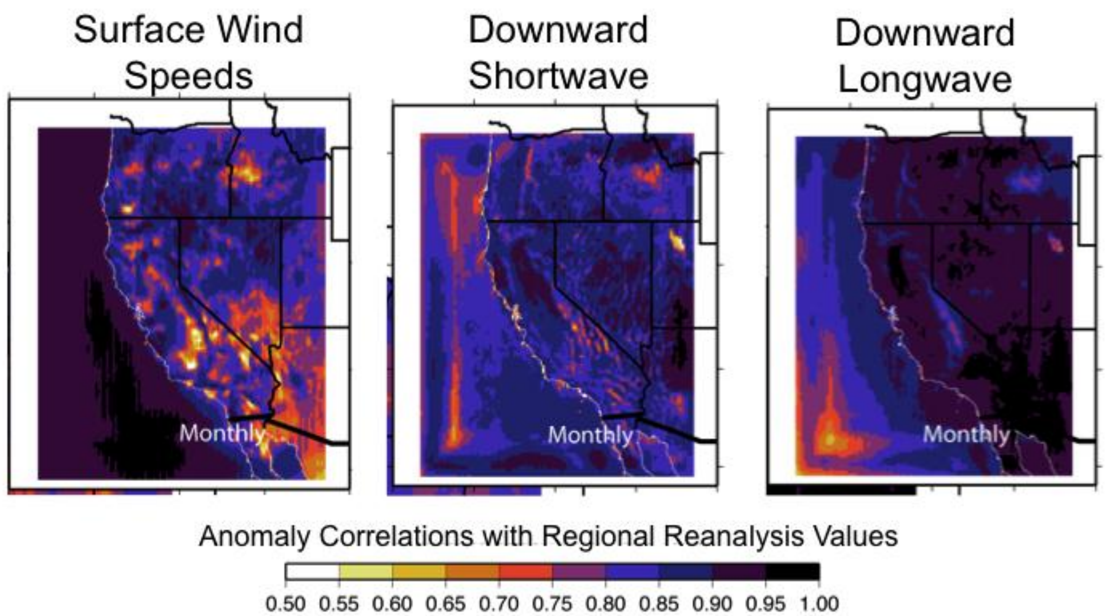

Figure 2-6. Same as Figure 2-3, except for monthly surface-wind speeds, downward shortwave (solar) insolation, and downward longwave radiation.

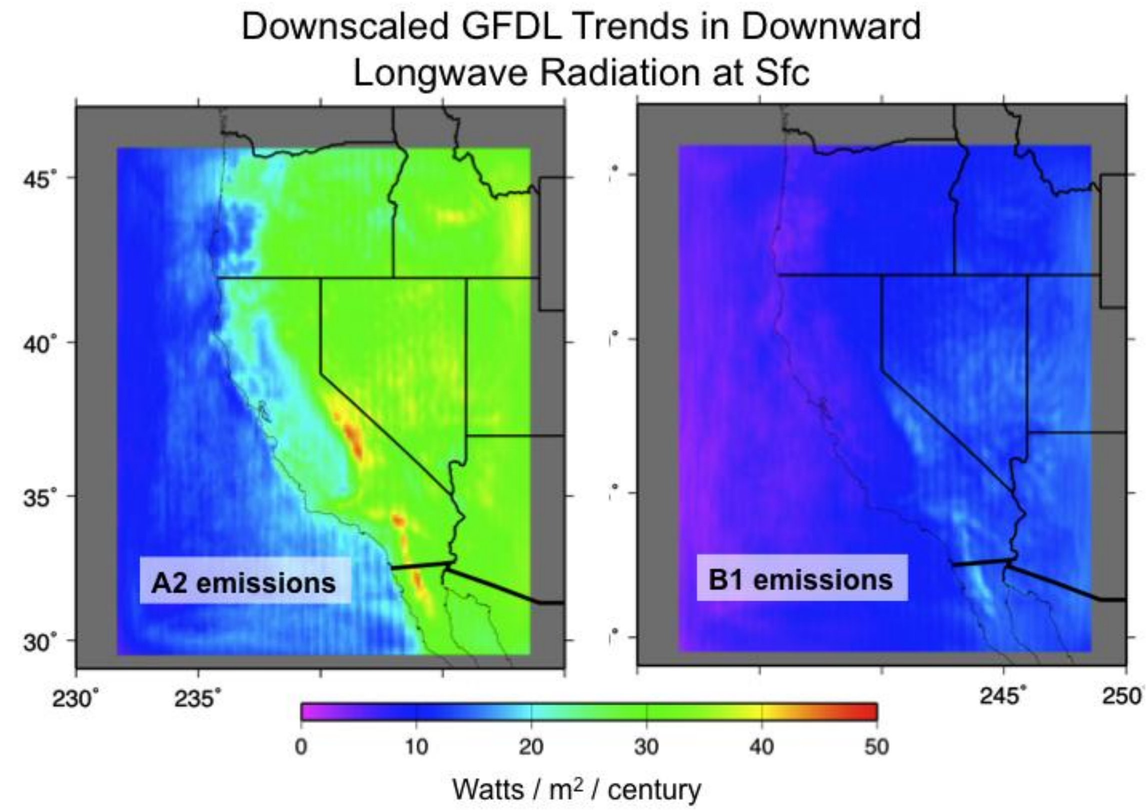

Figure 2-7. Trends in downscaled projections of downward longwave radiation from the GFDL global climate model under A2 (left) and B1 (right) emissions scenarios.

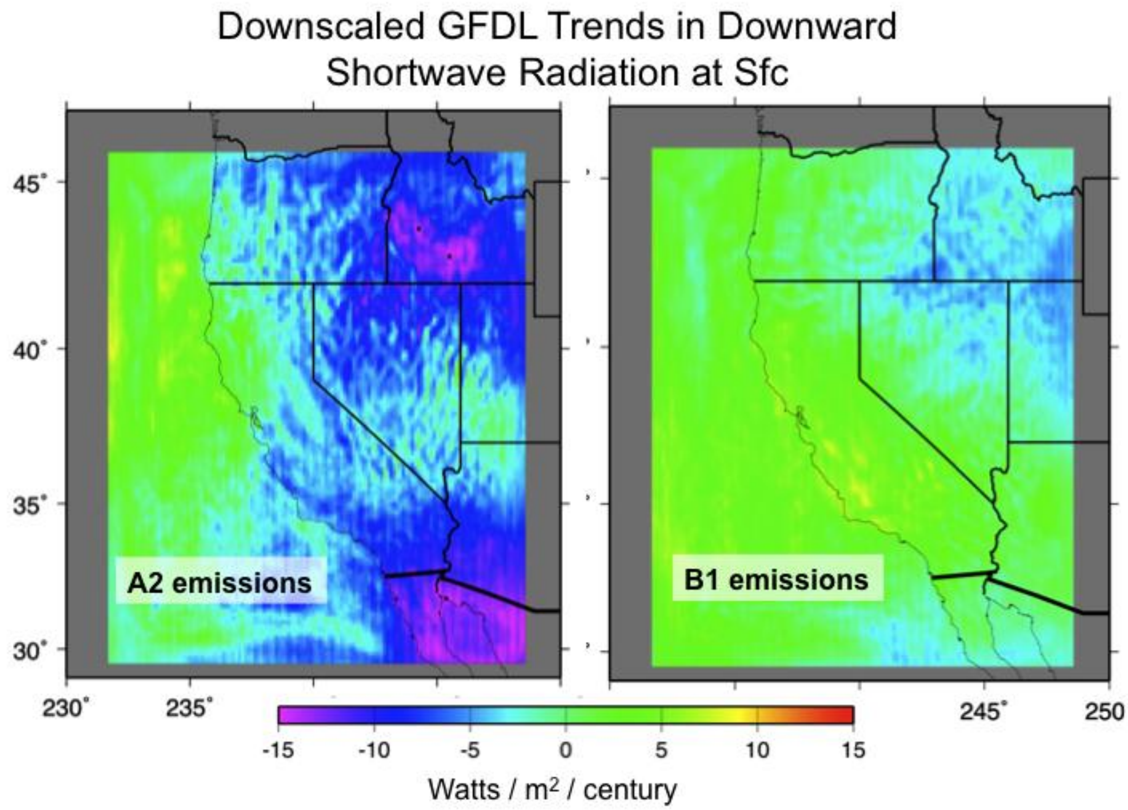

Figure 2-8. Same as Figure 2-7, except for downward shortwave (solar) insolation.

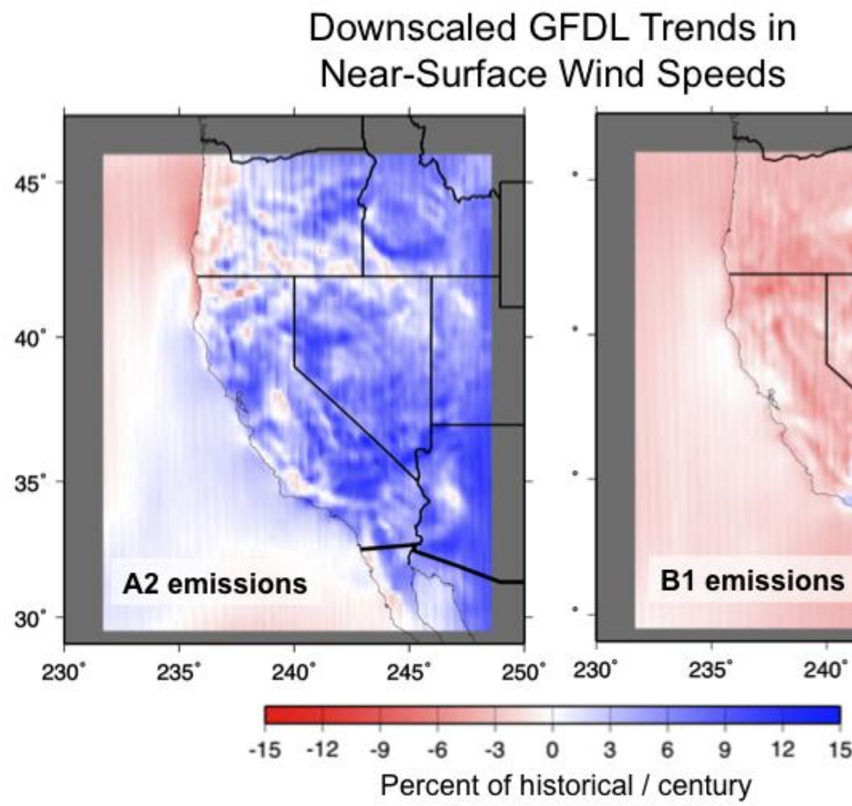

Figure 2-9. Same as Figure 2-7, except for surface-wind speeds.

3.0 HYDROLOGIC IMPACTS: PAST AND PROJECTED TRENDS

Authors: Robert N. Coats Ph.D. and Mariza Costa-Cabral Ph.D.

3.1 Methods

3.1.1 Air temperature and precipitation

The downscaled daily maximum and minimum air temperatures were used to calculate daily and annual averages for individual grid points, as well as basin-wide averages for the 12 grid cells used for the Tahoe basin. The results were plotted to illustrate the future temperature trends, and the average daily temperature for the basin was used with the adjusted precipitation data to examine the trend in fraction of precipitation falling as snow over the basin.

Global climate models adequately represent large-scale (200-500 km) circulation patterns, temperature and precipitation (the latter with lesser accuracy). Before GCM results can be useful for hydrologic applications, a number of computational techniques must be applied. First, there is a mismatch between the needs of a hydrologic model (typically working at a spatial scale within 0.01°-0.5°) and the coarse scale of GCMs (2°-5°). "Downscaling" refers to the process of generating finer-resolution data from the coarse GCM data. The daily GCM results were first downscaled to a 7.5 min (1/8°) grid scale, using the method of constructed analogues (Hidalgo et al., 2008; also see Sections 2.2 and 2.3, this volume).

The precipitation dataset resulting from constructed analogues downscaling, when compared to observations at local meteorological stations, showed an excess of precipitation days over the historical period. In the present case the issue was not an over-abundance of low-precipitation days (the "model mist" that is common in daily GCM results) but an excess of event days of all daily-precipitation magnitudes. Therefore, the simulated precipitation time series for the historical period (1950-1999) by either GCM was treated to remove precipitation events by random event selection. Any precipitation event in each of the 12 months was subject to removal with equal likelihood, regardless of event length or precipitation total, a process we termed "resampling". Resampling continued until the number of event days for each of the 12 months matched the observations. Prior to resampling, the simulated distribution of event lengths approximately matched observations. Our resampling technique, by construct, preserved the distribution of simulated event lengths.

For the simulated future time series, resampling was carried out under the assumption that each GCM produces, for any given month, a consistent proportion of excess number of precipitation days, regardless of a climate warming trend. Thus, the same percentage of precipitation days was removed for the 100 months of September (e.g.) in a future simulated time series, as the percentage removed for the 50 months of September in the historical time period for the same model. (September was cited as an example. The same applies to all 12 months.)

The GCM-simulated precipitation time series for the historical period was then subjected to "quantile mapping," as in the BCSD (bias correction and statistical downscaling) technique introduced in Wood et al. (2002 and 2004). In quantile mapping, for any one of the 12 months each simulated daily precipitation value *x* is replaced by the observed value *x'* having the same plotting position as *x*. As a result of quantile mapping, the distribution (eCDF) of simulated daily precipitation in the historical period matches the observed distribution.

An important difference between our quantile mapping procedure and that introduced in Wood et al. (2002 and 2004) is that we performed it at the daily time scale rather than monthly. We found that mapping at the daily time scale resulted in monthly distributions in good agreement with observations for the winter months (i.e., the main precipitation months), and in annual distributions that are in good agreement with observations.

For the future (projected) time series of precipitation, a similar technique was used. Each simulated value *y* is replaced by an observed value *x'* having the same plotting position as a value *x=y* in the historical simulations. If the exact value *x=y* is not found in the historical simulations, then interpolation between the two nearest points is used. In the case of an extremely high value *y* that is larger than any value in the simulated historical time series, then a fitted theoretical distribution is used that extends the range of that historical distribution for that month. We experimented with several theoretical distributions and chose the Exponential distribution because it provides one of the best fits and is computationally simple. The method is described in more detail in Appendix 9.2.

The distribution of annual maxima is well represented in the downscaled time series for the annual 1-day maxima, but under-represents the highest values of 3-day annual maxima (for both GFDL and PCM). This is tentatively attributed to a lower degree of temporal correlation in the simulated time series during heavy storms, as compared to observations.

3.1.2 Wind Speed

Downscaled wind speed for the Tahoe basin was available only for the GFDL (A2 and B1 scenarios), but not for the PCM. The only long-term wind daily data that can be used to calibrate the modeled GFDL wind are from the South Lake Tahoe Airport, for the period 1989-2004. An examination of the modeled winds showed that they were primarily unrealistically high. To adjust them downward, we used a quantile mapping approach similar to the bias correction method used for precipitation. The details of the wind adjustment are shown in Appendix 9.1.

3.1.3 The Palmer Drought Severity Index

The Palmer Drought Severity Index (PDSI) is a widely-used and convenient index of regional drought, and has been used to characterize the effect of climate change on drought duration and severity (Kothavala 1999). Palmer (1965) defined a drought period as "an interval of time…during which the actual moisture supply at a given place rather consistently falls short of the climatically expected…moisture supply." The index is based on a soil water balance model in which the soil is treated as two connected "buckets". Evapotranspiration is calculated by the empirical Thornthwaite (1948) method. PDSI can be calculated at a weekly or monthly time scale from average weekly or monthly temperature, precipitation and the available water capacity (AWC) of the soil. Soil water deficit in the model is cumulative, so that the index reflects the persistence of a drought. The simplicity and relatively low data requirements are both an advantage and weakness of the PDSI (Alley 1984).

The PDSI calculation involves calculating a set of four water balance coefficients from regional climate data, for potential evapotranspiration, potential recharge, potential loss and potential runoff. The formulation of the model that we used is “self-calibrating” in that these four coefficients are calculated for each set of input precipitation and temperature data, to produce a predetermined distribution of the PDSI (Wells et al. 2004). This means that the PDSI values for one climatic region or time period cannot be compared with those of another, because both results will have about the same distribution of PDSI values. The method can, however, but used to compare time trends between regions or between climate change scenarios.

To calculate PDSI, we selected a subwatershed near Tahoe City. We used the LSPC hydrology model (see Section 4.0) to generate daily rainfall, snowmelt and runoff, along with average daily temperature. Daily snowmelt was added to rainfall to generate total soil water input, so the model results should reflect the impact of changes in snowfall and snowmelt timing on available soil water. Daily values of soil water input were added and daily temperature values were averaged to get weekly input data for use in the model. AWC was taken from the NRCS Soil Survey Report for the Tahoe basin.

3.1.4 Streamflow Statistics

For characterizing the projected shift in snowmelt timing over the 21st century, we used the date of the centroid of the annual hydrograph (Barnett et al. 2008; Stewart et al. 2005). This value, called the Center Timing (CT), is calculated as the discharge-weighted mean day in the water year, i.e. $CT = \Sigma(t_i q_i)/ \Sigma(q_i)$, where t_i = the ith day in the water year, and q_i = discharge on the ith day.

Previous work on the shift in snowmelt timing in the Tahoe basin examined the trends in both the spring snowmelt peak timing (SMPT) and CT (Coats 2010). The former is more sensitive spring temperature trends, and for 5 streams in the Tahoe basin, the timing shift (1972-2007) averaged -0.4 days yr^{-1}, whereas the CT did not show significant trends for basin streams. The CT is thus is a more conservative measure of the shift in runoff timing than the SMPT, possibly because springtime air temperatures in the Sierra are increasing faster than those in fall and winter (Coats 2010; Cayan et al. 2001). The CT also has the advantage that it is influenced by large winter rainstorms as well as by snowmelt, whereas the SMPT only reflects snowmelt timing.

The Upper Truckee River (UTR) is the largest tributary watershed of Lake Tahoe (142 km^2), accounting for about 17 percent of the annual runoff to the Lake (Jeton 1999). The highest elevation in the UTR is 3,067 m, and at higher elevations much of the annual precipitation falls as snow. The LSPC hydrology model calculates the hourly streamflow for the 183 defined subwatersheds in the Tahoe basin for the GFDL B1 and A2 scenarios, and routes the discharge downstream to the Lake (Riverson et al. 2010). We averaged the UTR hourly discharge by day over the modeled 21st century to calculate mean daily discharge (MDQ) and calculated the CT date for each year.

For the MDQ values from the GFDL B1 and A2 scenarios, we developed flow duration curves for the UTR, for the periods 2001-2033, 2034-2066 and 2067-2099. A flow duration curve shows the percent of the time that a given discharge is equaled or exceeded. To remove apparent bias in the GFDL/LSPC daily discharge, we first calculated flow duration curves from the USGS record, and from the GFDL/LSPC output for the same historic period (1972-1999). We then interpolated log discharge at equal values of exceedance (e.g. 0.1, 0.2…100 percent of the time), and found the equation (a 3rd - order polynomial, with $R^2 = 0.995$) that mapped the historic modeled curve onto the curve from the gage data. We then used this equation to adjust the projected future flow duration curves.

A flow-duration curve is useful for characterizing the total time distribution of stream discharge, but it is not very useful for showing the frequency of extreme high and low discharge events. To analyze the projected changes in flood frequency for the UTR over the 21st century, we first compared the flood frequency curve from the historic (1972-1999) gage record for the UTR (USGS Station No. 10336610) with the curve derived from the maximum annual GFDL/LSPC hourly discharge for the same period. Log-Pearson flood frequencies were estimated with the method of Bulletin 17B (USGS 1982) for flood flow frequency (http://www.usgs_pub_17b_flood_flow.pdf, except that outliers were not excluded.

The comparison of the two curves showed that the GFDL/LSPC curve was somewhat higher than the curve from the gage data. To adjust the modeled output to the same scale as the measured discharge, we used a linear regression of the log flood magnitude from the USGS data versus the modeled log flood magnitude, at equal recurrence intervals ($R^2 = 0.997$). The resulting equation was then used to adjust the modeled flood frequency curves downward. We then calculated confidence limits for the estimated flood frequencies according the Bulletin 17B method, and compared the calculated flood frequencies from the USGS gage record (1972-2008) with the projected frequencies for the three 33-yr periods in the 21st Century (Zou and Donner, 2007).

The shift in snowmelt timing suggests that we might expect an increase in frequency of low-flow events. To test this hypothesis, we calculated the annual minimum 5-day low flow for the UTR for the GFDL A2 and B1 cases, and tested for a time trend over the 21st century, using Mann-Kendall test (Helsel et al. 2005; Helsel and Franz 2006).

3.2 Results and Discussion

3.2.1 Air Temperature

Figure 3-1, panels a-d shows the projected average annual T_{max} and T_{min}, spatially averaged over the Tahoe basin, for the A2 and B1 emissions scenarios, according to output from the PCM and GFDL models. The upward trends for the A2 scenario are greater than for the B1, and the GFDL model tends to produce a more rapid warming trend than the PCM. The trend for the GFDL A2 amounts to an increase over the 21st century of about 5°C. At an average adiabatic lapse rate, this is theoretically equivalent to moving the lake from its present elevation of 1900 m down to an elevation of about 1130 m. This would have a major effect on lake temperature, as well as on the equilibrium climax vegetation in the basin.

3.2.2 Precipitation

The modeled 21st century trends in total annual precipitation are shown in Figure 3-2 (a-d). These totals represent bias-corrected basin-wide averages, as explained above. The curves are from a LOWESS smoothing (Helsel and Hirsch 1995). The trends are not very striking, except perhaps for the drying trend for the GFDL A2 case during the latter half of the century. The important change is not in the total amount, but in the form of precipitation. The shift from snow to rain (averaged over the 12 7.5' cells for the Tahoe basin) is shown in Figure 3-3. Since the average includes cells centered over the lake, the trend slope is greater than the trends shown for the 183 LSPC watersheds in Figures 4-3 and 4-4, since average elevation of the watersheds is higher than the Tahoe basin average.

The shift from snow to rain will result in less springtime water storage in the pack. This will decrease the water availability for plants, and contribute to earlier drying of fuels on the forest floor (Westerling et al. 2006). A thinner snowpack will also likely have a negative effect on winter recreation.

The slope of the trend from snow to rain in Figure 3-3 may be on the low side. In a study based on 30 years of snow survey data (1966-1996) from 260 snow courses in the Sierra Nevada, Johnson et al. (1999) found that the Tahoe basin had the highest loss—54 percent—in May snow water equivalent (SWE) of any of the 21 river basins studied. This is consistent with the observation of Coats (2010) that the historic warming trend for the Tahoe basin is higher than that for the surrounding region. The modeling and downscaling procedure used in this study cannot capture such regional differences.

3.2.3 Wind

Trends in wind enter into our modeling in two ways. First, wind plays a role in the snowmelt routine of the LSPC, since warm winds accelerate snowmelt. During a rain-on-snow event, the transfer of sensible heat from the air by advection contributes more to the melting of the pack than the heat content of the rain. Second, wind plays a major role in mixing the lake.

Different climate models can produce conflicting results for trends in wind. Unfortunately there were technical problems in downscaling the PCM winds, so the hydrologic and lake modeling proceeded with only the GFDL.

It is important to consider both the trends in average and extreme winds, since both may play a role in lake mixing. The seasonal distribution is critical, since summer winds may deepen the warm epilimnion (increasing stability) and winter winds are responsible for deep mixing and breaking down the thermal stratification. Figure 3-4 shows the significant trends in average monthly winds, and Figure 3-5 shows the trends in maximum monthly wind. Note that winds tend to increase during the summer, and decrease in fall and winter. Both of these trends will contribute to increased thermal stability of the lake.

3.2.4 Drought

The Palmer Drought Severity Index (PDS) responds to changes in temperature and precipitation over the 21st century. Figure 3-6 shows the results for Tahoe City, for the GFDL A2 scenario. There is a downward trend (increasing drought) to about 2045, followed by a 15-yr trend toward wetter conditions, and then a steep trend toward drought for the remainder of the century.

3.2.5 Streamflow Statistics for the Upper Truckee River

With both the B1 and A2 scenarios, the GFDL shows a downward trend in the Center Timing of annual runoff of the UTR (Figures 3-7a and 3-7b) over the 21st century. The shift toward earlier timing of the hydrograph centroid reflects both earlier spring snowmelt and the shift in precipitation from snow to rain. The trend in CT is consistent with the scientific literature (e.g. Dettinger et al. 2004; Cayan et al. 2001; Dettinger and Cayan 1995; Johnson et al., 1999; Stewart et al. 2005).

The shift in CT is reflected in the flow duration and low-flow statistics, at least for the A2 scenario. Figure 3-8 shows the flow duration curves for the UTR from both the USGS gage record (1972-1999) and the modeled runoff from the GFDL and LSPC for the same period. These are the curves used in the quantile mapping to adjust the B1 and A2 flow duration curves for the three 33-yr periods shown in Figures 3-9a and 3-9b. In the B1 scenario, the curve for the 2034-66 period falls below the other three curves, but the difference is slight. For the A2 scenario, the daily streamflow for last third of the century falls well below the curves for the first two thirds of the century, and below the historic gage data curve. The shifts in the flow duration curves are reflected in the annual yields for the UTR. The downward trend in annual yield over the 21st century is -0.37 x 10^6 m^3/yr ($P < 0.04$) for the A2 scenario, and -0.29 x 10^6 m^3/yr for the B1 scenario ($P < 0.11$).

From a resource management perspective, the changes in low-flow and flood frequency may be more important than the flow duration statistics. Figure 3-10 shows the time trend in the annual minimum 5-day low flow for the UTR for the A2 scenario ($P < 0.0007$, by the Mann-Kendall trend test). There is no trend in the 5-day low flow under the B1 scenario.

The downward trend in the 5-day low flow may understate the seriousness of the problem from a biological standpoint. The UTR (like many of the Basin streams) flows through coarse alluvium in its downstream reaches, and in very dry years, there is no surface flow. The modeled output of streamflow from the LSPC does not take account of this hydrogeomorphic condition. With the A2 scenario, the frequency of complete drying in the lower reaches of basin streams will increase.

Figure 3-11 shows the calculated flood frequency curves for the UTR gage record (1972-2008) the GFDL/LSPC modeled flood data. The USGS curve is based on the annual maximum instantaneous flow, whereas the modeled curve is based on the annual maximum hourly flow. The latter should be slightly lower than the former, although for a basin the size of the UTR, the two values would not be much different. The modeled curve, however, is higher than the curve for the gage data. The equation relating the two curves that was used to adjust the 21st century computed curves is shown on the figure ($R^2 = 0.997$).

The curves for the two scenarios and three 33-yr periods are shown Figures 3-12a and 3-12b, and the percent change for each from the historic gage record is shown in Figure 3-13a and 3-13b. The greatest impact of climate change on the future flood frequency estimates is for the middle third of the century under the B2 scenario. This is consistent with the GFDL/LSPC results, which show that the reduction in snowpack depth and duration in the middle third of the century (averaged over the Tahoe basin) is actually greater for the B1 than for the A2 scenario. In the latter, the snowpack depth and duration in the middle third of the century are greater than in the first or last thirds of the century (Riverson et al., 2010).

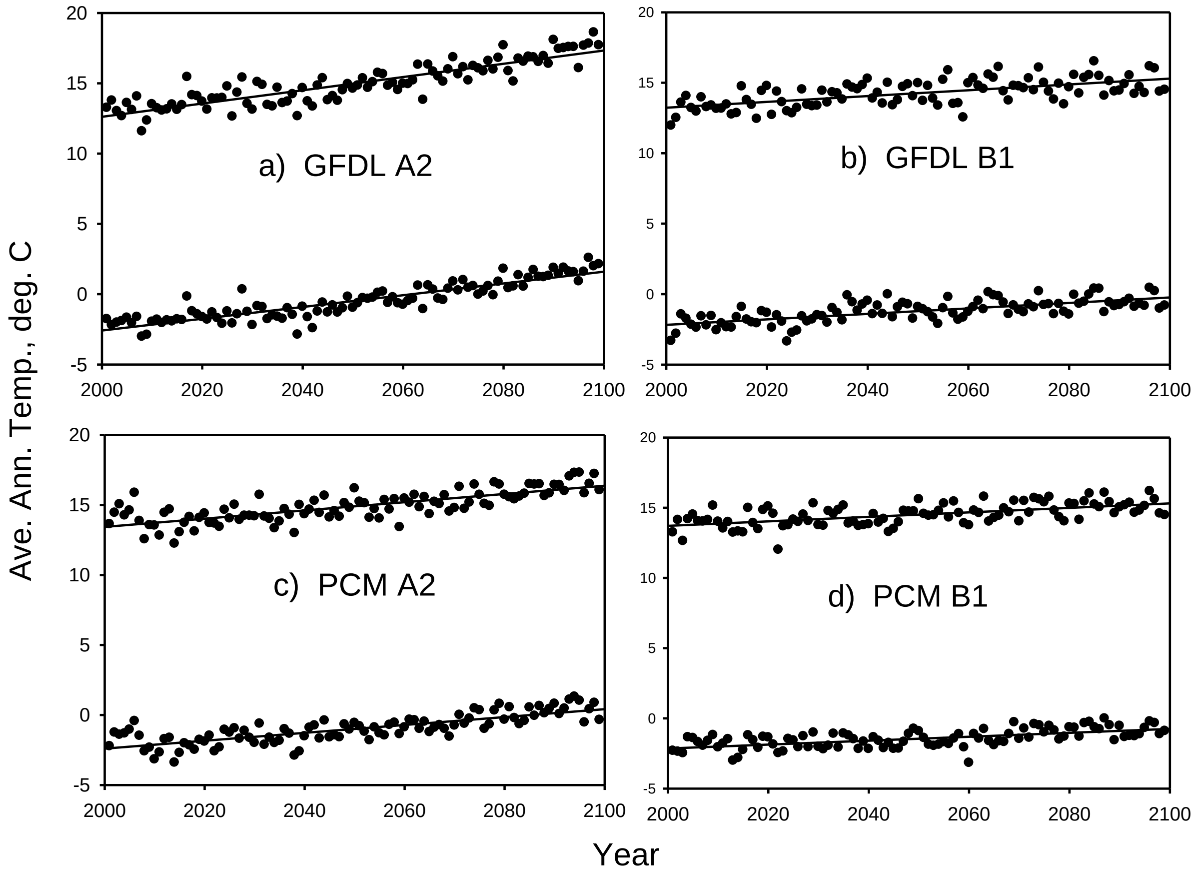

Figure 3-1 (a-d). Projected average annual T_{max} and T_{min}, averaged over the Tahoe basin, for the A2 and B1 emissions scenarios, from the GFDL and PCM results.

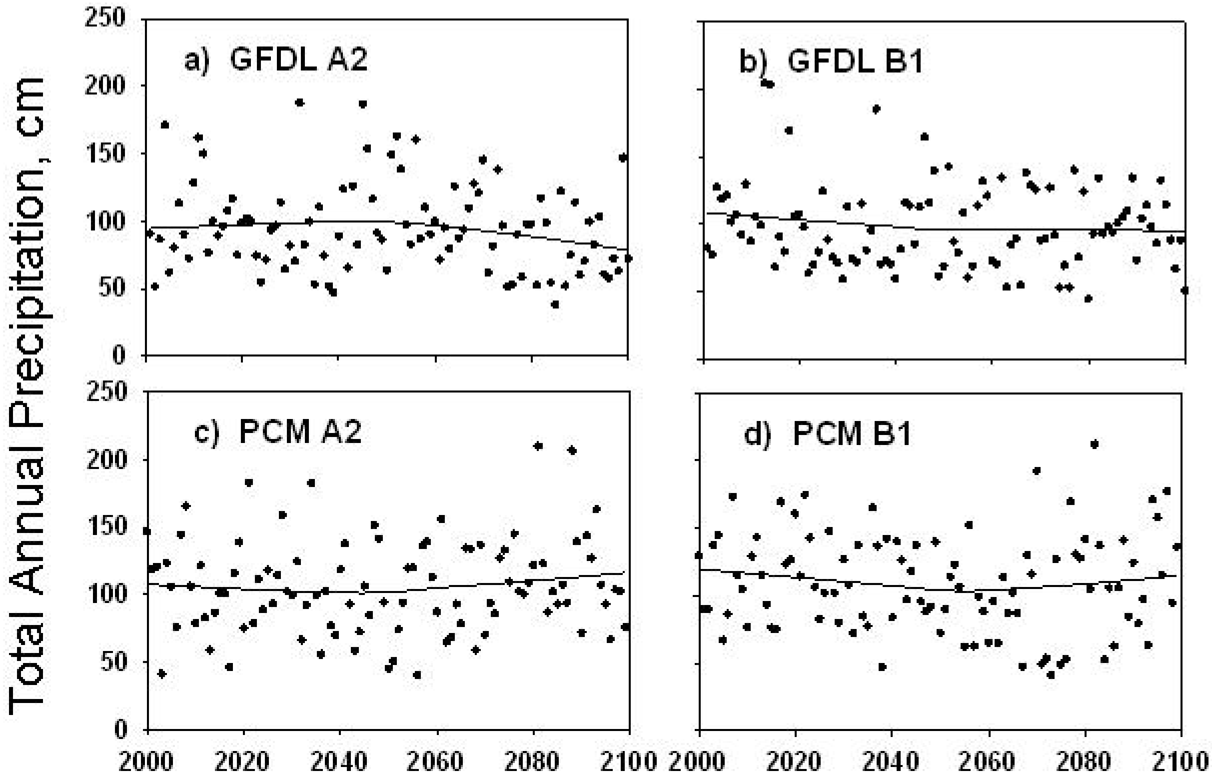

Figure 3-2 (a-2). Bias-corrected annual precipitation, averaged over the Tahoe basin, for the A2 and B1 emissions scenarios, from the GFDL and PCM results.

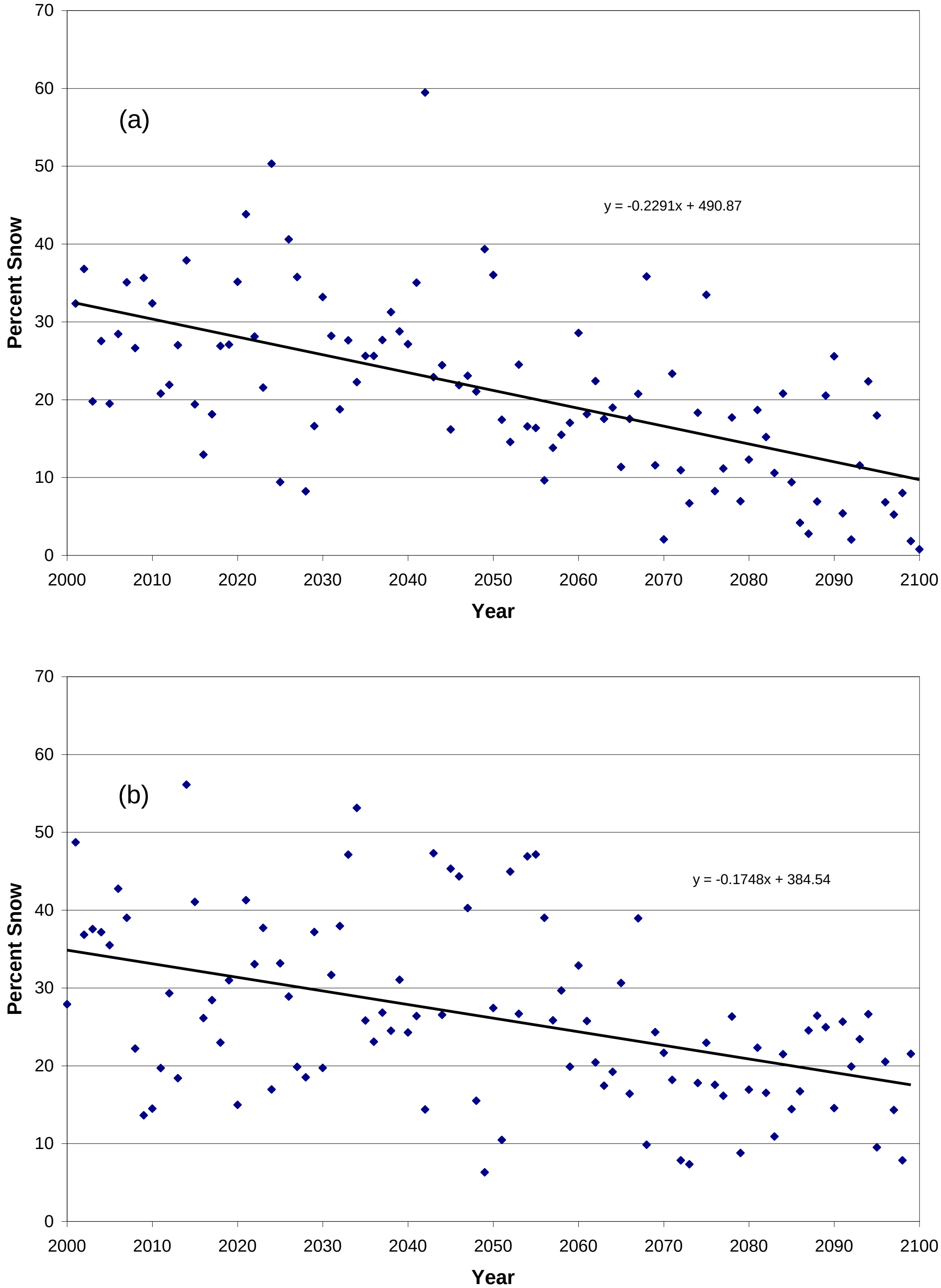

Figure 3-3 (a-b). The trend in the percentage of precipitation falling as snow in the 21st century, averaged over the Tahoe basin. (a) GFDL A2; (b) PCM B1.

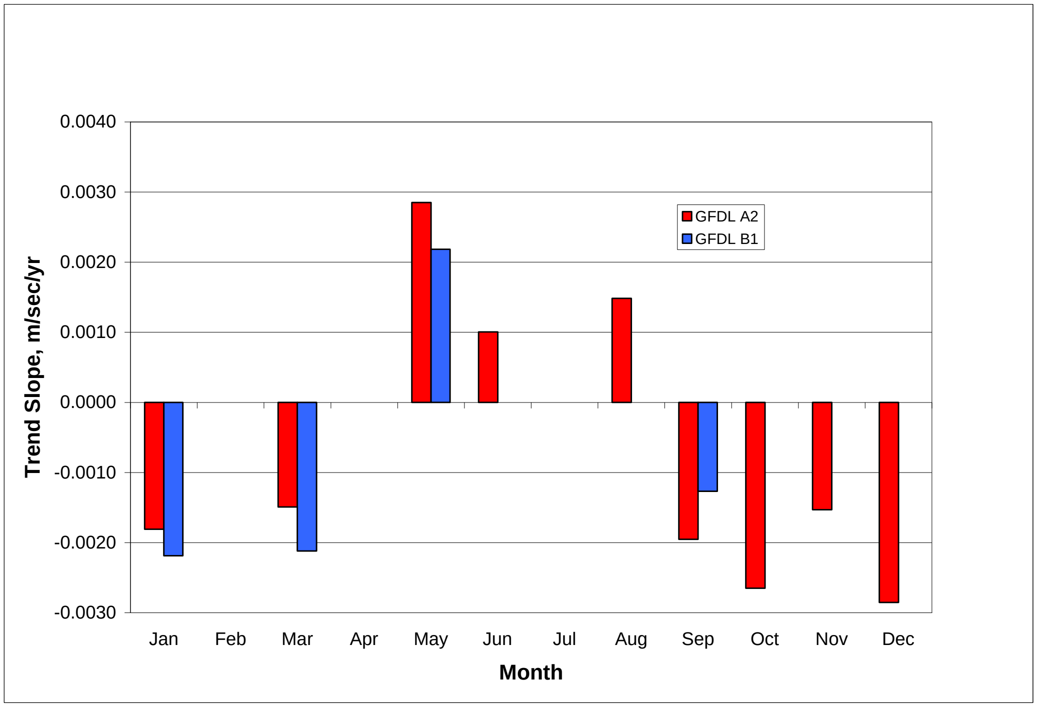

Figure 3-4. Trends in average monthly wind speed. Data are average of daily wind speed for 8 grid cells over Lake Tahoe. P < 0.10 for all slopes.

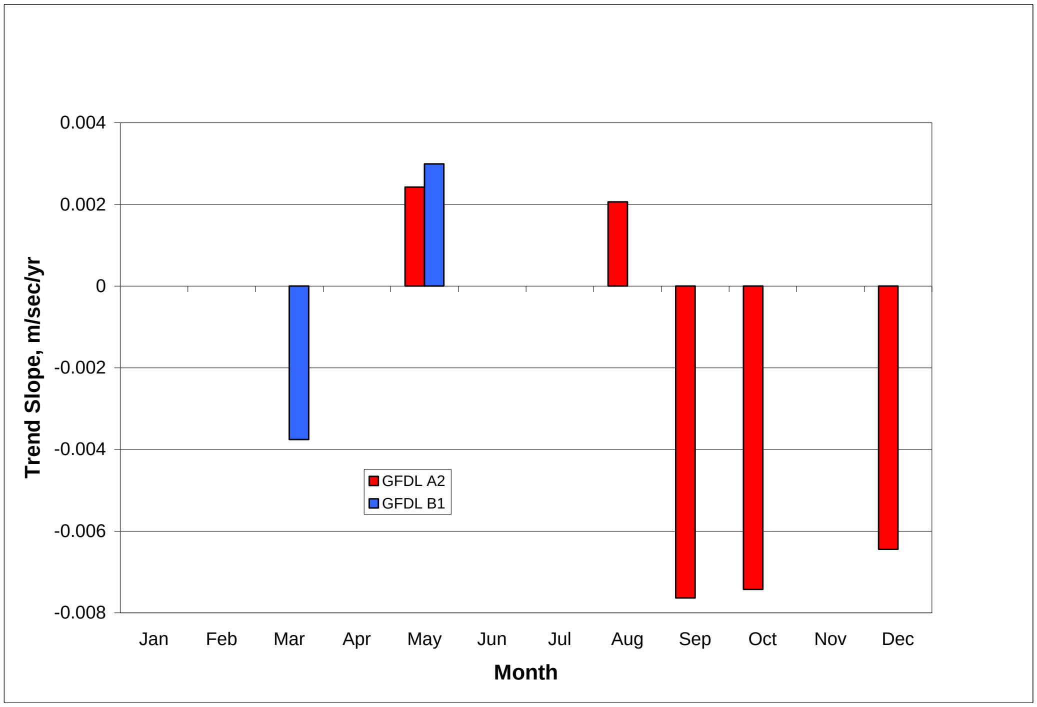

Figure 3-5. Trends in the maximum of daily average wind speed, by month, for the GFDL A2 and B1 scenarios. P < 0.10 for all slopes.

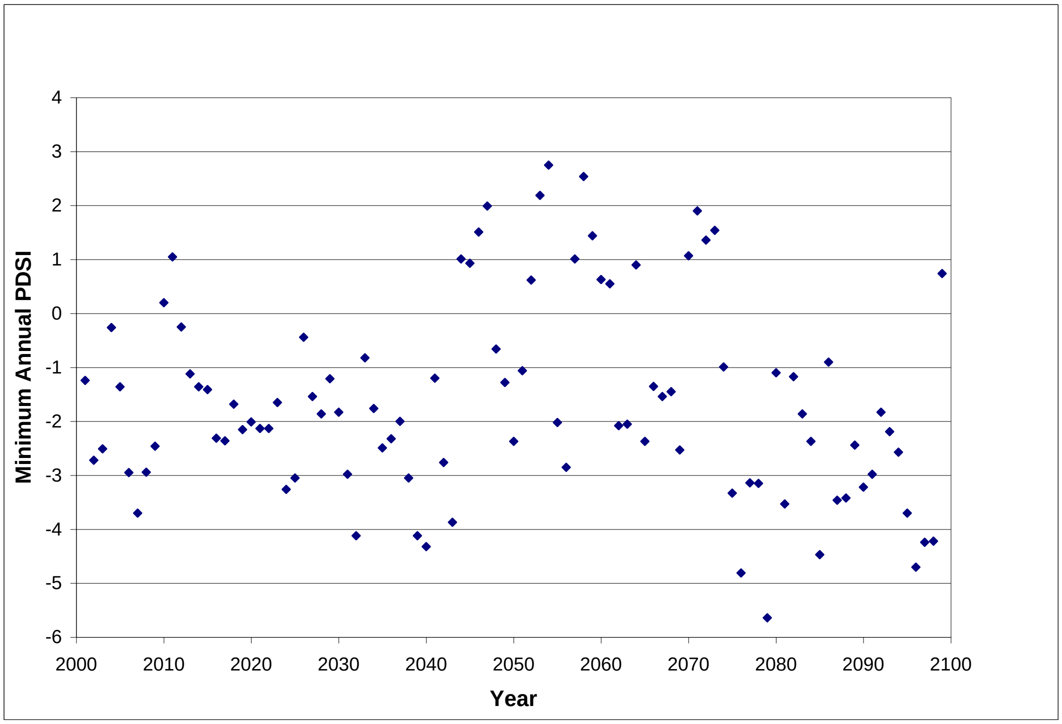

Figure 3-6. Palmer Drought Severity Index at Tahoe City, for the GFDL A2 Scenario. A low value indicates drought.

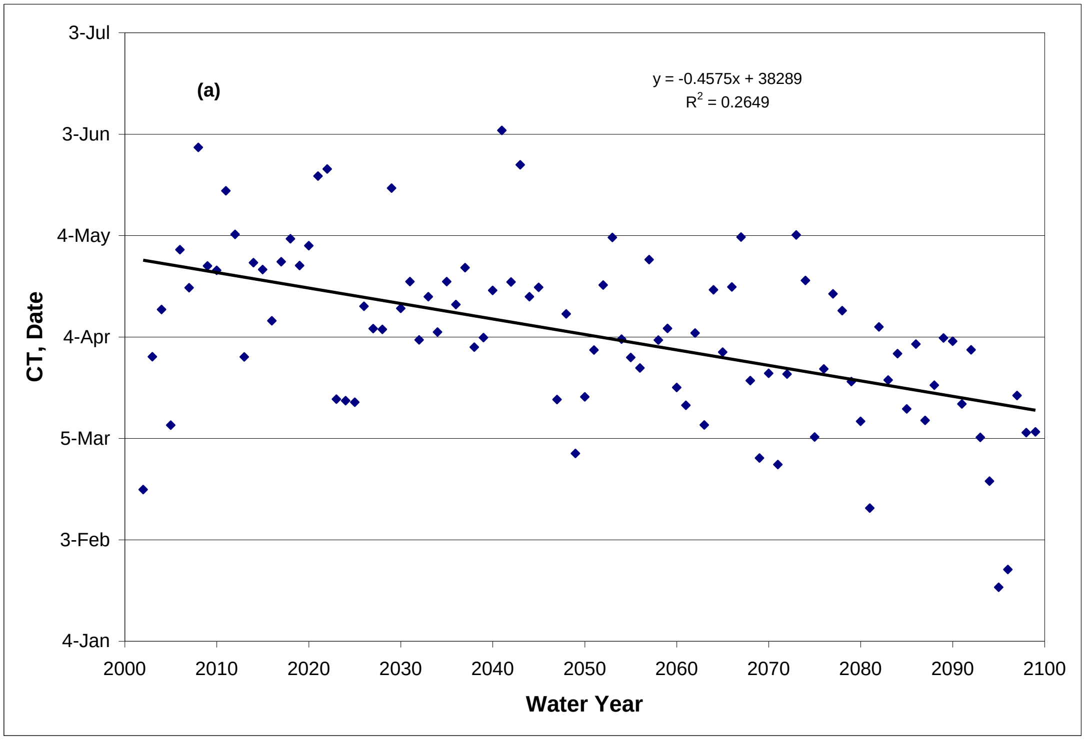

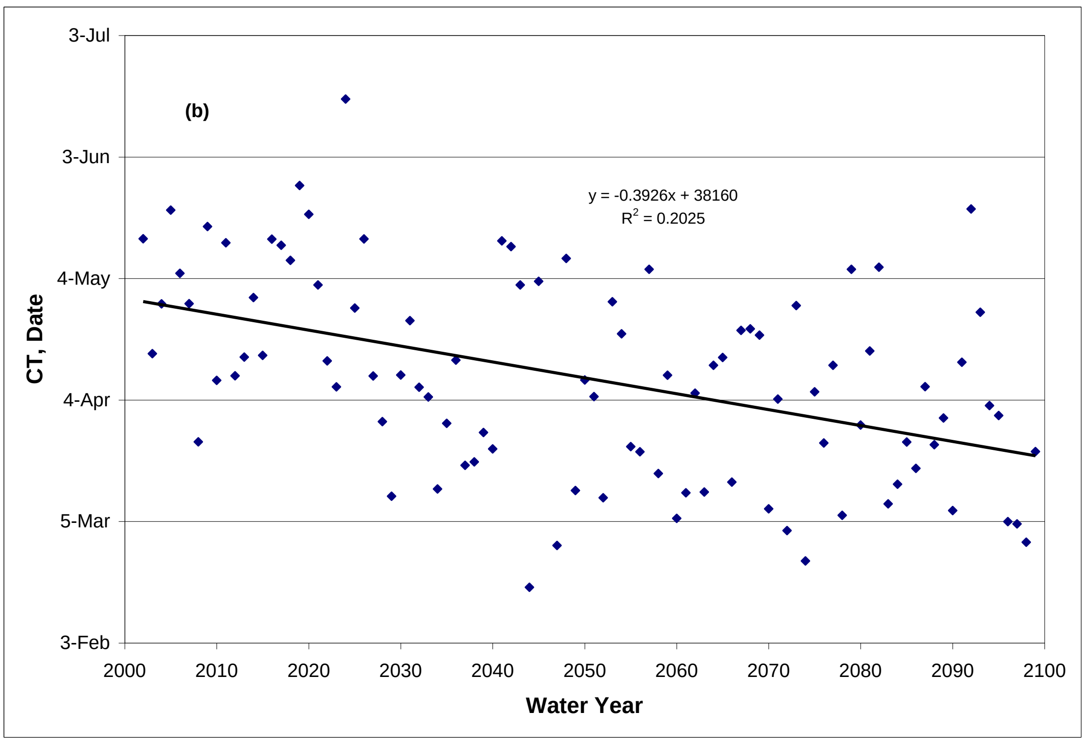

Figures 3-7 (a-b). Trends in the Center Timing of annual runoff for the Upper Truckee River. (a) A2 scenario; (b) B1 scenario

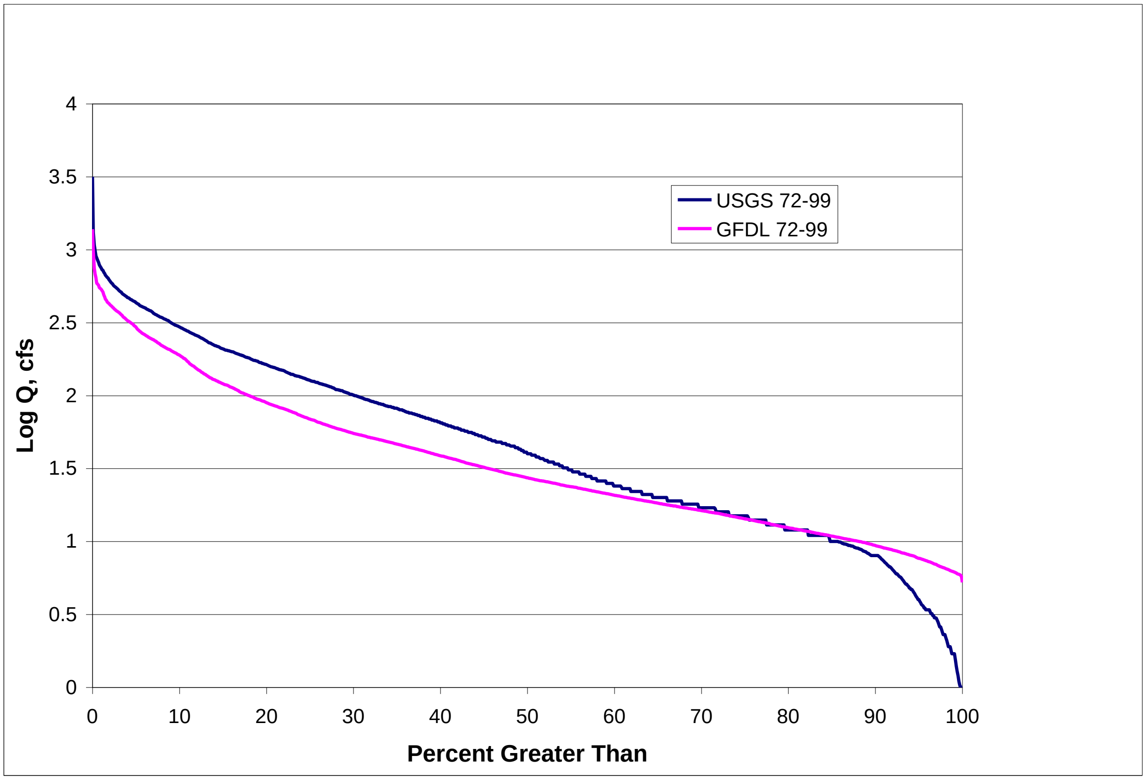

Figure 3-8. Flow duration curves for the UTR gage record, 1972-1999 and the modeled runoff from the GFDL/LSPC for the same period.

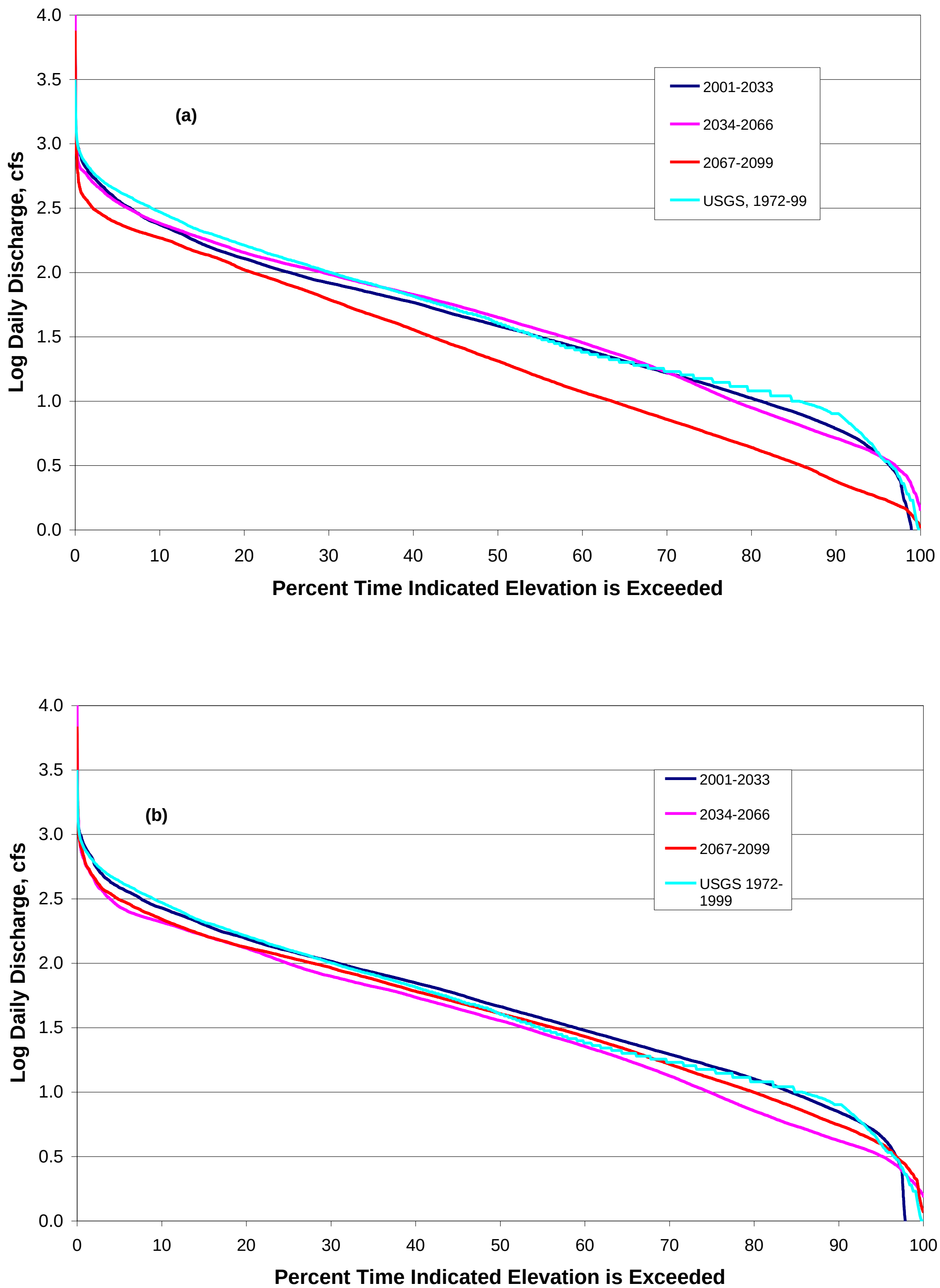

Figure 3-9 (a-b). Adjusted flow duration curves for the UTR for the periods 2001-2033, 2034-2066 and 2067-2099, according the GFDL A2 (a) and B1 (b) scenarios.

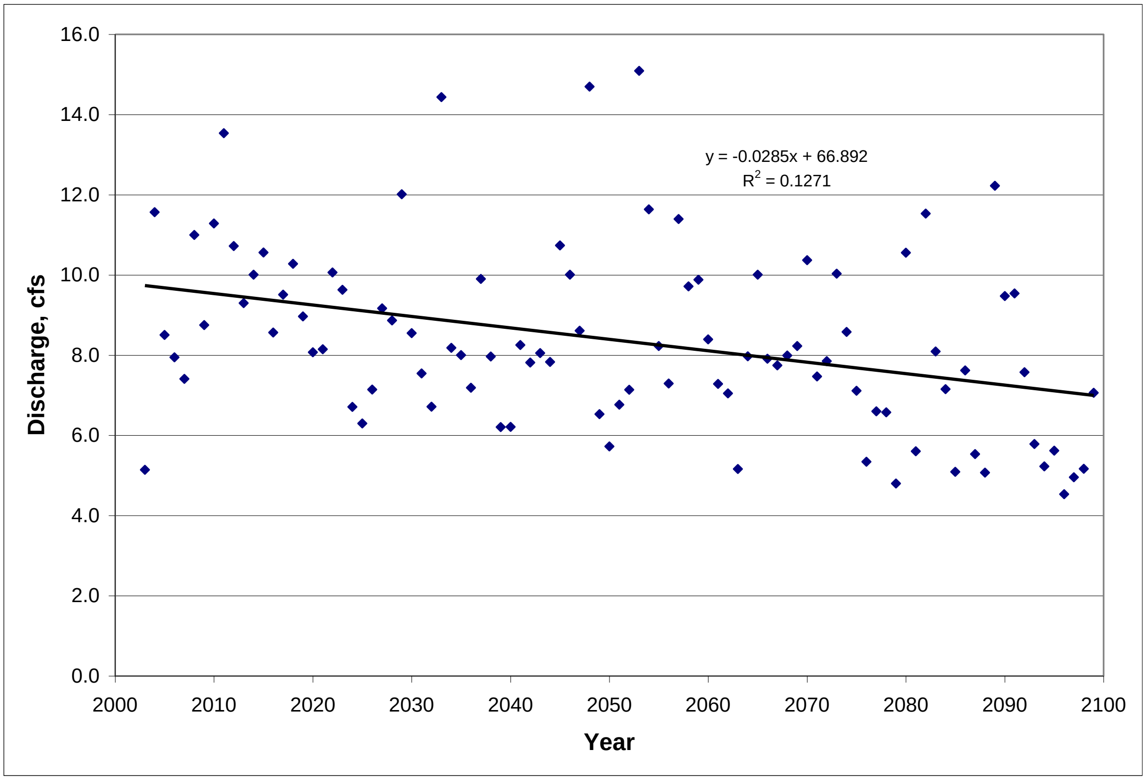

Figure 3-10. Trend in the annual minimum 5-day low-flow for the UTR, for the GFDL A2 scenario.

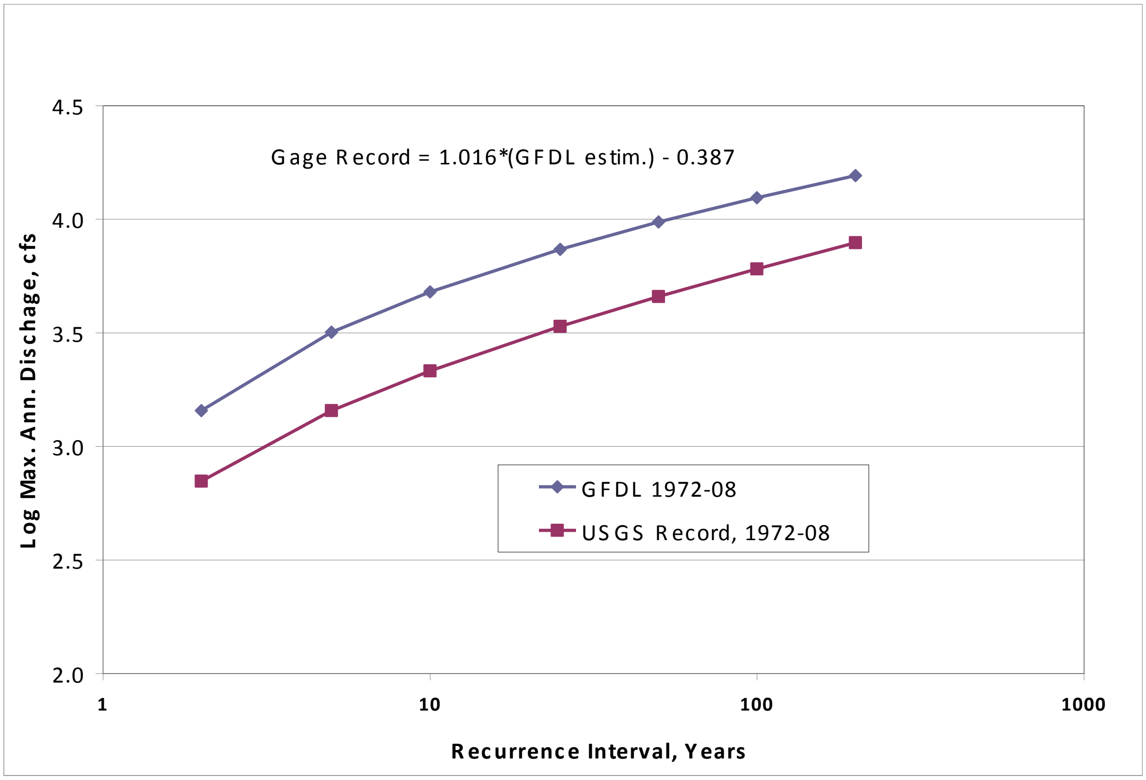

Figure 3-11. Calculated flood frequency curves for the UTR gage record (1972-2008) and the modeled GFDL/LSPC data.

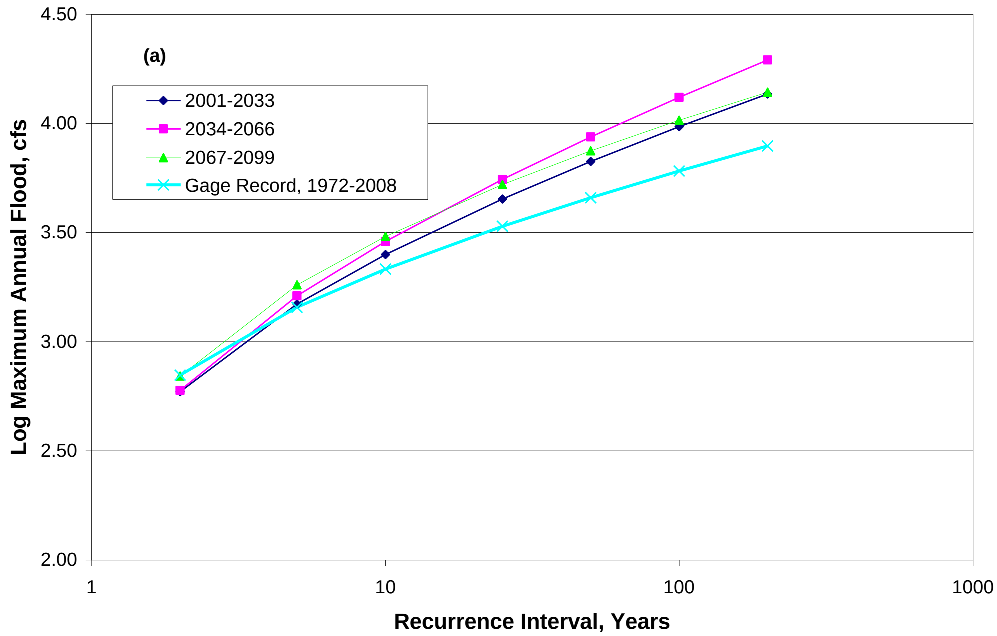

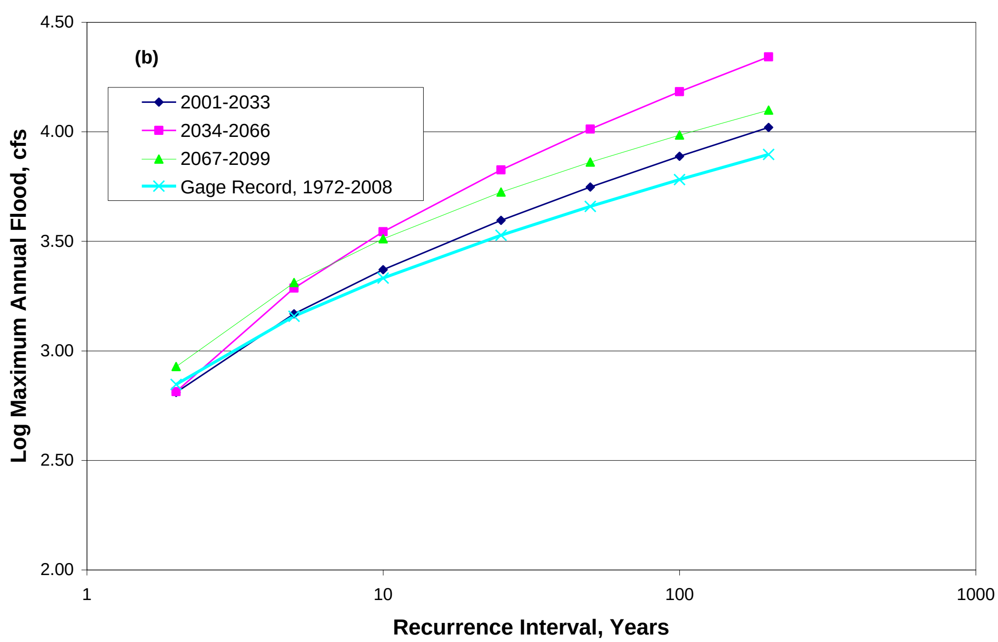

Figure 3-12 (a-b). Adjusted flood frequency curves from the GFDL/LSPC A2 (a) and B1 (b) scenarios, for the periods 2001-2033, 2034-2066 and 2067-2099, along with the historic curve from the gage record.

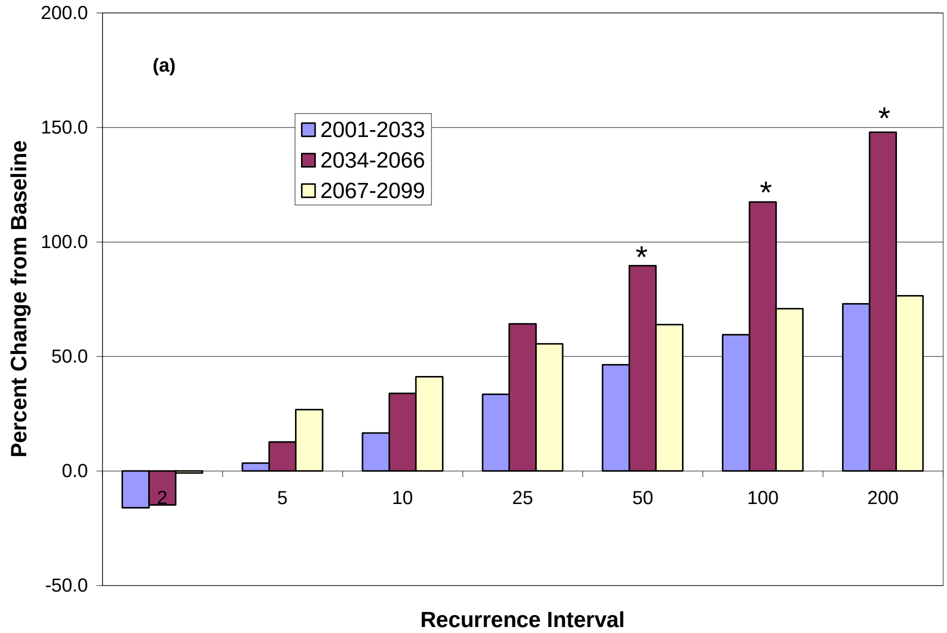

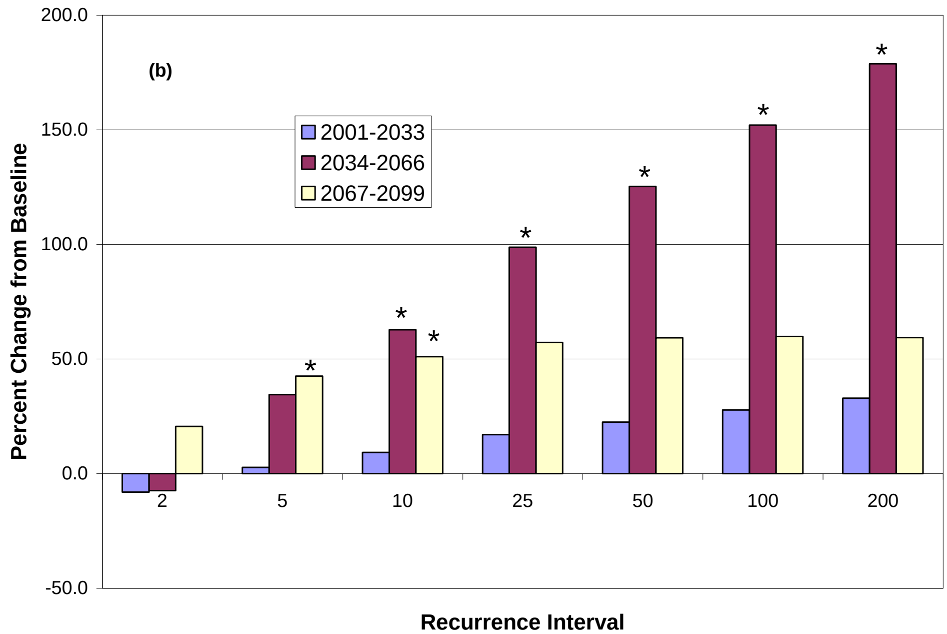

Figure 3-13 (a-b). Percent change in the modeled and adjusted GFDL/LSPC A2 (a) and B1 (b) flood frequency curves from the gage record (1972-2008). Asterisks indicate differences significant at the 90 percent level or greater.

4.0 PROJECTED FLOW, NUTRIENT AND SEDIMENT LOADS BASED ON CLIMATE CHANGE USING OUTPUT FROM THE LAKE TAHOE WATERSHED MODEL

4.1 The Lake Tahoe Watershed Model

The Lake Tahoe Watershed Model (LSPC or Load Simulation Program in C++; Tetra Tech 2007) provides a process-based numerical representation of key watershed boundary conditions. Outputs include daily stream discharge and concentrations of suspended sediment, total N, and total P. The model was developed for use in the Lake Tahoe TMDL (Lahontan and NDEP 2010a) and was calibrated using both land use specific and instream discharge monitoring data from the Lake Tahoe Interagency Monitoring Program. The model subdivides the basin into 184 subwatersheds and uses hourly values of precipitation, air temperature, wind speed, dew point, evapotranspiration and solar radiation. Weather data are what drive hydrologic and water quality processes in the model. A conceptual representation of the model is shown Figure 4-1.

The method used to simulate snow behavior is the energy balance approach. The LSPC SNOW module uses the meteorological forcing information to determine whether precipitation falls as rain or snow, how long the snowpack remains, and when snowpack melting occurs. Heat is transferred into or out of the snowpack through net radiation heat, convection of sensible heat from the air, latent heat transfer by moist air condensation on the snowpack, rain, and conduction from the ground beneath the snowpack. Figure 4-2 is a schematic of the snow process. The snowpack essentially acts like a reservoir that has specific thermodynamic rules for how water is released. Melting occurs when the liquid portion of the snowpack exceeds the snowpack's holding capacity; melted snow is added to the hydrologic cycle.

4.2 Watershed Modeling Assumptions

This study applies the Lake Tahoe Watershed Model to evaluate only the impact of climate change in isolation of all other possible changes that could be occurring within the watershed. In other words, only the “Climate Data” component shown in Figure 1 changes, while all other components remain at present-day conditions. The following assumptions were made for the watershed model runs:

1. Existing watershed conditions remain the same for the entire projected years; that is land use, geology, and vegetation are constant.
2. Existing management practices remain the same.
3. Existing condition stormwater pollutant concentrations are used with predicted future flows.
4. Stream bank erosion, atmospheric deposition, and near shore impacts are not considered.
5. Climate is the only changing variable between different scenarios.

Three alternative climate datasets were run through the watershed model to generate the watershed-based comparisons described in this report:

- Model Baseline: GFDL Historical (1967 – 1999)
- Scenario 1: GFDL A2 (2002 – 2099)
- Scenario 2: GFDL B1 (2002 – 2099)

The two climate change scenario reporting intervals were divided into third-century-blocks (2002-2033, 2034-2066, and 2067-2099) for comparison with the baseline scenario. Modeled historical data (from GFDL) was used in simulations instead of measured historical data to focus comparison of results on climate change signals and avoid the influence of residual discrepancies between measured and modeled data. Various statistical properties of modeled and measured historical climate data were checked for consistency as described in Section 5 and Appendix 9.2 to ensure the analysis was representative.

4.3 Weather Data Disaggregation

The downscaled climate datasets (presented on a daily basis) were disaggregated down to an hourly timestep to drive the watershed model. The procedure for weather data processing is briefly outlined and described below:

4.3.1 Precipitation

1. The SNOTEL hourly data at each station were categorized into 12 bins by month.
2. For each monthly bin, daily totals were computed and ranked by magnitude.
3. These daily totals within each monthly bin were further categorized into 10-percentile interval bins (yielding a total of 120 month-percentile bins). The corresponding hourly SNOTEL distributions from the original watershed model simulation were stored in each of these 120 bins. There was an average of 28 hourly precipitation distributions for each of the 120 month-percentile bins (5-10 summer wet days, 35-55 winter wet days).
4. The daily downscaled grid data were likewise classified by month and percentile (according to rainfall magnitude).
5. The nearest, most representative SNOTEL gage was assigned to each of the 12 grid centroids as listed in Table 4-1.

Table 4-1. The selected SNOTEL gage associations for each of the 12 grid centroids.

Grid number	Grid ID	SNOTEL gage
1	4	ECHOPEAK
2	5	HAGENS
3	9	RUBICON
4	10	FALLENLEAF
5	11	HEAVENLY
6	15	WARDCREEK
7	16	RUBICON
8	17	MARLETTELAKE
9	21	TAHOECITY
10	22	TAHOECITY
11	23	MARLETTELAKE
12	29	MARLETTELAKE

For each day at each grid, the month and rank of precipitation magnitude were used to determine which of the 120 observed data bins from which to select a distribution. One hourly precipitation distribution was randomly selected from the corresponding SNOTEL month-percentile bin and used to disaggregate the daily data to hourly for day.

4.3.2 Temperature/Dewpoint

The MIN and MAX temperature values for each day were disaggregated using average monthly observed diurnal distributions at South Lake Tahoe Airport (12 diurnal distributions - one for each month - were computed using averages of each hour for the entire period of record). For each day, the respective (1 of 12) distribution was scaled between the projected MIN and MAX from the downscaled record.

4.3.3 Shortwave Radiation

Total daylight hours for each day were calculated using the latitude of each grid cell and rotation/revolution of the earth. A sin function was used to disaggregate the total daily radiation to hourly over the daylight hours, with the peak value at the middle hour between sunrise and sunset.

4.3.4 Wind Speed

Wind was disaggregated to hourly using a similar procedure as precipitation. Observed hourly wind behavior at South Lake Tahoe airport was organized into month and percentile-magnitude bins. Average wind speeds for the downscaled data were converted to total daily wind travel by multiplying by 24. For each day, the downscaled wind travel totals were disaggregated to hourly by randomly selecting a wind distribution from the month-percentile bins of observed distributions.

4.3.5 Potential Evapotranspiration

Daily potential ET was computed using the Penman method and the downscaled min/max temperature, dewpoint, solar radiation, and wind speed timeseries. Daily computed potential ET was disaggregated to hourly with a sin curve across the daylight hours, which were computed as a function of latitude and the rotation/revolution of the earth.

4.4 Projected Hydrologic Impacts of Climate Change

4.4.1 Snowfall versus Rainfall

Climate change results shown in Figure 4-3 and Figure 4-4 indicate a gradual shift in the distribution of snowfall events towards rainfall. This shift is consistent regardless of which approach is taken for this analysis (see Sections 3.0 and 5.0). The trend seems to be gradually increasing with increasing emissions and associated warming trend, resulting in increased rainfall versus snowfall. The A2 scenario shows a more rapid and intense trend as compared to the B1 scenario. The 100-year projected results are divided into three groups (33 years in each group) in order to compare against the 33 years of baseline scenario.

4.4.2 Average Snow Pack Changes

The results shown in Figure 4-5 and Figure 4-6 indicate a gradual decrease in average snow pack depth. Figure 4-7 and Figure 4-8 show the annualized average daily snowpack depth for GFDL A2 and B1 scenario respectively. For these graphs, each of the 33-year time intervals were annualized by area-weighting snowpack depth for each subwatershed and sorting the averaged values by calendar day. In other words, 33 x 184 values (number of years times number of subwatersheds) were averaged for each calendar day (Oct 1, Oct 2, … Sep 30).

There are potentially notable impacts on the snowpack duration (-5% to -25%) and magnitude (-3% to -60%), relative to existing conditions. Table 4-2 and Table 4-3 present synoptic summary statistics for projected average snowpack start, peak, end, duration and associated percent change (relative to baseline), and peak depth and associated percent change (relative to baseline).

Figure 4-9 through Figure 4-11 for A2 scenario and Figure 4-12 through Figure 4-14 for B1 scenario show the spatial variation of percent change for snow pack depth for all subwatersheds in the Tahoe basin. The trend shows that the projected impact of snowpack depth changes spatially during the course of the climate change scenarios, with the east side of the Lake being more strongly affected relative to the west side towards the latter part of the century under Scenario A2, but less affected relative to the west side under Scenario B1.

Table 4-2. Summary table of the snowpack depth for GFDL A2 scenario.

Period	**Start**	**Peak**	**End**	**Duration**	**Percent Change**	**Peak Depth (in)**	**Percent Change**
1967-1999 (Baseline)	6-Nov	8-Mar	11-Jul	248	-	13.6	-
2002-2033	9-Nov	23-Mar	28-Jun	232	-6.5%	9.5	-29.6%
2034-2066	16-Nov	5-Mar	29-Jun	226	-8.9%	10.9	-19.2%
2067-2099	29-Nov	22-Feb	31-May	184	-25.8%	5.6	-58.6%

Table 4-3. Summary table of the snowpack depth for GFDL B1 scenario.

Period	**Start**	**Peak**	**End**	**Duration**	**Percent Change**	**Peak Depth (in)**	**Percent Change**
1967-1999 (Baseline)	6-Nov	8-Mar	12-Jul	249	-	13.5	-
2002-2033	9-Nov	22-Mar	2-Jul	236	-5.2%	13.0	-3.7%
2034-2066	16-Nov	3-Mar	19-Jun	216	-13.3%	8.3	-38.8%
2067-2099	24-Nov	28-Feb	1-Jul	220	-11.6%	8.6	-36.3%

4.4.3 Average Evapotranspiration (ET) Changes

The results shown in Figure 4-15 and Figure 4-16 indicate a gradual increase in average ET. Figure 4-17 through Figure 4-19 for A2 scenario and Figure 4-20 through Figure 4-22 for B1 scenario show the spatial variation of ET over the entire Lake Tahoe subwatersheds. The trend shows that the impact of ET change is higher in the eastern subwatersheds of the Lake Tahoe basin as compared to the western side of the lake.

4.4.4 Water Yield

Total water yield to Lake Tahoe is defined as the sum of all direct-draining tributaries plus intervening zone flows. This is the resulting water after any and all transport losses or gains have been considered. Figure 4-23 and Figure 4-24 show total water yield for scenarios A2 and B1, respectively.

4.5 Projected Water Quality Impacts

The changes in sediment yield to Lake Tahoe based on the expected climate change anticipated for the Basin are shown in Figure 4-25 (A2 scenario) and in Figure 4-26 (B1 scenario). They indicate that sediment load may stay uniform or increase slightly – up to 5 percent - relative to baseline loads. However, because the model predicts there will be a decrease in total flow over the same period, instream sediment concentrations would show an increase under climate change. Nutrient loads are shown in Figure 4-27 (A2 scenario) and in Figure 4-28 (B1 scenario). The trends suggest that nutrient loading should generally decline in association with the predicted decreasing water yield to the lake (Figures 4-23 and 4-24). For the first two-thirds of the 21st Century, nutrient loads are predicted to decline by about 5-10 percent relative to baseline conditions. Thereafter (until 2099) total N and total P loads could drop by 75-80 percent.

Spatial analyses were also performed to identify the locations that most contributed to maintaining the sediment load relatively constant compared to baseline, in spite of decreasing flows. Fine sediment particle loads (number of particles) were estimated using the urban and rural land-use distribution by subwatershed, together with the particle count converters used in the TMDL analysis (Lahontan and NDEP 2009). Figure 4-29 (A2 scenario) and Figure 4-30 (B1 scenario) show the spatial variation of fine sediments at the watershed level.

A few notable observations appear in these maps. The higher elevation watersheds (northern and western) show the largest increase in fine sediment particle generation. This is most likely because the effect of the shift from snow to rain is most pronounced in areas that are already wetter under baseline conditions. Shifting from snow to rain is linked to increased urban runoff, which increases the fine sediment count more dramatically. On the other hand, the southern and eastern subwatersheds generally show a decrease in fine sediment load. In these areas, although the shift from snow to rain holds true, the overall drop in water volume under climate change projections has more of an impact in reducing sediment load than the shift from snow to rain. Therefore, these areas show a net decrease in fine sediment particle loading under climate change projections. Overall, the increase in the higher and wetter elevation subwatersheds is balanced by the decrease in the lower elevation dryer subwatersheds.

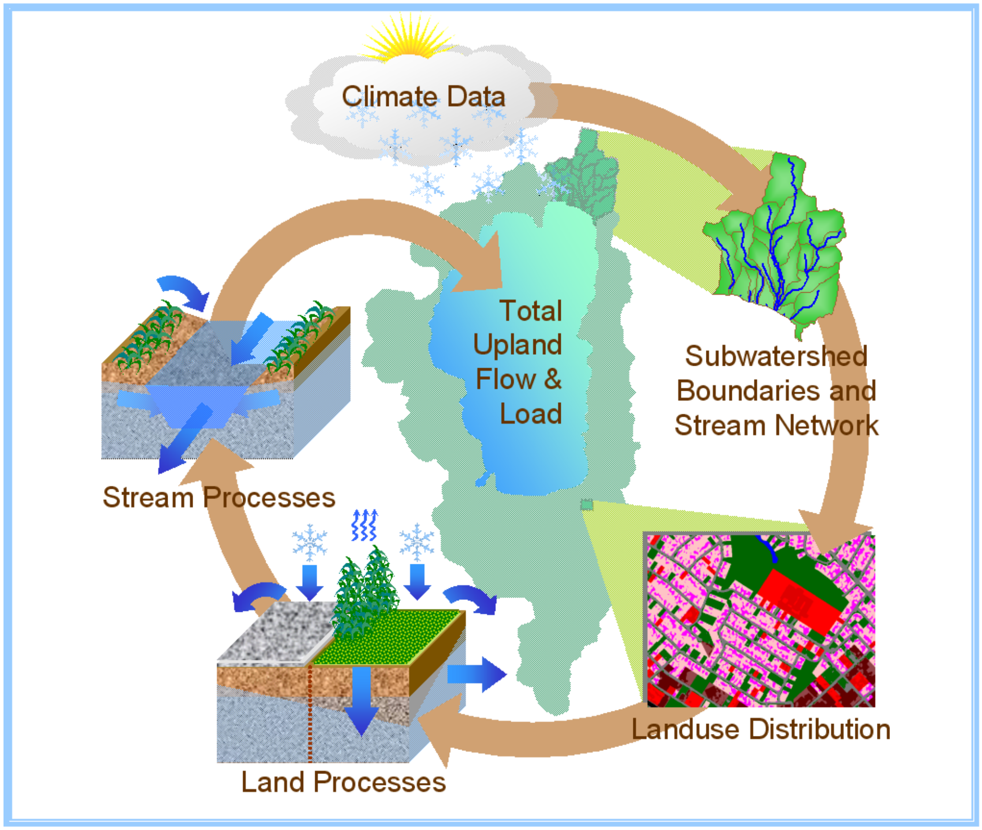

Figure 4-1. Lake Tahoe Watershed Model conceptual process interaction diagram.

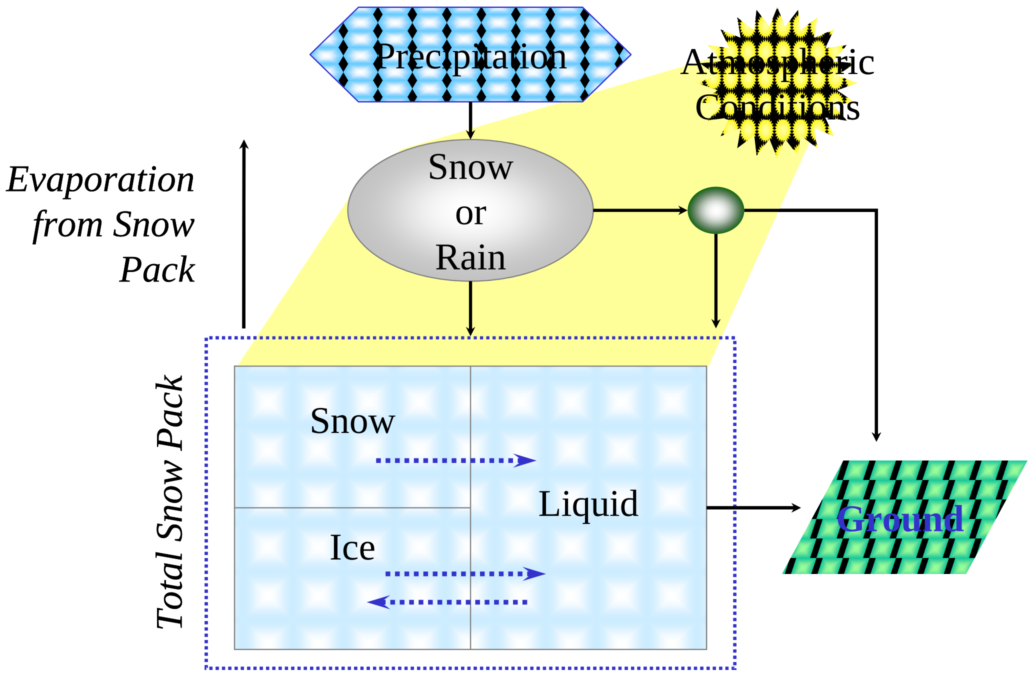

Figure 4-2. Lake Tahoe Watershed Model conceptual snow simulation schematic

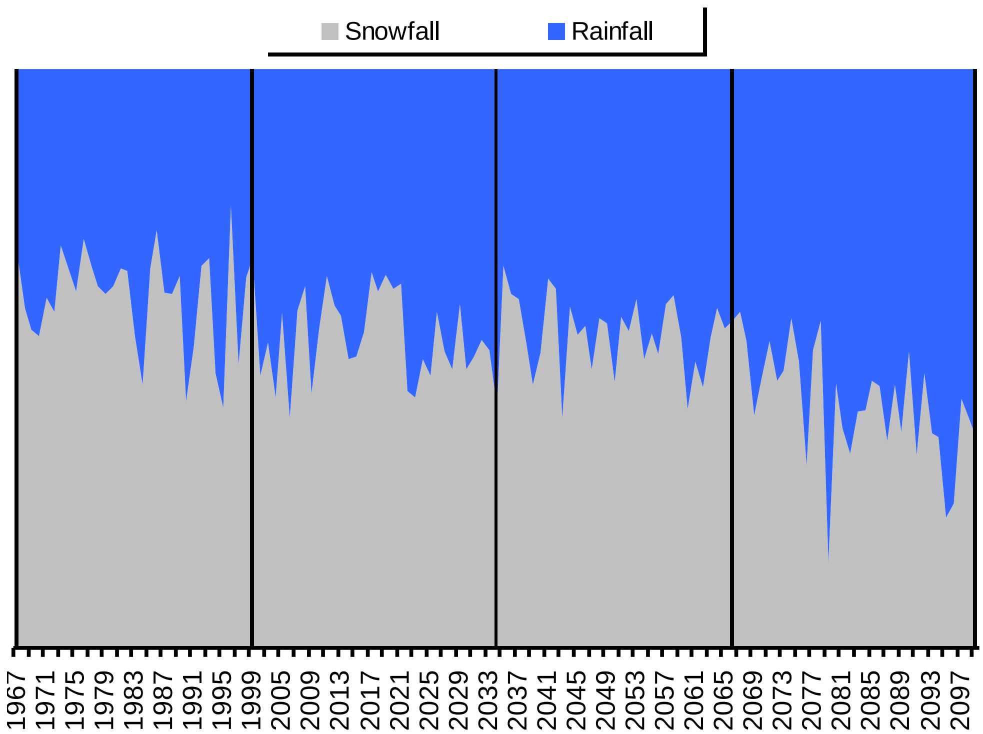

Figure 4-3. Snowfall versus rainfall trend for GFDL A2 scenario. Y-axis is expressed as percent.

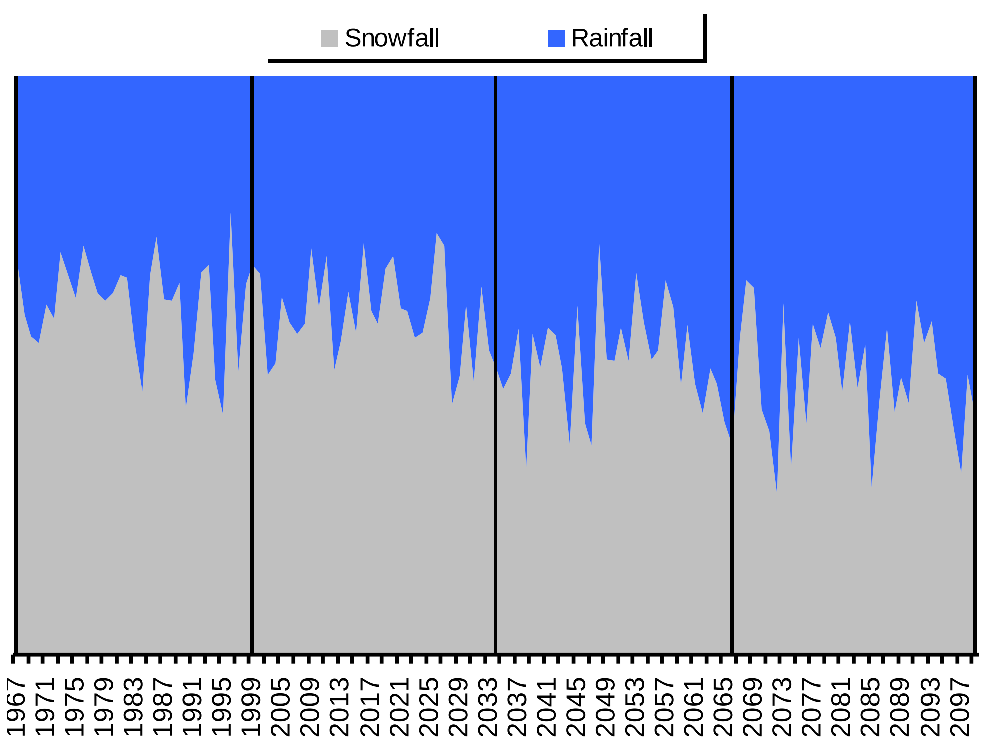

Figure 4-4. Snowfall versus rainfall trend for GFDL B1 scenario.

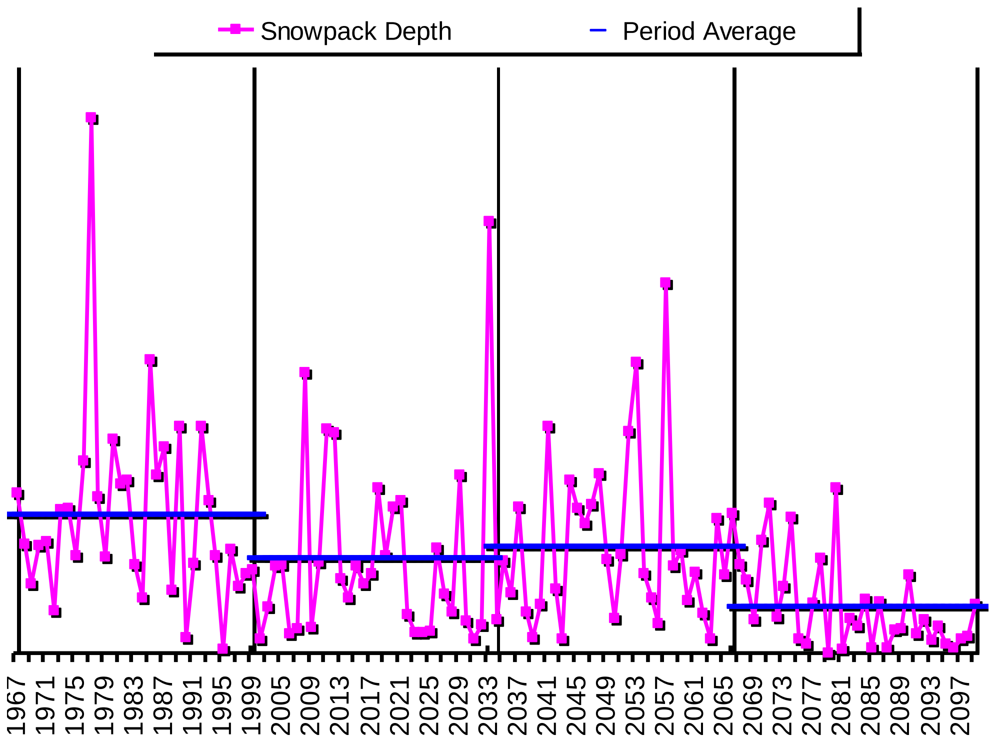

Figure 4-5. Average snowpack depth time series for GFDL A2 scenario.

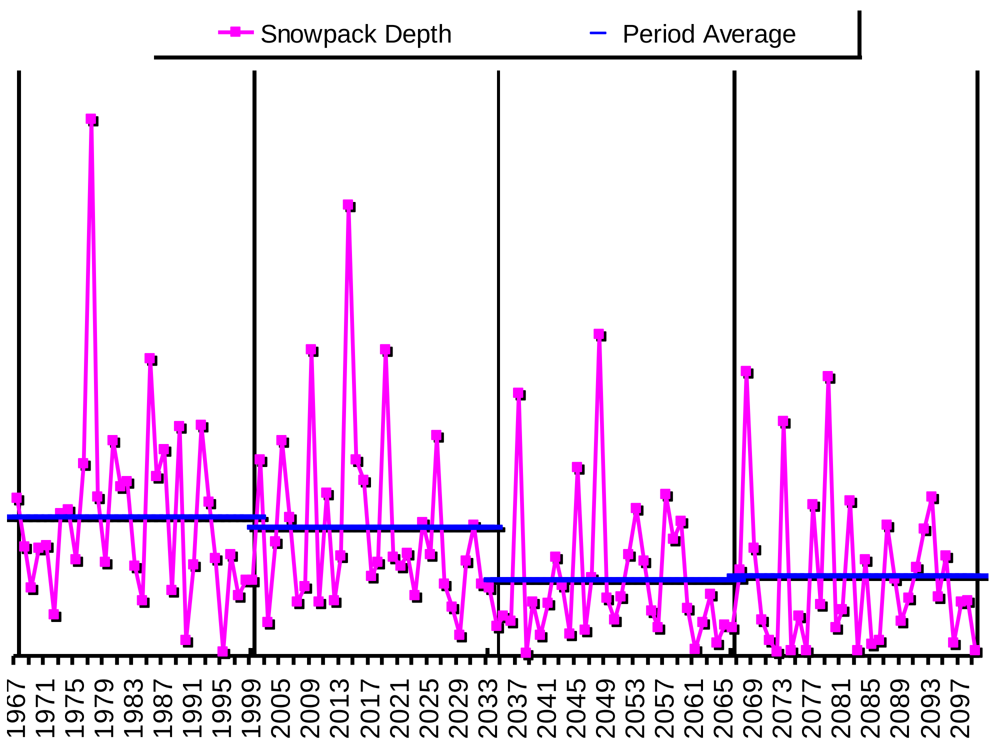

Figure 4-6. Average snowpack depth time series for GFDL B1 scenario.

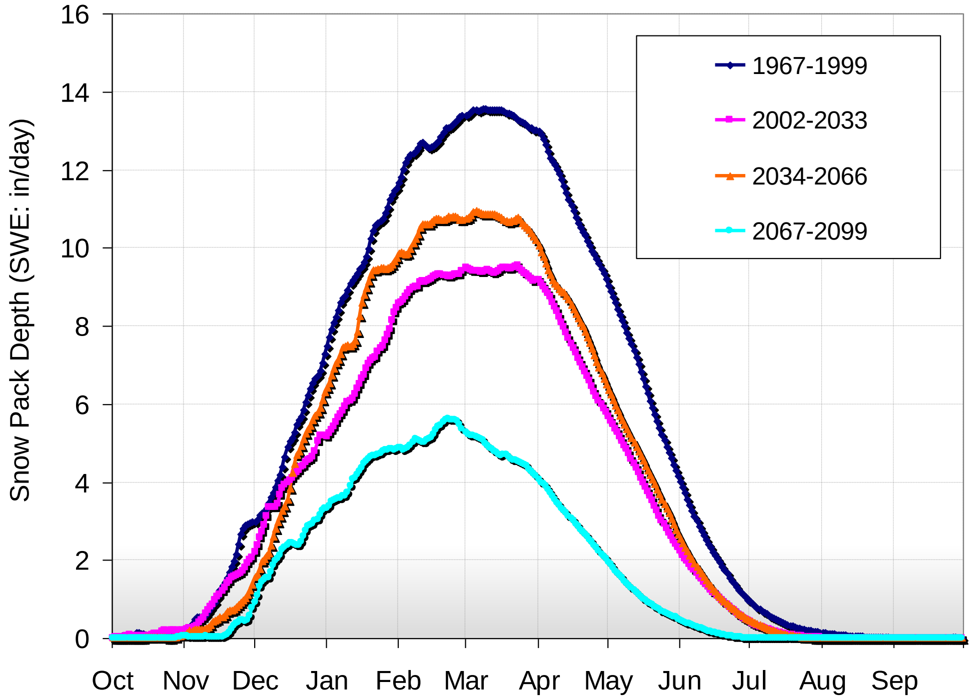

Figure 4-7. Annualized average daily snowpack depth for GFDL A2 scenario.

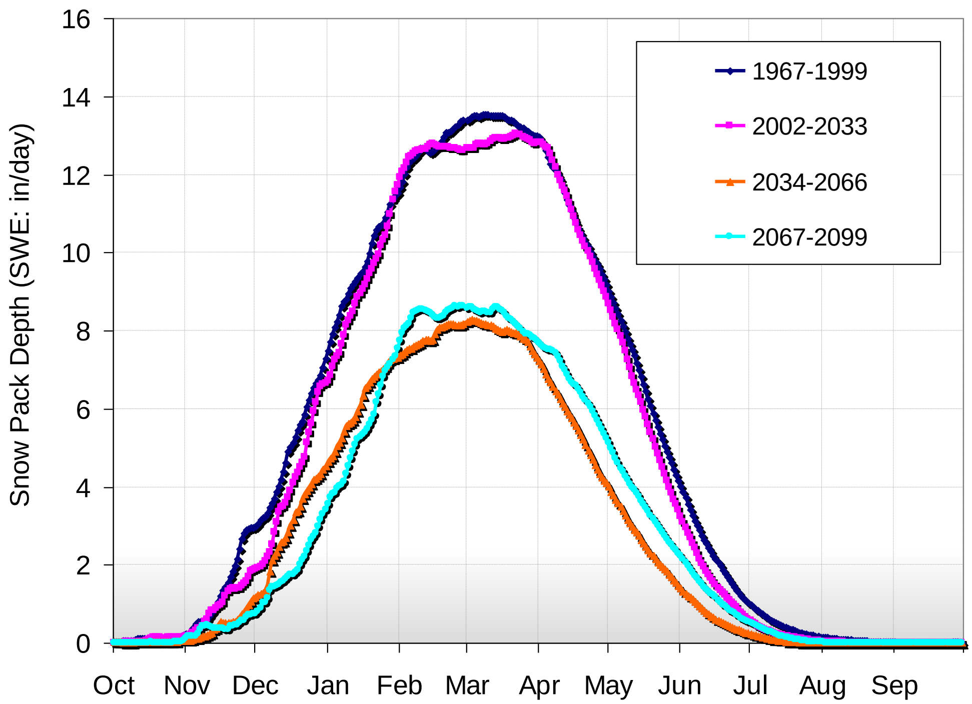

Figure 4-8. Annualized average daily snowpack depth for GFDL B1 scenario.

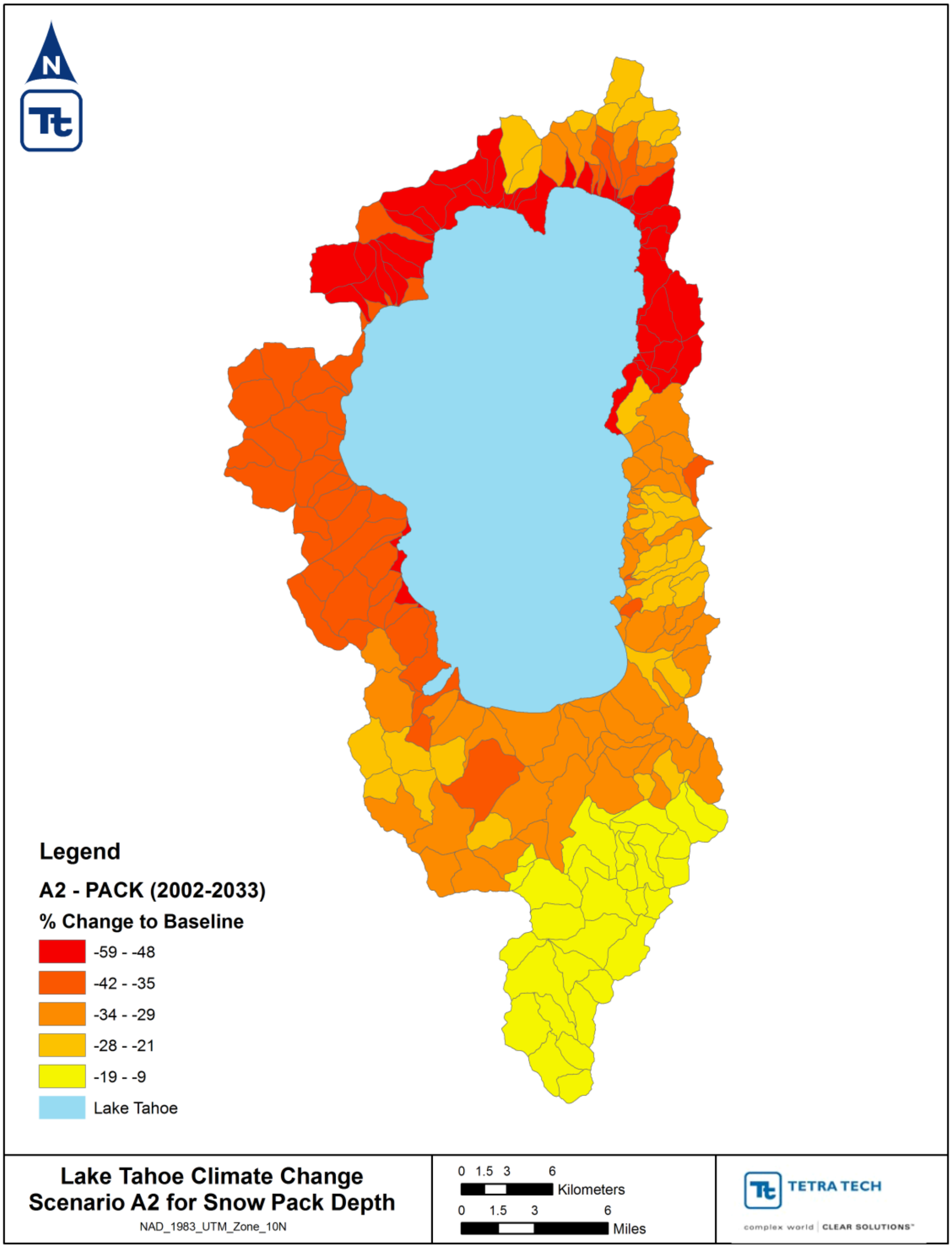

Figure 4-9. Spatial variation of snowpack depth for GFDL A2 scenario (2002-2033).

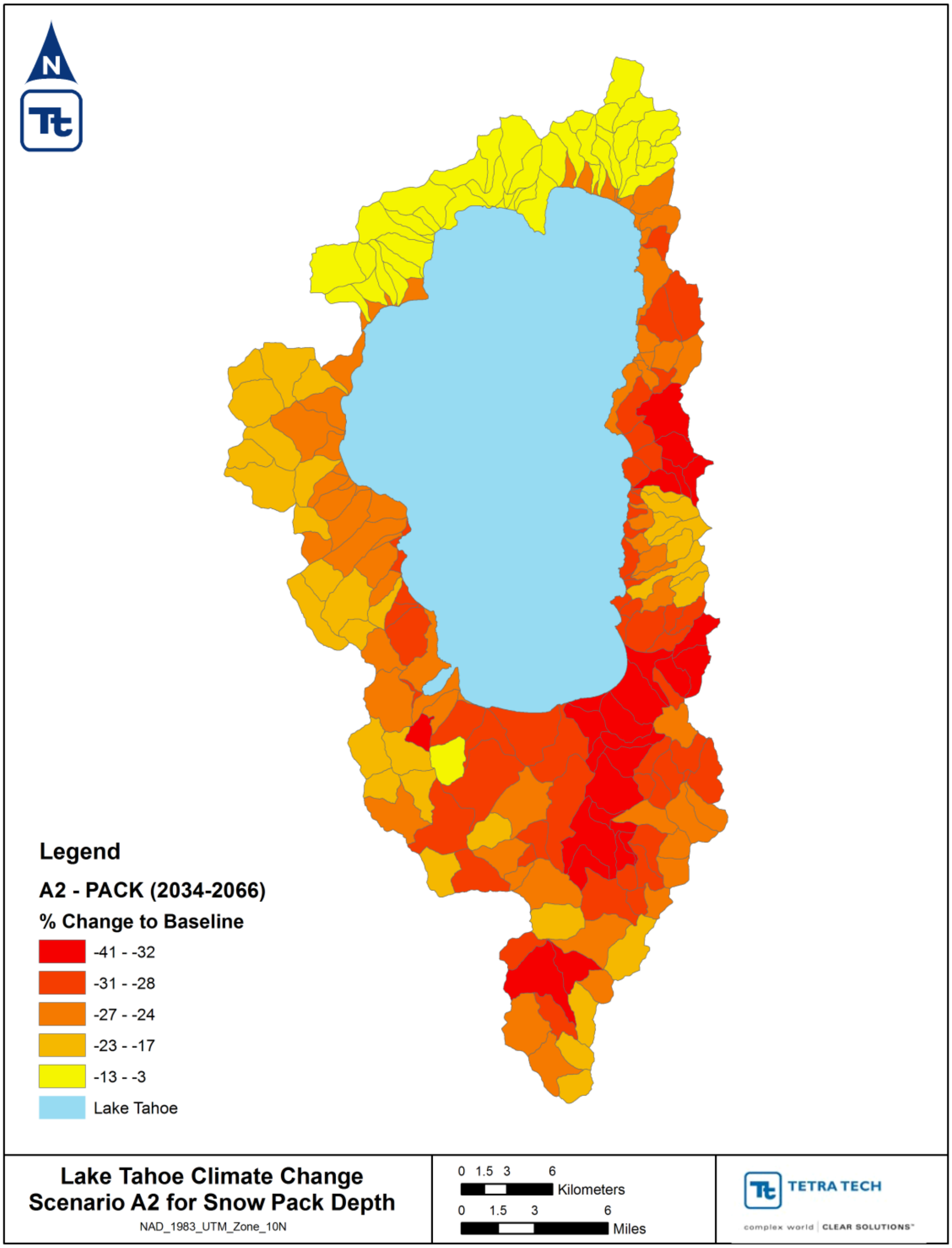

Figure 4-10. Spatial variation of snowpack depth for GFDL A2 scenario (2034-2066).

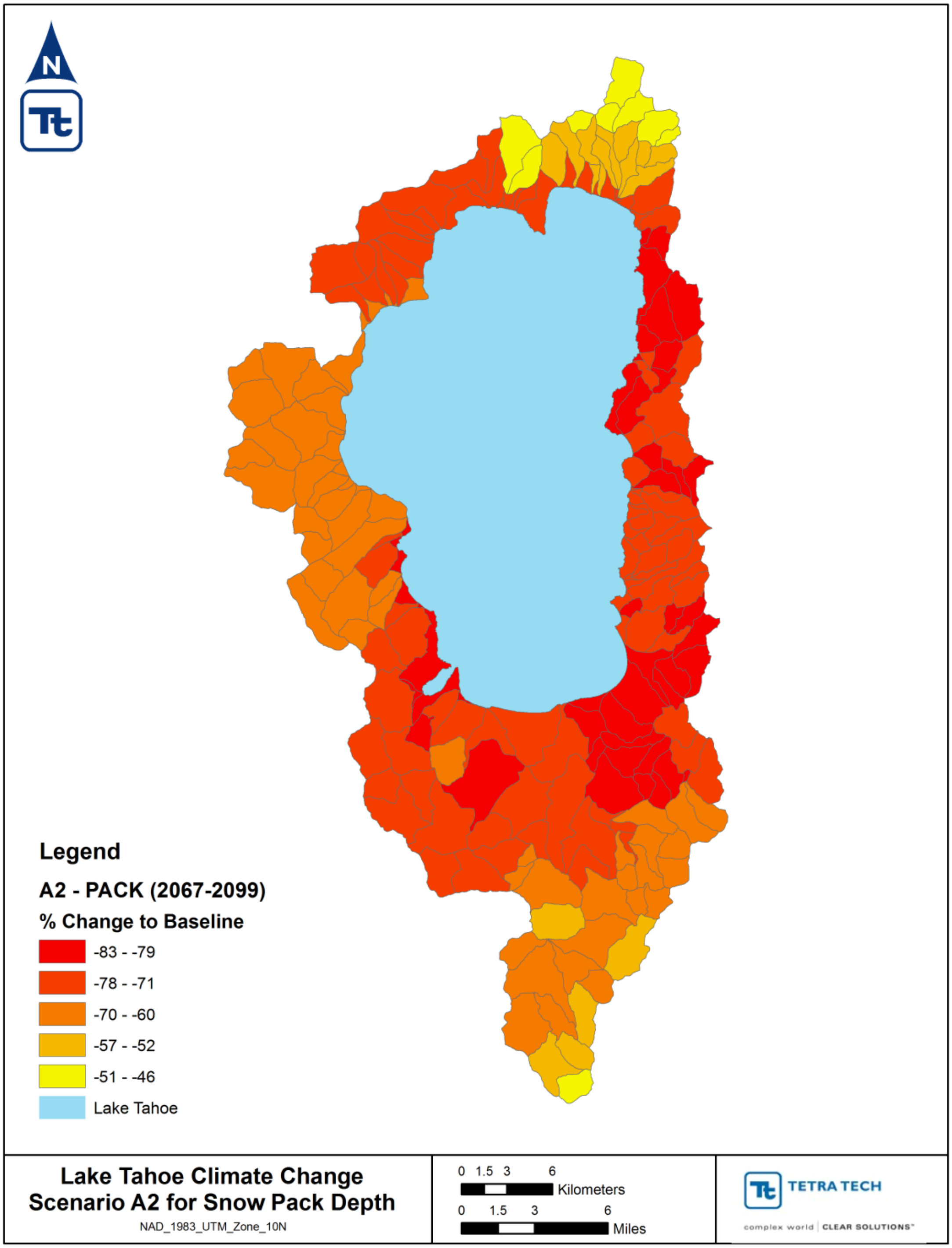

Figure 4-11. Spatial variation of snowpack depth for GFDL A2 scenario (2067-2099).

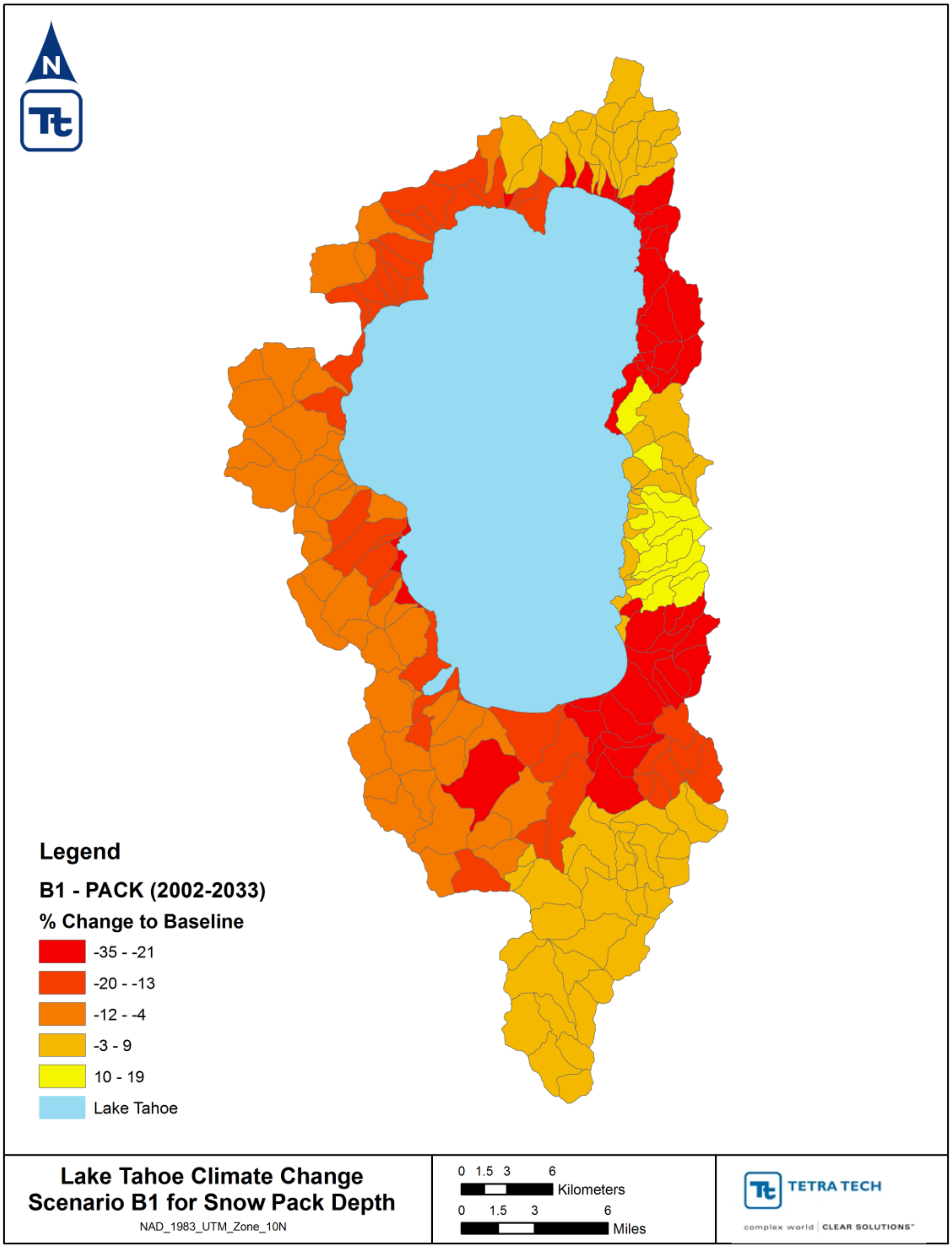

Figure 4-12. Spatial variation of snowpack depth for GFDL B1 scenario (2002-2033).

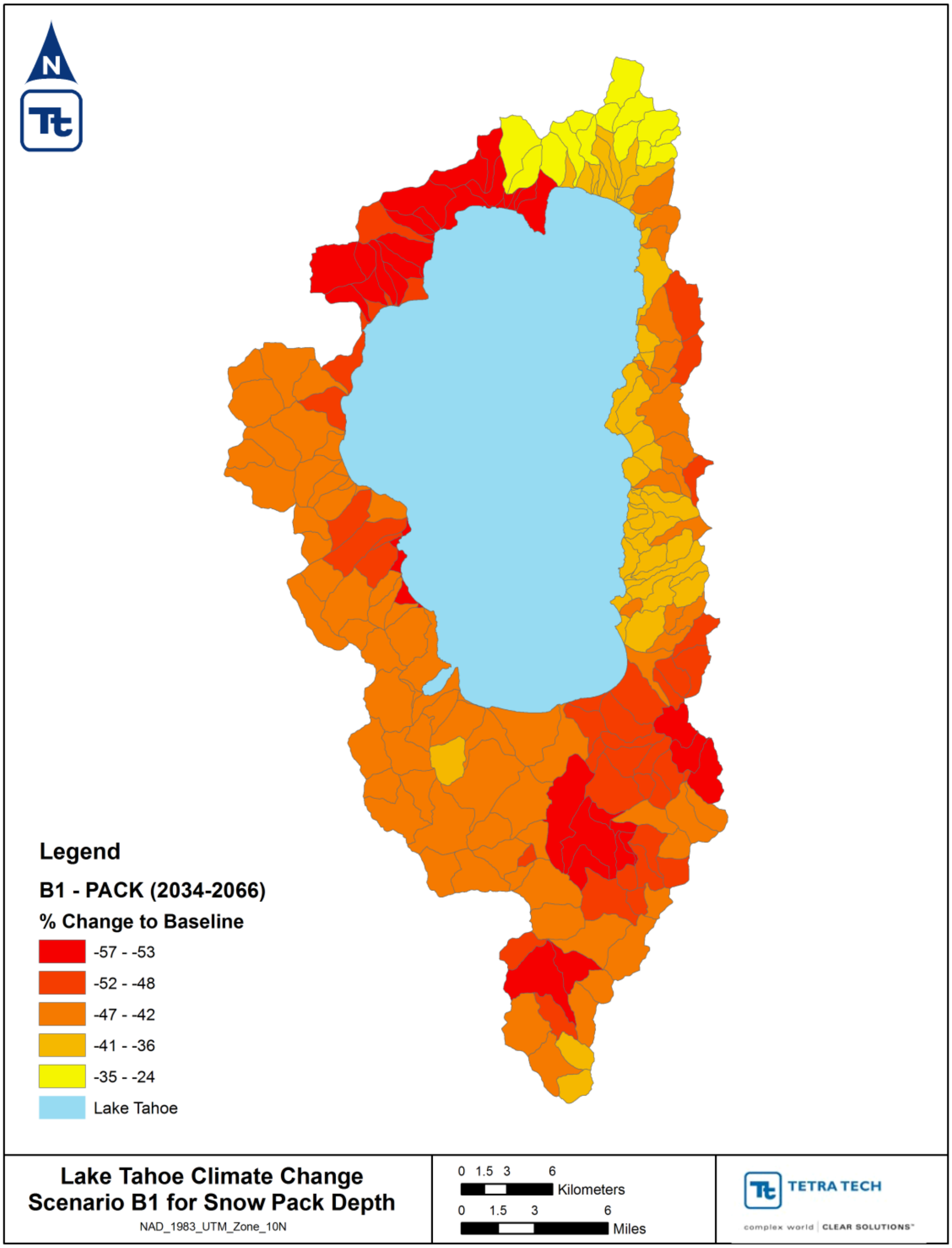

Figure 4-13. Spatial variation of snowpack depth for GFDL B1 (2034-2066) scenario.

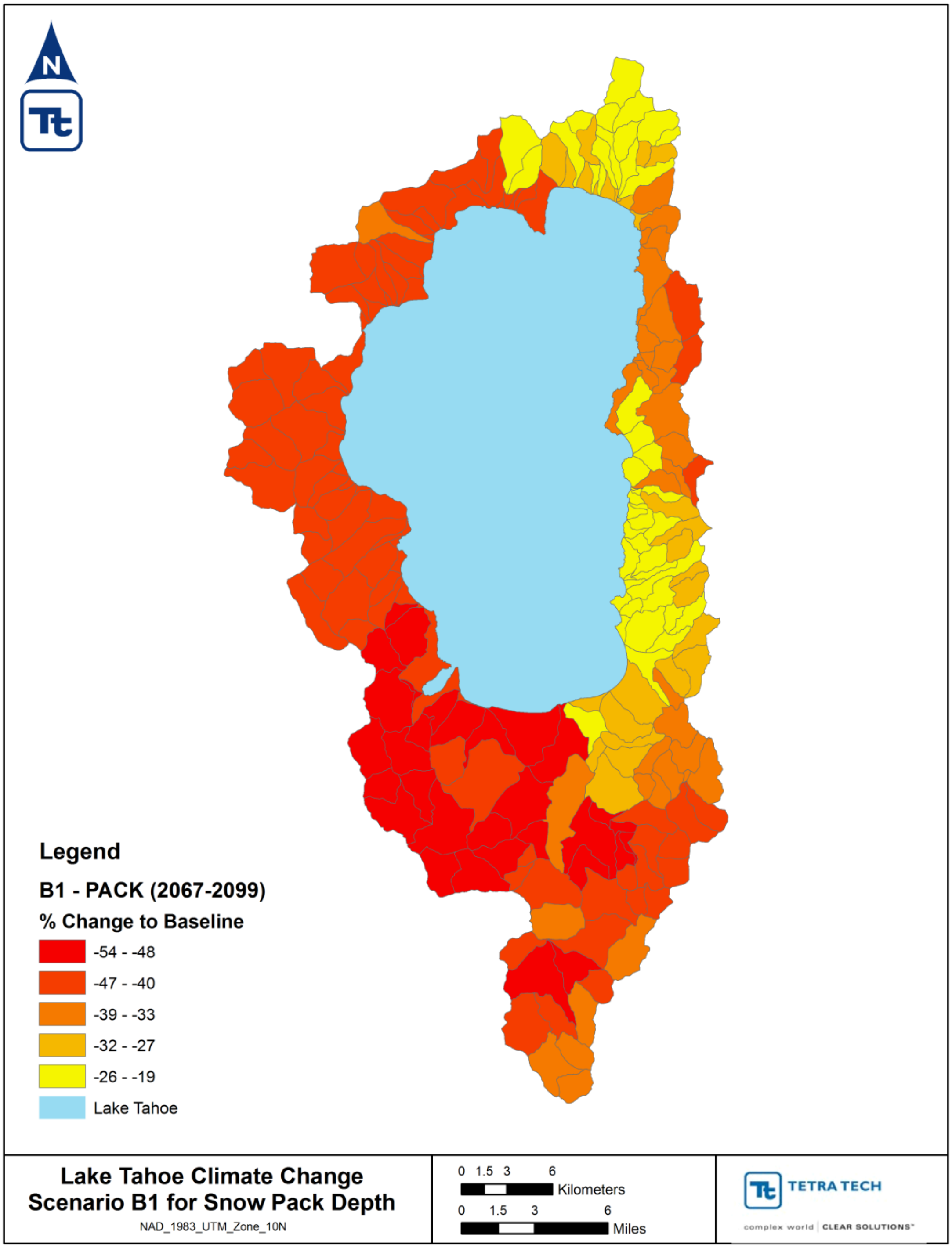

Figure 4-14. Spatial variation of snowpack depth for GFDL B1 scenario (2067-2099).

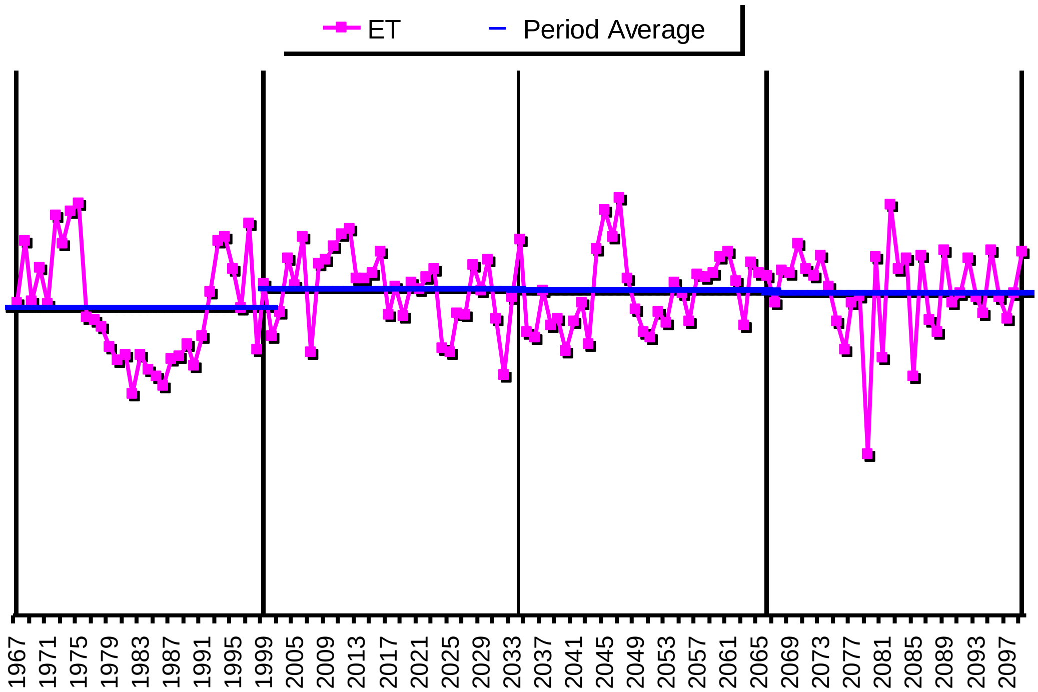

Figure 4-15. Model-predicted evapotranspiration (ET) for the GFDL A2 scenario.

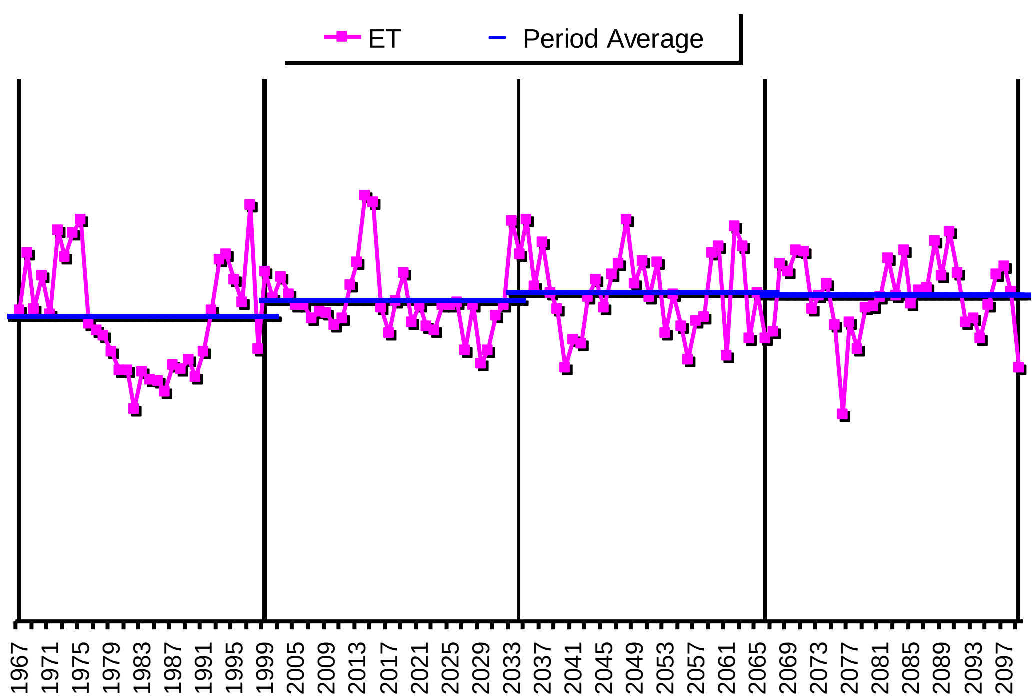

Figure 4-16. Model-predicted evapotranspiration (ET) for the GFDL B1 scenario.

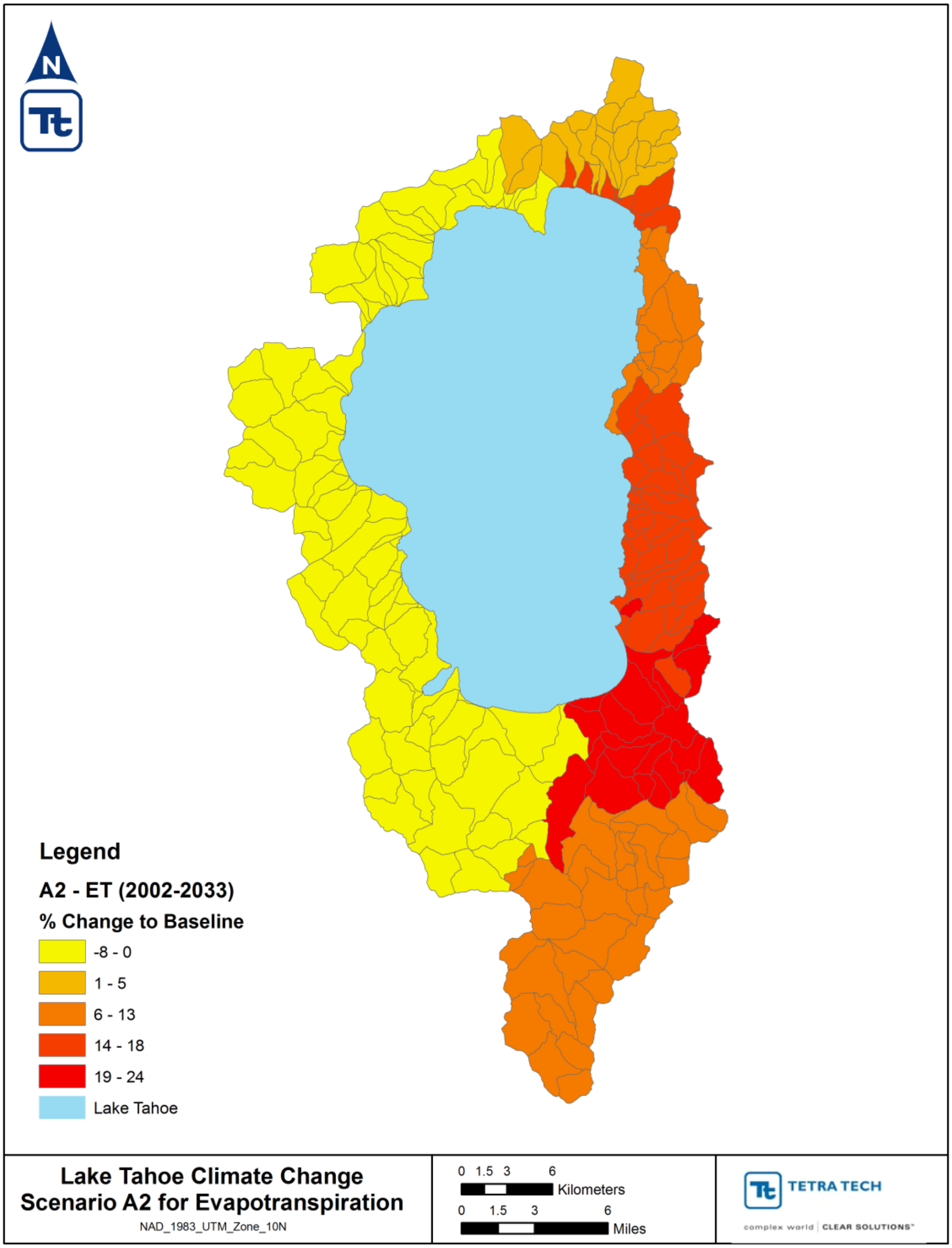

Figure 4-17. Spatial variation of evapotranspiration (ET) for GFDL A2 (2002-2033).

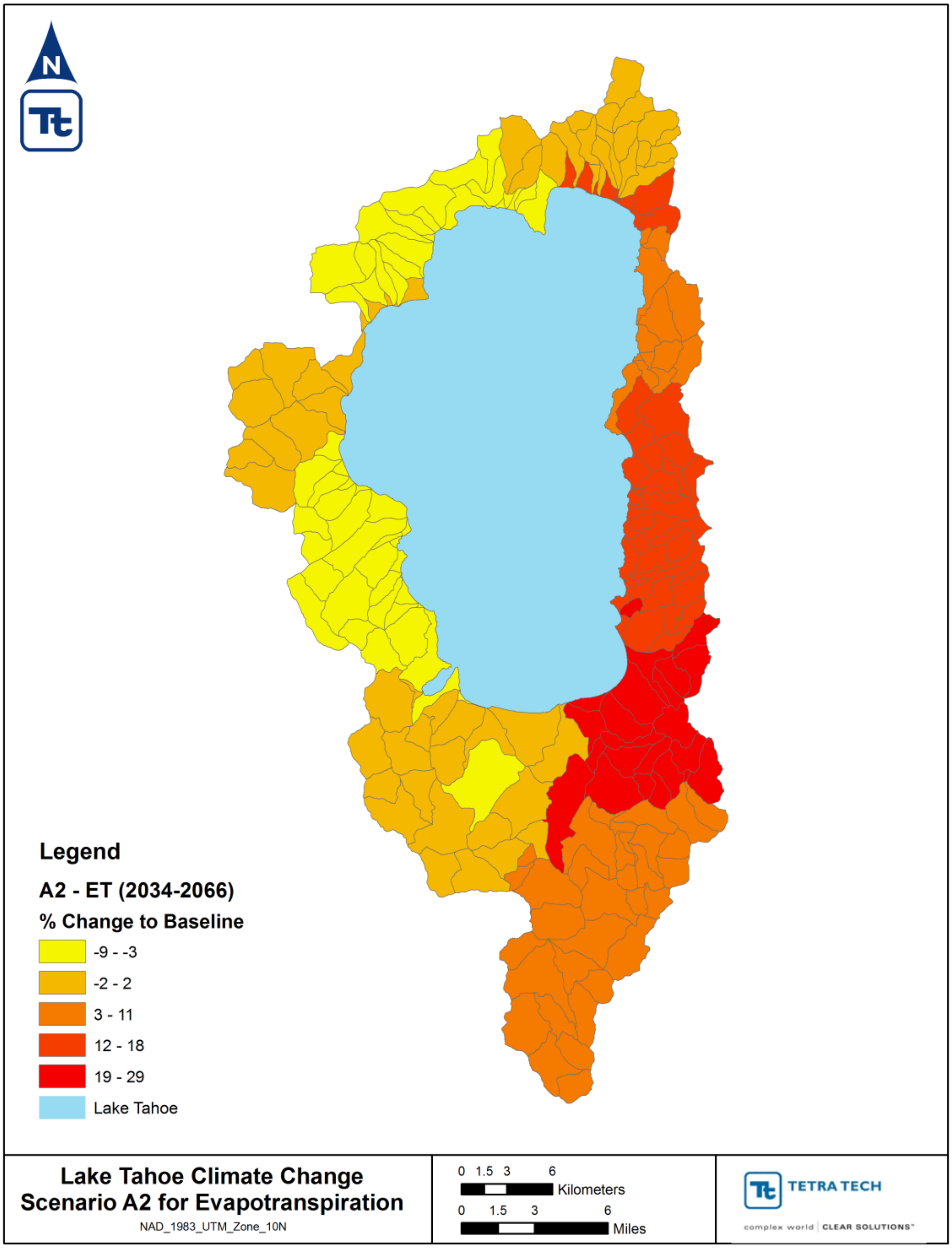

Figure 4-18. Spatial variation of evapotranspiration (ET) for GFDL A2 (2034-2066).

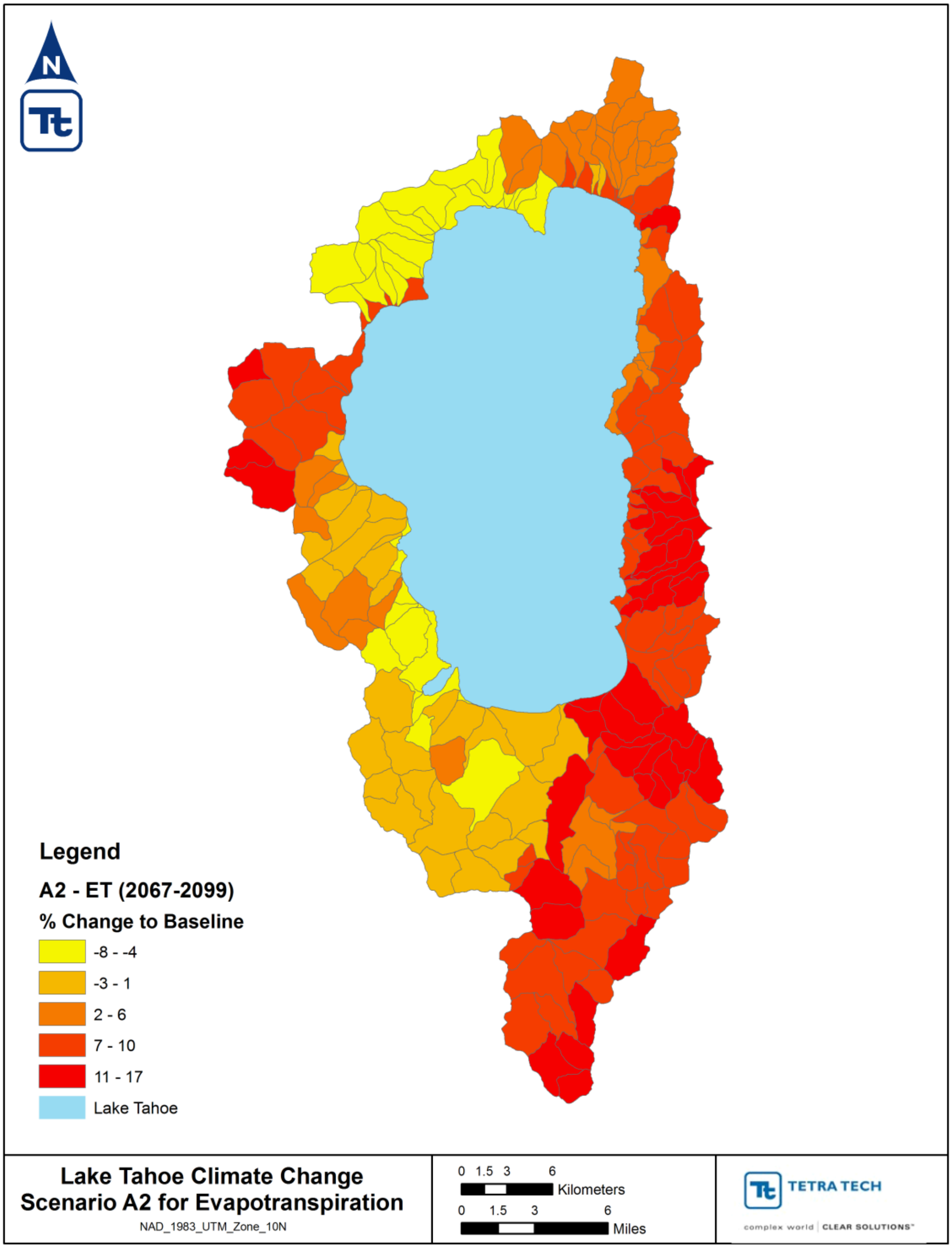

Figure 4-19. Spatial variation of evapotranspiration (ET) for GFDL A2 (2067-2099).

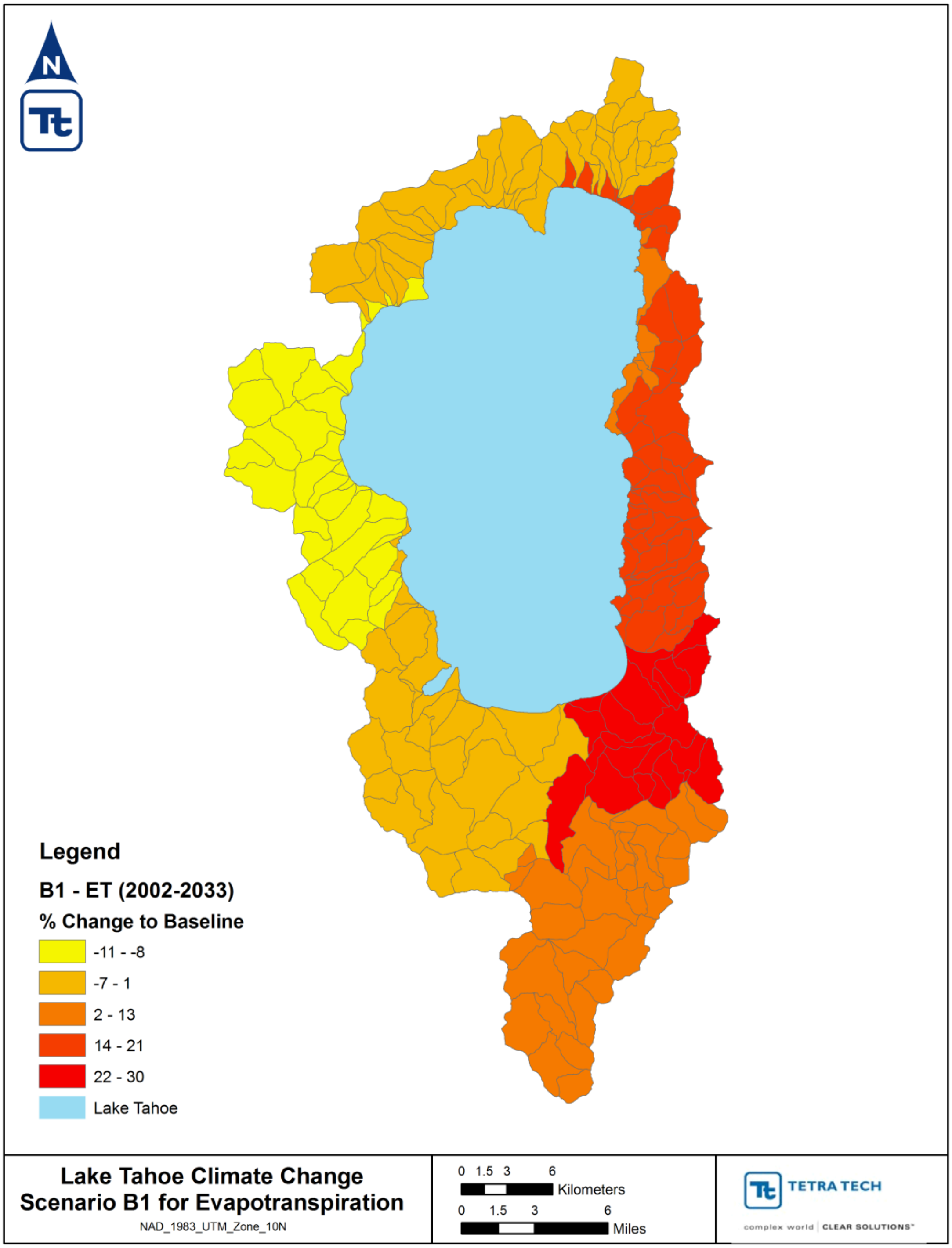

Figure 4-20. Spatial variation of evapotranspiration (ET) for GFDL B1 (2002-2033).

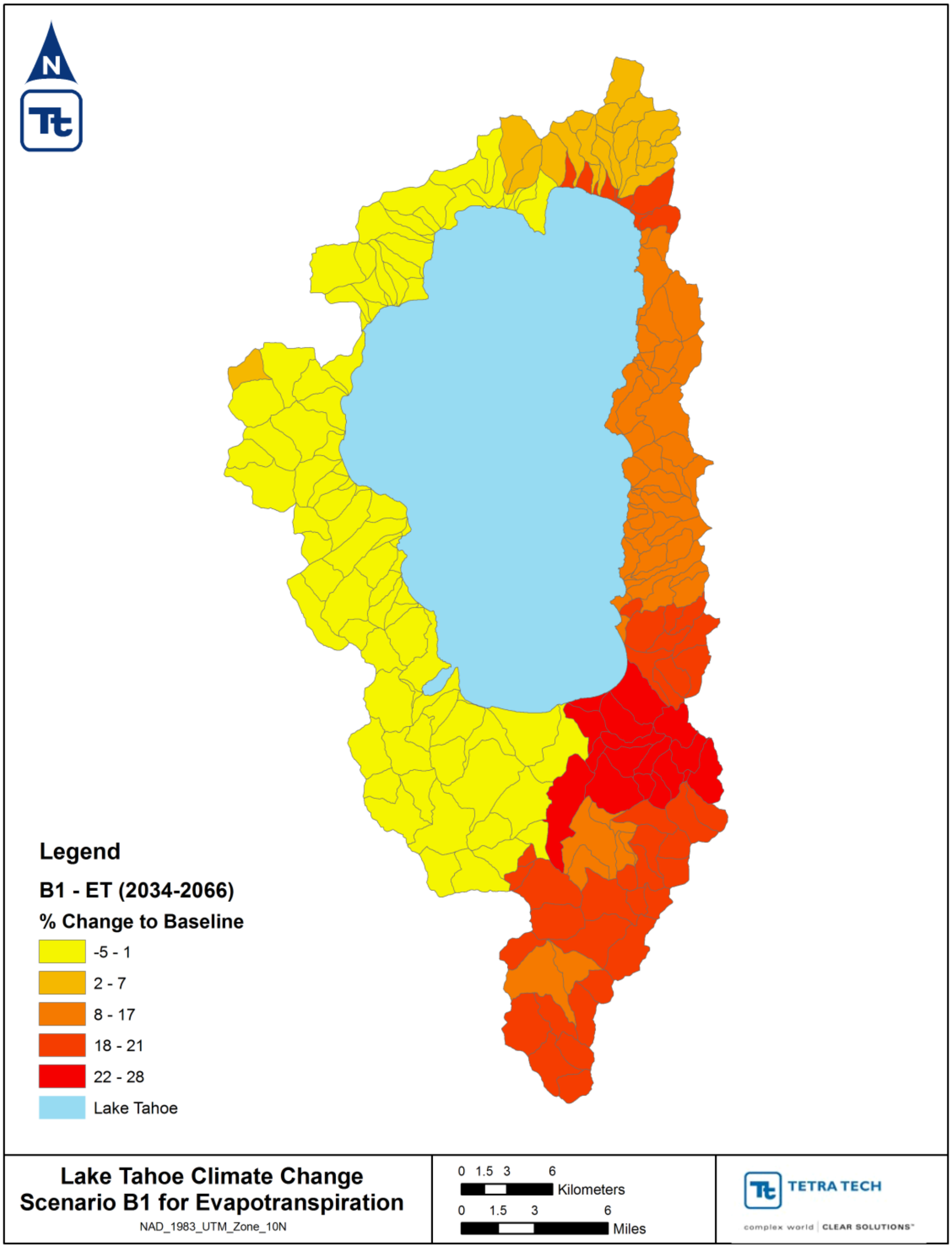

Figure 4-21. Spatial variation of evapotranspiration (ET) for GFDL B1 (2034-2066).

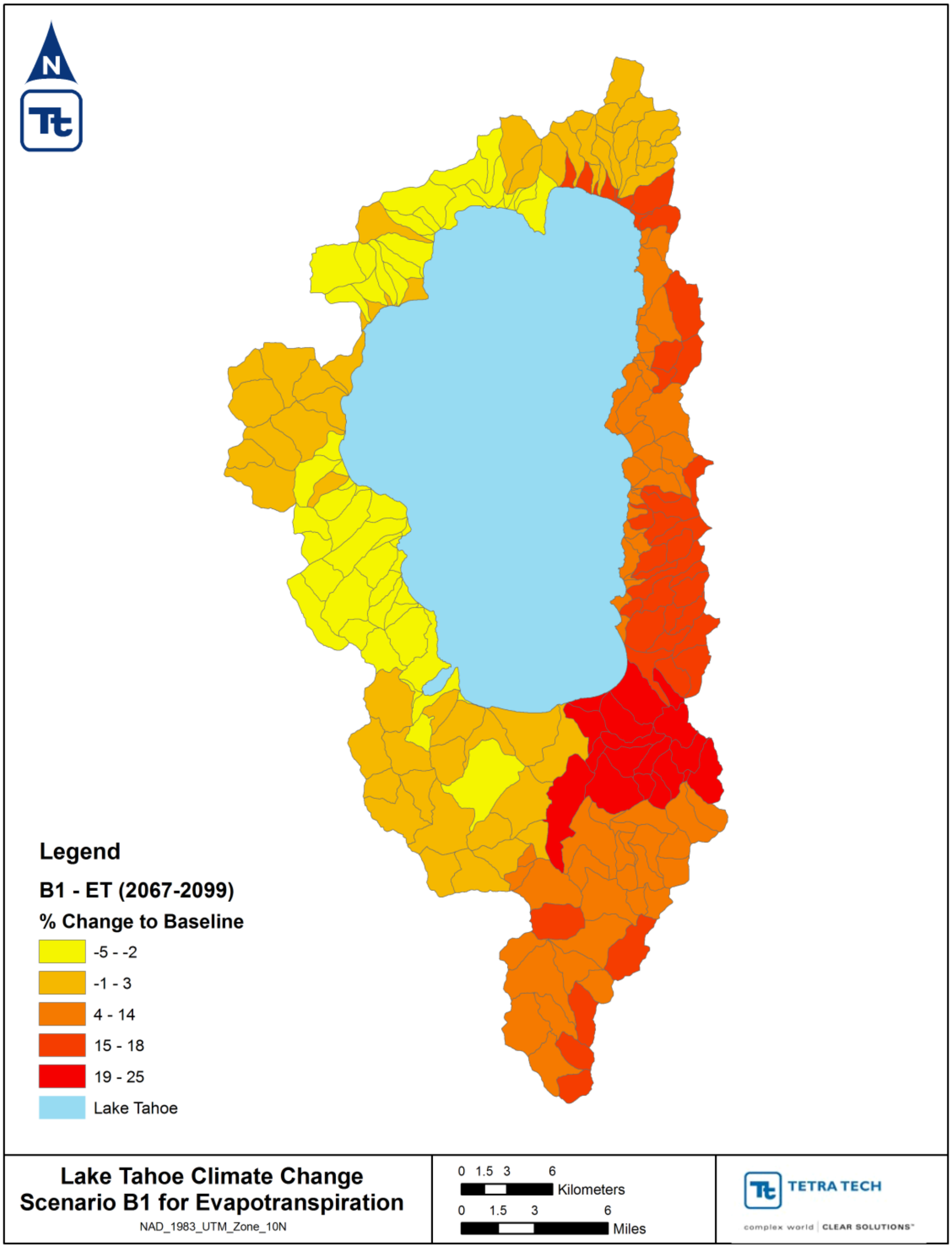

Figure 4-22. Spatial variation of evapotranspiration (ET) for GFDL B1 (2067-2099).

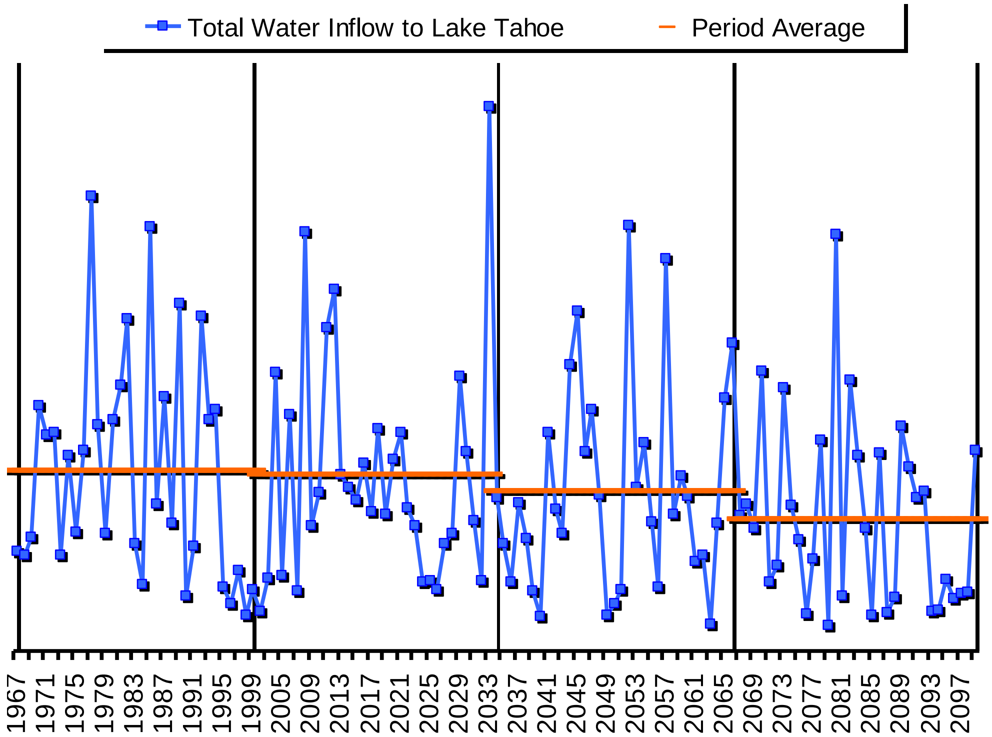

Figure 4-23. Total water yield to Lake Tahoe for GFDL A2.

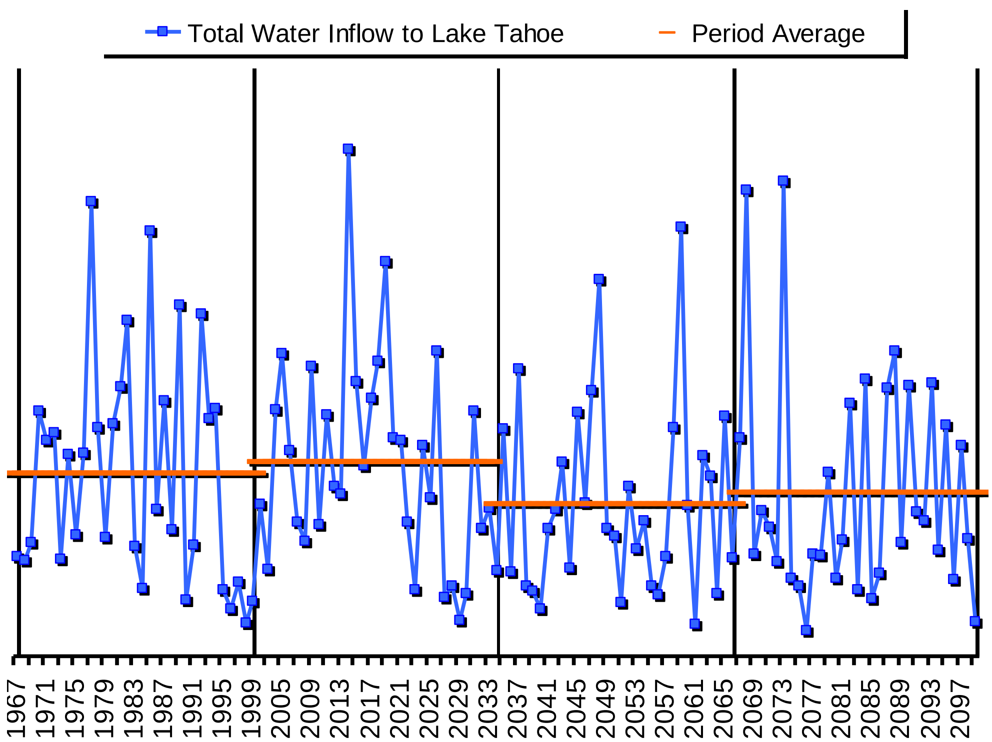

Figure 4-24. Total water yield to Lake Tahoe for GFDL B1.

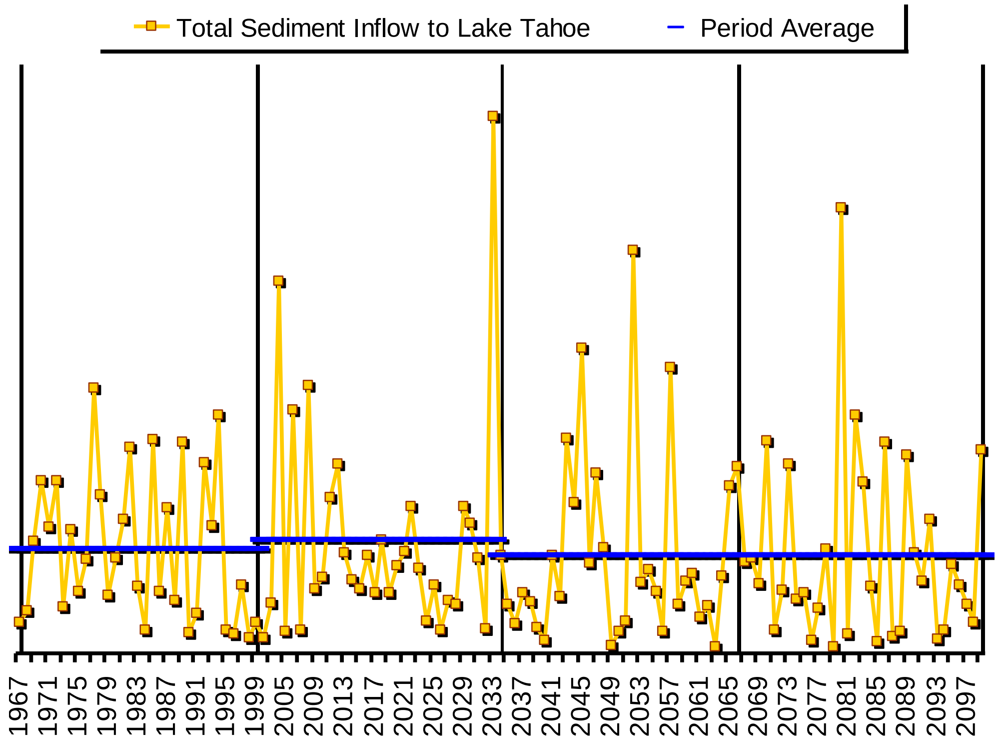

Figure 4-25. Sediment yield pattern to Lake Tahoe for GFDL A2 scenario.

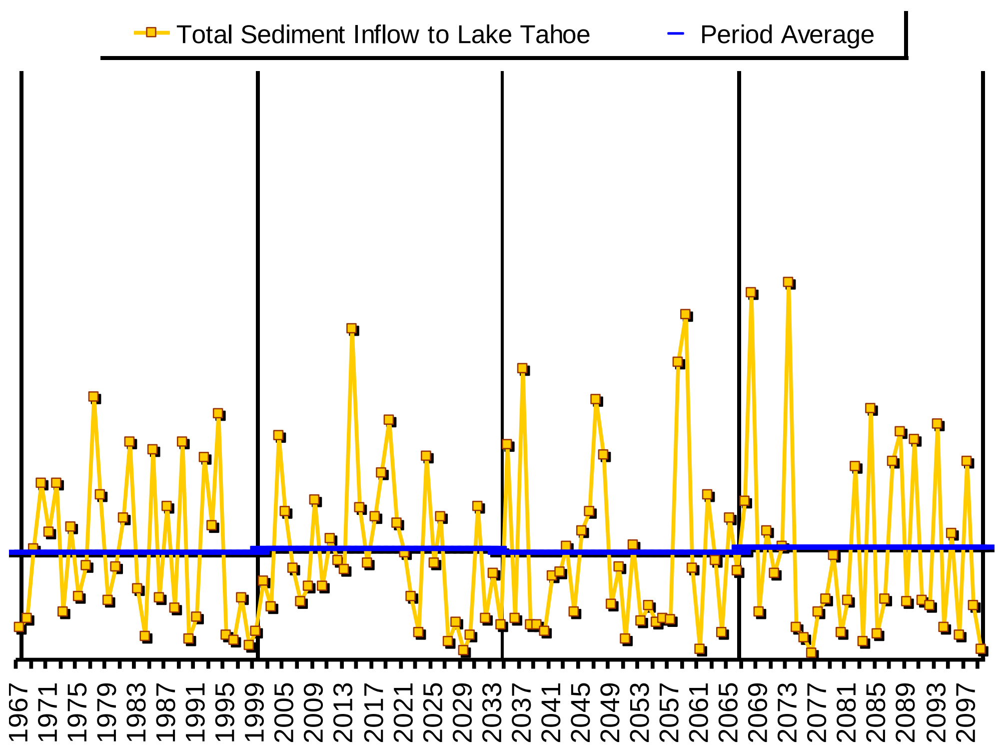

Figure 4-26. Sediment yield pattern to Lake Tahoe for GFDL B1 scenario.

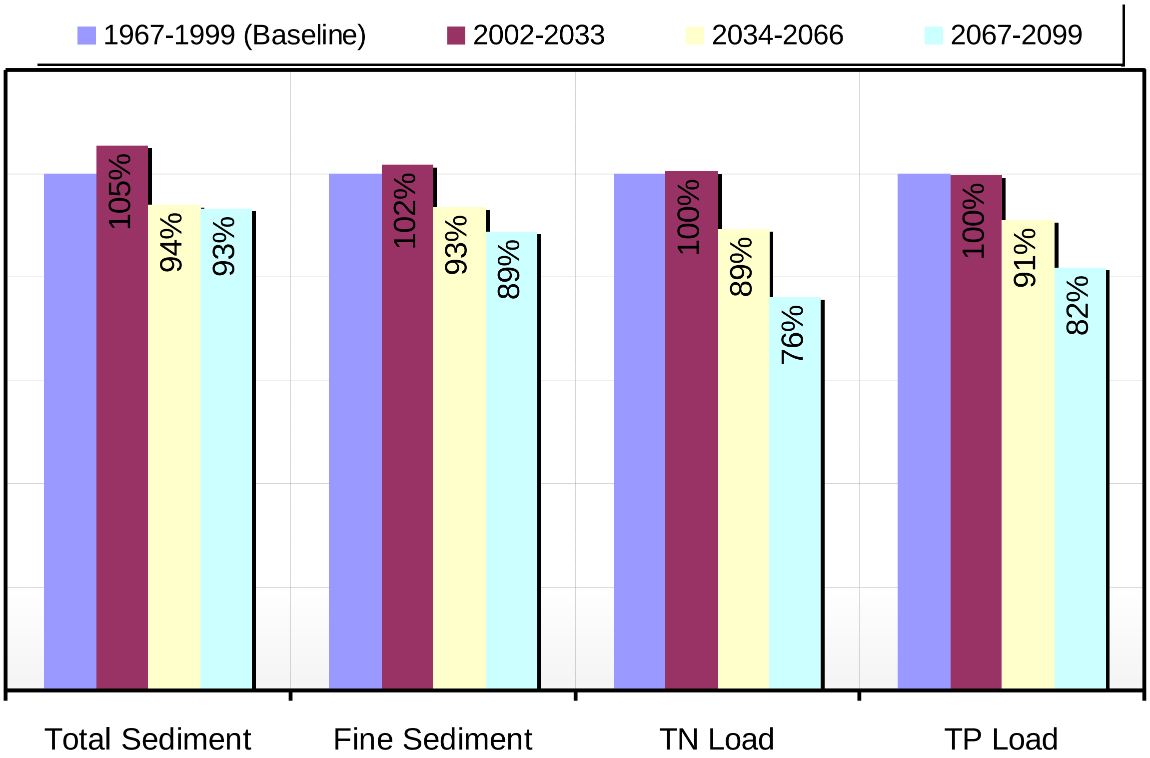

Figure 4-27. Water quality summary for GFDL A2 scenario.

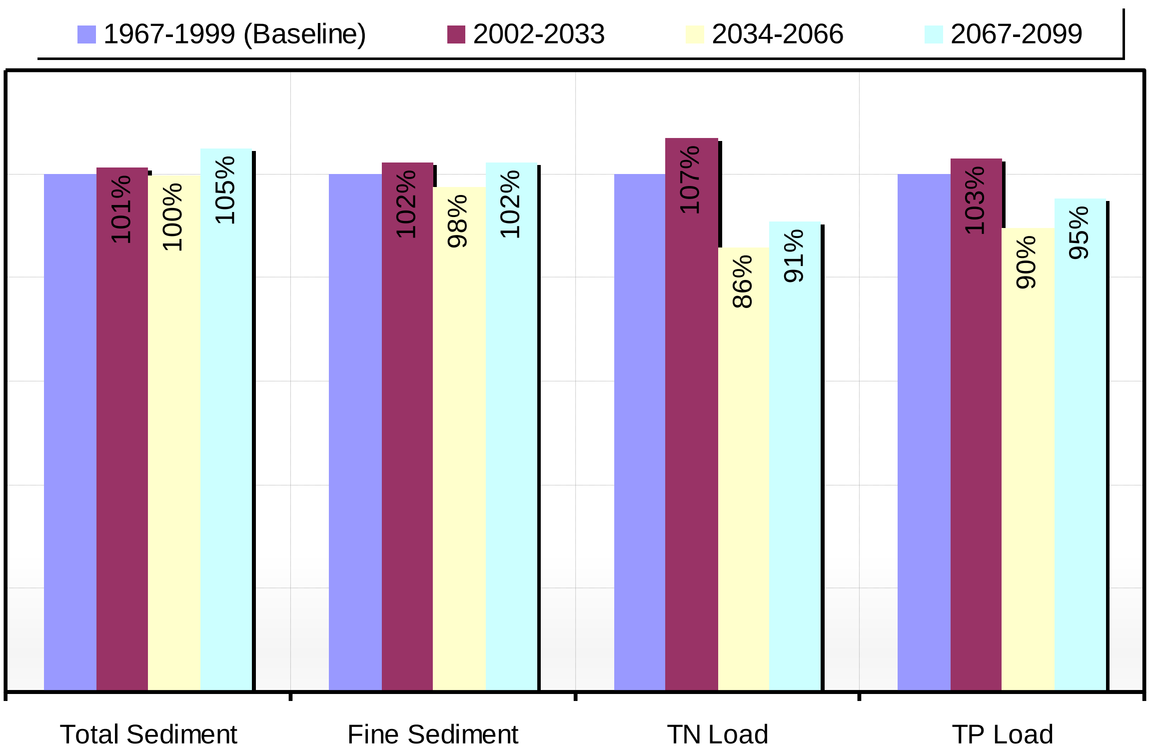

Figure 4-28. Water quality summary for GFDL B1 scenario.

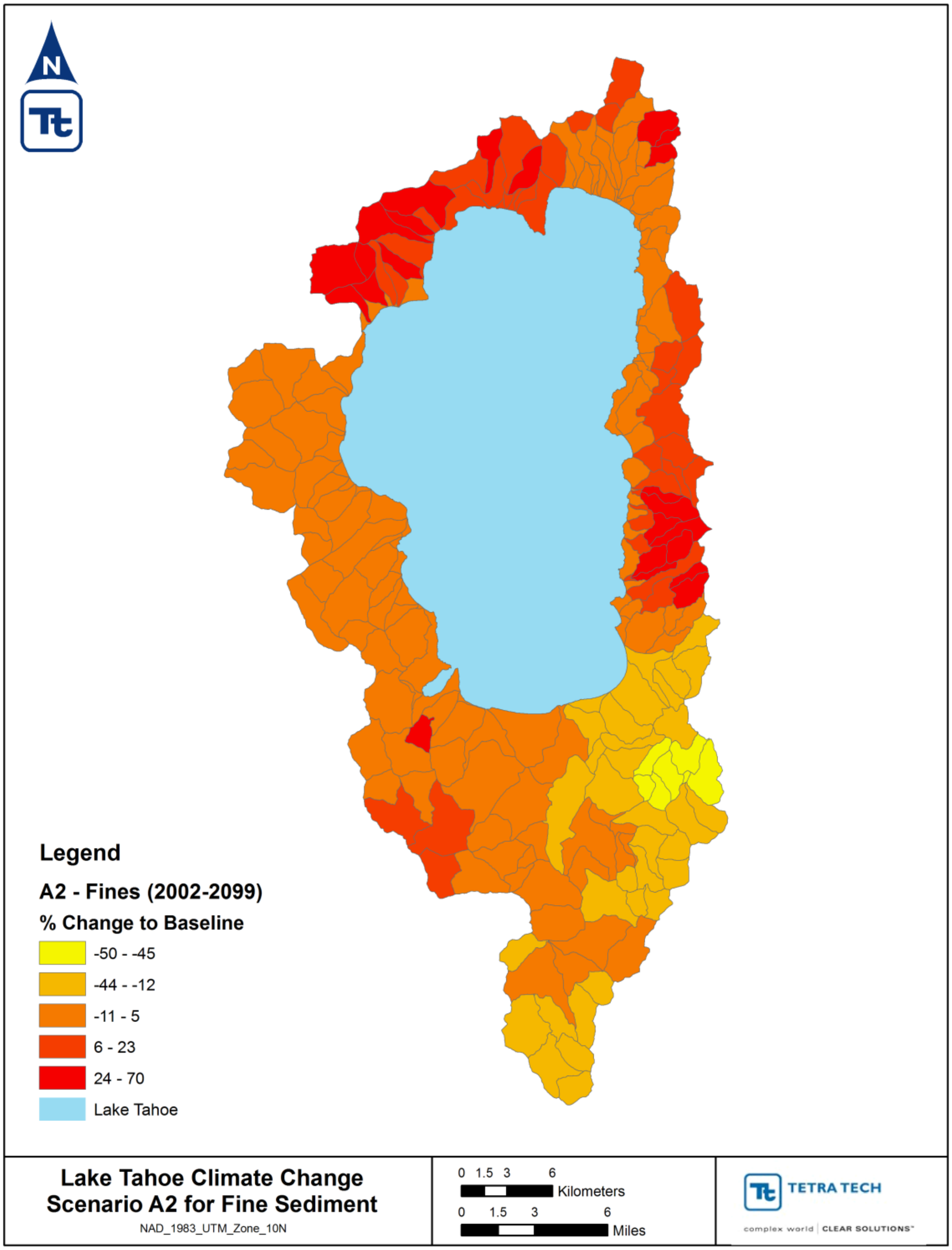

Figure 4-29. Spatial variation of fine sediment for GFDL A2 (2002-2099) scenario.

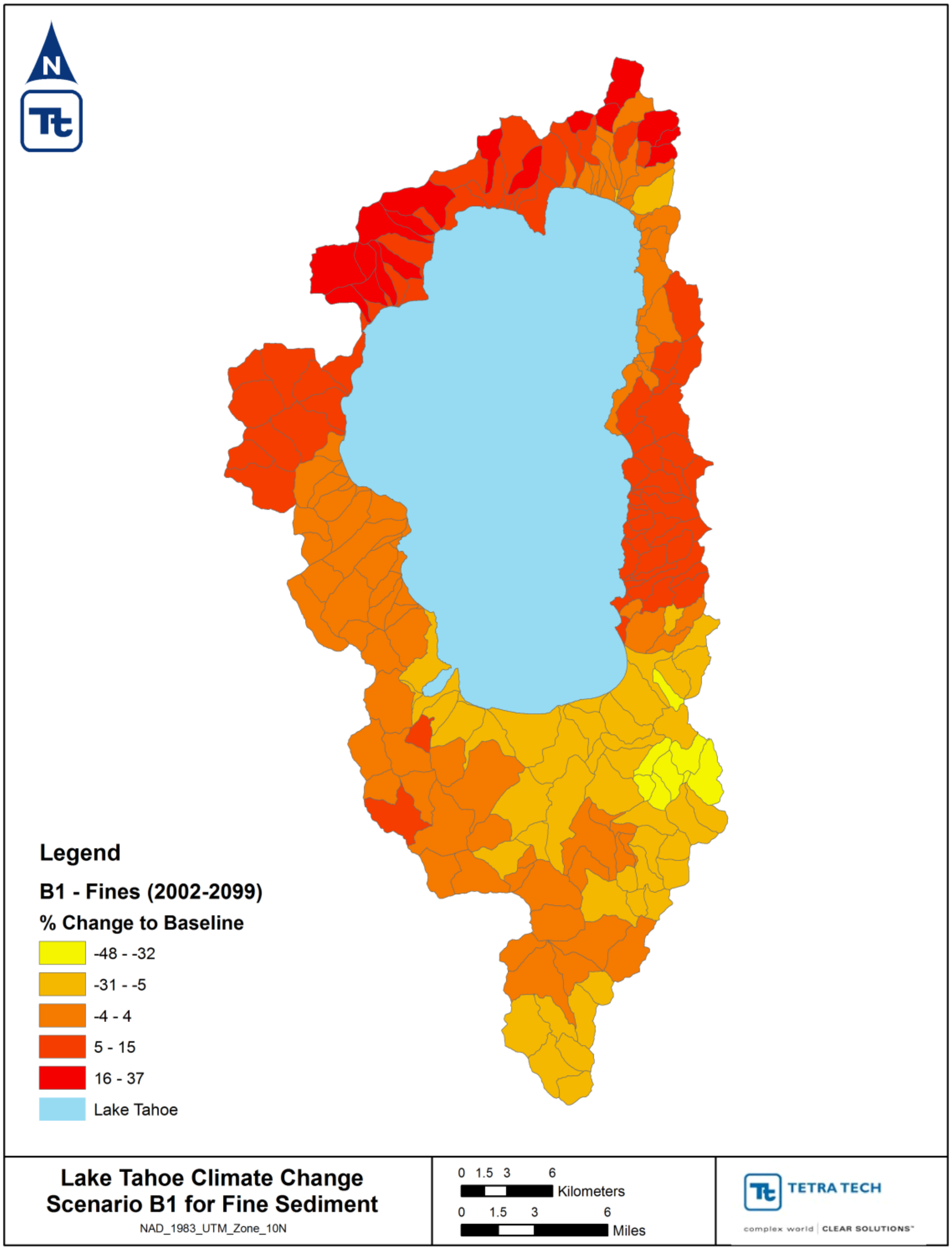

Figure 4-30. Spatial variation of fine sediment for GFDL B1 (2002-2099) scenario.

5.0 IMPLICATIONS OF CLIMATE CHANGE FOR DESIGN OF BMPs IN THE LAKE TAHOE BASIN

Author: Brent Wolfe P.E.

5.1 Background

The Lake Tahoe TMDL has identified stormwater retrofit of existing development as the key action to reduce pollutant loading to Lake Tahoe. Stormwater retrofit projects in the Tahoe basin are primarily implemented at two spatial scales: 1) neighborhood-scale water quality improvement projects (WQIPs) - designed and constructed by local agencies to reduce pollutant loads generated from roads and public parcels and 2) parcel-scale best management practices (BMPs) - constructed by private property owners to reduce pollutant loading generated from their individual parcel.

Climate change could potentially impact the long-term effectiveness of WQIPs and BMPs for reducing stormwater runoff and associated pollutant loads. The implications of climate change relative to the planning and design of WQIPs and BMPs are analyzed in this section. The assessment uses the meteorological data developed from the climate change scenarios and downscaling methods described in Section 2 and Appendix 2. Performance is assessed using the climate change data and long-term continuous simulation models of runoff and pollutant loading to estimate how climate change may affect pollutant load reduction performance.

5.2 Technical Approach

This section summarizes key aspects of the long-term continuous hydrologic and pollutant load modeling effort designed to represent runoff and water quality treatment within developed areas of the Tahoe basin.

5.2.1 Meteorological Assessment

The modeling analysis uses downscaled meteorological data developed from Global Climate Models (GCMs), which is described in Section 2 and Appendix A. Modeled historical data was used in simulations instead of measured historical data to focus comparison of results on climate change signals and avoid the influence of residual discrepancies between measured and modeled data. Various statistical properties of modeled and measured historical climate data were checked for consistency as described below to ensure the analysis was representative.

Figure 5-1 displays the locations of the SnoTel sites (measured data) and the centroid of each downscaled GCM grid cell (modeled data) within the Tahoe basin. GCM Cell 22 was selected for use in the analysis because the meteorological data for GCM Cell 22 was found to reasonably reflect historical meteorological conditions for the developed portion of the Tahoe basin.

Figure 5-2 shows the percentage of precipitation that falls as snow in the Tahoe basin at varying elevations. Figure 5-2 was developed using hourly SnoTel gage data for water years 1989 to 1999. For each SnoTel gage, the volume of precipitation that occurred when the temperature was at or below 34 degrees Fahrenheit was summed. This precipitation volume was divided by the total precipitation volume recorded at each SnoTel gage to estimate the percentage of precipitation that historically occurs as snow.

Figure 5.2 also displays the percentage of precipitation that falls as snow for GCM Cell 22. The procedure and time period for the calculation at GCM Cell 22 was identical to that conducted for the SnoTel gages. GCM Cell 22 is located at an elevation of 6,350 feet and is therefore within the elevation band where most development has occurred within the Tahoe basin (i.e. predominantly around the lake margins at elevations ranging from 6,230 feet to 6,600 feet). As shown in Figure 5.2, the modeled historical record at GCM Cell 22 estimates that roughly 55% of precipitation falls as snow, which compares well with the measured trend predicted by the SnoTel gages for the elevation of GCM Cell 22.

Figure 5.3 displays precipitation intensity exceedance curves for the Tahoe City SnoTel gage (measured) and the downscaled data for GCM Cell 22 (modeled) for water years 1989 to 1999. The data at GCM Cell 22 was downscaled using a procedure that relied upon data from the Tahoe City SnoTel gage (see Appendix 2). The x-axis of Figure 5.3 displays the number of hours when precipitation occurs at or greater than the corresponding intensity on the y-axis. The distribution of modeled precipitation intensities at GCM Cell 22 compares well with the measured precipitation intensities recorded at the SnoTel Gage. Note that the discrepancy seen in Figure 5.3 for a few hours of maximum precipitation intensity is caused by the measured data record including a rare and extreme precipitation event (New Year's Day event in 1997).

5.2.2 Modeled Period of Record

Hourly inputs of modeled temperature and precipitation data from GCM Cell 22 were used in the simulations for the periods of record shown below. The GFDL B1 and A2 emission scenarios were simulated to estimate potential future pollutant loading. The simulation dates for the water resource modeling in this section are:

Historical Simulation: 1961-1999
B1 Emission Scenario: 2001-2099
A2 Emission Scenario: 2001-2099

5.2.3 Project Area Representation and Assumptions

Figure 5.4 displays a typical project area for stormwater quality improvement within the Tahoe basin. The project area is located in Kings Beach, California and has a total area of roughly 85 acres. The project area was subdivided into four drainage areas for the model simulations to better characterize differences in land uses and land use conditions. The larger upper portion of the project area is predominantly single-family residential development serviced by local roads. The smaller lower portion of the project area is adjacent to the lakeshore, where commercial and highway land uses dominate.

Two representations of the project area were developed to compare pollutant load performance with and without stormwater quality improvements: 1) a Baseline Condition with modeling assumptions reflecting current land use conditions, maintenance practices, and pollutant sources and 2) an Improved Condition with modeling assumptions reflecting implementation of a hypothetical WQIP that addresses all pollutant sources from public lands and complete implementation of BMPs for all private parcels within the project area. Consequently, the historic (modeled), GFDL A2 and GFDL B1 scenarios were all used to model the project area under baseline and improved conditions.

Table 5-1 compares key modeling assumptions influencing differences in computed pollutant loads between the Baseline Condition, the Improved Condition, and the general effect of each assumption. Note that the Improved Condition represents a hypothetical but comprehensive level of improvements that exceeds typical current WQIP practice in the Tahoe basin. In existing practice, project funding is rarely sufficient to treat every pollutant source at a uniform or standard level, and site constraints (especially land availability) typically limit the options for stormwater treatment facilities.

Tahoe Regional Planning Agency code requires containment of the runoff volume generated by a 20-year return period, 1-hour duration "design storm" for BMPs on private parcels. This design storm is generally taken as one inch of rain in one hour. The calculation of the desired storage volume for design of a facility using this standard is made by multiplying the area of impervious surfaces tributary to the facility by 1-inch of rain. Although not a code requirement, this standard has also typically been applied as a target or objective for WQIPs. As shown in Table 5-1, the 20-year 1-hour design standard was used as a modeling assumption to size all infiltration and treatment facilities in the Improved Condition. As noted above, uniform application of this standard or objective is not always achieved in typical WQIP projects.

5.2.4 Models Applied

Both the Lake Tahoe Pollutant Load Reduction Model (PLRM) and EPA's Stormwater Management Model version 5 (SWMM5) were used to complete the analysis. The PLRM is a customized version of SWMM5, and was designed to evaluate and compare alternatives for stormwater quality improvement projects in the Tahoe basin. The PLRM uses long-term continuous simulations of hydrology and Tahoe basin water quality data to quantify stormwater runoff and pollutant loads for pollutant of concern to lake clarity. The PLRM program code augments the source code from SWMM5 to include customized user input forms with data entry needs specific to Tahoe basin stormwater management practices.

For the analysis, the PLRM was used to create the Baseline Condition and Improved Condition models. The simulations were performed in SWMM5 to accommodate the climate change data as the meteorologic inputs, and to allow detailed assessments of modeled output using the reporting functions available in SWMM5. The interested reader is directed to the following websites for a more detailed discussion of the functions and capabilities of the PLRM and SWMM5. The websites provide each model's technical documentation, user's manuals, and program executables:

- PLRM - http://www.tiims.org/TIIMS-Sub-Sites/PLRM/docs-downloads.aspx
- SWMM5 - http://www.epa.gov/ednnrmrl/models/swmm/

Table 5-1. Modeling Assumptions for the Baseline and Improved Condition.

Type of Project	Condition	Model Representation		Effect of Improved Relative to Baseline
		Baseline Condition	Improved Condition	
WQIP	Pollutants available for transport from roads and road shoulders	1. Road shoulders are generally unstable and susceptible to erosion. 2. Street sweeping to collect abrasives applied for winter traffic safety occurs infrequently.	1. All road shoulders susceptible to erosion are stabilized. 2. Street sweeping occurs frequently to recover abrasives applied for winter traffic safety.	Characteristic runoff concentrations generated from roads have better water quality
	Stormwater generated from roads	Roads are steep and/or have drainage systems, which results in a high degree of directly connected impervious area (DCIA). For this project area DCIA is estimated at 80% for roads.	Some roads are disconnected from the drainage system and runoff is routed to pervious areas. The improvements are assumed to result in 60% DCIA for roads (a reduction in DCIA of 20%).	Stormwater runoff generated from roads is reduced
	Stormwater treatment of runoff	1. One stormwater treatment facility exists and collects runoff from roughly 10 acres of developed area. 2. Maintenance of the stormwater treatment facility is minimal.	1. All runoff from roads is routed to stormwater treatment facilities. 2. Each facility is sized to capture 1-inch of runoff from the road area tributary to the facility that is classified as DCIA. 3. The stormwater treatment facilities are well-maintained.	Stormwater quality is improved for pollutants of concern
BMP	Pollutants available for transport from parcels	Many parcels have compacted or disturbed pervious areas that erode and generate pollutants.	All compacted and disturbed pervious areas are restored and protected from future disturbances.	Characteristic runoff concentrations generated from parcels have better water quality
	Stormwater generated from parcels	1. The project area is relatively steep and many parcels have impervious area that is directly connected to roads and drainage systems. 2. Very few parcels have facilities constructed to intercept, detain, and infiltrate stormwater.	1. Runoff from impervious areas are routed to infiltration facilities on each parcel. 2. Each infiltration facility is sized to detain and infiltrate 1-inch of runoff from the impervious area tributary to the facility.	Stormwater runoff generated from parcels is reduced

5.3 Results and Discussion

This section summarizes results from the long-term continuous simulations as shown in Figures 5-5 through 5-8. Results are mainly presented as 10-year moving averages of annual pollutant loading to better illustrate long-term trends by smoothing variations in modeled output affected by inter-annual variability in predicted meteorology.

In most cases, results are presented for both the Baseline Condition and Improved Condition for the entire simulation period, which covers a historical period (1961-1999) and a projected period (2001-2099). Results are generally presented for both the GFDL B1 and A2 emission scenarios for the projected period (2001-2099). Also note that the assumptions used in the model runs representing the Baseline Condition and Improved Condition are static over the simulation period (1961-2099). Meaning that over the entire 140-year simulation period, the assumptions do not vary (e.g. infiltration rates are constant, storage volumes are constant, etc.).

5.3.1 Fine Sediment Loading

Figure 5-5 displays the 10-year moving average of annual fine sediment particle (FSP) loading generated from the project area over the simulation period. For the purpose of this analysis, and consistent with the Lake Tahoe TMDL, FSP is defined as sediment particles, 16 µm in diameter. Both the Baseline Condition (Figure 5-5a) and Improved Condition (Figure 5-5b) are presented. For the Baseline Condition, no statistically significant trend was found in FSP loading over the simulation period. For the Improved Condition, a statistically significant trend was found displaying a modest increase in FSP loading over the simulation period. This trend was statistically significant for both the B1 and A2 emission scenarios.

5.3.2 Stormwater Treatment Performance

Figure 5-6 displays the 10-year moving average for the percentage of the annual runoff volume captured and treated in the Improved Condition, where the storm water treatment facilities were sized using the 20-year 1-hour design criterion discussed above.

The simulated stormwater treatment facilities captured and treated between 80-90 percent of the annual runoff volume throughout the simulation period. Typical standards for national practice for design of stormwater treatment facilities target capture and treatment of 80-90 percent of the average annual runoff volume (Roesner et al. 1998; Urbonas and Stahre 1993). A modest trend is apparent in Figure 5-6 showing a decline in the total annual runoff volume captured and treated for both the A2 and B1 emission scenarios. However, the reduction in performance is on the order of 10 percent, or approximately the range in typical standards of practice. At the end of the simulation period, capture remains above about 80 percent of runoff, indicating that load reductions consistent with current national stormwater management practice would still be achievable under the climate change scenarios analyzed using the 20-year 1-hour design criterion.

5.3.3 Implications of Climate Change on Pollutant Loading

Figure 5-7a displays precipitation intensity exceedance curves comparing the historical time period (1961-1999) to a 40-year segment of the projected time period (2061-2099). Relative to the historical time period, the segment of time analyzed for the A2 emission scenario exhibits more frequent occurrences of slightly higher precipitation intensity. The B1 emission scenario has a similar distribution of precipitation intensity relative to the historical period examined. Figure 5-7b displays exceedance curves for peak flows in stormwater runoff that compare the same time periods used in Figure 5-7a. Both the A2 and B1 emission scenarios exhibit more frequent occurrences of higher peak flows relative to the historical period. Note that the B1 distribution of precipitation intensities in Figure 5-7a is similar to the historical period but peak flows for stormwater runoff are generally higher relative to the historical period.

Figure 5-8 displays the 10-year moving average of the annual volume of precipitation occurring as snow for the simulated project area. There is a notable declining trend in the amount of precipitation that occurs as snow for both the A2 and B1 emission scenarios, highlighting a shift towards more rain and less snow. Figures 5-7 and 5-8 suggest that changes in temperature, and possibly precipitation intensity under the A2 emission scenario, could increase the frequency of peak flows in stormwater runoff in developed portions of the Tahoe basin.

Figure 5-9 displays the 10-year moving average of annual fine sediment particle (FSP) loading generated from the project area over the entire simulation period. Both the Baseline Condition and Improved Condition for the B1 emission scenario are shown in Figure 5-9. The simulated results for the Improved Condition show a modest decline in performance for FSP load reductions (i.e. increase in average pollutant load) as a result of climate change. However, the Improved Condition continues to provide more than 80% FSP reduction potential relative to the Baseline Condition throughout the entire simulation period. These results suggest that while there may be an influence of climate change in the 21st Century, the relative deviation from historic conditions should be small. In other words, climate change will have some effect on the performance of these improvements, but any diminished performance will be relatively small and load reduction would still be significant.

5.3.4 Limitations of Analysis

The following summarizes some of the key limitations of the modeling analysis. Limitations below do not discuss uncertainties associated with the GCM data or downscaling methods applied to the GCM data.

1. Changes in erosion-based processes were not modeled. The results of the analysis suggest a shift in precipitation patterns will produce more frequent runoff events with higher peak flows relative to historical conditions. Higher peak flows in stormwater runoff could increase erosion in drainage channels and streams, resulting in increased pollutant loading to the lake. In addition, the energy associated with rain falling directly onto soil as opposed to snowmelt is likely to promote erosion The potential effect that increased erosion may have on pollutant loading was not analyzed.

2. Potential changes in management actions are not modeled. Some management actions affecting pollutant loading may be altered in reaction to climate change and are not characterized in the analysis. For example, a decline in the number of snow storms could potentially decrease the quantity of road abrasives applied for winter safety,

which in turn could potentially produce better characteristic runoff concentrations from roads relative to historical conditions.

Figure 5-1. SnoTel gages and centroid of GCM cells in Tahoe basin.

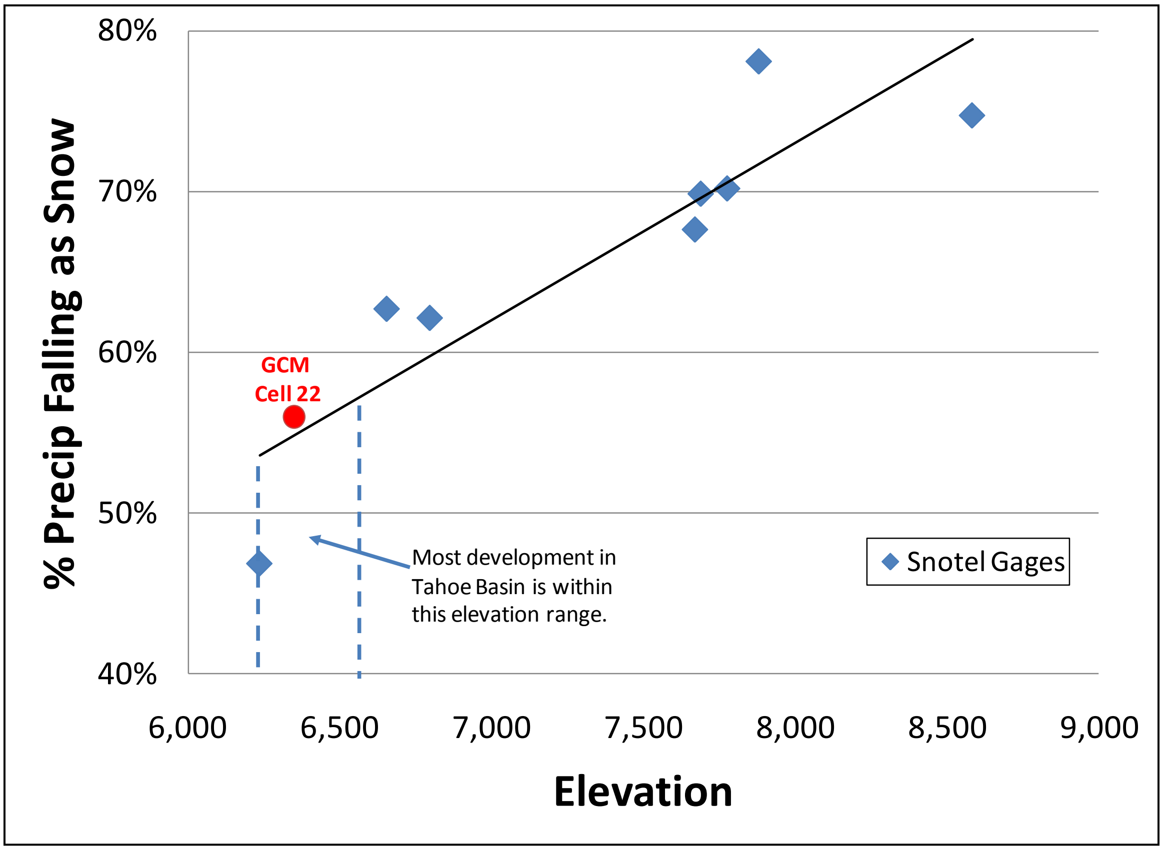

Figure 5-2. Percentage of precipitation falling as snow in Tahoe basin by elevation (Period of record analyzed: Water Years 1989 – 1999).

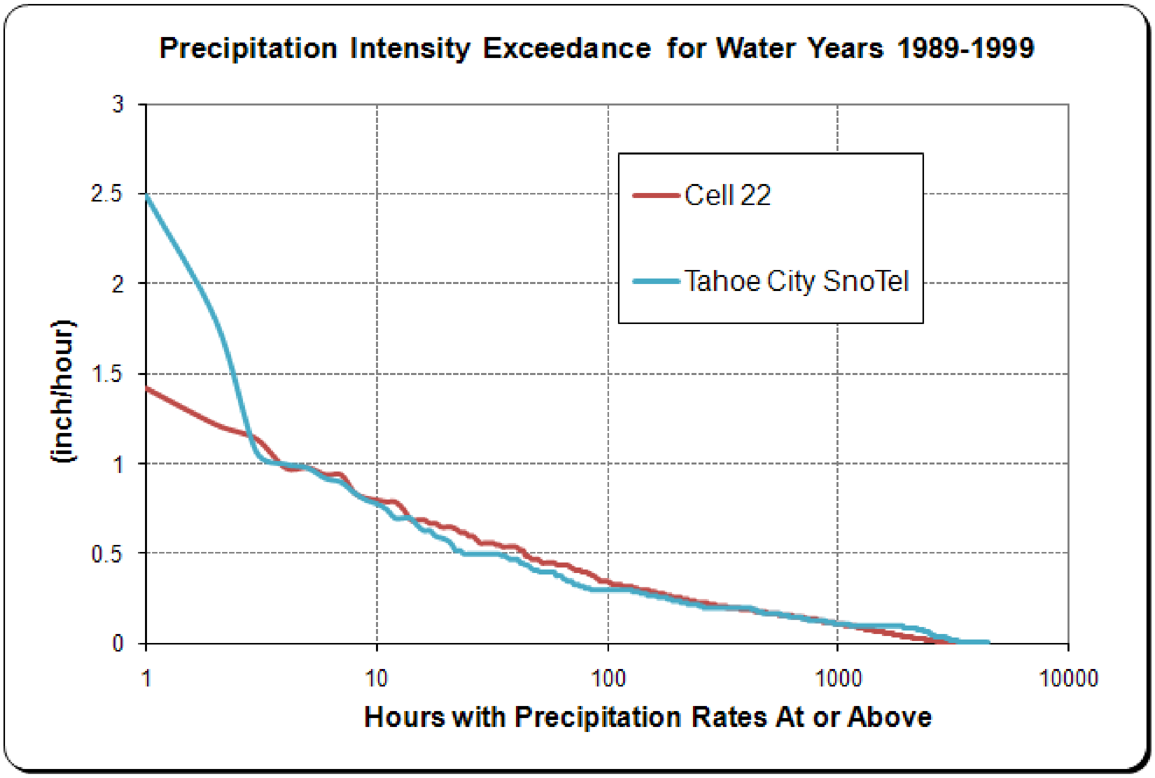

Figure 5-3. Comparison of hourly precipitation intensity exceedance for the Tahoe City SnoTel gage and GCM Cell 22 (Period of record analyzed: Water Years 1989 – 1999).

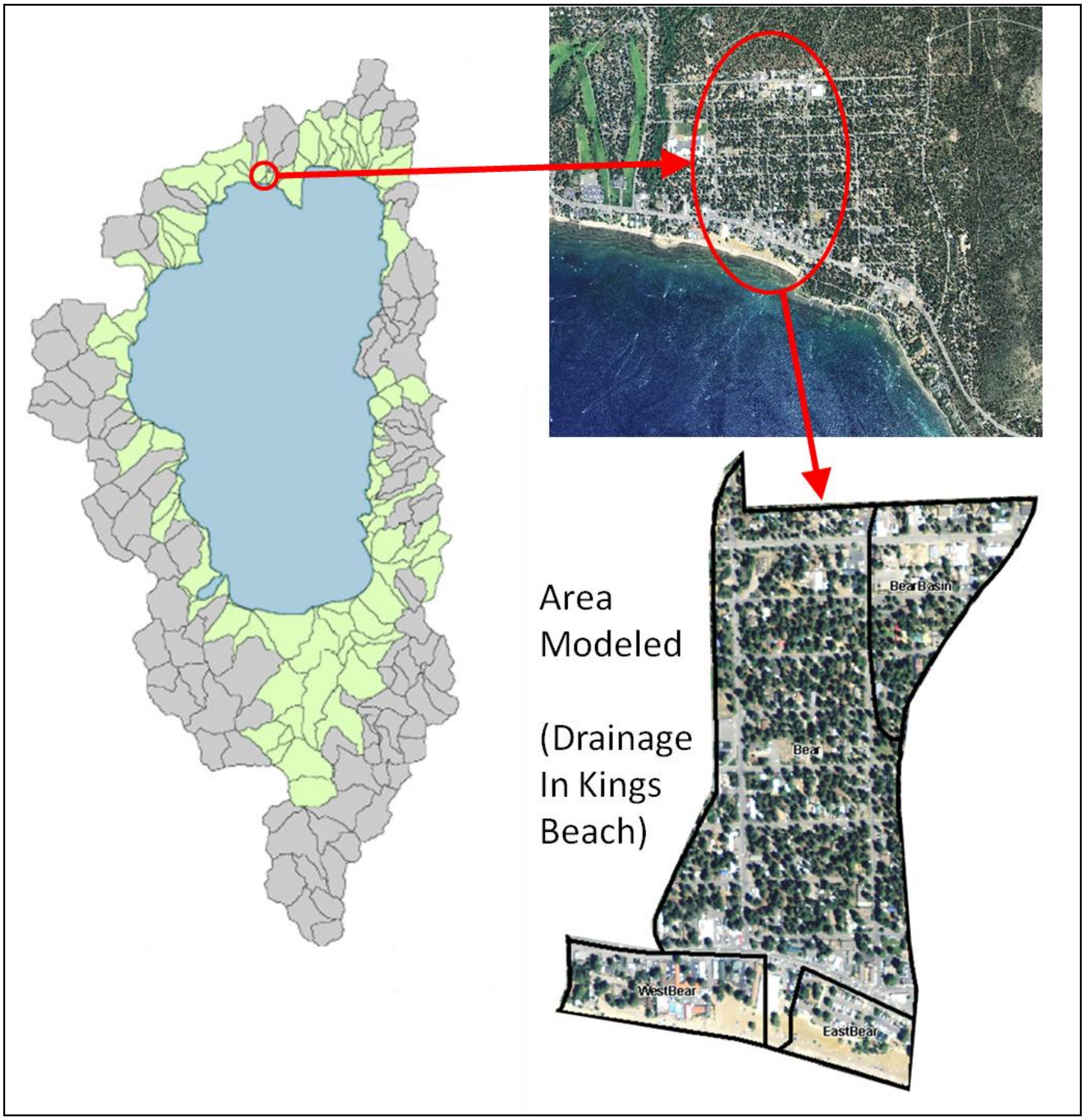

Figure 5-4. Project area modeled.

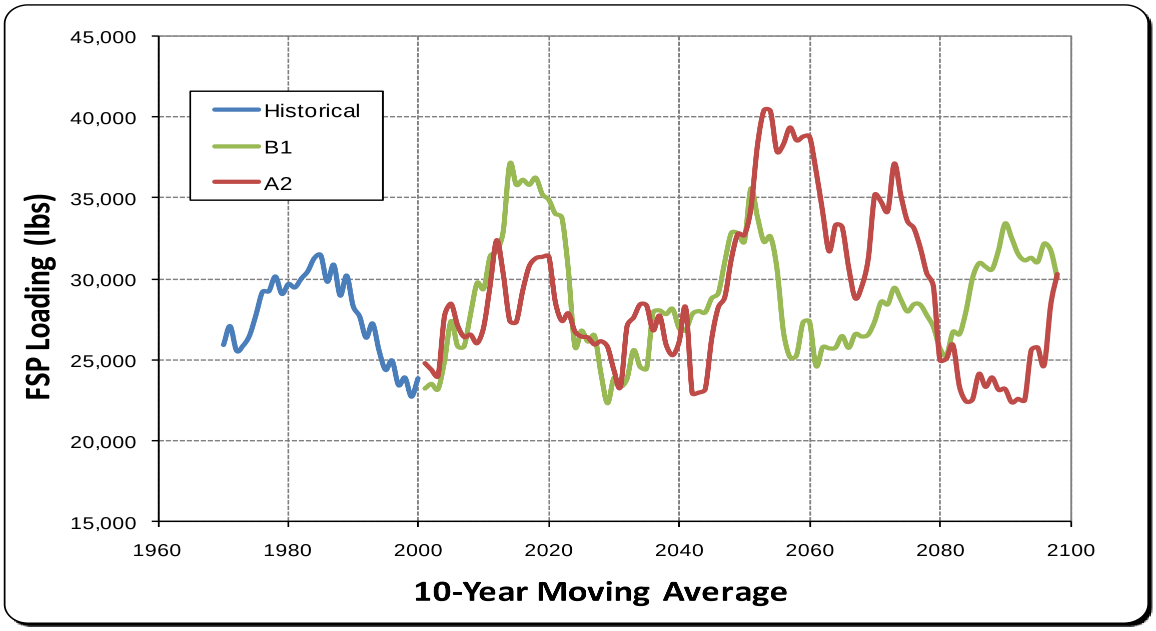

Figure 5-5a. 10-year moving average: annual fine sediment particle loading for Baseline Condition.

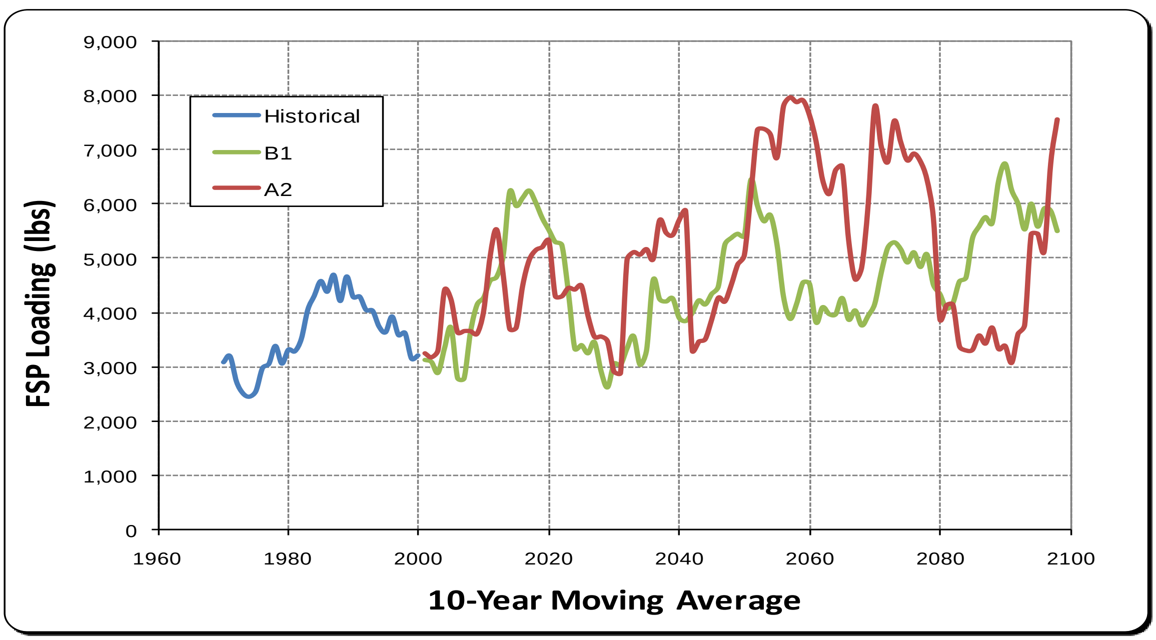

Figure 5-5b. 10-year moving average: annual fine sediment particle loading for Improved Condition.

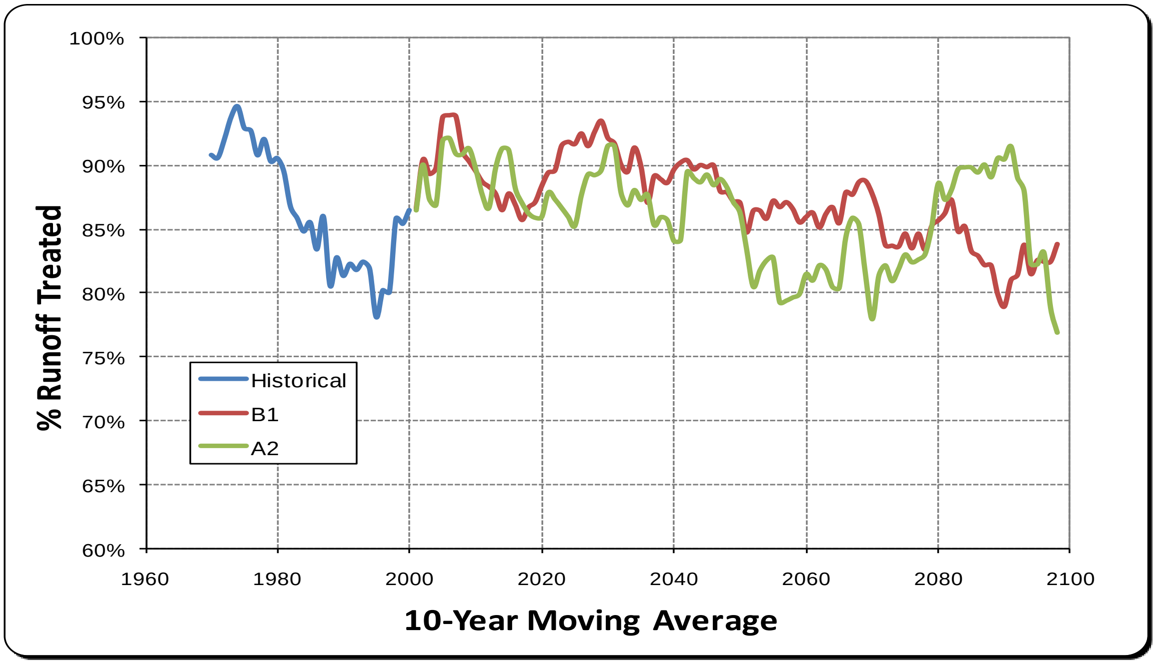

Figure 5-6. 10-year moving average: annual percentage of runoff volume treated by stormwater treatment facilities (Improved Condition).

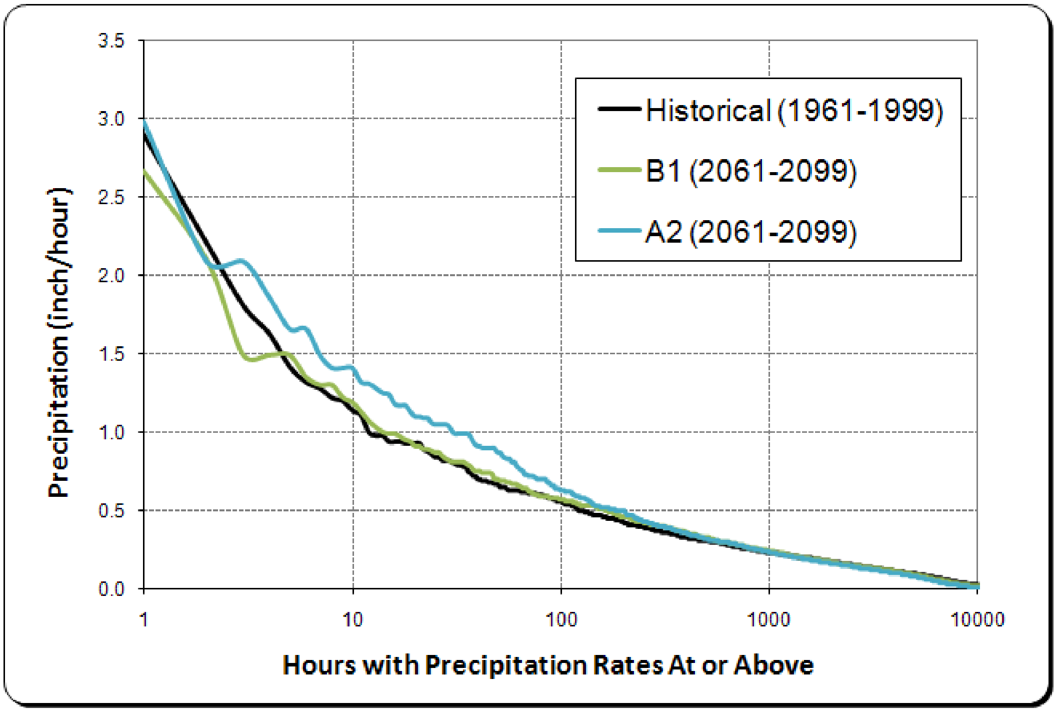

Figure 5-7a. Hourly precipitation exceedance for 40-year periods (Historical: 1961-1999; B1 and A2 emission scenarios: 2061-2099).

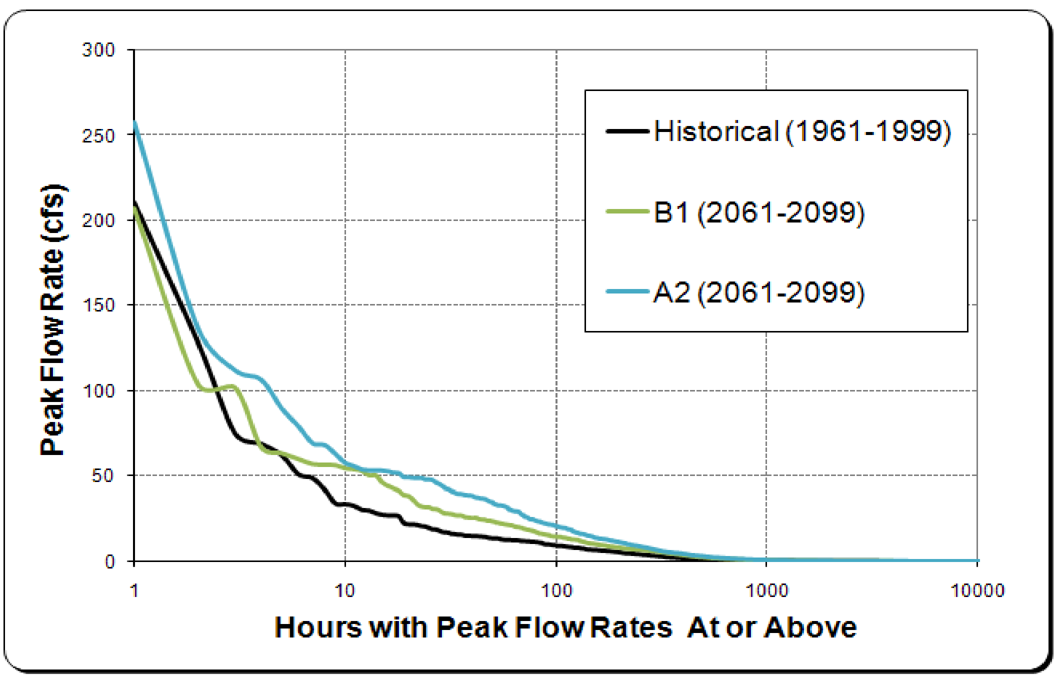

Figure 5-7b. Hourly runoff exceedance for 40-year periods (Historical: 1961-1999; B1 and A2 emission scenarios: 2061-2099).

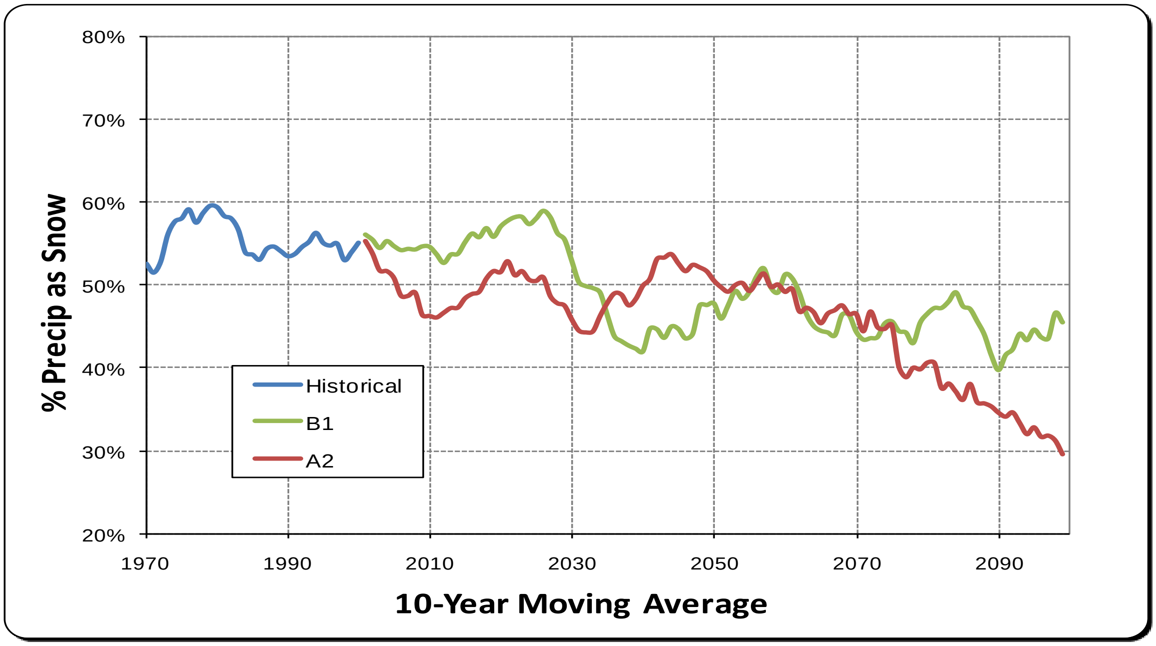

Figure 5-8. 10-year moving average: annual precipitation volume falling as snow at an elevation of 6,350 feet.

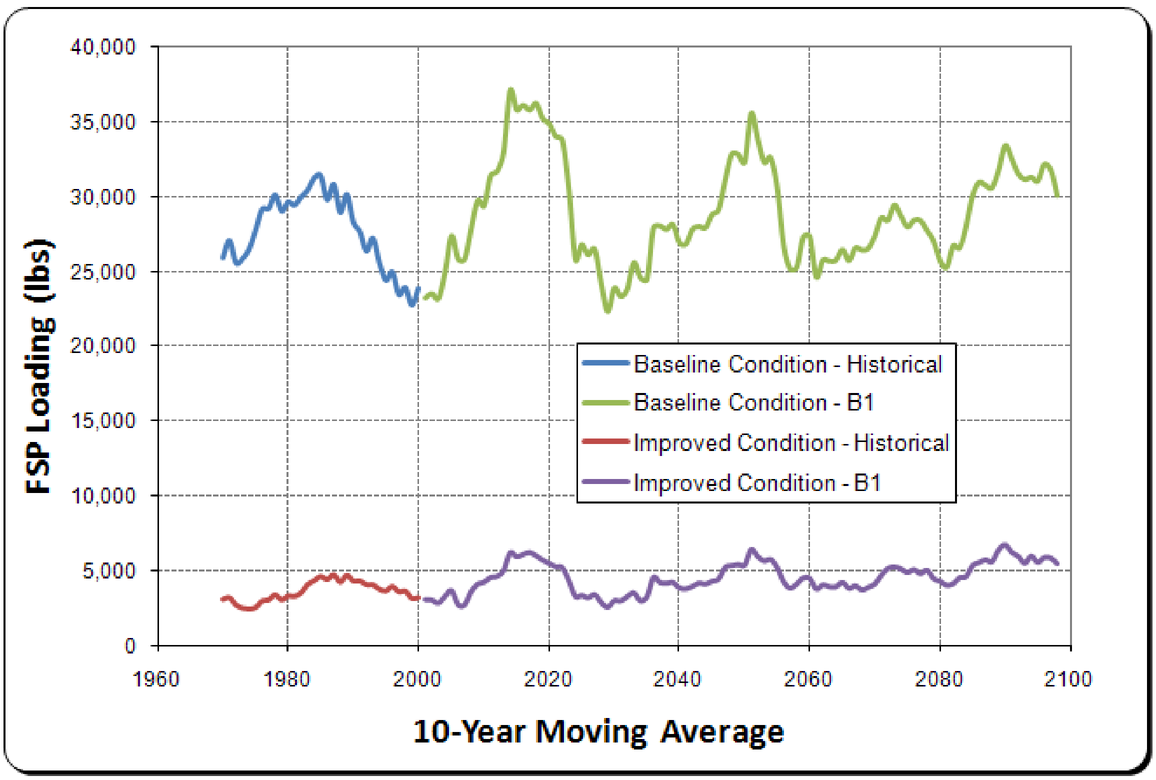

Figure 5-9. 10-year moving average: annual fine sediment particle loading for Baseline Condition and Improved Condition (B1 emission scenario).

6.0 THE RESPONSE OF LAKE TAHOE TO CLIMATE CHANGE

Authors: Goloka B. Sahoo Ph.D., S. Geoffrey Schladow Ph.D. and John E. Reuter Ph.D.

6.1 Lake Clarity Model

The lake response to climate change was estimated using the Lake Clarity Model (LCM) (Sahoo et al. 2010), the customized model based on the UC Davis water quality model DLM-WQ (e.g. Hamilton and Schladow 1997; Fleenor 2001; Perez-Losada 2001; Heald et al.,2005; Chung et al. 2009). The hydrodynamic component of the model is based on the original DYRESM (Imberger et al. 1978). Fleenor (2001) added the river plunging algorithms in the hydrodynamic module. The primary hydrodynamic model is one-dimensional (1-D) and is based on a horizontally mixed Lagrangian layers approach (Hamilton and Schladow 1997); however, the stream inflows and mixing due to stream turbulence is two-dimensional (2-D). Figure 6-1 shows the conceptual design of LCM. All the ecological modules are incorporated into the 1-D hydrodynamic model (double line box). The hydrodynamic model simulates stratification, mixing, the transport of all pollutant in the vertical direction, and determines the stream plunging depths. The ecological modules simulate transformation processes associated with algal photosynthesis. Flows and pollutants (nutrients and fine particles) from atmosphere, streams and intervening zones (both urban and non-urban), groundwater and shoreline erosion into the lake are shown at the top of the double line box. Figure 6-2 shows pools of dissolved oxygen (DO) sources and sinks. Sahoo et al. (2010) demonstrated the ability of the LCM to capture the seasonal temperature and DO patterns.

Figures 6-3 and 6-4 present the calibrated and validated temperature and DO results for the period 2000 to 2004. In-situ measurement records for water temperature and dissolved oxygen concentration were available monthly at depths of 0, 10, 50, 100, 150, 200, 250, 300, 350, 400, and 450 m below water surface at the mid-lake station, and these measured values were compared to the LCM-simulated values. Figure 6-3 shows that lake water temperature remains at approximately 5^{o}C at depths below 100 m year round. The winter deep mixing occurs during February and March. Stratification starts to build up in April and becomes strongest during August. Surface DO is strongly influenced by the water temperature because of the oxygen exchange at the air-water interface. Surface DO concentration is higher at lower water temperature and vice versa. The DO concentration away from the water surface depends on the sources and sinks shown in Figure 6-2, as well as mixing processes within the lake. Figure 6-4e and 6-4f illustrate that the sudden spike in DO concentration below 100 m are due to the deep mixing events. It is evident in Figure 6-5 that (1) DO concentrations continuously decreases in absence of deep mixing and (2) the lake becomes homogenized because of the winter mixing (see March 2007 winter mixing in Figure 6-5). Figure 6-5 shows that DO concentration declines at 0.1 mg/L per month for the BOD, COD, DOC, SOD and nitrification processes. Thus, DO concentration at the lake bottom reduces to zero in approximately 6 years in absence of deep mixing.

6.2 Model Changes and Assumptions

6.2.1 Sediment release rates

As part of this study, the treatment of sediment nutrient release was modified in the LCM. Nutrients are released from the sediments when anoxia/hypoxia is developed at the sediment-water interface. Due to the expected increase in lake stability (i.e. reduced mixing) under future climate conditions, a reduction in oxygen transfer to the sediments was expected.

Sahoo and Schladow (2008) using just the hydrodynamic model of LCM demonstrated that lake mixing reduces because of lake warming. However they did not show the detailed DO budget. The present study calculated DO concentrations in the lake at each modeling layer. The sediment nutrients release rates (Table 6-1) are assigned based on experimental results using Lake Tahoe water (Beutel 2000, 2006). In the study, it was assumed that the sediment is an infinite source of nutrient for the case of prolonged anoxic condition at the sediment-water interface. This study does not consider the potential release of other heavy metals due to anoxic condition.

Table 6-1. Sediment oxygen demand (SOD) and nutrient release rate of soluble reactive phosphorus (SRP), nitrate (NO_3) and ammonium (NH_4) in oxic and anoxic phases (Source: Beutel 2000, 2006).

Variables	Oxic phase (DO>0.01 mg/L)	Anoxic phase (DO≤0.01mg/L)
SOD	0.04 g-O m^{-2} d^{-1}	0.00 g-O m^{-2} d^{-1}
SRP	0.00 mg-P m^{-2} d^{-1}	0.22 mg-P m^{-2} d^{-1}
NO_3	0.18 mg-N m^{-2} d^{-1}	0.00 mg-N m^{-2} d^{-1}
NH_4	0.00 mg-N m^{-2} d^{-1}	0.49 mg-N m^{-2} d^{-1}

6.2.2 Lake water level

Lake water level is the direct response to the water balance of the lake. Water level is estimated based on the following equation:

$$DW_t = DW_{t-1}+S_t+GW_t+R_t-E_t-O_t-Ov_t$$

Where,

DW_t = Water level at current time step t

DW_{t-1} = Water level at previous time step t-1

S_t = Stream inflow contribution between time steps t-1 and t, expressed as an equivalent height of water at the surface.

GW_t = Groundwater inflow contribution between time steps t-1 and t, expressed as an equivalent height of water at the surface. Groundwater inflow rate is based on Trask's (2007) estimation. The daily value of groundwater is assumed to be the same for all years.

R_t = Direct precipitation on the lake between time steps t-1 and t, expressed as an equivalent height of water at the surface. Isoheytal map of Lake Tahoe (Simons et al., 2003; Lake Tahoe TMDL Report, 2009) shows that precipitation on the lake varies nearly 50% from the west shore to the middle of the lake. A multiplication factor ($1.0-0.35R_t$) was used for precipitation. This was derived from a best fit for estimating past water surface level during calibration and validation using the observed dataset (see Figure 6-6).

E_t = Evaporation contribution between time steps t-1 and t, expressed as an equivalent height of water at the surface.

O_t = Outflow contribution between time steps t-1 and t, expressed as an equivalent height of water at the surface. Outflow was estimated based on the regression equations (see Table 6-2).

Ov_t = Overflow contribution between time steps t-1 and t, expressed as an equivalent height of water at the surface. This applies if the water level goes above the maximum legal limit for Lake Tahoe (6229.1 ft or 1898.63 m above mean sea level) and water is spilled to the Truckee River.

The current study does not consider any loss due to authorized/unauthorized withdrawal of water because of lack of information. However, this is considered to be a relatively small component of the water budget. Figure 6-6(a) shows that water level closely follows to that of USGS-recorded water level except during 2005 and 2006. Note that these two years are wet year and LSPC overestimates streamflows approximately 25% to 40% to USGS records during 2003 to 2006 (Figure 6-6(b) and 6-6(c)). Though LCM-estimated water level is close to that of USGS-records except 2004 and 2005, Figure 6-6 demonstrates the overall ability of LCM to estimate the lake water level.

The regression equations for outflow are developed based on lake water depth above lake natural rim. When the lake level falls below the natural rim, there is no outflow to the Truckee River. The Truckee River and lake height data were downloaded from the USGS site to establish the relation between water depth above lake natural rim (D) and outflow (O). Although data are available since 1950, recent data 2000 to 2009 data were used in the analysis because recent data reflects the updated gate operation at Lake Tahoe. While a regression was developed between lake level and outflow, in reality the outflow rate is governed by operating rules determined by the Federal Water Master, based on downstream water needs. These rules change over time, and are not based solely on conditions at Lake Tahoe. The developed regression is used for predicting future release rates, however, it is recognized that these may deviate from our assumed rates.

Table 6-2. Regression equation between water depth above lake natural rim (D) and outflow (O) for the 10 years (based on the period 2000 to 2009). $O=c_0+c_1D+c_2D^2+c_3D^3+c_4D^4+c_5D^5+c_6D^6$.

Regression constants and R^2	Jan	Feb	Mar	Apr	May	Jun
c_0	0.489	0.670	-1.783	-9.913	18.688	41.972
c_1	-19.913	-16.443	46.138	135.662	-151.695	-154.017
c_2	257.376	189.193	-220.872	-563.485	537.389	125.547
c_3	-820.750	-537.824	447.035	1095.241	-944.191	144.110
c_4	1103.463	673.243	-407.378	-1060.098	868.631	-242.317
c_5	-655.312	-387.968	162.213	495.671	-398.316	105.994
c_6	140.902	83.631	-21.522	-89.320	71.554	-13.654
R^2	0.755	0.590	0.490	0.431	0.666	0.264

Regression constants and R^2	Jul	Aug	Sep	Oct	Nov	Dec
c_0	-79.781	-2.655	-0.281	0.078	0.416	0.037
c_1	670.025	12.663	2.411	1.745	-14.411	-2.035
c_2	-1939.354	165.264	119.406	58.184	239.329	91.011
c_3	2788.578	-480.785	-296.039	-87.201	-657.077	-297.659
c_4	-2126.939	514.250	302.391	12.804	714.983	482.213
c_5	823.923	-243.195	-149.478	42.270	-319.175	-367.620
c_6	-127.609	42.749	29.654	-20.157	41.874	102.921
R^2	0.329	0.765	0.824	0.746	0.958	0.887

6.3 Data Inputs

6.3.1 Meteorological data input

The meteorological data used for future climate change scenarios were based on the downscaled meteorological projections. Locations of the downscaled air temperature (maximum and minimum) and precipitation data for 36 grid points (Figure 6-7a) and shortwave radiation and wind speed for 81 grid points (Figure 6-7b) on and around the lake are shown. Unlike the basin hydrology model LSPC that requires meteorological information over the whole watershed, LCM (Sahoo et al. 2010) requires meteorological information at a single, representative grid point. That point was chosen to be grid point 16 for air temperature and precipitation (Figure 6-7a) and grid point 31 for shortwave radiation and wind speed (Figure 6-7b. In addition to precipitation, air temperature, shortwave radiation, and wind speed, LCM requires longwave radiation and vapor pressure data. Regression equations between air temperature and dew point (Table 6-3) were developed using South Lake Tahoe Airport meteorological station data from 1989 to 2004. The longwave radiation was estimated using algorithms described in TVA (1972) and air temperature and cloud fractions data. Vapor pressure was estimated using dew point temperature.

Table 6-3. Regression equation between air temperature (AT) and dew point (DP) for the 16 years (1989 to 2004) of South Lake Tahoe Airport meteorological data. $DP=a_0+a_1AT+a_2AT^2+a_3AT^3$.

Regression constants and R^2	AT>=25 °C	0<= AT <25 °C	AT <0 °C
a_0	-92.595	-4.159	-4.007
a_1	7.413	0.730	0.998
a_2	-0.163	-0.030	0.044
a_3	0.001	0.001	0.002
R^2	0.976	0.997	0.989

The one-year running average of the daily meteorological data, along with the best fit trend lines are shown for shortwave radiation, longwave radiation, air temperature, wind speed, and annual precipitation (Figures 6-8 to 6-12). The figures show that shortwave radiation remains unchanged overall while air temperature will increase approximately 4.5 °C and 2.0 °C and longwave radiation will increase approximately 10 percent and 5 percent for the A2 and B1 scenario, respectively by the end of the 21st century. Figure 6-11 shows the decreasing trend of wind speed (approximately 7 to 10 percent). Note that trends help to determine the future statistics of future climate; however, extreme weather conditions over periods of days has potential to change lake mixing and subsequent lake ecology without significantly altering the long term trend.

6.3.2 Stream inflow and pollutant loads

Streamflow and associated pollutant loads through year 2100 were provided by the LSPC watershed model (see Section 4.0) forced by the same downscaled meteorological data sets. Concentrations of fine particles are estimated from the LSPC-derived stream flow based on algorithms described in Lahontan and NDEP (2010a). The stream temperatures are estimated based on the algorithms described in Sahoo et al. (2009). Groundwater pollutant loads are based on the estimates of USACE (2003). However, the actual groundwater flux was based on the estimates of Trask (2007). Estimates of atmospheric deposition and shoreline erosion reported in Lahontan and NDEP (2010a) are used in this study. Inputs from atmospheric deposition, groundwater and shoreline erosion were assumed to be the same for all years because of the lack of adequate, long-term loading data from these sources.

These assumptions imply that the loads over the next 100 years will bear the same relationship to the meteorology and stream flows as they have in the past. In other words, no estimate for the success of the TMDL implementation has been made. The results indicate future conditions in the absence of any load reduction due to the TMDL.

6.3.3 Lake data

Lake data are required to provide initial conditions for the LCM model runs. Vertical profiles of temperature, chlorophyll *a*, DO, biological oxygen demand (BOD), soluble reactive phosphorous (SRP), particulate organic phosphorus (POP), dissolved organic phosphorus (DOP), nitrate

(NO3) and nitrite (NO2), ammonium (NH4), particulate organic nitrogen (PON), dissolved organic nitrogen (DON), and concentrations of seven classes of particles (0.5 – 1.0, 1.0 – 2.0, 2.0 – 4.0, 4.0 – 8.0, 8.0 – 16.0, 16.0 – 32.0, and 32.0 – 63.0 μm) are collected at two lake stations by TERC. Data from the mid-lake station in the deeper part of the lake (460 m depth) were used to provide the initial conditions. Since downscaled meteorological data are available starting from 2001, the lake profile data recorded on January 3, 2001 was used as the initial condition.

The elevation of a spillway constructed at the lake outlet is approximately 1899 m from MSL. Water level above 1899 m is discharged to the Truckee River. Bottom elevation of lake is approximately 1400 m from MSL. The elevation of each stream before it enters the lake was estimated from GIS DEM and used along with stream and lake water temperature to estimate the plunging depth of the stream discharge.

6.4 Results and Discussion

6.4.1 Lake stratification and mixing

Lake stratification and mixing are strongly influenced by the meteorological conditions. Typically in the summer, a lake stratifies (implying the increase of potential energy exceeds the input of external mechanical energy). In winter, the opposite occurs and a lake cools and the epilimnion deepens. The same processes occur on a diurnal basis with day-night differences in the meteorological conditions. When surface and bottom density differences reduce to zero, the lake completely overturns. At Lake Tahoe this has typically occurs every 3-4 years on average.

Lake mixing is important as it redistributes dissolves and particulate material. For example, nutrients such as nitrate, which typically accumulates in the hypolimnion through the summer, are reintroduced to the epilimnion when the lake mixes in the winter. Similarly, dissolved oxygen, which is introduced across the air-water interface, can be redistributed throughout the lake when deep mixing occurs.

The maximum annual mixing depths for the period 2001 to 2098 are shown in Figure 6-13. Figure 6-13 illustrates that deep mixing will shut down after 2060 for GFDL A2 scenario. Deep mixing will occur only 4 times during 1961 to 1998 for GFDL B2 scenario. There are many implications on lake ecology for based on reduced mixing. The results also indicate that deep mixing events persist for shorter periods of time than they have in the past, therefore allowing for less redistribution of dissolved and suspended material.

6.4.2 Implication of mixing effect on DO and nutrients

DO concentration at the bed of the lake reduces to zero in approximately 6 to 7 years in absence of deep mixing (Figures 6-14) as oxygen from the surface cannot be transferred due to the persistent stratification. NH4 and SRP will be release from sediment under these conditions. NH4 and SRP will continue to be released from the sediment at the assumed rate while DO concentration is less than 0.01 mg/L (Figures 6-15 and 6-16). It is clear from Figures 6-17 and 6-18 that the NH4 and SRP released from the sediment at the deepest part of the lake are confined in the bottom waters because of density stratification. Due to the absence of light at that depth, the released nutrients do not contribute to photosynthesis. That will only happen when the released nutrients are eventually mixed to the photic zone.

The annual sediment released in the form of SRP and DIN (end of 21st Century) are compared to TMDL estimated external annual load in Figure 6-19. When the hypolimnion is anoxic and sediment nutrient release occurs, the lake internal SRP load contributes approximately 67% of the total load. Although atmospheric deposited DIN is highest among all sources, sediment derived DIN is second highest and contributes approximately 25% to the DIN pool. Clearly, internal nutrient load due to climate change is significant to the lake nutrient budget.

6.4.3 Timing and delivery of the streams

The depth of insertion of each stream into Lake Tahoe is a complex process governed by the density (temperature) of each stream, the stratification of the lake, the streamflow and the geometry of the streambed and alluvial fan. A stream inflow that plunges into the hypolimnion of the lake results in different ecological consequences than when the stream inflow is inserted closer to the water surface. The seasonal pattern of Secchi depth will be affected. Stream temperature is estimated by artificial neural network based on shortwave radiation and air temperature (Sahoo et al. 2009). The insertion depth of the Upper Truckee River is shown in Figures 6-20 and 6-21 for GFDL A2 and GFDL B1 scenario respectively.

Figure 6-20a and Figure 6-21a show the daily insertion depth for 2005 to 2098 and Figure 6-20b and Figure 6-21b show the close view of 2001 to 2004 for GFDL A2 and GFDL B1 scenarios, respectively. The river plunges deep most of the time during January to March (Figure 6-20b and Figure 6-21b) but discharge the flows and pollutants at the photic zone (approximately 0 to 50 m) during rest of the year. The stream temperature is estimated using average air temperature and shortwave radiation. Due to climate change, the lake water becomes warmer for the GFDLA2 case (Figure 6-22). The deeper part of the lake (>100 m) becomes significantly warmer after 2070 for GFDL A2 case while the warming effect on the lake's deeper part is less for the GFDL B1 scenario. Although the overall stream water temperature of the Upper Truckee for the GFDL A2 scenario increases at higher rate than for the GFDL B1 scenario (Figure 6-23), winter (December to April) water temperature for the Upper Truckee increase at a higher rate for the GFDL B1 scenario (Figure 6-24). As a result, the Upper Truckee River eventually plunges deeper during winter for the GFDL A2 scenario. By contrast, for the case of GFDL B1 scenario more of the winter discharge occurs in the photic zone.

6.4.4 Lake Secchi depth

Annual lake Secchi depth for the GFDL A2 and GFDL B1 scenarios were modeled. The Secchi values reached an equilibrium value that varied from year-to-year, but stayed within the 15-20 m range. In the latter portion of the 21st Century (2070-2099) the estimated Secchi depth (~15-17 m) for GFDL B1 was less (less clear) than for the GFDL A2 scenario (~17-20 m). This is due partly to higher stream flow and associated pollutant load because of higher precipitation (Figure 6-12) and (2) partly to plunging depths near the water surface (Figures 6-20 to 6-24). Moreover, as deep mixing occurs four times during 2061 to 2098 in the B1 scenario, nutrients released at the bottom are transferred to the photic zone. The modeled annual Secchi depths based on climate change (i.e. in the 15-20 m range) are lower than those measured over the past 10 years – 21.7±1.0 m.

It is important to note that DLM Lake Clarity Model is a one-dimensional model, and there is a limit to the extent it can predict the transfer rate of nutrients from the hypolimnion to the photic zone. Even in the absence of deep mixing there will be some entrainment of nutrients from the deep into the shallow waters. Also, previous works has shown that lake clarity is most affected by fine sediment particles (<16 μm); however, the process of nutrient release from the deep sediments under anoxic conditions is not associated with fine sediment release. Consequently, the exact impact of deep-water anoxia on lake clarity should be viewed at this time as an estimate with some uncertainty. Because a deep chlorophyll layer resides in Lake Tahoe at a depth of 30-50 m during the summer (and below the Secchi depth), nutrients release from the bottom could be taken up by algae in this layer and therefore reduce the impact on the Secchi depth. The specific mechanisms at play here are complex and would require additional investigation.

The intention in this report was to provide a preliminary assessment of possible climate change consequences. In this regard, we are confident that should the lake's deep mixing be restricted to the extent the models suggest, internal loading of nutrients from the sediments will be very significant and will drive a fundamental change in the biological productivity status of both the pelagic and littoral regions of the lake if these nutrients periodically enter the upper waters. These nutrients, particularly the phosphorus will be available to drive algal growth. This will reduce light penetration in deeper depths and affect the lake's food web.

6.4.5 Lake level

Figure 6-25 shows water level of the lake for both the GFDL A2 and GFDL B1 scenarios. Note that outflows are estimated based on the lake level above natural rim and the regression analysis developed using 2000 to 2009 lake level and discharge data. Outflow is zero when the lake level falls below the natural rim. The lake level dips down the natural rim when evaporation rate is higher than sum total of stream inflows, groundwater contributions and on-lake precipitation over the lake.

It is clear in Figure 6-22 that that lake temperature may significantly warms in the last 30 years of the 21st century for the GFDL A2 scenario. This is due in large part to the air temperature and longwave radiation increasing at a higher rate for GFDL A2 case (nearly at double rate) than those of the GFDL B1 case. As a result, lake evaporation is higher. Figure 6-12 also indicates that precipitation over the lake during 2075 to 2095 is lower for the GFDL A2 case than for GFDL B1. Due to the combination of all these reasons, the lake surface level dips down the natural rim after 2086 for the GFDL A2 but not the GFDL B1 scenario.

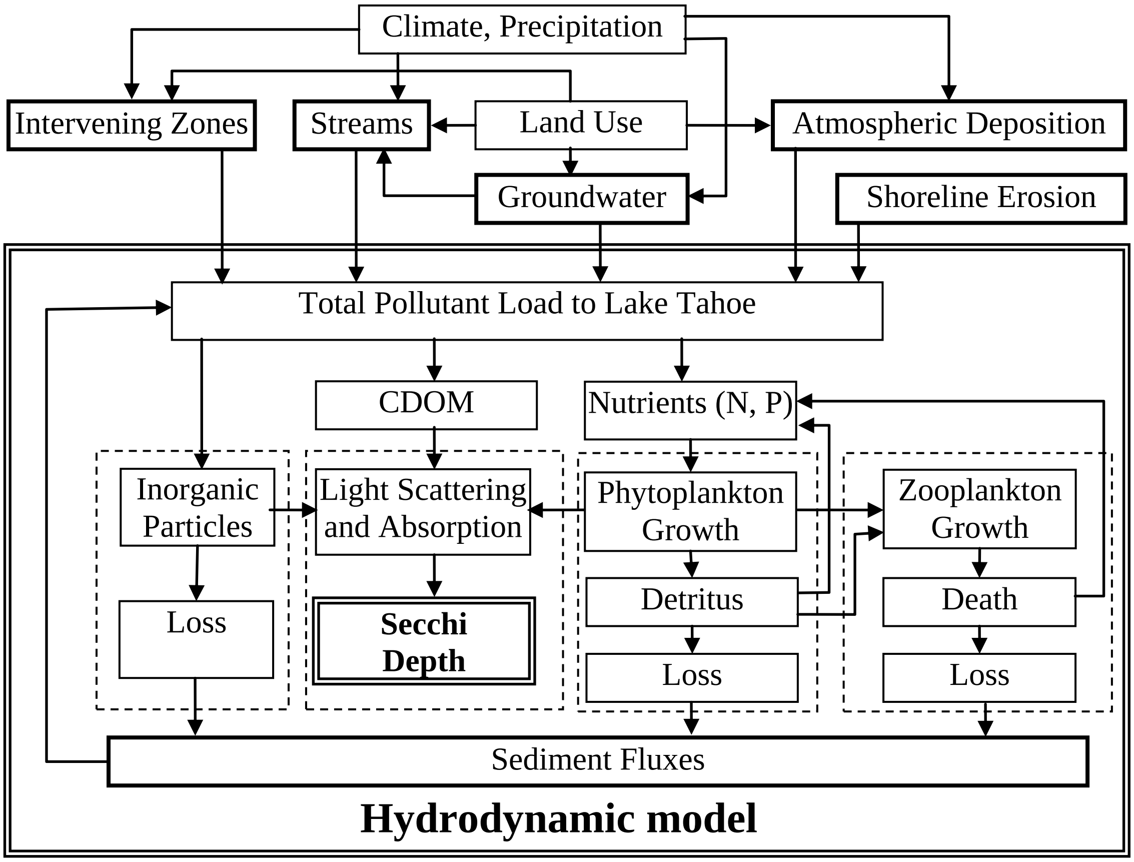

Figure 6-1. Schematic of lake clarity model (LCM). The double lines box includes all in-lake processes and a hydrodynamic model. The four broken line boxes from left to right represent for fine inorganic particle, light, phytoplankton and zooplankton sub-model, respectively. Shown are external sources (streams, intervening zones, atmosphere, groundwater, and shoreline erosion (thick line boxes on the top of double line box)) and internal source (sediment fluxes (thick line box inside the double line box)) of the pollutant loads. CDOM represents colored dissolved organic matters.

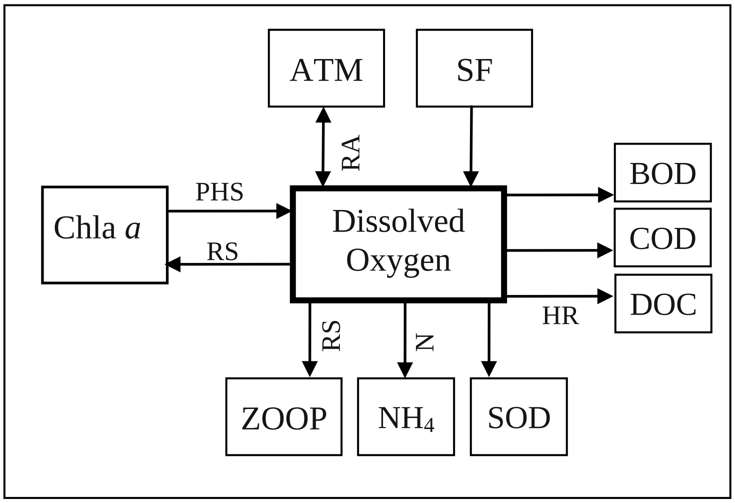

Abbreviations

ATM : Atmosphere
BOD : Biological oxygen demand
Chla *a*: Phytoplankton concentration
COD : Chemical oxygen demand
DOC : Dissolved organic carbon
HR : Heterotrophic respiration
N : Nitrification
NH_4 : Ammonia
PHS : Photosynthesis
RA : Re-aeration
RS : Respiration
SF : Stream flow
SOD : Sediment oxygen demand
ZOOP : Zooplankton

Figure 6-2. Linkages between various dissolved oxygen pools in the lake clarity model. Stream outflow concentrations are not shown.

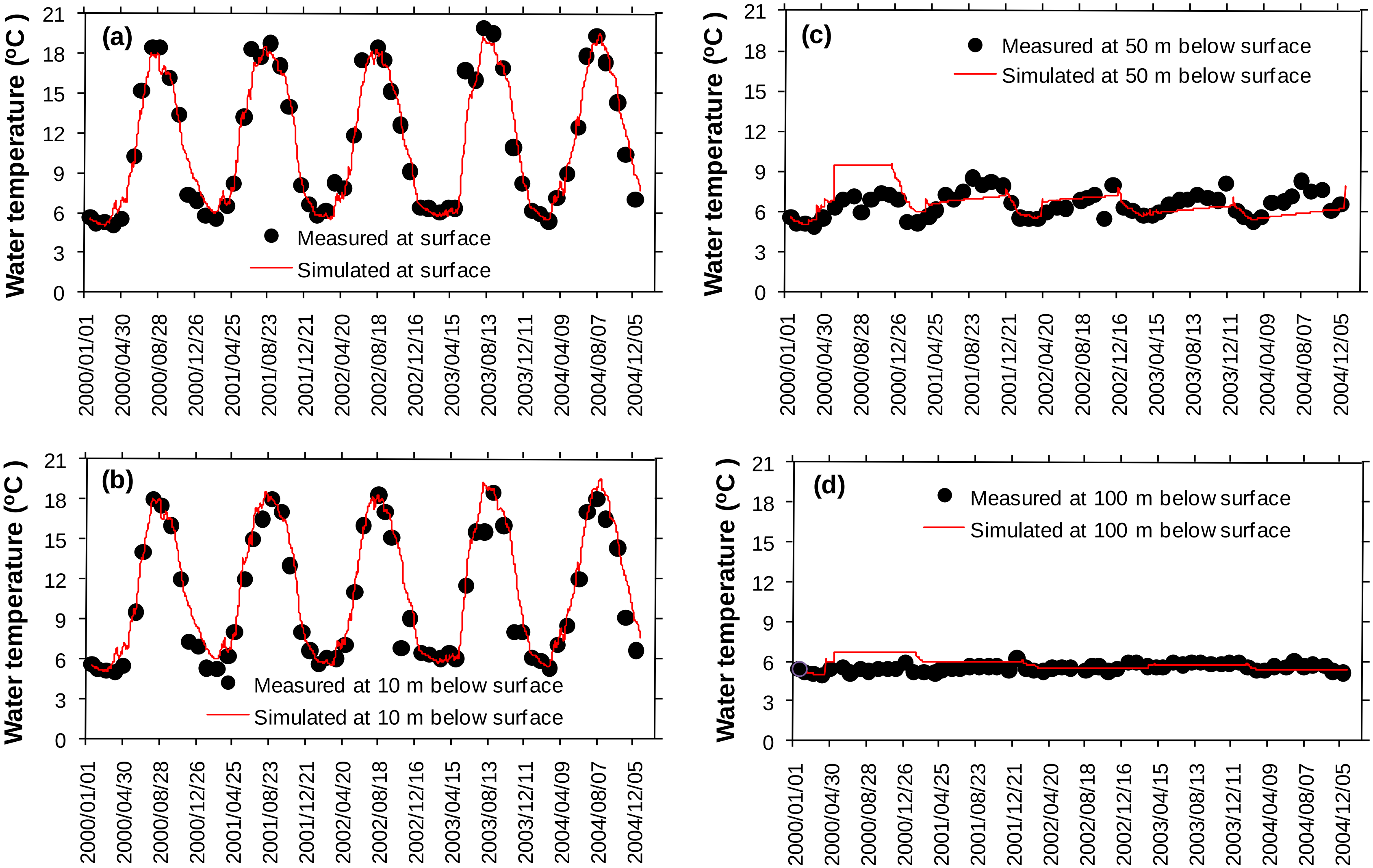

Continued on next page

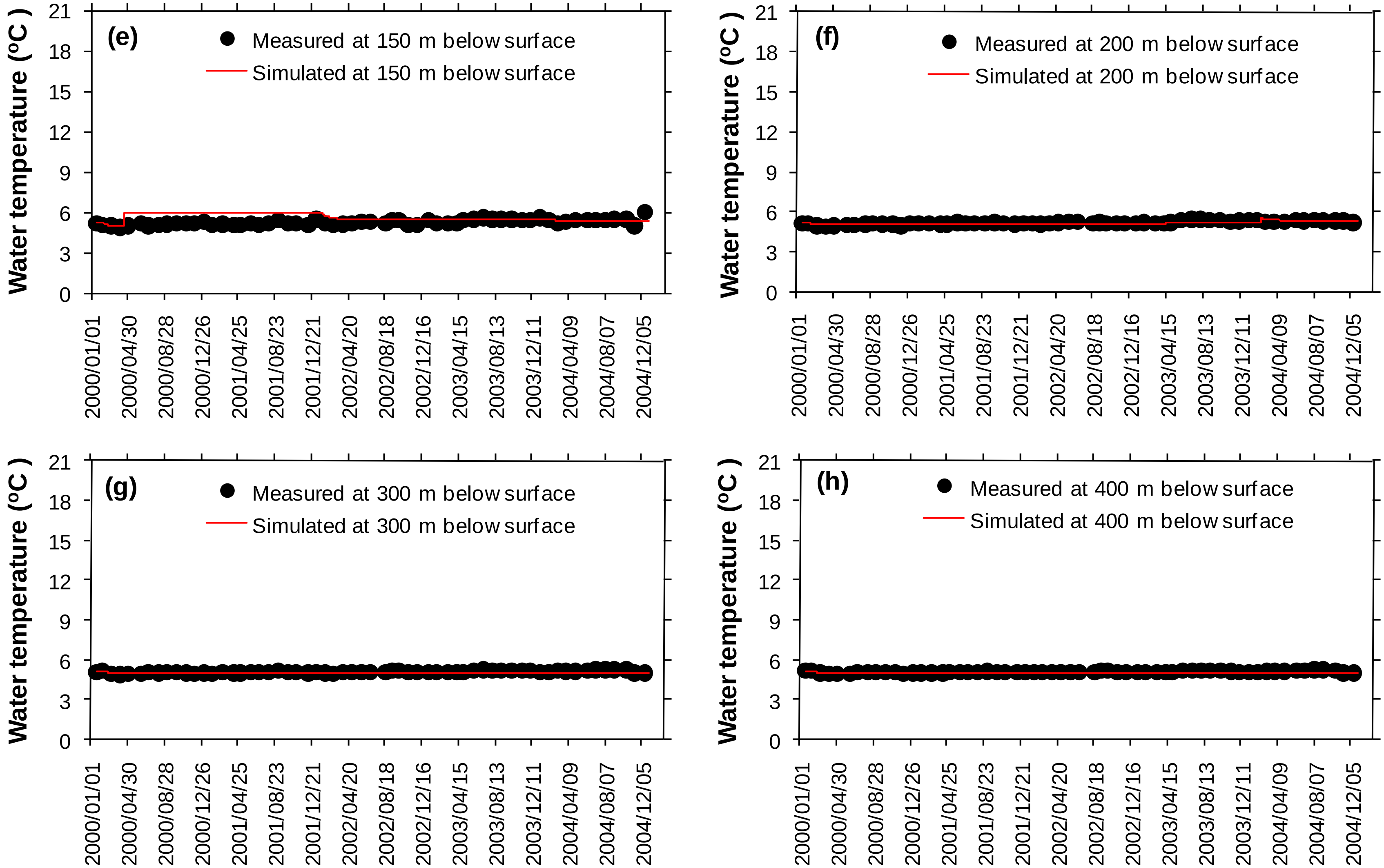

Figure 6-3. Comparison of LCM-estimated daily and event-based measured lake water temperature at different depths (Sahoo et al. 2010).

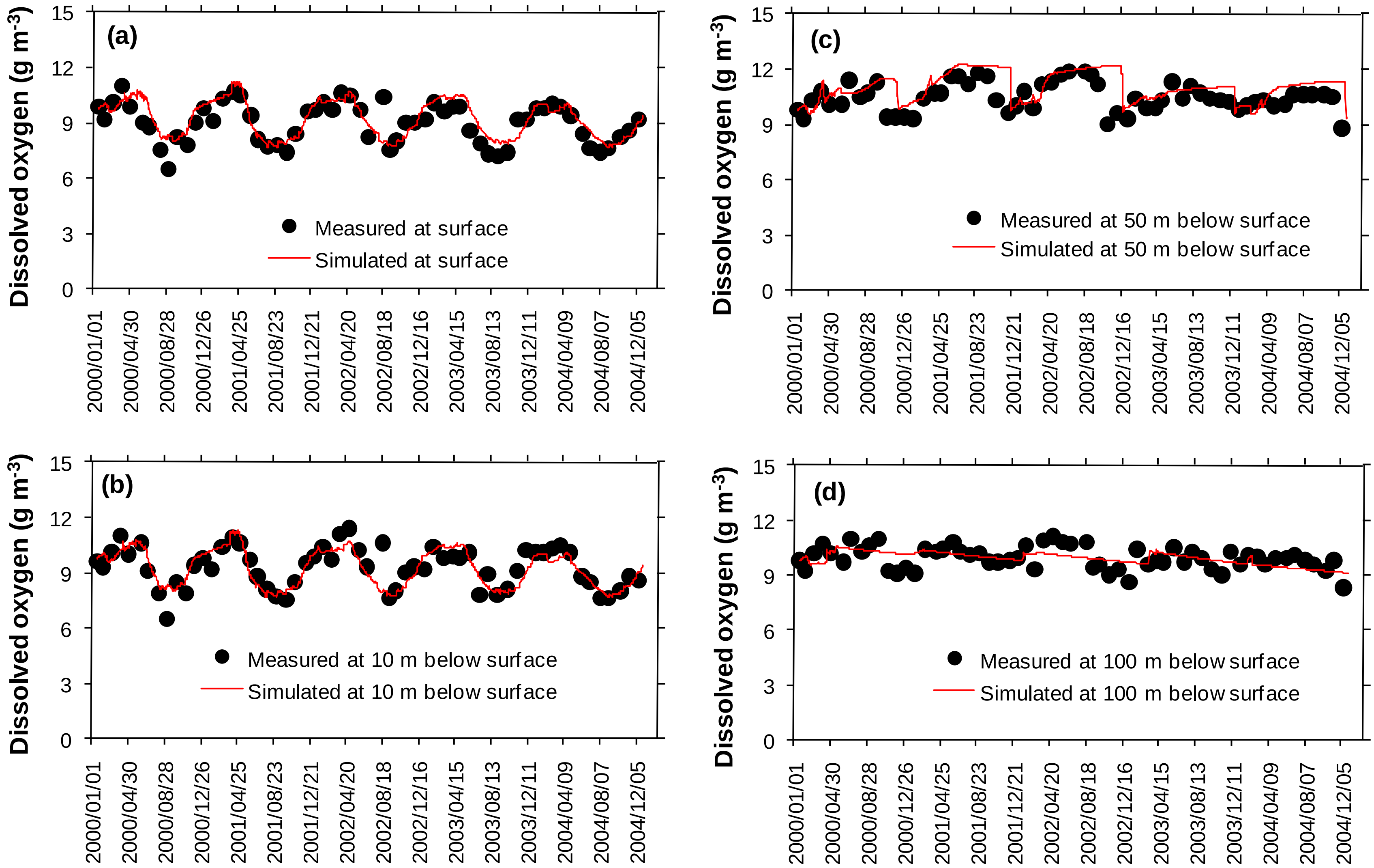

Continued on next page

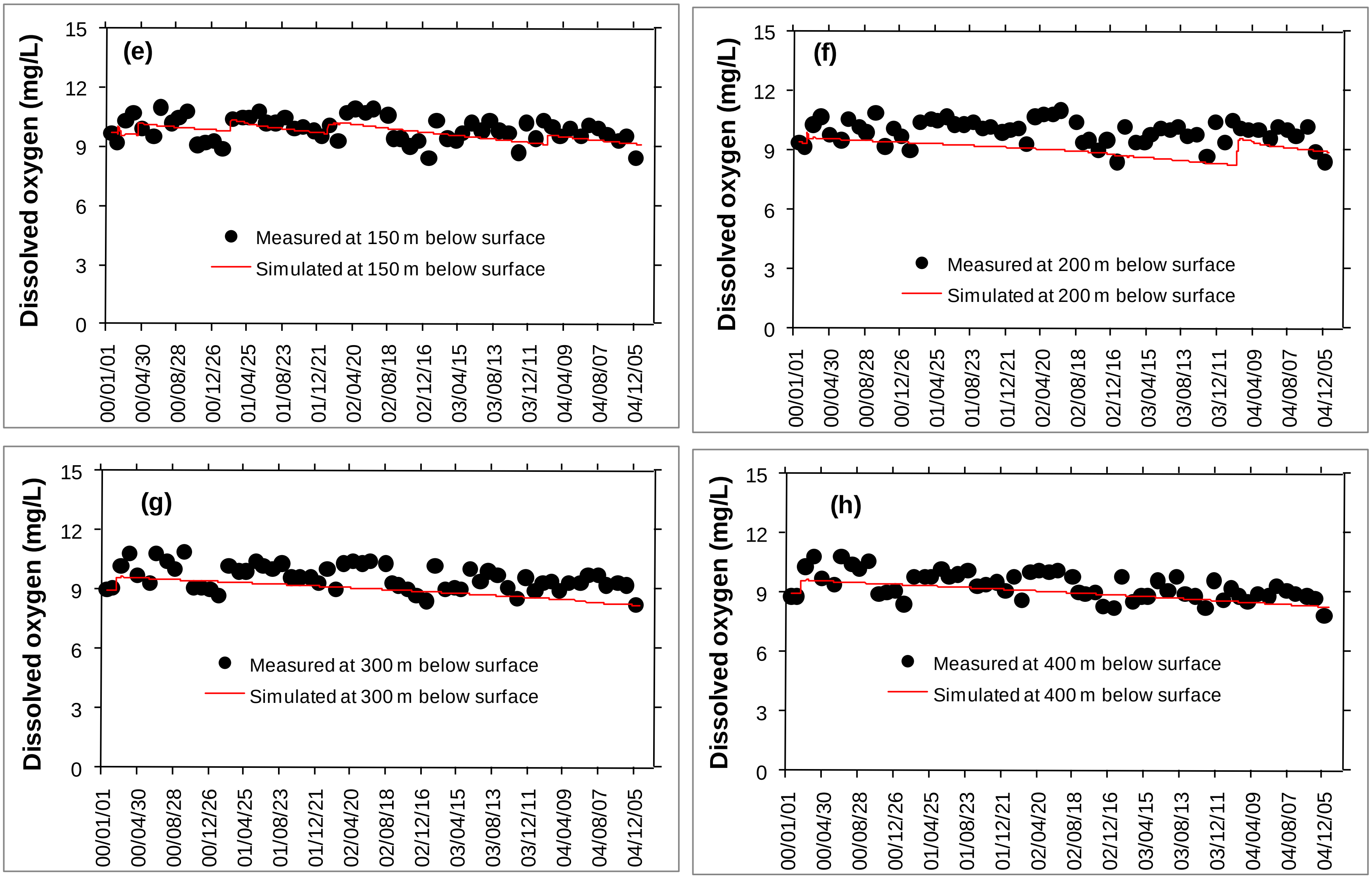

Figure 6-4. Comparison of LCM-estimated daily and event-based measured lake water dissolved oxygen at different depths (Sahoo et al. 2010).

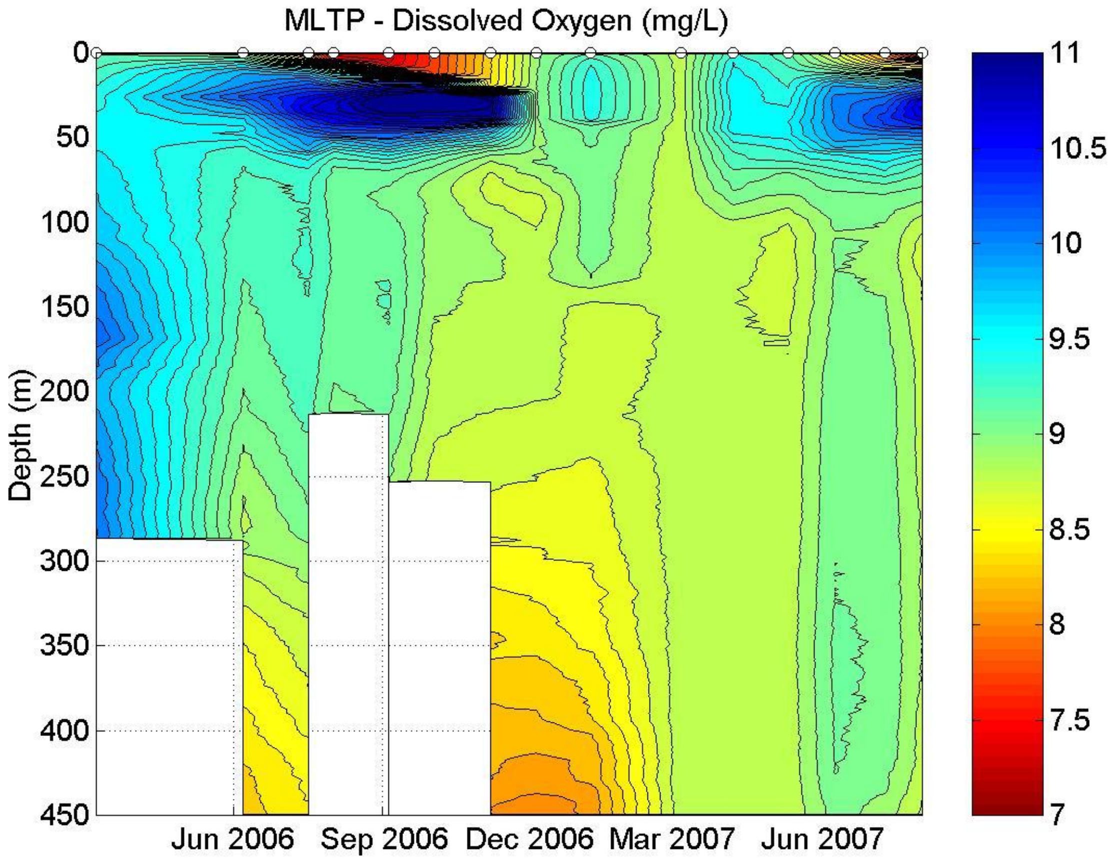

Figure 6-5. Dissolved oxygen concentrations based on SEABIRD profiles taken at approximately monthly intervals at the mid-lake station. The open circles at the top of the figure indicate the profiling dates. Vertical resolution is approximately 0.5 m.

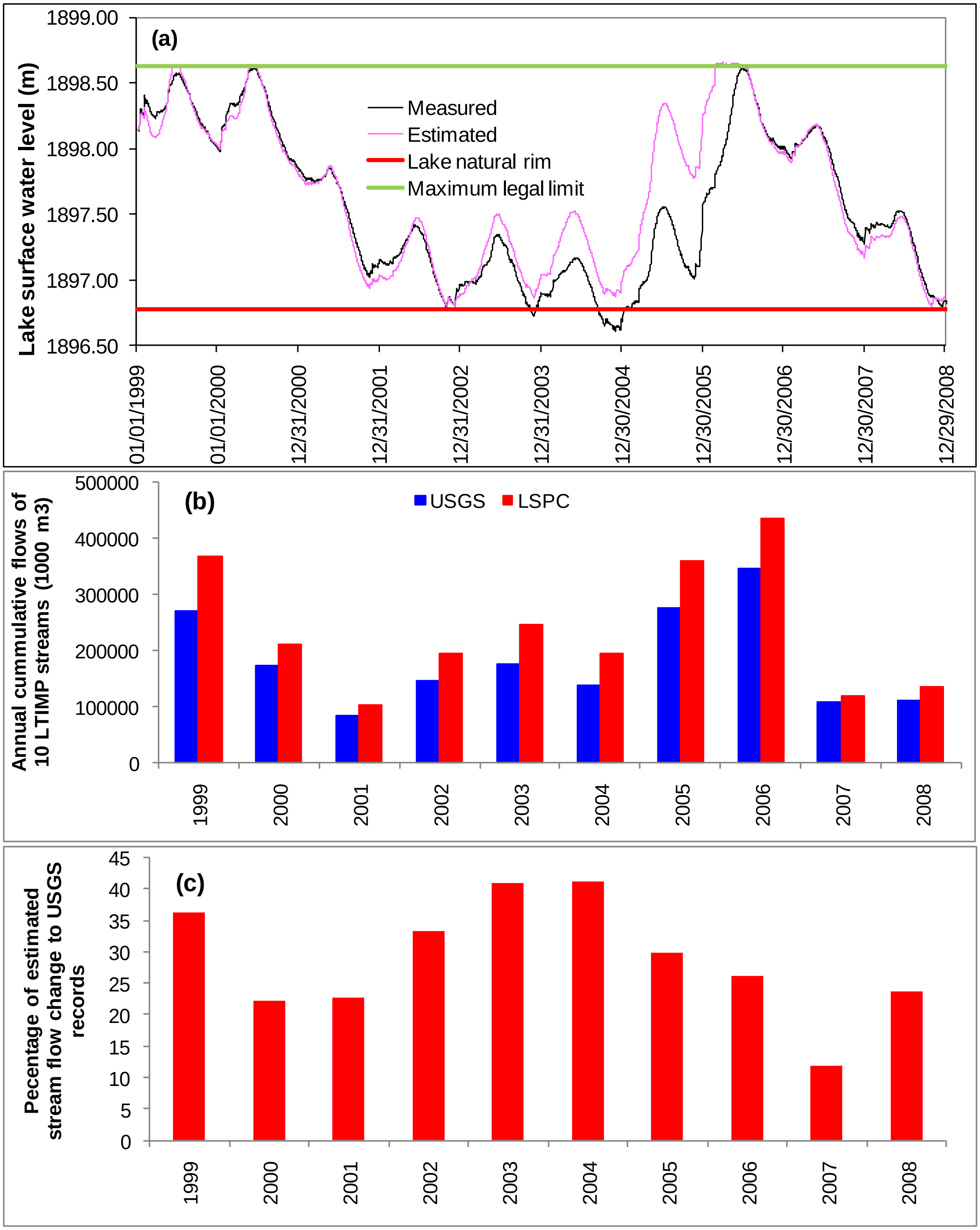

Figure 6-6. (a) USGS-recorded and LCM-estimated lake water surface and (b) LSPC-estimated and USGS-recorded stream inflow of the 10 LTIMP streams, and (c) estimated flow percentage change to USGS recorded flow.

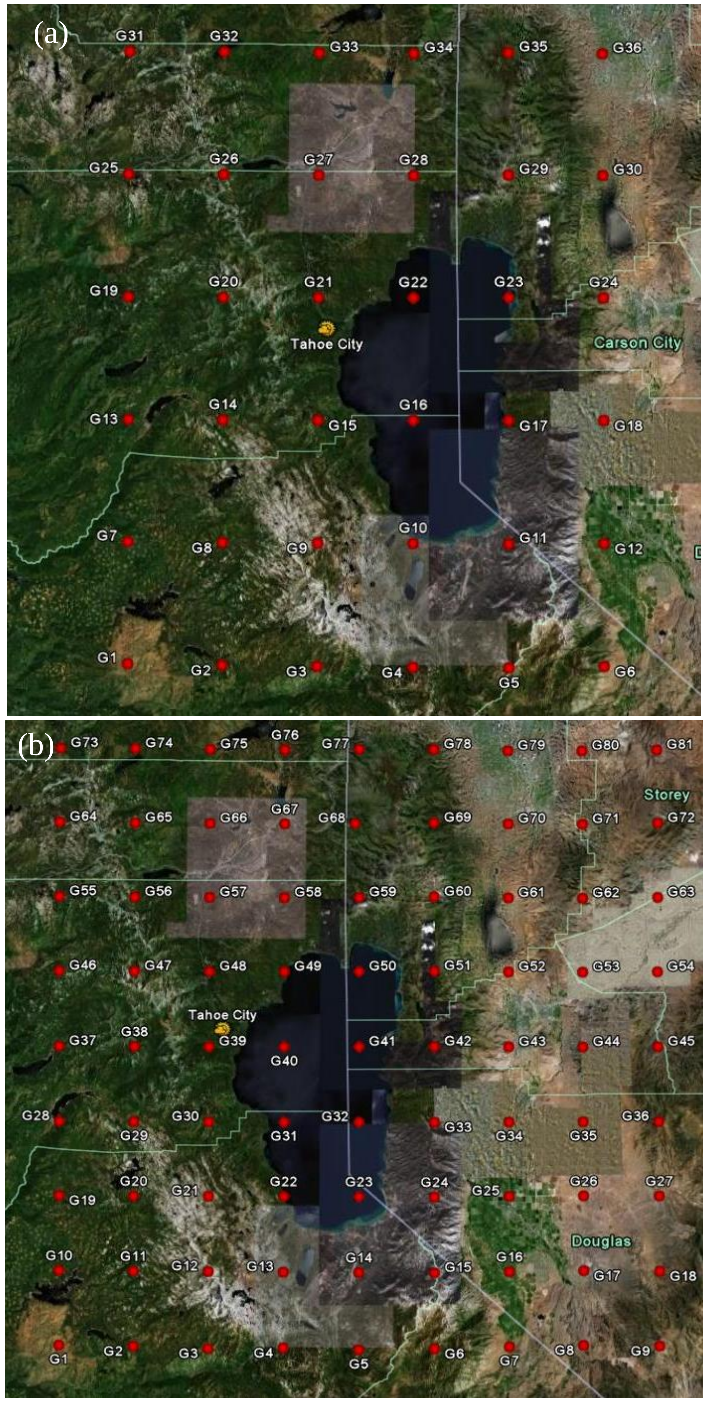

Figure 6-7. Grid points of statistically downscaled (a) air temperature and precipitation at 0.125° latitude × 0.125° longitude (i.e. approximately 12 × 12 km) (b) wind speed and shortwave radiation at 0.081° latitude × 0.104° longitude (i.e. approximately 12 × 12 km).

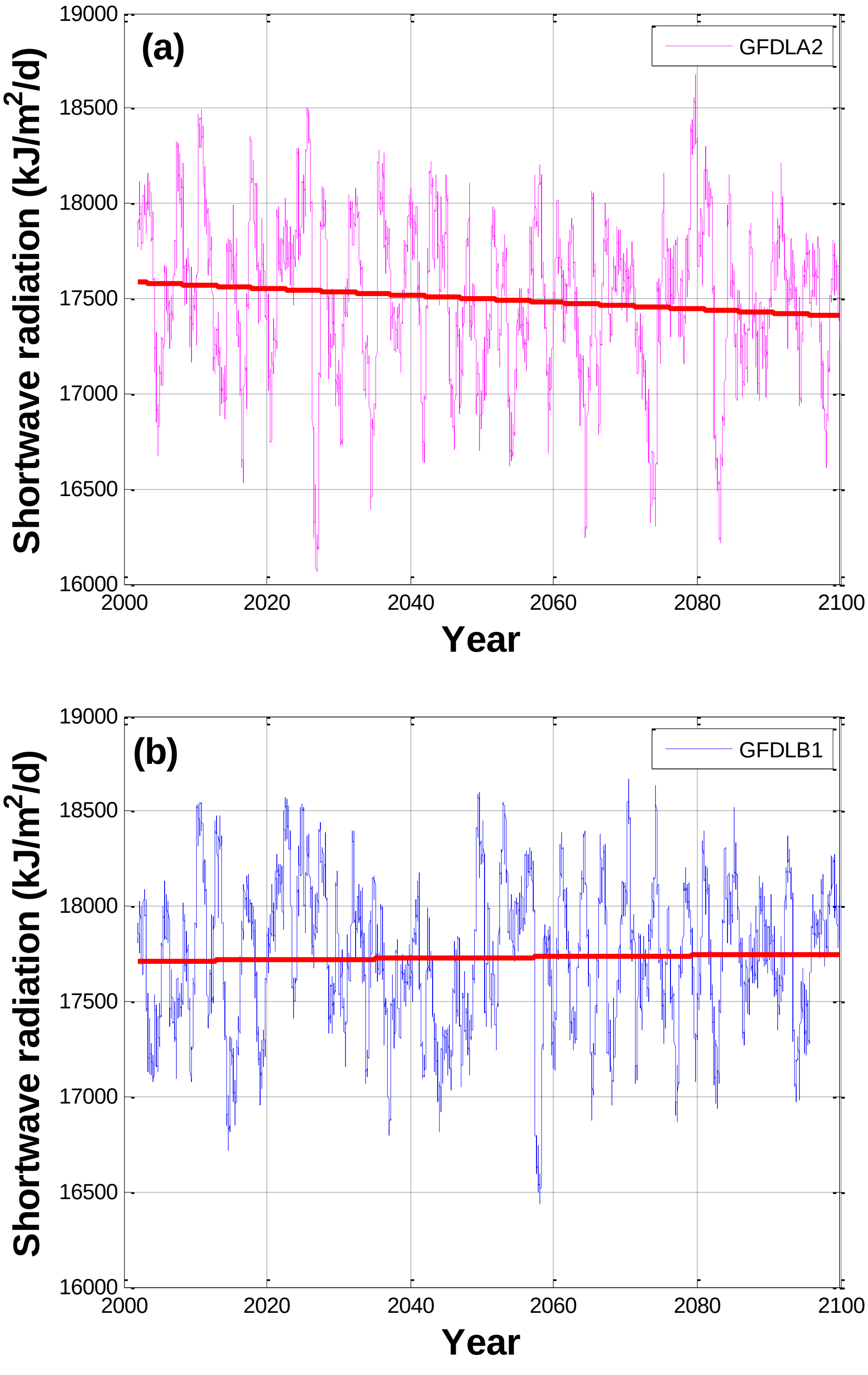

Figure 6-8. One year running average unbiased shortwave radiation at Grid 31 of Figure 6-6 (b).

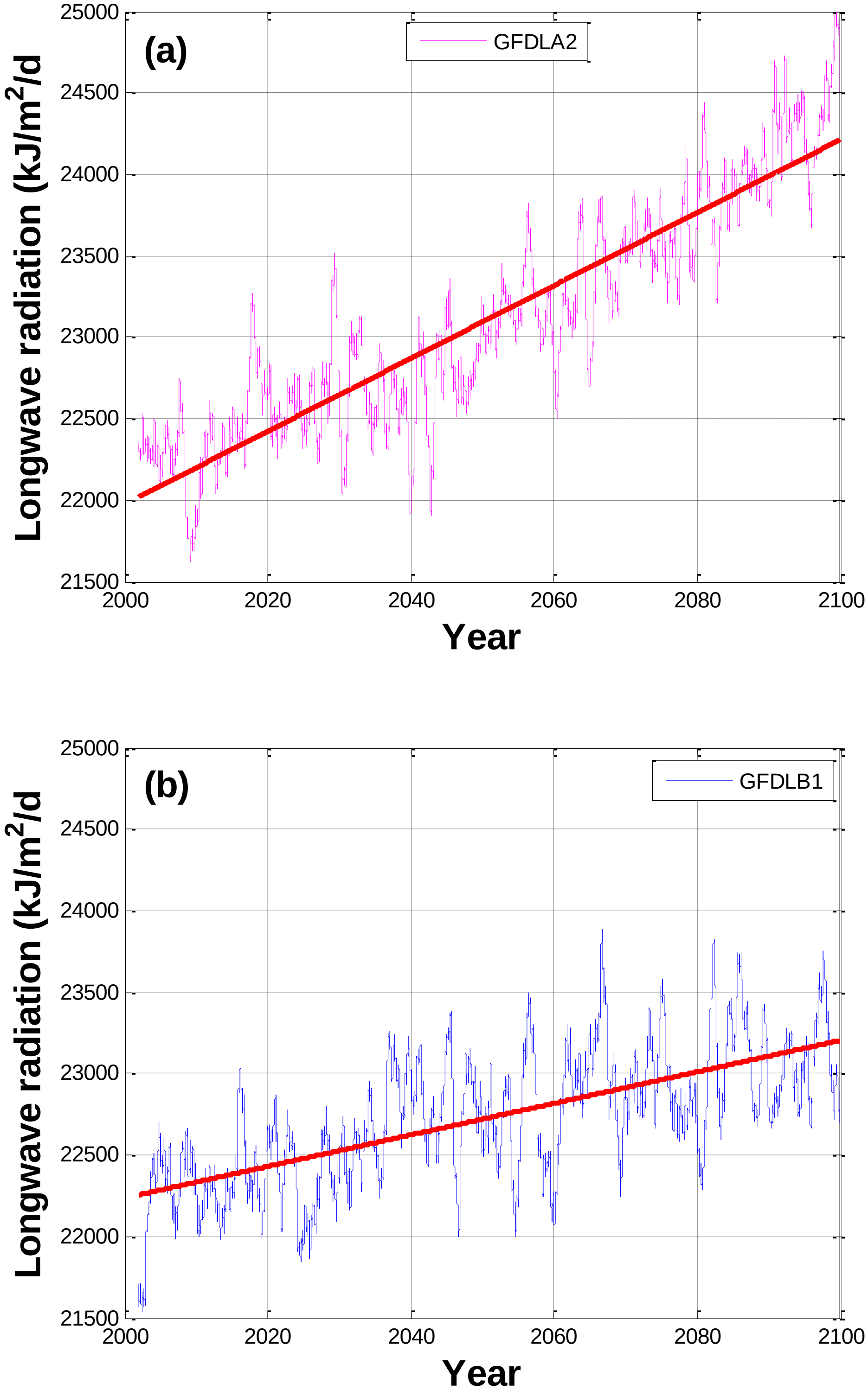

Figure 6-9. One year running average estimated longwave radiation at Grid 16 of Figure 6-6 (a).

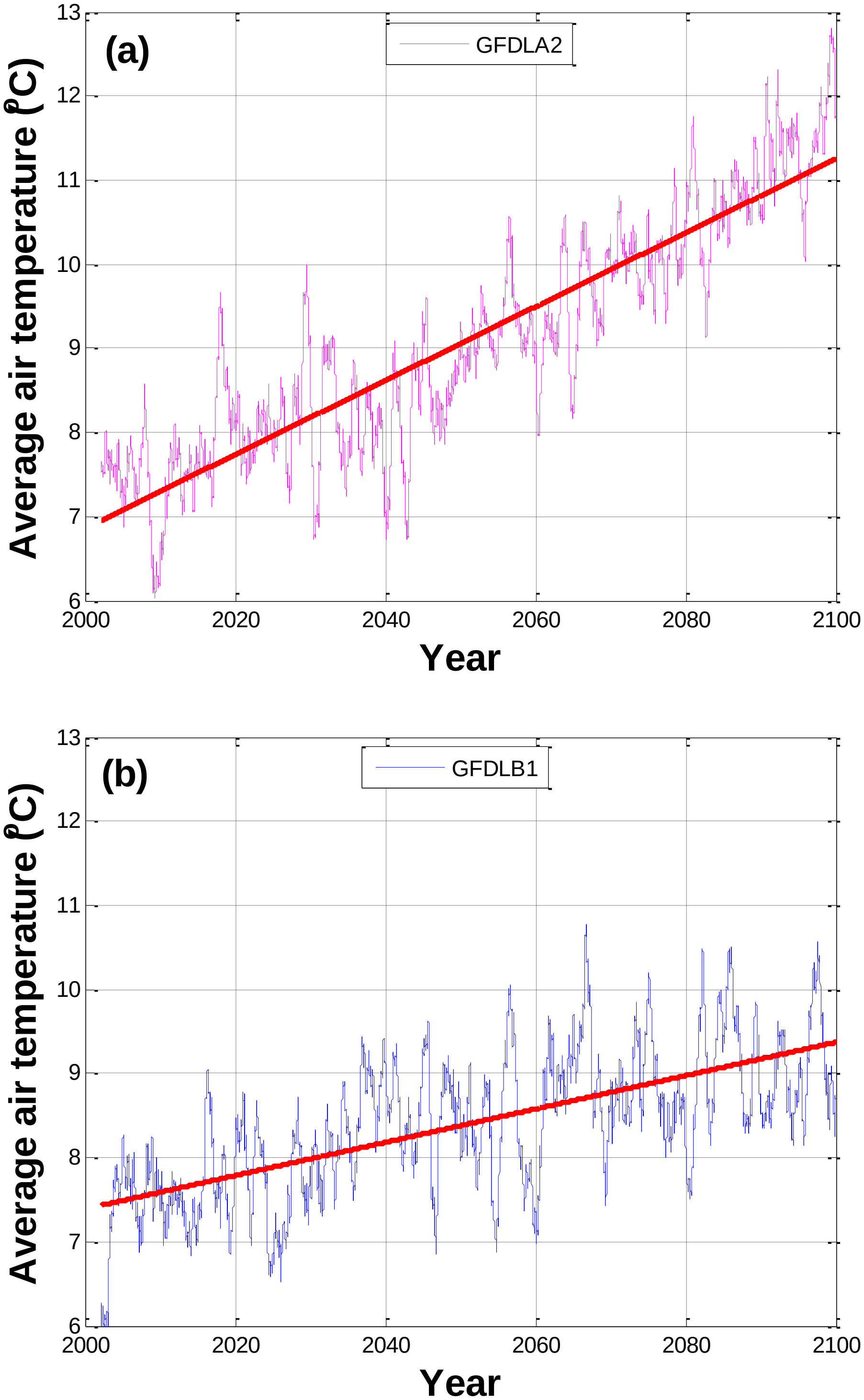

Figure 6-10. One year running average air temperature at Grid 16 of Figure 6-6 (a).

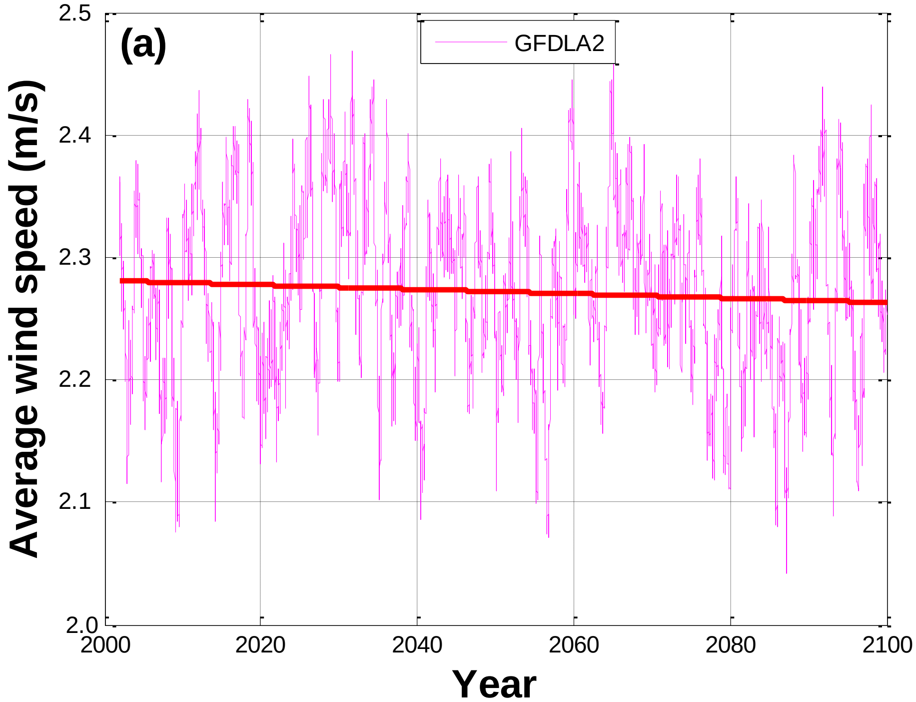

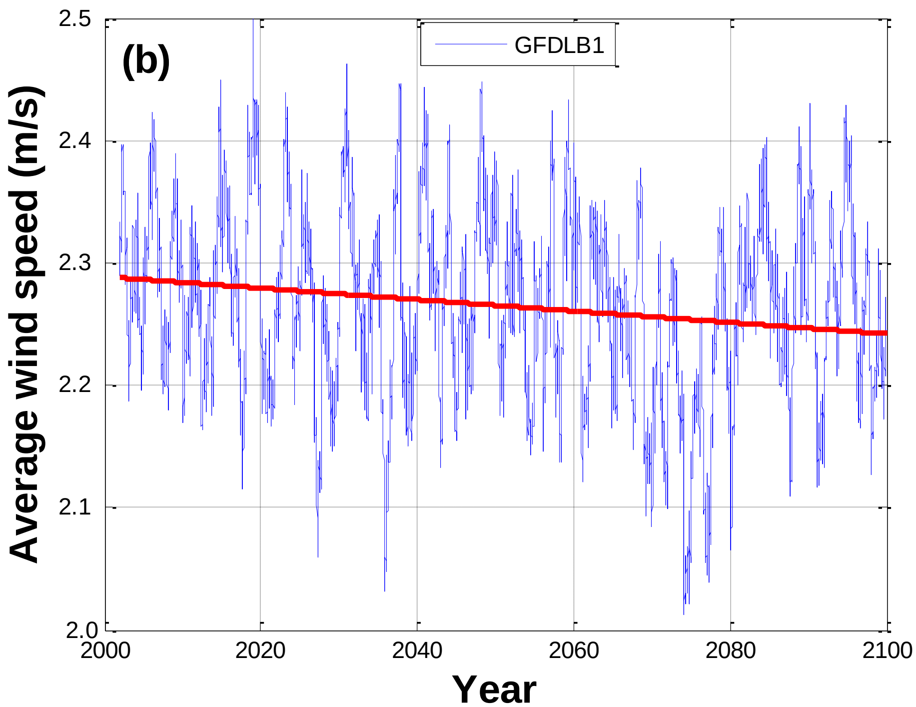

Figure 6-11. One year running average unbiased wind speed at Grid 31 of Figure 6-6 (b).

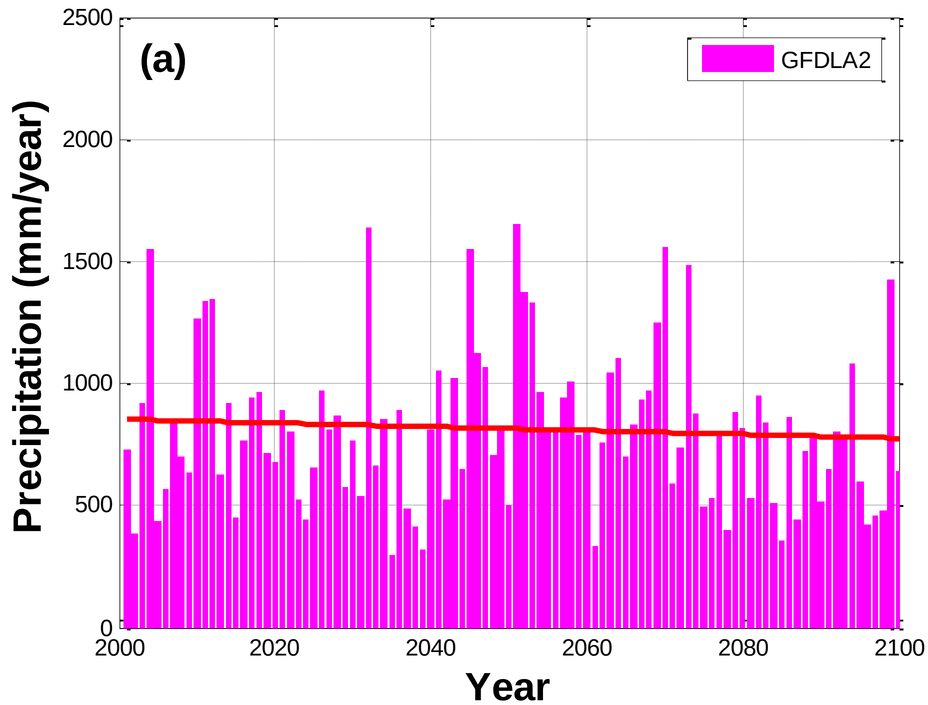

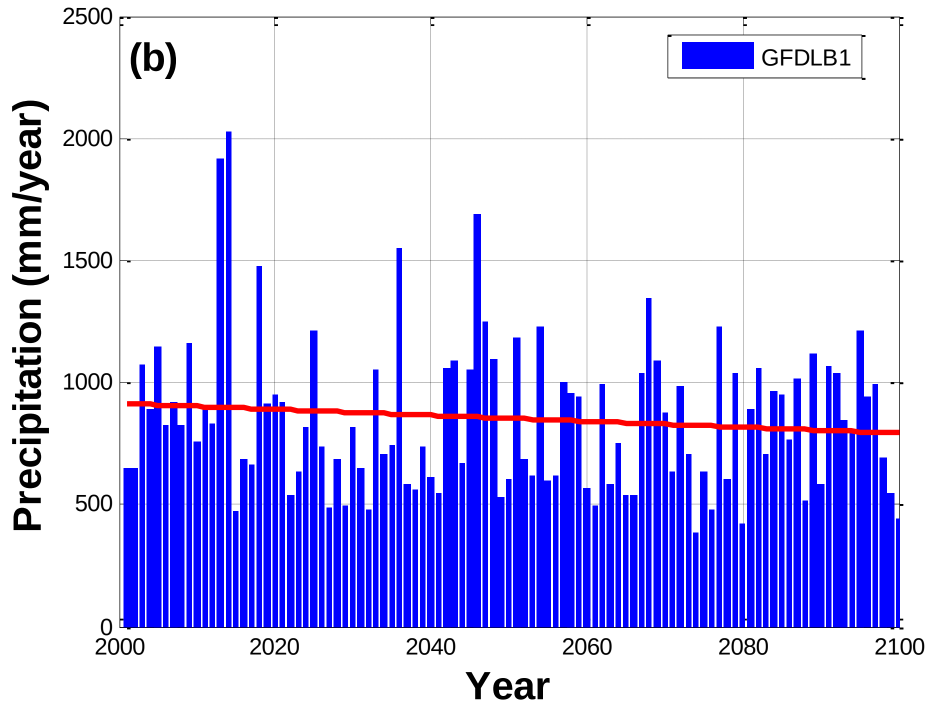

Figure 6-12. Unbiased annual precipitation at Grid 16 of Figure 6-6 (a).

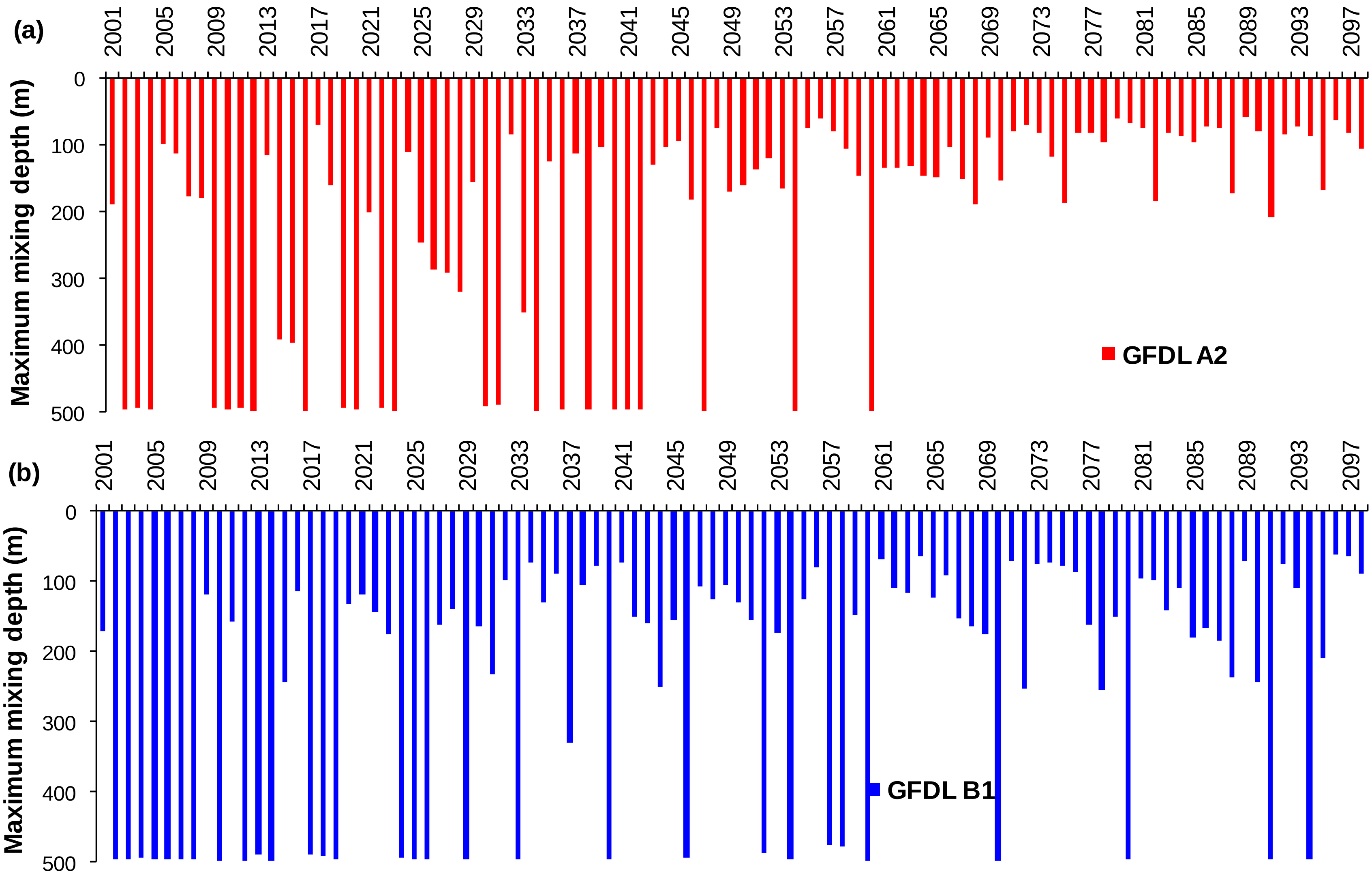

Figure 6-13. Maximum annual mixing depth for (a) GFDL A2 scenario and (b) GFDL B1 scenario.

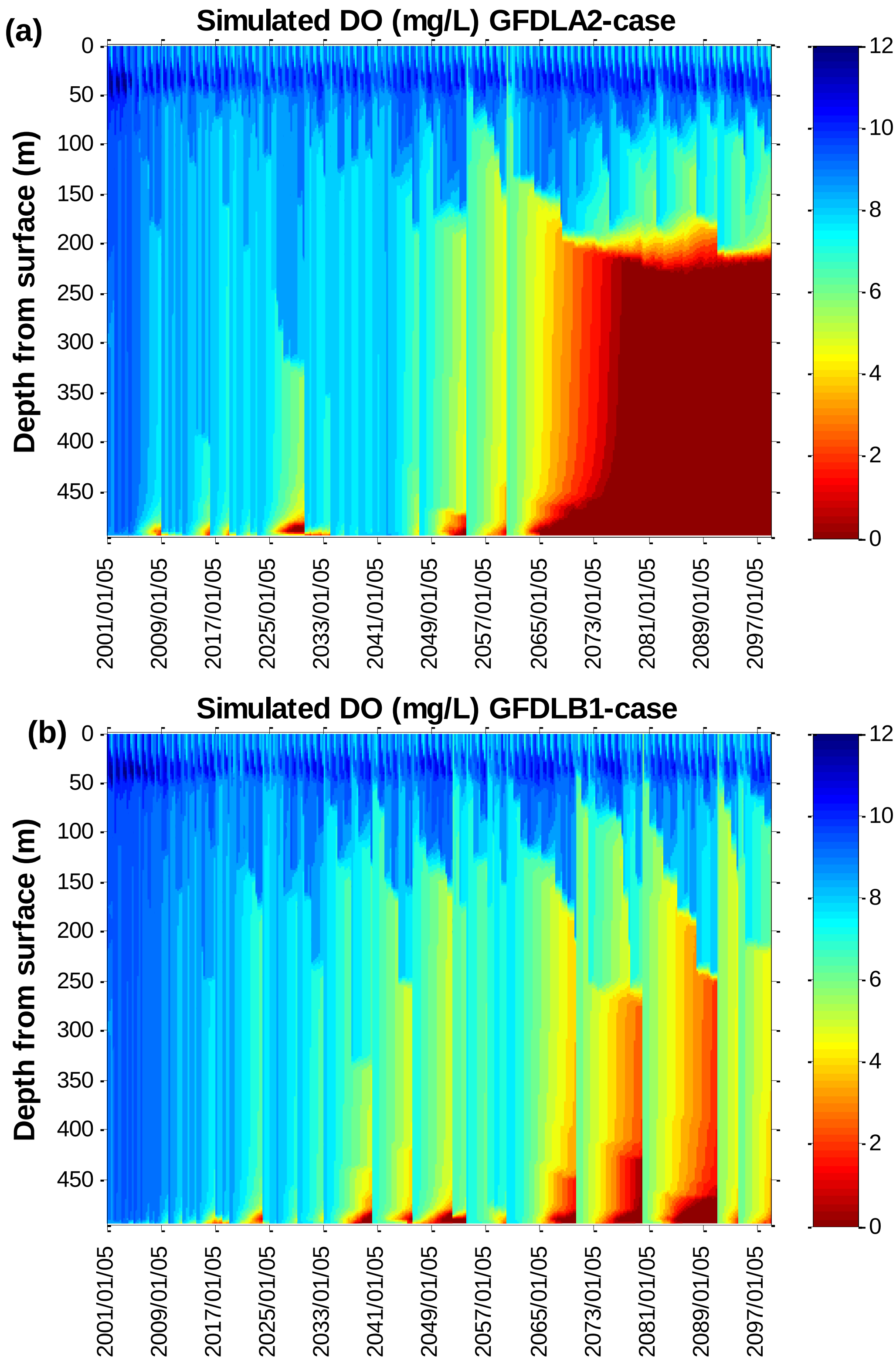

Figure 6-14. Simulated DO concentration (a) for GFDL A2 and (b) GFDL B1 scenarios.

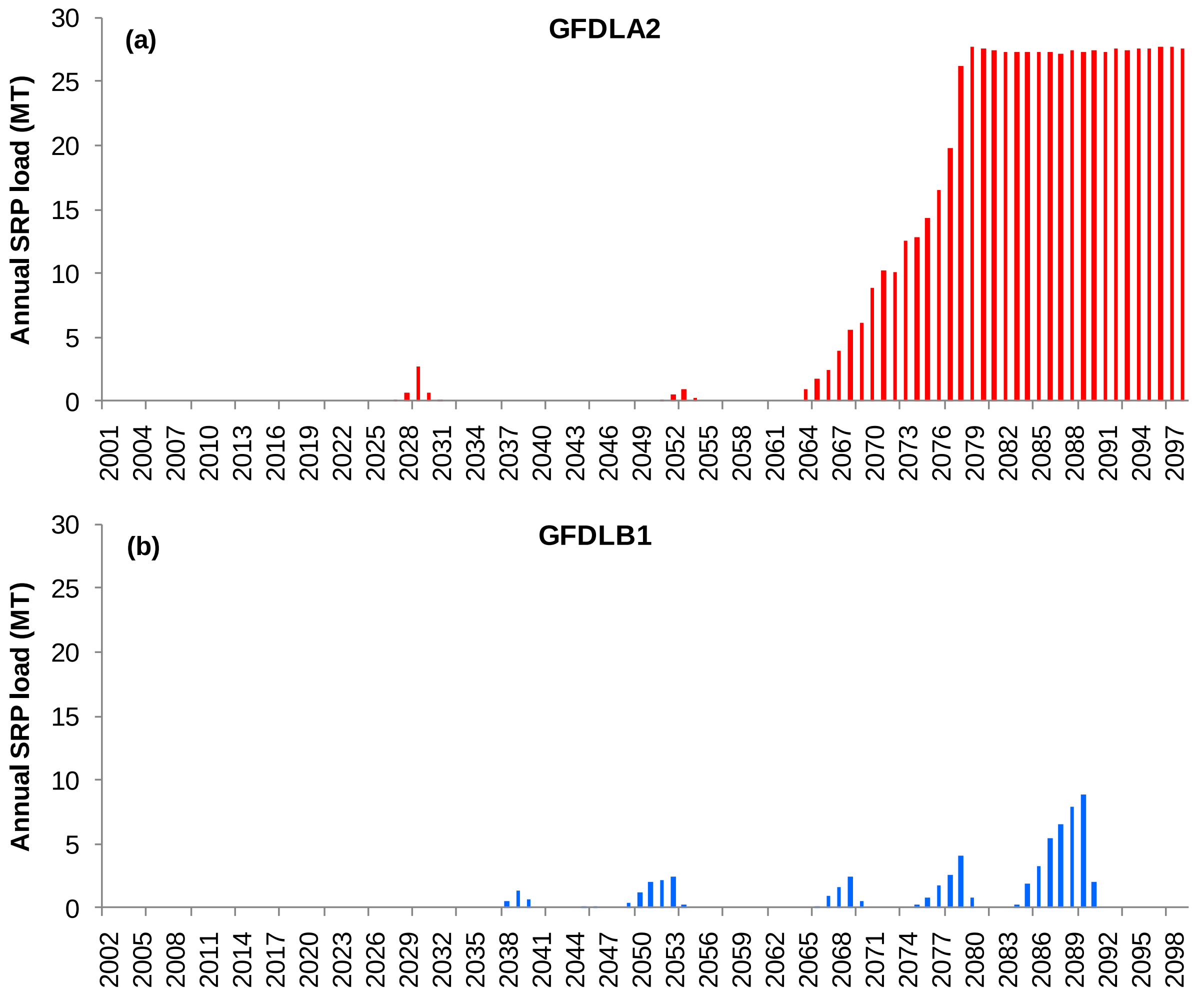

Figure 6-15. Simulated annual average soluble reactive phosphorus release from the sediments for (a) GFDL A2 and (b) GFDL B1 scenario.

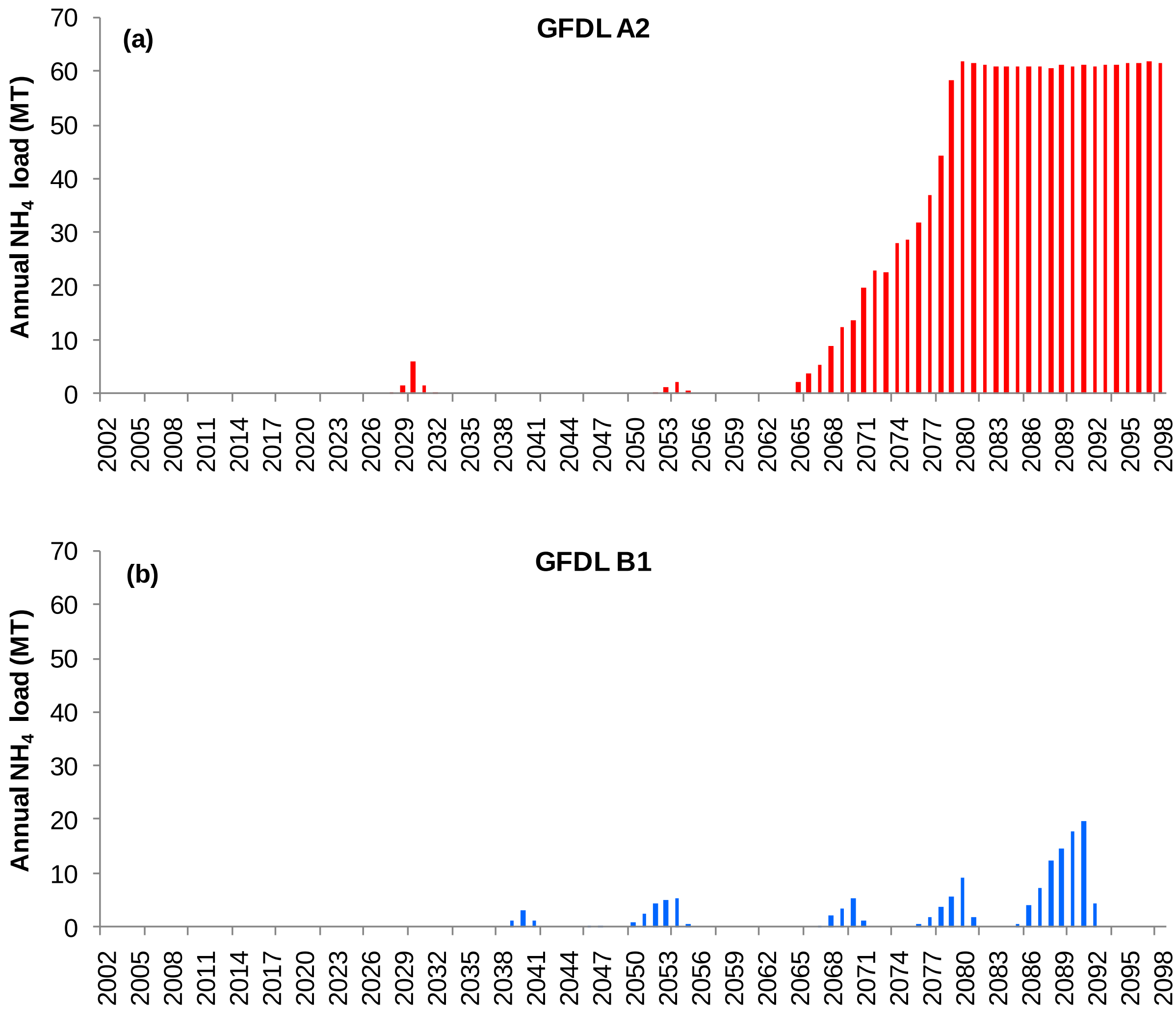

Figure 6-16. Simulated annual average ammonium release from the sediments for (a) GFDLA2 and (b) GFDLB1 scenario.

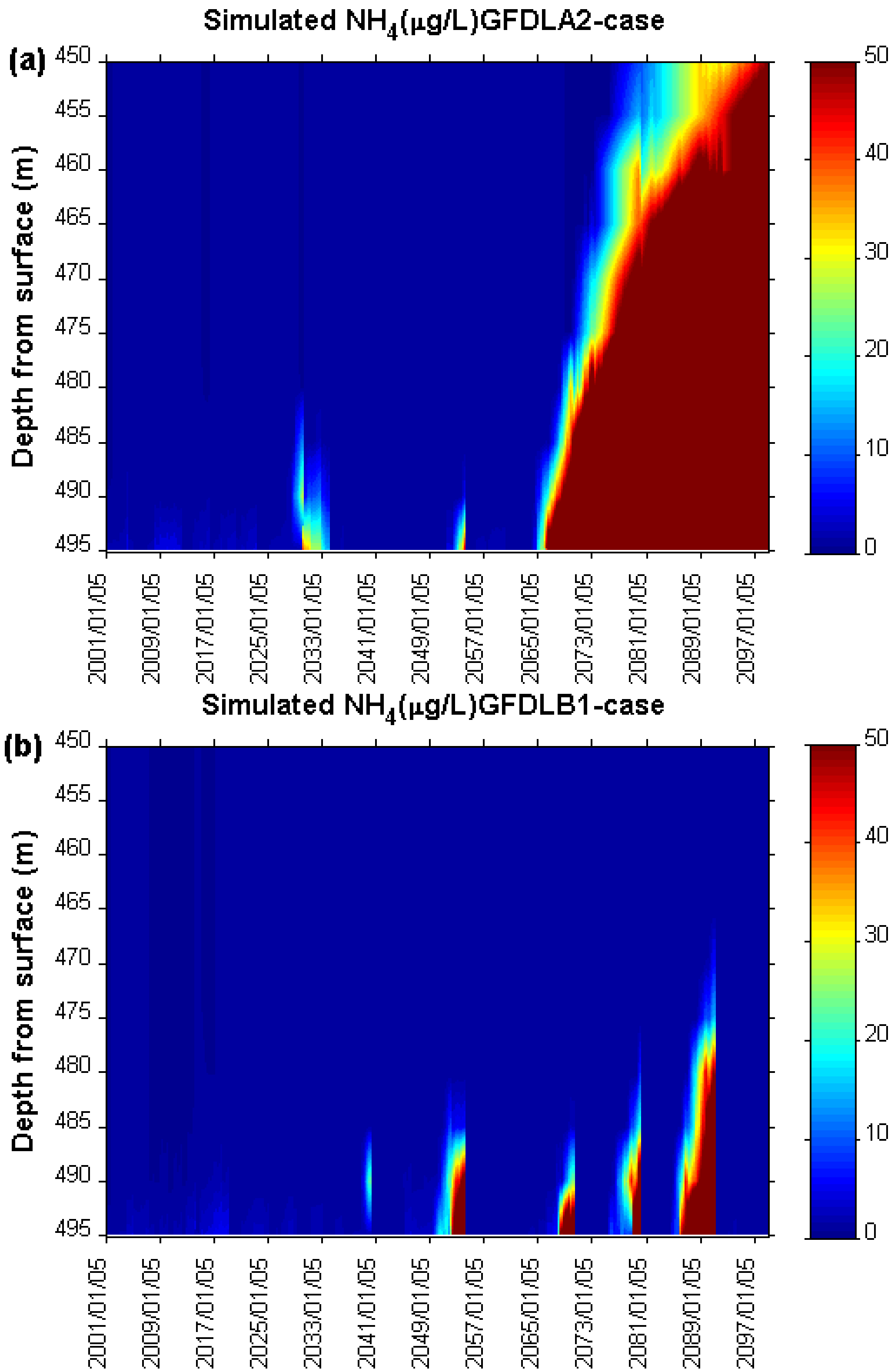

Figure 6-17. Close view of the bottom 45 m (450 m to 495 m) simulated ammonium release for (a) GFDLA2 (b) GFDLB1 scenario.

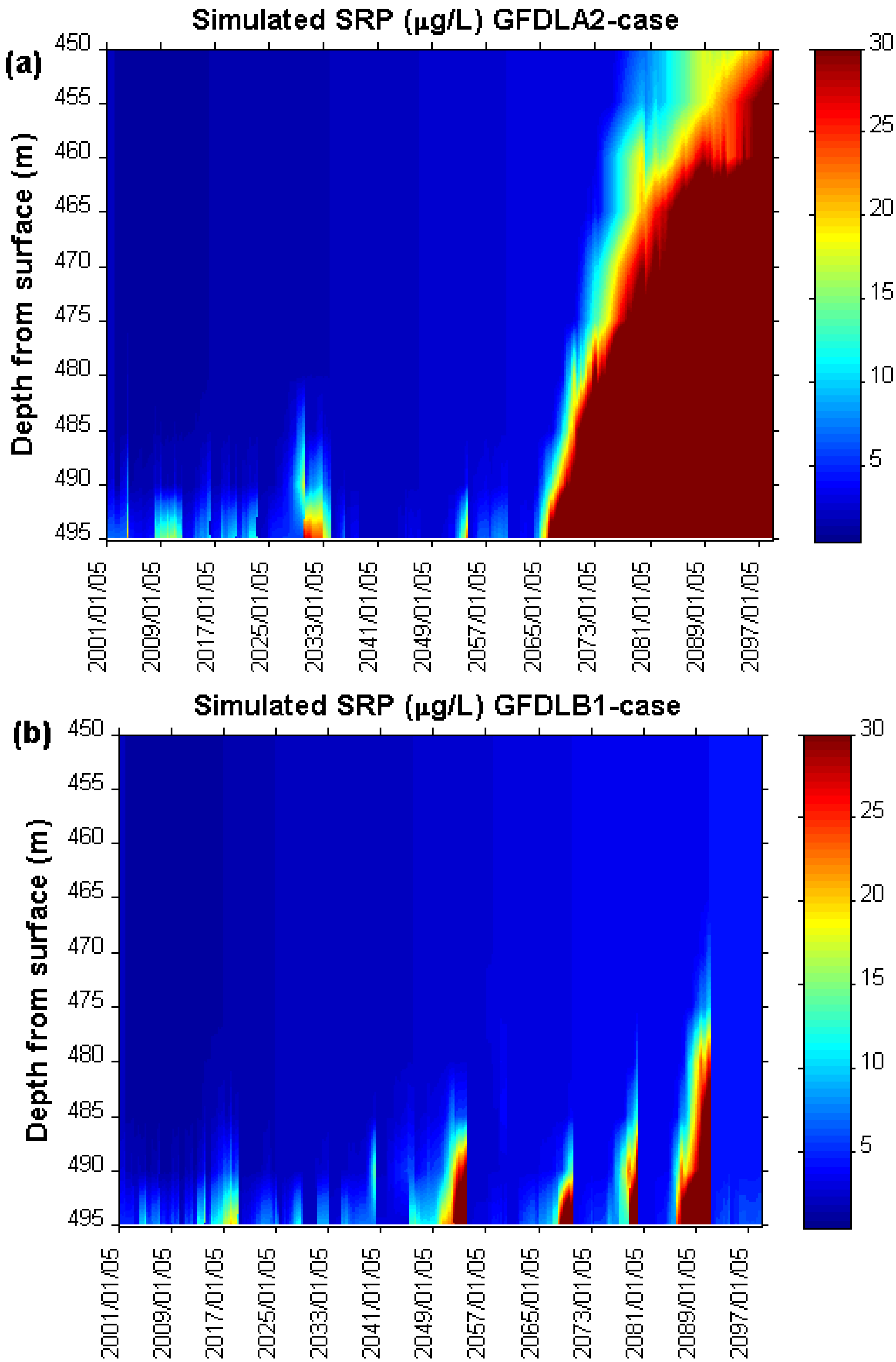

Figure 6-18. Close view of the bottom 45m (450m to 495m) simulated soluble reactive phosphorus release for (a) GFDLA2 (b) GFDLB1 scenario.

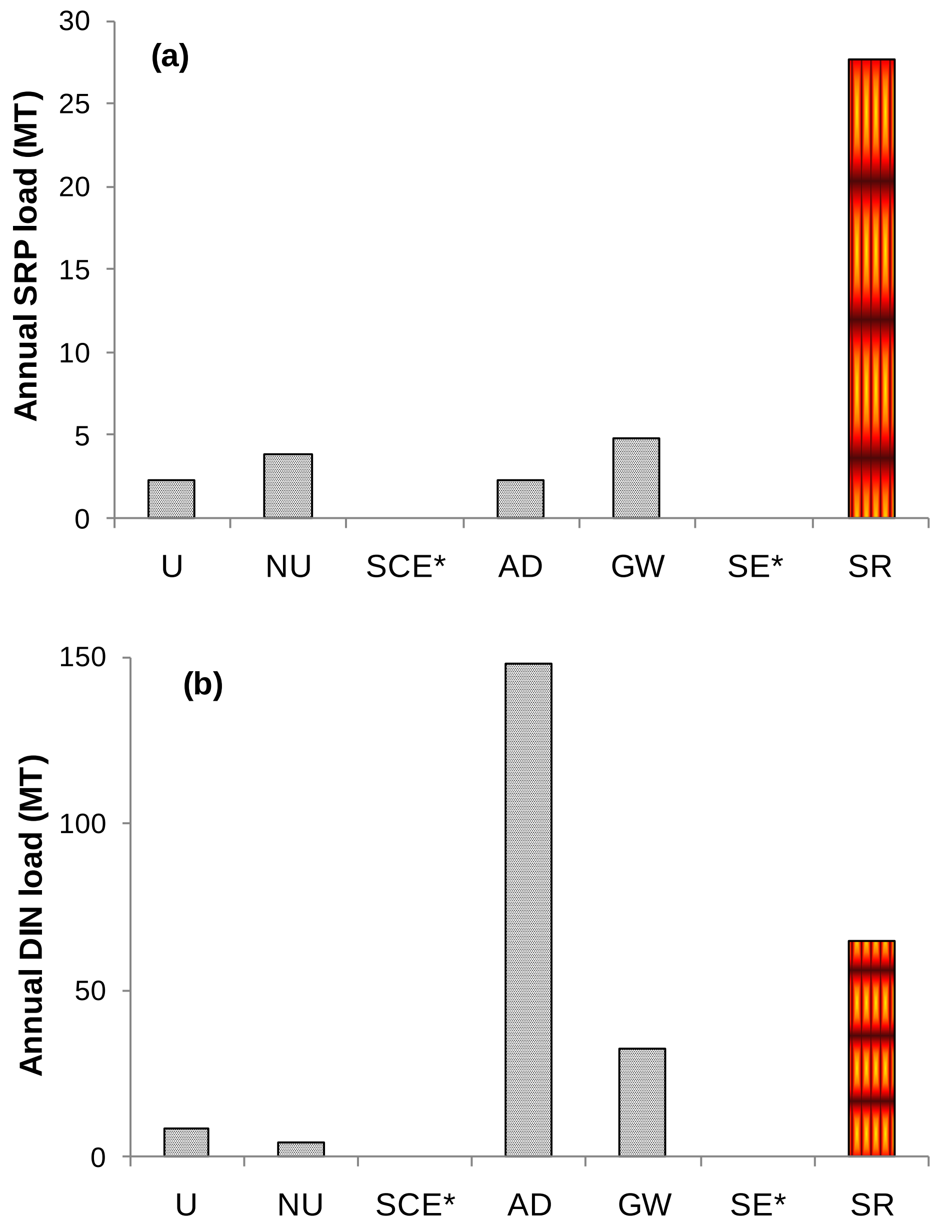

Figure 6-19. Comparison of average external and internal annual (a) soluble reactive phosphorus (SRP) (b) dissolved inorganic nitrogen (DIN). External loads come from estimates in Lahontan and NDEP (2010a). Sediment release (SR) were calculated in this study and represent modeled values at the end of the 21st Century. U, NU, SCE, AD, GW, SE, and SR represent urban, non-urban, stream channel erosion, atmospheric deposition, groundwater, shoreline erosion and sediment release, respectively. The symbol '*' represents no data.

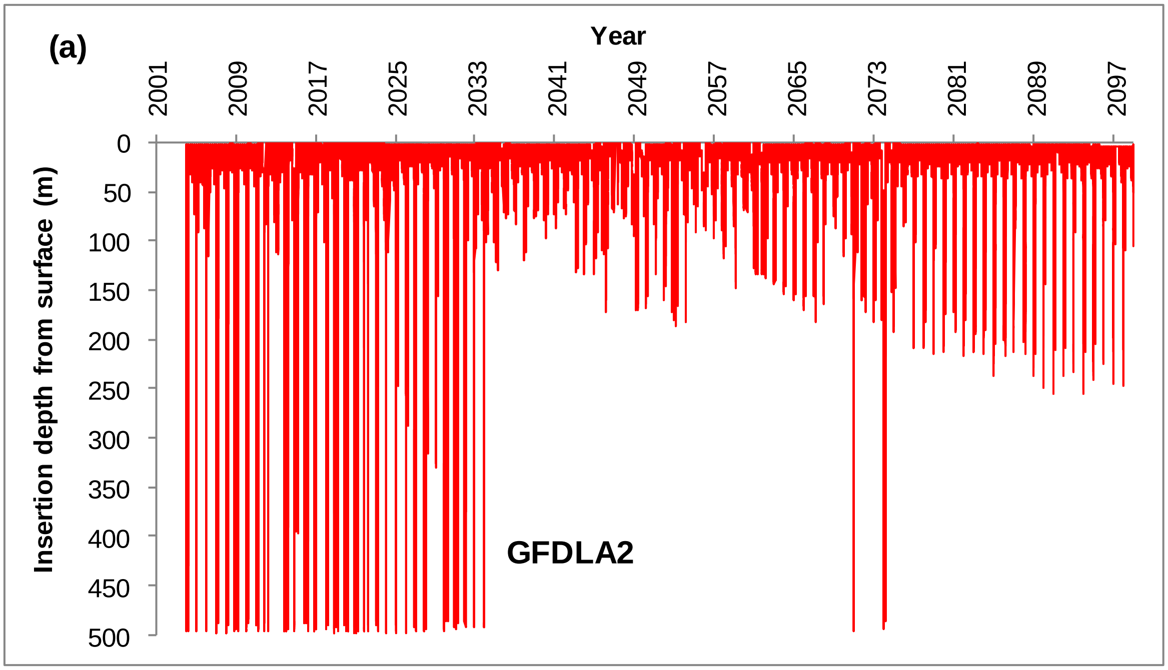

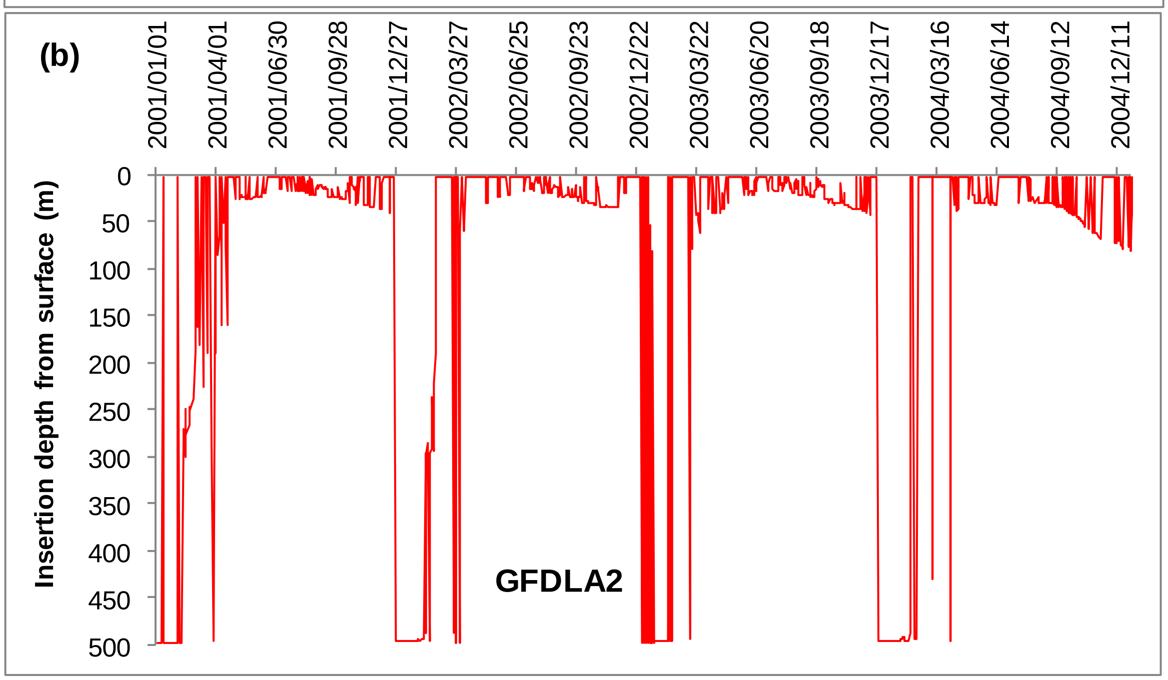

Figure 6-20. Daily insertion depth of Upper Truckee River (a) for the period 2005 to 2098 and (b) 2001 to 2004 for GFDL A2 scenario.

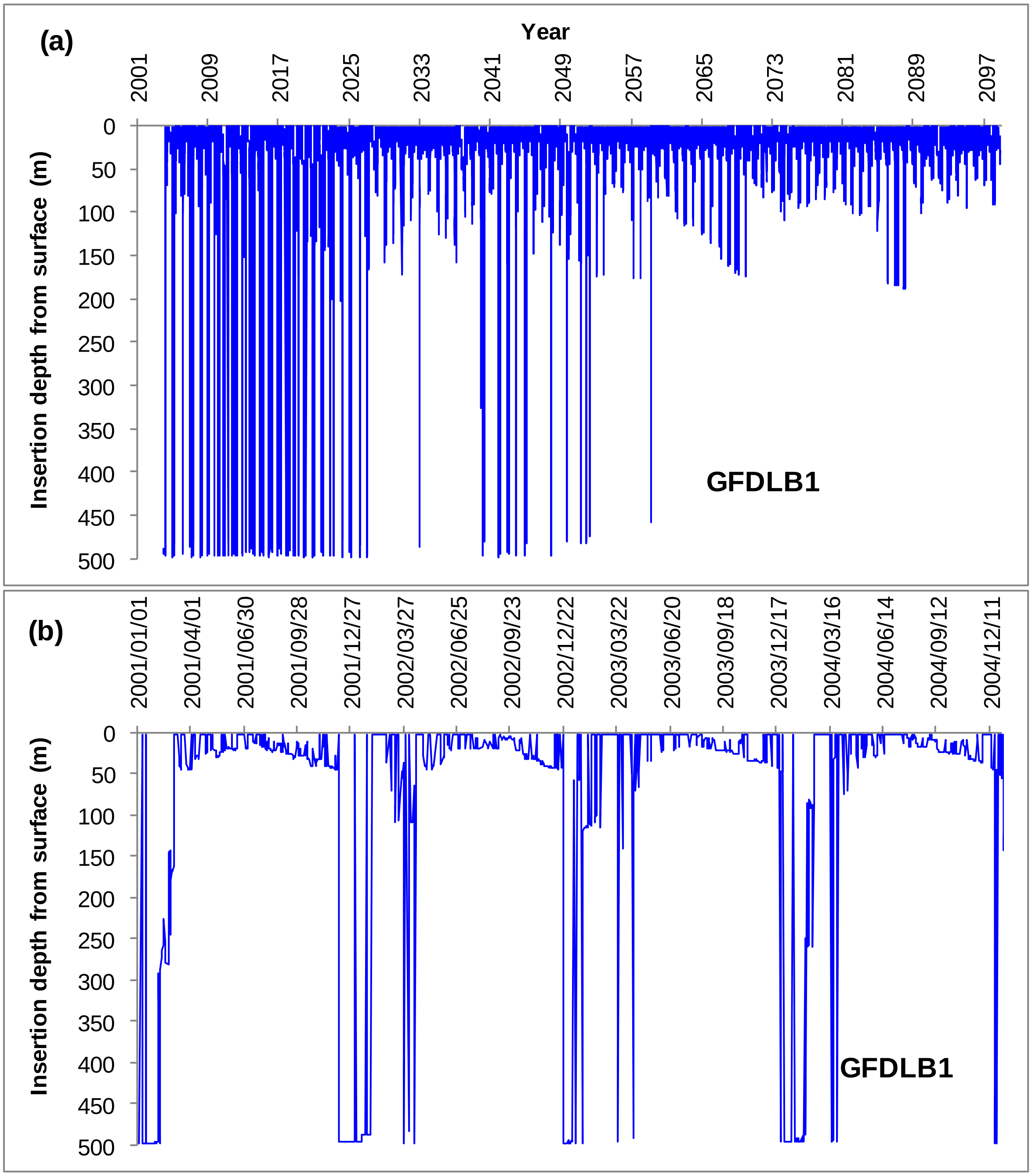

Figure 6-21. Daily insertion depth of Upper Truckee River (a) for the period 2005 to 2098 and (b) 2001 to 2004 for GFDL B1 scenario.

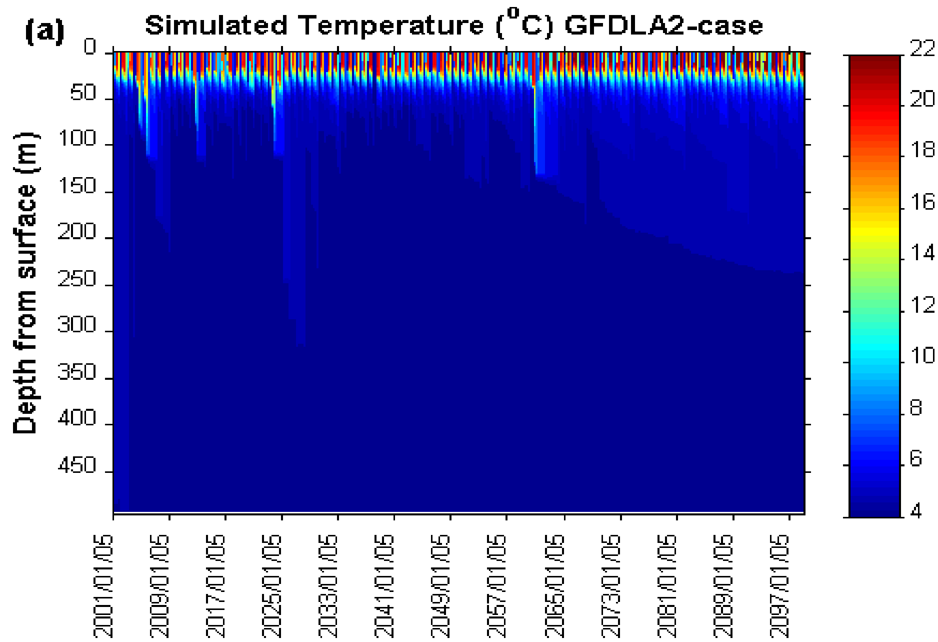

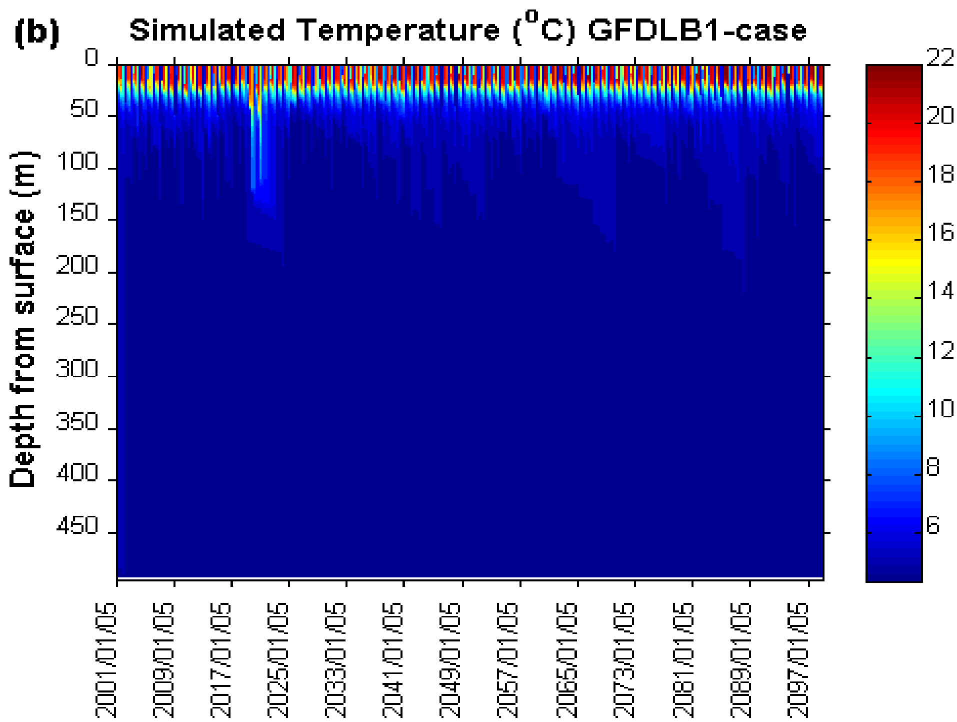

Figure 6-22. Simulated lake water temperature for GFDL A2 and GFDL B1 scenario. The upper limit of water temperature scale is set at 8°C to show the warming effect in deep water. The surface water temperatures are higher than 8 °C.

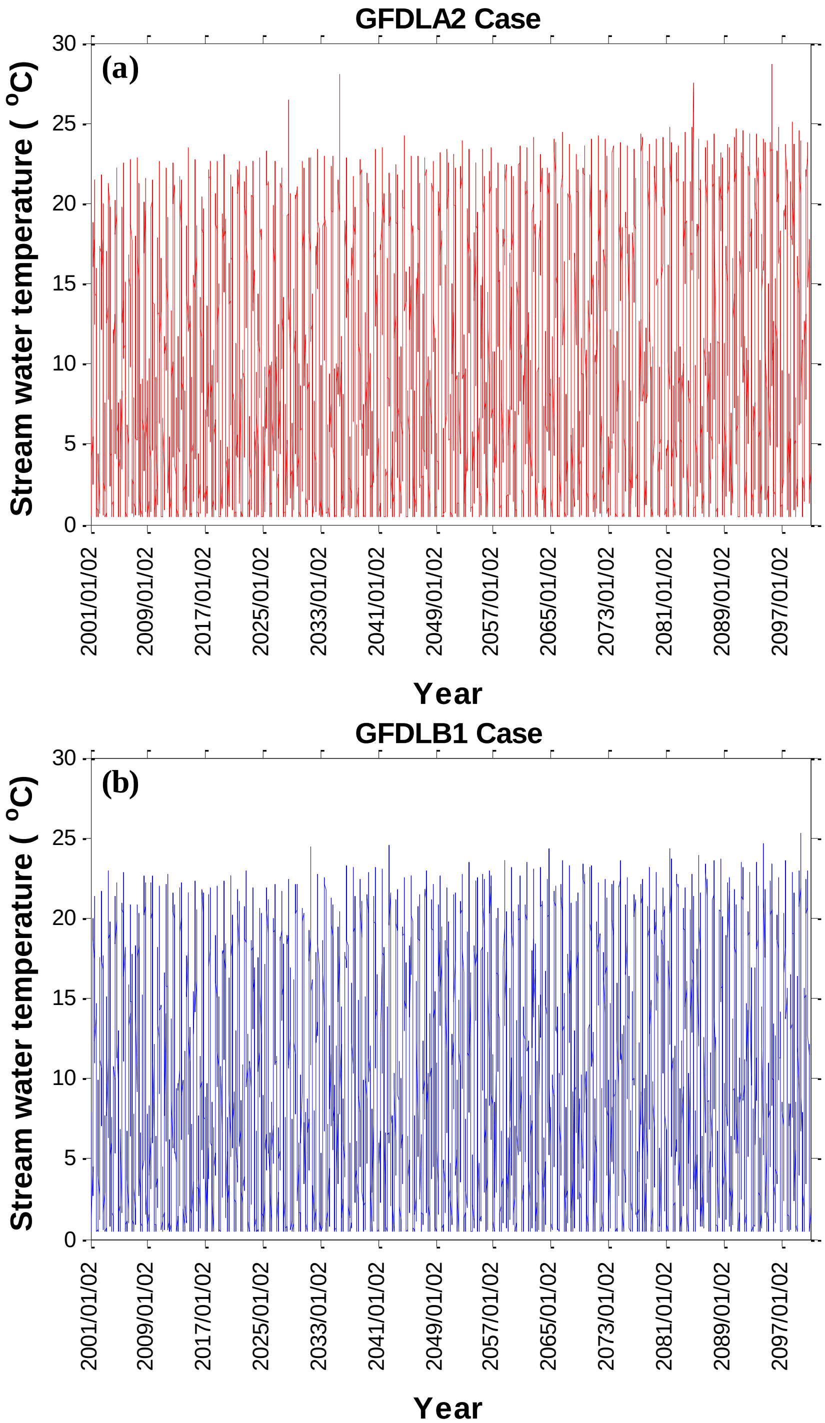

Figure 6-23. Simulated Upper Truckee River temperature for GFDL A2 and GFDL B1 scenario.

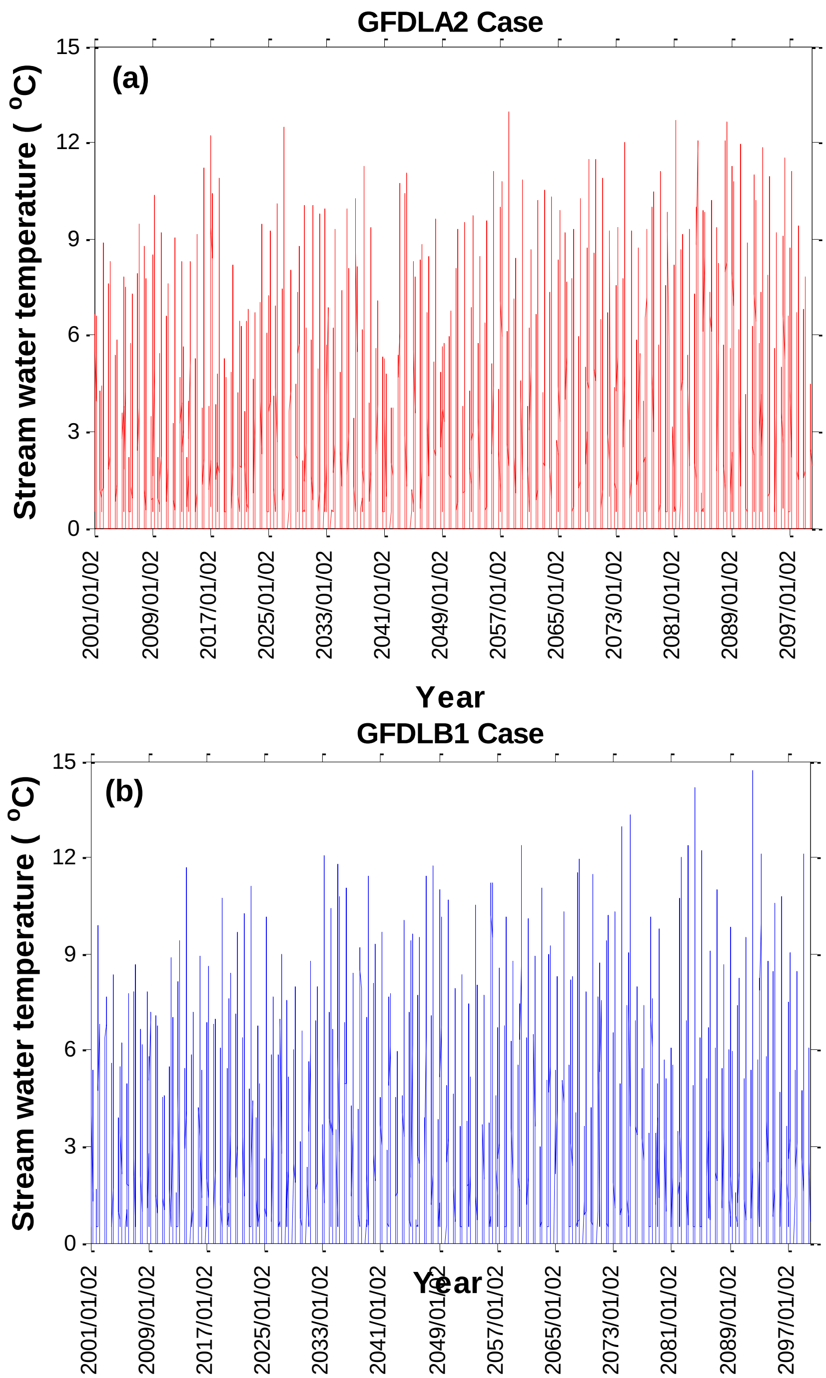

Figure 6-24. Simulated Upper Truckee River water temperature for (a) GFDL A2 and (b) GFDL B1 scenario for only winter (December to April).

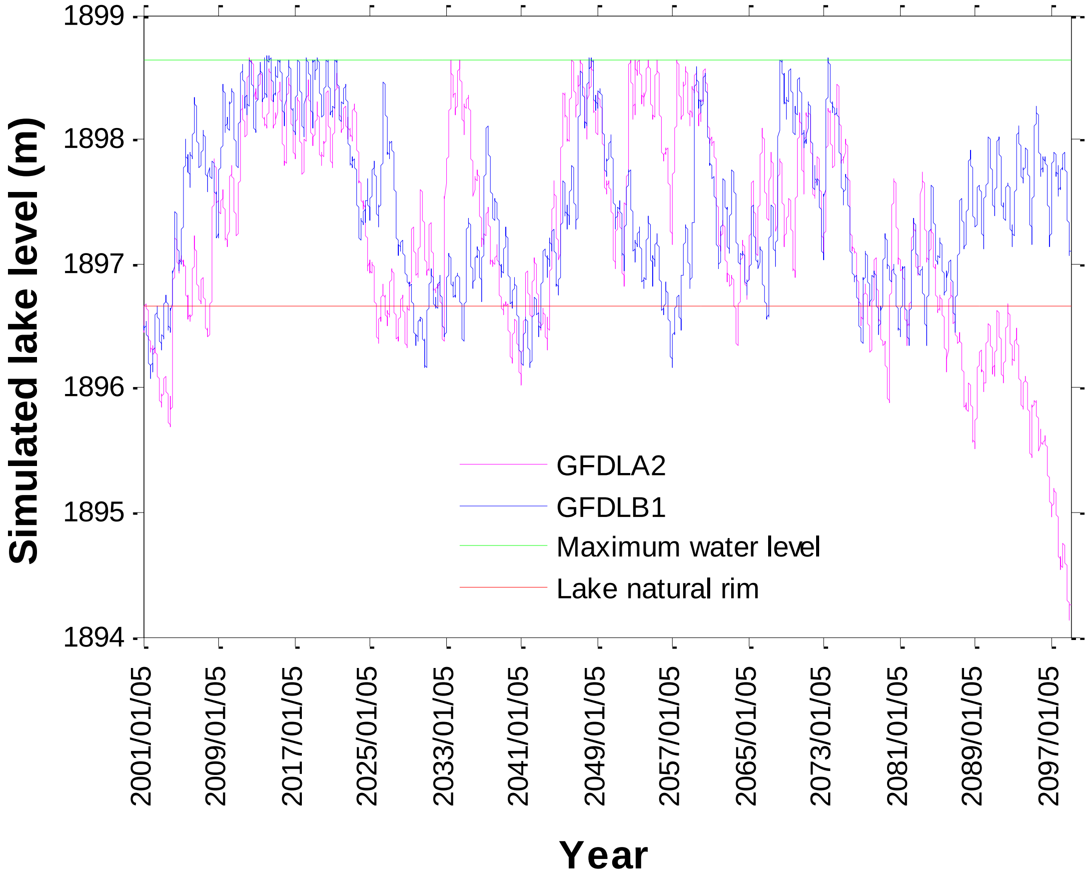

Figure 6-25. Daily lake water level for GFDL A2 and GFDL B1 scenario. Shown are the lake maximum water level and natural rim level.

7.0 KEY FINDINGS AND CONCLUSIONS

7.1 Downscaling of Climate Data

- Output from General Circulation Models or GCMs (often referred to as Global Climate Models) used to study changes in global climate do not nearly have the degree of spatial resolution required for a quantitative analysis of future meteorological conditions for topographically complex landscape such as the Tahoe basin. Typically, GCM output is provided at approximately 20 locations throughout the states of California and Nevada combined. Using downscaling techniques, the spatial coverage and therefore resolution was increased significantly to 12-16 grid points for the Tahoe region.
- A sophisticated statistical downscaling methodology (constructed analogs method) was applied to the A2 and B1 emissions scenarios of the GFDL (Geophysical Fluid Dynamics Laboratory Model) and the PCM (Parallel Climate Model) GCMs to produce a simulated data record for the 21st Century (2000-2099). The A2 and B1 scenarios were chosen to bracket projected emission scenarios with A2 considered a high emission condition and B1 a lower, albeit still increasing emission condition.
- Compared to historical observations (1950-1999) the level of agreement for temperature and precipitation within the study area of the Lake Tahoe Basin was very good. The anomaly correlations for maximum temperature and daily root-precipitation ranged from 0.70-0.95. Lake modeling also requires output for meteorological variables such as shortwave and longwave radiation, and surface wind speeds. In comparison to historical data, downscaling worked well for these variables and was adequate for our modeling purposes.
- In an attempt to ensure that the downscaled GCM data was as representative of conditions in the Tahoe basin as possible, it was further refined using a quantile mapping process so that the modeled historical precipitation related to the nearest in-basin SnoTel meteorology gage.
- The resulting meteorological output for future conditions represents a deliverable that was used to inform watershed and lake modeling. However, this output is now also available for other researchers studying the effects of climate change on forest vegetation, wildfires and other terrestrial processes.
- The team used the output of the GCMs, as appropriate, and the two emissions scenarios, downscaled to a 12 km grid scale. The daily output (temperature, precipitation, wind and radiation) was used to drive an existing numerical lake clarity model (DLM), and (after "disaggregation" of daily to hourly values) to drive an existing watershed model (LSPC^{++}) that calculates runoff, sediment and nutrient loads. In addition, the Pollutant Load Reduction Model (PLRM) was used to assess the effect of changes in hydrology on the design and operation of BMPs, such as treatment basins.

7.2 Hydrologic Impacts – Past and Projected

- Down-scaled climatic data from two General Circulation Models (GFDL and PCM) and two emissions scenarios (B1 and A2) were used to evaluate projections of 21st century hydrologic conditions in the Tahoe basin.
- The meteorological data were corrected for bias and adjusted to local temperature, precipitation and wind data, and the results used to drive a distributed hydrology model and a lake hydrodynamic model. The output from the hydrology model has been used to analyze future projected trends in annual precipitation, the relative fraction of precipitation falling as snow, and the Palmer Drought Severity Index. For the Upper Truckee River, the hydrology model was also used to analyze the trend in timing of the annual hydrograph centroid, the shifts in the flow-duration curves and flood frequency curves, and the trend in the annual minimum 5-day low flow.
- The results show 1) upward trends in T_{max} and T_{min}, with trends for the GFDL > PCM, and trends for the A2 > B1; 2) no strong trends in annual precipitation amount, except for declining precipitation for the GFDL A2 case toward the end of the century; 3) a continuing shift from snowfall to rain, toward earlier snowmelt and runoff during the water year, for both scenarios; 4) a downward shift in the flow-duration curve for the A2 scenario in the last third of the century; 5) declining minimum 5-day low-flow for the A2, but not for the B1 case; 6) some increases in drought severity especially toward the end of the century; 7) dramatic increases in flood magnitude in the middle third of the century, especially with the B1 scenario.
- These changes will create stresses on both terrestrial and aquatic ecosystems in the Basin, and pose serious challenges to resource managers, especially in the latter half of this century. These challenges include increased risk of wildfire, increased tree mortality from insects and disease, increased erosion and sediment yield, and losses of aquatic habitat.

7.3 Projected Changes in Flow, Nutrient and Sediment Loads Under Climate Change Conditions

- This project uses the Lake Tahoe Watershed Model to analyze the potential impacts of climate change (meteorology and hydrology) on nutrient and sediment loading to Lake Tahoe on a basin-wide scale. Watershed modeling in this project assumed that existing conditions remained constant (e.g. land use patterns, vegetation, geology and existing management practices) and that the projected change in meteorological factors (using the downscaled output) was the only changing variable. The GFDL A2 and B1 emission scenarios were run for the period 2002-2099.
- Climate change resulted in a shift in the distribution of snowfall towards rainfall.
- The LSPC modeled time series for snowpack under the A2 emission scenario showed a 55-60 percent reduction during the last one-third of the century (2067-2099) relative to that seen in the period 1967-1999. During 2000-2066 the modeled values were intermediate at 20-30 percent reduction. Under the B1 emission scenario a 35-40 percent reduction in snowpack was predicted between 2034 and 2099.

- The beginning and end dates for the snowpack period in the Lake Tahoe Basin are predicted to change in the 21st Century. During the period 2067-2099 – under the GFDL A2 emissions scenario - it is expected that the start of the snowpack could be three weeks later than the 1967-1999 historic baseline; peak snowpack could occur two weeks earlier; and that the end of the snowpack could be five weeks later weeks later. The estimated durations of the snowpack under the GFDL A2 emissions scenario are 232 days (2002-2033), 226 days (2034-2066) and 184 days (2067-2099). These compare to a baseline condition (1967-1999) of 248 days.
- Water yield to Lake Tahoe declined under both the A2 and B1 emission scenarios. Under the GFDL A2 emissions scenario, flow declined by about 5-10 percent between 2034 and 2066. A further decline in flow, approximately 15-30 percent of the baseline, was seen between 2067 and 2099. The GFDL B1 emission scenario showed less of a difference than the A2 model run.
- The watershed model indicates that sediment load may stay uniform or increase slightly – up to 5 percent - relative to baseline loads. The modeled trends also suggest that nutrient loading should generally decline in association with the predicted decreasing water yield to the lake (Figures 4-23 and 4-24). For the first two-thirds of the 21st Century, sediment and nutrient loads are predicted to decline by about 5-10 percent. Thereafter (until 2099) total N and total P loads could drop by 75-80 percent.
- In all, the output from the watershed model suggests that pollutant loading to Lake Tahoe should not increase as a result of climate change, but that some decline may be possible. It is noteworthy that it was beyond the technical scope of this project to ascertain the quantitative impact of rainfall–mediated erosion on loading. Runoff concentrations used in the watershed model are based on current conditions where both snowmelt and rainfall cause pollutants to enter runoff. Theoretically, since rainfall has move erosive energy, some of the loads could be underestimated.

7.4 Implications for Load Reduction and BMP Design

- Historically, the percentage of precipitation that falls as snow ranges between 50%-60% for elevations in the Tahoe basin where most development has occurred (predominantly around the lake margins at elevations ranging from 6,230 feet to 6,600 feet). At the end of the 21st century, the modeling analysis predicts that the percentage of precipitation that falls as snow will decline to an annual range of 30%-40% or even less for developed areas in the Tahoe basin.
- The net result of this potential shift in precipitation patterns is more rain and less snow, which could increase the frequency and magnitude of peak flows in stormwater runoff. This simulated trend of increasing temperature appears to be the most likely factor that may impact the effectiveness of water quality improvement projects (WQIPs) and private parcel best management practices (BMPs).
- Typical standards for national practice for design of stormwater treatment facilities target capture and treatment of 80-90 percent of the average annual runoff volume. The results of modeled simulations showed that increases in stormwater runoff caused roughly a 10 percent decline in treatment performance for WQIPs and BMPs with storm water treatment facilities sized using the 20-year 1-hour design standard for the Tahoe basin (i.e. one inch of rain in one hour). However, at the end of the simulation period, capture

remains above about 80 percent of average annual runoff. This indicates that while performance may be reduced, load reductions consistent with current national stormwater management practice would still be achievable if storm water treatment facilities are sized using the 20-year 1-hour design standard for the Tahoe basin.

- Two representations of a storm water project area were developed to compare pollutant load performance with and without stormwater quality improvements: 1) a Baseline Condition with modeling assumptions reflecting current land use conditions, maintenance practices, and pollutant sources; and 2) an Improved Condition with modeling assumptions reflecting implementation of a hypothetical WQIP that addresses all pollutant sources from public lands and complete implementation of BMPs for all private parcels within the project area. The Improved Condition resulted in roughly an 80-85 percent reduction in fine sediment particles (FSP) loading relative to the Baseline Condition at the beginning of the simulation period. The simulated results for the Improved Condition showed a modest decline in performance for FSP load reductions (i.e. increase in average pollutant load) as a result of climate change. However, the Improved Condition continues to provide more than 80 percent FSP reduction relative to the Baseline Condition throughout the entire simulation period.

7.5 Response of Lake Tahoe

- The Lake Clarity Model was developed for use in the Lake Tahoe TMDL to quantify the impact of pollutant loads and load reduction on transparency. This model includes a variety of modules such as a hydrodynamic sub-model, water quality and ecology sub-model, optical sub-models, and most recently a fully calibrated and validated dissolved oxygen sub-model. This combined model was used to evaluate the potential impacts of climate change on lake mixing and associated ramifications.
- Measured data from Lake Tahoe has shown that since 1968, the lake mixes (circulates) completely to the bottom (~500 meters) on the average of once every four years. Using output from the GFDL A2 emissions scenario the Lake Clarity Model suggests that by the middle of the 21st Century (after about 2050) Lake Tahoe will cease to mix to the bottom, with a mixing depth of only 100 m as the most commonly seen value. A similar, albeit not as severe, outcome is seen for the GFDL B1 emissions scenario. As the surface water heats, the resulting density difference between the warmer surface water and the colder deeper water will be too strong for the wind energy to overcome. Indeed, this change in density can already be seen in the measured historic data.
- When the lake fails to completely mix, the bottom waters are not replenished with oxygen and eventually dissolved oxygen at these depths will fall to zero. When this occurs both soluble reactive phosphorus and ammonium-nitrogen (both are readily available for algal growth) are released from the deep sediments resulting in an increase in nutrient loading that would not have happened under the lake's current deep mixing regime. The model shows this as a new and significant source of nutrients, heretofore not seen in Lake Tahoe. By the 2075 or there about the model indicates that under the GFDL A2 scenario dissolved oxygen below 200 m could reach a sustained level of zero year round. At the same depths, oxygen concentrations could drop to levels (< 6 mg/L) that are inhospitable to salmonids even earlier. The model also suggests that intermittent periods of anoxia in the deepest waters could occur within the next 20 years. Under the

GFDL B1 scenario, deep-water anoxic will also occur, albeit not as sustained as seen in the GFDL A2 scenario; this results from the observation that while complete mixing will be less frequent than historically observed, it will occur.

- Based on published results for soluble phosphorus (SRP) and ammonium release from anoxic Lake Tahoe sediments, the annual loading of SRP under sustained conditions of lake stratification (no deep mixing) and anoxic sediments would be twice the current load from all other sources. Loading of ammonium under these conditions would increase the amount of biological available nitrogen that enters the lake by 25 percent. This affect on the nutrient loading budgets to Lake Tahoe could have a dramatic and long-lasting impact on the food web and trophic status of Lake Tahoe.
- The resulting annual Secchi depth in the later portion of the 21st Century will be in the range of 15-20 m as compared measured values of 21-22 m since 2000.
- Should the nutrients release from the bottom sediments periodically mix or otherwise become entrained into the upper waters we expect that the impact on algal growth below the Secchi depth should be significant, with an attendant impact of lake food web dynamics and trophic status.
- The lake model suggests that climate change will drive the lake surface level down below the natural rim after 2086 for the GFDL A2 but not the GFDL B1 scenario.

7.6 Conclusions

The most significant impacts of a future, modeled climate change at Lake Tahoe are changes in hydrologic conditions and reduced frequency of complete vertical mixing of the lake. Hydrology output from the downscaled climate modeling suggests a significant reduction in the amount of precipitation falling as snow in the Tahoe basin. This could have consequences for water supply as well as winter recreational sports. Should the lake's deep mixing be restricted to the extent the models suggest, internal loading of nutrients from the sediments will be very significant and will drive a fundamental change in the biological productivity status of both the pelagic and littoral regions of the lake. These nutrients, particularly phosphorus, will be available to drive algal growth. Reducing the load of external nutrients entering the lake in the coming decades may be the only possible mitigation measure to reduce the impact of climate change on lake clarity and trophic status.

The meteorologic and geographic conditions in the Tahoe basin combine to create a vulnerable ecosystem. Temperatures in the Basin are increasing faster than in the surrounding region. This may be due to the influence of the lake and its heat (energy) budget on local air temperature, although a decrease in the albedo of the snowpack from deposition of soot (black carbon) may also play a role. Second, under historic and current conditions the lake mixes to the bottom on the average of only once every four years. Continued warming will increase the lake's thermal stability, and likely shut down its vertical mixing altogether. Third, on occasion, the lake historically has fallen below its natural outlet elevation during prolonged dry years. Lake level modeling in our study suggests that under some greenhouse gas emission scenarios, outflow from Lake Tahoe could cease by the end of the 21st Century.

This project represents the first attempt to evaluate water quality and water resources at Lake Tahoe under the anticipated conditions of climate change. The results indicate that continued climate changes could pose serious threats to the characteristics of the Lake that are most highly valued. Future water quality planning must take these results into account.

7.7 Acknowledgment

This research was supported using funds provided by the Bureau of Land Management through the sale of public lands as authorized by the Southern Nevada Public Land Management Act (SNPLMA), and was funded in part through grant 08-DG-11272170-101 from the USDA Forest Service Pacific Southwest Research Station. The views in this report are those of the authors and do not necessary reflect those of the USDA Forest Service Pacific Southwest Research Station or Bureau of Land Management.

8.0 REFERENCES

Aguado E., Cayan, D., Riddle, L., Roos, M. 1992. Climatic fluctuations and the timing of west coast streamflow. Jour. Clim. 5: 1468-1483.

Alley W. 1984. The Palmer drought severity index: limitations and assumptions. Jour. Clim Appl. Met. 23: 1100-1109.

Barnett T. P., Pierce, D. W., Hidalgo, H. G., Bonfils, C., Santer, B. D., Das, T., Gala, G., Wood, A.W., Nozawa, T., Mirin, A.A., Cayan, D.R., and Dettinger, M. D. 2008. Human-Induced Changes in the Hydrology of the Western United States. Sciencexpress 10.1126/science.1152538: 1-9.

Brown T.J., Hall, B. L., and Westerling, A. L. 2004. The impact of twenty-first century climate change on wildland fire danger in the western United States: an applications perspective. Climatic Change 62: 365-388.

Beutel, MW. 2000. Dynamics and Control of Nutrient, Metal and Oxygen Fluxes at the Profundal Sediment-Water Interface of Lakes and Reservoirs. PhD Dissertation, University of California, Berkeley.

Beutel, M. W. 2006. Inhibition of ammonia release from anoxic profundal sediment in lakes using hypolimnetic oxygenation. Ecol, Engineering. 28: 271-279.

Cayan D. R., Kammerdiener, S., Dettinger, M., Caprio, J., and Peterson, D. 2001. Changes in the onset of spring in Western United States. Bull. Amer. Meteor. Soc. 82: 319-415.

Cayan, D.R., Maurer, E.P., Dettinger, M.D., Tyree, M., Hayhoe, K. 2008. Climate change scenarios for the California region. Climatic Change, 87 (Suppl 1): S21-42. doi10.1007/s10584-007-9377-6 .

Cayan, D., Tyree, M., Dettinger, M., Hidalgo, H., Das, T., Maurer, E., Bromirski, P., Graham, N., Flick, R. 2009. Climate change scenarios and sea level rise estimates for California 2008 Climate Change Scenarios Assessment. California Energy Commission Report CEC-500-2009-014-D, 62 p.

Coats, R., J. Perez-Losada, G. Schladow, R. Richards and C. Goldman. 2006. The warming of Lake Tahoe. Climate Change 76: 121-148.

Coats R. 2010. Climate change in the Tahoe basin: regional trends, impacts and drivers Climatic Change DOI 10.1007/s10584-010-9828-3.

Chung, E.G.; Bombardelli, F.A., Schladow, S.G. (2009) Sediment resuspension in a shallow lake. Water Resources Research, 45 W05422, doi:10.1029/2007WR006585.

Dettinger M. D., and Cayan, D. R. 1995. Large-scale atmospheric forcing of recent trends toward early snowmelt runoff in California. Jour. Climate 8: 606-623.

Dettinger M.D., Cayan, D., Knowles, N., Westerling, A., and Tyree, M. 2004. Recent projections of 21st-century climate change and watershed responses in the Sierra Nevada. USDA Forest Service. Report no. Gen. Tech. Rep. PSW-GTR-193.

Fleenor, W.E. 2001. Effects and Control of Plunging Inflows on Reservoir Hydrodynamics and Downstream Releases. Dissertation, UC Davis.

Hamlet A.F., Mote, P. W., Clark, M. P., and Lettenmaier, D. P. 2005. Effects of Temperature and Precipitation Variability on Snowpack Trends in the Western United States. Jour. Clim. 18: 4545-4561.

Hansen J., Sato, M., Kharecha, P., Beerling, D., Masson-Delmotte, V., Pagani, M., Raymo, M., Royer, D. L., and Zachos, J. C. 2009. Target atmospheric CO2: Where should humanity aim? Open Atmos. Sci. Jour. 2: 217-231.

Heald, P.C.; Schladow, S.G.; Reuter, J.E.; Allen, B.C. (2005) Modeling MTBE and BTEX in lakes and reservoirs used for recreational boating, Environmental Science and Technology, 39:1111-1118.

Helsel D. R., and Hirsch, R. M. 1995. Statistical Methods in Water Resources. New York: Elsevier.

Helsel D. R, Mueller, D. K., and Slack, J. R. 2005. Computer Program for the Kendall Family of Trend Tests. Reston, VA: U.S. Geol. Surv. Report no. Scientific Investigations Report 2005-5275.

Helsel DR, and Frans, L. M. 2006. Regional Kendall Test for Trend. Environ. Sci. Tech. 40: 4066-4073.

Heyvaert, A.C. 1998. The biogeochemistry and paleolimnology of sediments from Lake Tahoe, California-Nevada. Davis, CA: University of California, Davis. 194 p. Ph.D. dissertation.

Hidalgo HG, Dettinger, M. D., and Cayan, D. R. 2008. Downscaling with Constructed Analogues: Daily Precipitation and Temperature Fields Over the United States. California Climate Change Center. Report no. 2007-027.

Imberger, J., J.C. Patterson, B. Hebbert, I. Loh. 1978. Dynamics of reservoirs of medium size. Journal of Hydraulic Division, ASCE, 104: 725-743.

Intergovernmental Panel on Climate Change (IPCC). 2007. Climate change 2007—The physical science basis. Available from http://www.ipcc.ch/ipccreports/ar4-wg1.htm.

Jeton AE. 1999. Precipitation-Runoff Simulations for the Lake Tahoe Basin, California and Nevada. Carson City, NV: U.S. Geol. Surv. Water-Resources Investigations. WRI 99-4110.

Johnson T, Dozier, J., and Michaelsen, J. 1999. Climate change and Sierra Nevada snowpack. Pages 63-70 in Tranter M AR, Blum E, Jones G, Sharp M, and Williams, M, ed. Interactions Between the Cryosphere, Climate and Greenhouse Gases. Proc. IUGG 99 Symp. HS2. Birmingham: IAHS.

Kanamitsu, M., Kanamaru, H. 2007a. 57-Year California Reanalysis Downscaling at 10km (CaRD10) Part I. System Detail and Validation with Observations. *J. Climate* **20:**5527-5552.

Kanamaru, H., Kanamitsu, M. 2007b. 57-Year California Reanalysis Downscaling at 10km (CaRD10) Part II. Comparison with North American Regional Reanalysis. *J. Climate* **20**:5553-5571.

Knowles N, Dettinger, M., and Cayan., D. 2006. Trends in snowfall versus rainfall in the western United States. J. Clim. 19: 4545-4559.

Kothavala Z. 1999. The duration and severity of drought over eastern Australia simulated by a coupled ocean-atmosphere GCM with a transient increase in CO2. Environ. Modelling & Software 14: 243-252.

Lahontan Regional Water Quality Control Board (Lahontan) and Nevada Division of Environmental Protection (NDEP). 2010a. Lake Tahoe Total Maximum Daily Load Technical Report. Lahontan Water Board, South Lake Tahoe, California, and Nevada Division of Environmental Protection, Carson City, NV. 340 p.

Lahontan Regional Water Quality Control Board (Lahontan) and Nevada Division of Environmental Protection (NDEP). 2010b. Final Lake Tahoe Total Maximum Daily Load Report. Lahontan Water Board, South Lake Tahoe, California, and Nevada Division of Environmental Protection, Carson City, NV. 175 p.

Mote P.W., Hamlet, A. F., Clark, M., and Lettenmaier, D. 2005. Declining mountain snowpack in western North America. Bull. Amer. Meteor. Soc. 86: 19-49.

Nakicenovic, N., Alcamo, J., Davis, G., de Vries, B., Fenham, J., Gaffin, S., Gregory, K., Grubler, A., Jung, T.Y., Kram, T., La Rovere, E.L., Michaelis, L., Mori, S., Morita, T., Pepper, W., Pitcher, H., Price, L., Riahi, K., Roerhl, A., Rogner, H.-H., Sankovski, A., Schlesinger, M., Shukla, P., Smith, S., Swart, R., van Rooijen, S., Victor, N., Dadi, Z. 2000. Special report on emissions scenarios. Cambridge University Press, 599 p.

Palmer W. C. 1965. Meteorological drought. Washington, D.C. Report no. 45.

Perez-Losada, J. 2001. A Deterministic Model for Lake Clarity: Application to Management of Lake Tahoe, California-Nevada. Dissertation, UC Davis.

Pierce DW, Barnett, T.P., Hidalgo, H., Das, T., Bonfils, C., Santer, B., Bala, G., Dettinger, M., Cayan, D., Mirin, A, Wood, A., and Nozawa, T. 2008. Attribution of declining western U.S. snowpack to human effects. Jour. Clim. 21: 6425-6444.

Potter C, Shupe, J., Gross, P., Genovese, V., and Looster, S. 2010. Modeling river discharge rates in California watersheds. Jour. Water & Clim. Change 01.1.

Rabidoux, A.A. (2005), Spatial and temporal distribution of fine particles and elemental concentrations in suspended sediments in Lake Tahoe streams, California-Nevada, M.Sc. Thesis, University of California, Davis.

Regonda S, B. Rajagopalan, B., Clark, M., and J. Pitlick, J. 2005. Seasonal cycle shifts in hydroclimatology over the western United States. J. Clim. 18: 372-384.

Roesner et al.1998. Urban Runoff Quality Management. WEF Manual of Practice No. 23, ASCE Manual and Report on Engineering Practice No. 87. ISBN 1-57278-039-8.

Running S. 2006. Is global warming causing more, larger wildfires? Sciencexpress 10.11262/science/113070.

Sahoo, G. B. and Schladow, S. G. 2008. Impacts of climate change on lakes and reservoirs dynamics and restoration policies. Sustainability Science, 3(2) 189-200.

Sahoo, G.B., Schladow, S.G., Reuter, J.E. 2009. Forecasting stream water temperature using regression analysis, artificial neural network, and chaotic nonlinear dynamic models, Journal of Hydrology, 378, 325-342, doi: 10.1016/j.jhydrol.2009.09.037.

Sahoo, GB, Schladow, S.G., Reuter, J. E. 2010. Effect of Sediment and Nutrient Loading on Lake Tahoe (CA-NV) Optical Conditions and Restoration Opportunities Using a Newly Developed Lake Clarity Model. *Water Resources Research*, doi:10.1029/2009WR008447.

Stewart I, Cayan, D. R. ,and Dettinger, M. 2005. Changes toward earlier streamflow timing across western North America. Jour. Clim. 18: 1136-1155.

Tennessee Valley Authority (TVA) (1972), Heat and mass transfer between a water surface and the atmosphere. Water Resources Research Laboratory report No. 14, Norris, Tennessee.

Tetra Tech, Inc. 2007. Watershed Hydrologic Modeling and Sediment and Nutrient Loading Estimation for the Lake Tahoe Total Maximum Daily Load. Final modeling report. Prepared for the Lahontan RWQCB and University of California, Davis.

Thornthwaite CW. 1948. An approach toward a rational classification of climate. Geogr. Rev. 38: 55-94.

Trask, J.C. (2007). Resolving hydrologic water balances through novel error analysis, with focus on inter-annual and long-term variability in the Tahoe Basin. Dissertation, UC Davis.

Urbonas, B.R. and Stahre, P. 1993. Stormwater: Best Management Practices and Detention for Water Quality, Drainage, and CSO Management, Prentice Hall, Englewood, Cliffs, NJ.

USGS. 1982.Guidlines for Determining Flood Flow Frequency. Bulletin 17b of the Hydrology Subcommittee. Interagency Advisory Committee on Water Data. US DOI, USGS, Reston, VA, 191 p.

USACE (United States Army Corps of Engineers), Sacramento District (2003), Lake Tahoe basin framework study groundwater evaluation, Lake Tahoe basin, California and Nevada.

Wells N, Goddard, S., and Hayes, M. J. 2004. A self-calibrating Palmer drought severity index. Jour. Clim. 17: 2335-2351.

Westerling AL, Hidalgo, H. G., Cayan, D. R., and Swetnam, T. 2006. Warming and earlier spring increases western U.S. forest wildfire activity. Scienceexpress 10.1126/science.1128834: 1-9.

Wood, A.W., Maurer, E.P., Kumar, A. and D.P. Lettenmaier, 2002. Long Range Experimental Hydrologic Forecasting for the Eastern U.S., J. Geophys. Res., 107(D20), doi:10.1029/2001JD000659.

Wood, A.W., Leung, L.R., Sridhar, V., and others. 2004. Hydrologic implications of dynamical and statistical approaches to downscaling climate model outputs. Climatic Change 62:186-216.

Zou GY, and Donner, A. 2008. Construction of confidence limits about effect measures: A general approach. Statistics in Medicine 27: 1693-1702.

9.0 APPENDICES

APPENDIX 1- Bias-correction for downscaled downward shortwave radiation and wind speed.

Author: Goloka B. Sahoo

This Appendix provides the background, methodology and results used for bias-correction for downscaled shortwave radiation and wind speed as used in the water quality models.

9.1 Bias correction in downscaled downward shortwave radiation

The daily downscaled downward shortwave radiations (DWSR expressed in units of W/m^2) provided by the GFDL A2 scenario for Grid 14 were compared with measured data at the South Lake Tahoe Airport (SLTA) meteorological station for the period 1/1/1989 to 12/31/1998 (Figure 9-1). The GFDL A2 DWSR values were lower in the winter and higher in the summer when compared to the observed measurements. Moreover, the mean and standard deviation (SD) of GFDL A2 DWSR are high compared to those of measured records (Table 9-1). Consequently, the methods of quantile mapping (Wood et al. 2002) were used to correct the bias in the downscaled GFDL A2 DWSR values. In the quantile mapping method, values are arranged in rank-ordered categories (i.e. quantiles) to establish a relationship. The established relationship was applied to correct the bias in the downscaled dataset. The GFDL A2 DWSR dataset (Figure 9-2) was divided into three parts, each with a relationship with the observed data (Table 9-2). The regression equations were used to correct bias in the GFDL A2 scenario for all grid points. Figure 9-3 shows that our bias-corrected DWSR was able to closely follow the trend of observed records. Similar to bias correction of GFDL A2 DWSR, the bias in the GFDL B1 DWSR data were also corrected (Table 1.3). The observed DWSR were compared with down scaled GFDL B1 DWSR and bias corrected GFDL B1 DWSR in Figures 9-4 and 9-5.

Table 9-1. Statistics of the measured, downscaled and corrected downscaled GFDL A2 and GFDL B1 downward short wave radiation (W/m^2) using data for the period 1989 to 1998. SD represents standard deviation.

Statistics	Scenario				
	Measured	GFDL A2	Corrected GFDL A2	GFDL B1	Corrected GFDL B1
Mean (W/m^2)	213.2750	244.7285	213.2739	246.0476	213.2750
SD (W/m^2)	96.1623	131.8197	96.1610	132.2215	96.1599

Table 9-2. Regression equations between GFDL A2 DWSR (x) and Observed DWSR (y) for the 10 years (1989 to 2098). $y=c_0+c_1x+c_2x^2+c_3x^3+ c_4x^4+c_5x^5+c_6x^6$.

Regression coefficients and R^2	GFDLA2 ≥ 350	100< GFDLA2 < 350	GFDLA2 < 100
c_0	14855.7694	-1039.2383	51.4973
c_1	-196.9896	35.6630	0.4683
c_2	1.0661E+00	-4.4755E-01	2.3352E-03
c_3	-2.9824E-03	2.8903E-03	-2.0474E-05
c_4	4.5863E-06	-1.0014E-05	-1.7579E-07
c_5	-3.6952E-09	1.7796E-08	1.3279E-09
c_6	1.2230E-12	-1.2750E-11	1.0874E-11
R^2	0.9996	0.9998	0.9990

Table 9-3. Regression equations between GFDLB1 DWSR (x) and Observed DWSR (y) for the 10 years (1989 to 2098). $y=c_0+c_1x+c_2x^2+c_3x^3+ c_4x^4+c_5x^5+c_6x^6$.

Regression coefficients and R^2	GFDL B1 ≥ 350	100< GFDL B1 < 350	GFDL B1 < 100
c_0	21998.65	-1361.4894	50.8338005
c_1	-281.66983	46.1055615	0.43960983
c_2	1.4807E+00	-5.8393E-01	2.0064E-03
c_3	-4.0572E-03	3.8073E-03	-8.5604E-06
c_4	6.1440E-06	-1.3358E-05	-1.1399E-07
c_5	-4.8931E-09	2.4069E-08	5.0670E-10
c_6	1.6052E-12	-1.7489E-11	6.6424E-12
R^2	0.9997	0.9998	0.9990

9.2 Bias correction in downscaled wind speed

Downscaled wind speed (m/s) values from the GFDL A2 scenario was compared with measured records at SLTA meteorological station for the period 1989 to 1998. Figure 9-6 illustrates that downscaled wind speed were either very high or low compared to the actual measured values. The average and standard deviation of downscaled wind speed of GFDL A2 and B1 scenarios were higher than the measured records (Table 9-4). The methods of quantile mapping (Wood et al., 2002) are again used to correct the bias in the downscaled wind speed (m/s) values for both GFDL A2 and B1 scenarios. Figures 9-7 and 9-10 show the fit best to correct the bias in the downscaled wind speed dataset based on the multiple regression equations (Tables 9-5 and 9-6). Figures 1.8 and 1.11 show that bias corrected downscaled wind speed closely follow the trend of measured records.

Table 9-4. Statistics of the measured, downscaled and corrected downscaled GFDL A2 and GFDL B1 wind speed (m/s) using data for the period 1989 to 1998. SD represents standard deviation.

Statistics	Scenario				
	Measured	GFDL A2	Corrected GFDL A2	GFDL B1	Corrected GFDL B1
Mean (m/s)	2.7901	3.3358	2.7901	3.2466	2.7901
SD (m/s)	1.5325	2.1399	1.5313	2.1351	1.5317

Table 9-5. Regression equations between GFDLA2 wind speed (x) and observed wind speed (y) for the 10 years (1989 to 2098). $y=c_0+c_1x+c_2x^2+c_3x^3+ c_4x^4+c_5x^5+c_6x^6$ for wind speed <11 m/s and $y= c_0x^{c1}$ for wind speed >11 m/s.

Regression coefficients and R^2	GFDLA2 <11	GFDLA2 >11.0
c_0	0.152644	0.7788
c_1	0.546818	0.9493
c_2	0.207148	
c_3	-0.046685	
c_4	0.003390	
c_5	-2.77922E-05	
c_6	-3.77294E-06	
R^2	0.9995	0.946

Table 9-6. Regression equations between GFDLB1 wind speed (x) and observed wind speed (y) for the 10 years (1989 to 2098). $y=c_0+c_1x+c_2x^2+c_3x^3+ c_4x^4+c_5x^5+c_6x^6$ for wind speed <11 m/s and $y= c_0x^{c1}$ for wind speed >11 m/s.

Regression coefficients and R^2	GFDLB1 <11	GFDLB1 >11.0
c_0	0.145942	0.50677
c_1	0.534936	1.11489
c_2	0.287384	
c_3	-0.084436	
c_4	0.010332	
c_5	-0.000591	
c_6	1.29636E-05	
R^2	0.9996	0.9779

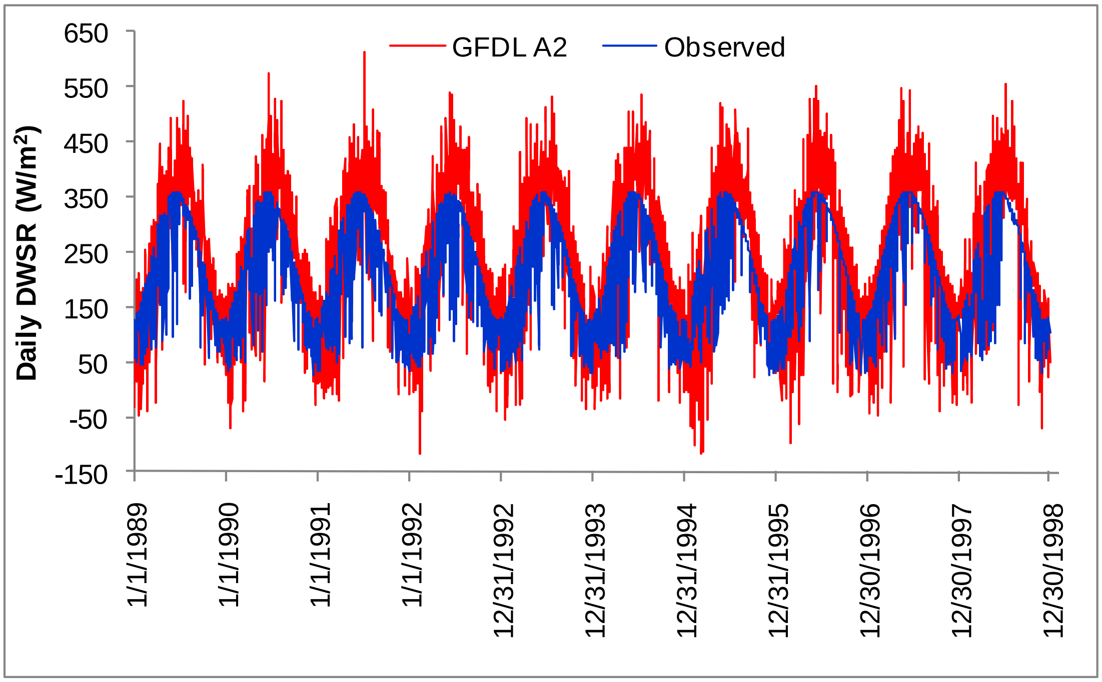

Figure 9-1. Comparison of daily downscaled downward shortwave radiation with observed records from the South Lake Tahoe Airport.

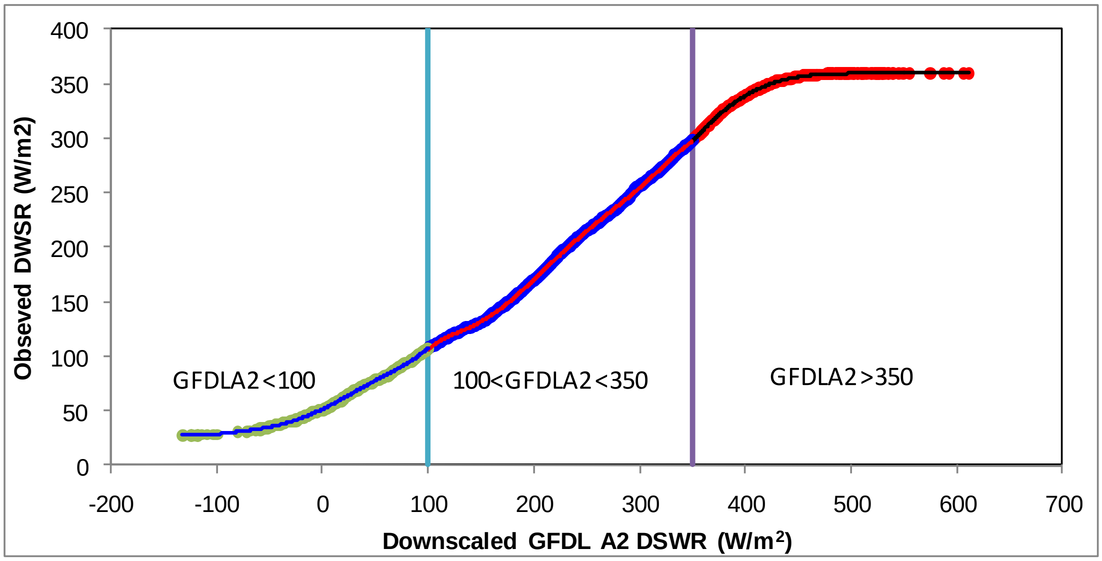

Figure 9-2. Non-linear relations between rank-ordered GFDL A2 DWSR and rank-ordered observed records. Solid lines represent 6th order polynomial trend lines. The regression coefficients are presented in Table 9-2.

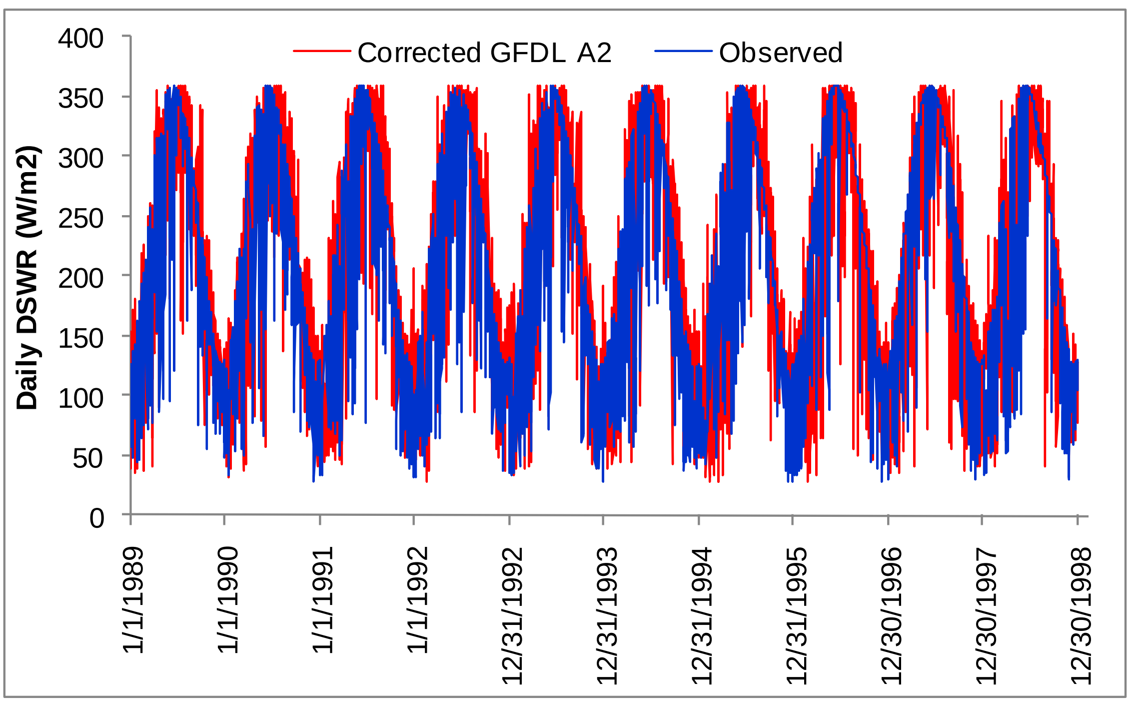

Figure 9-3. Bias-corrected GFDL A2 DWSR and observed records at SLTA.

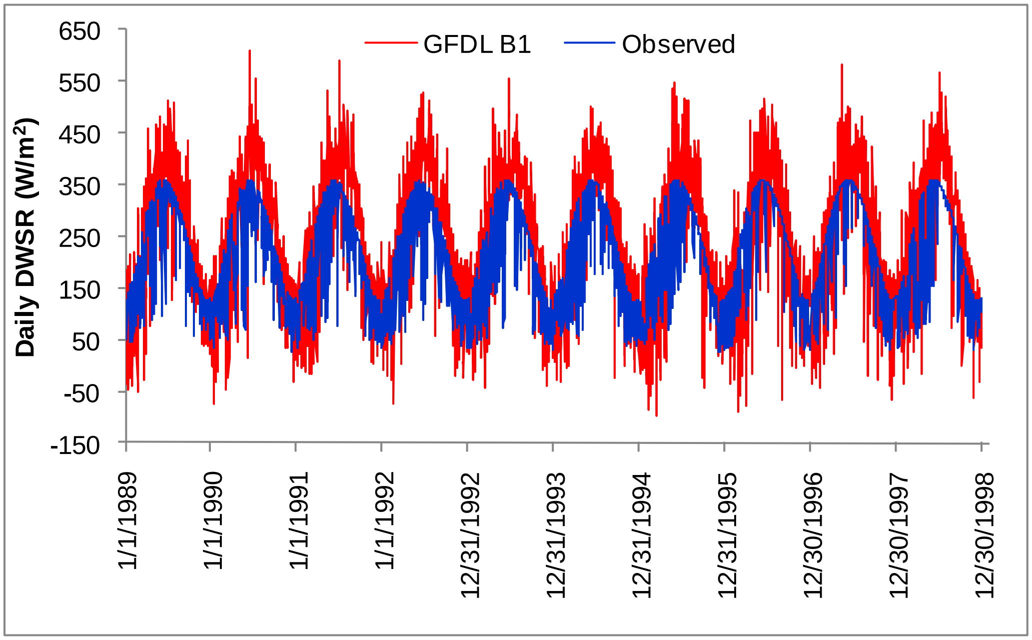

Figure 9-4. Comparison of daily downscaled downward shortwave radiation with observed records.

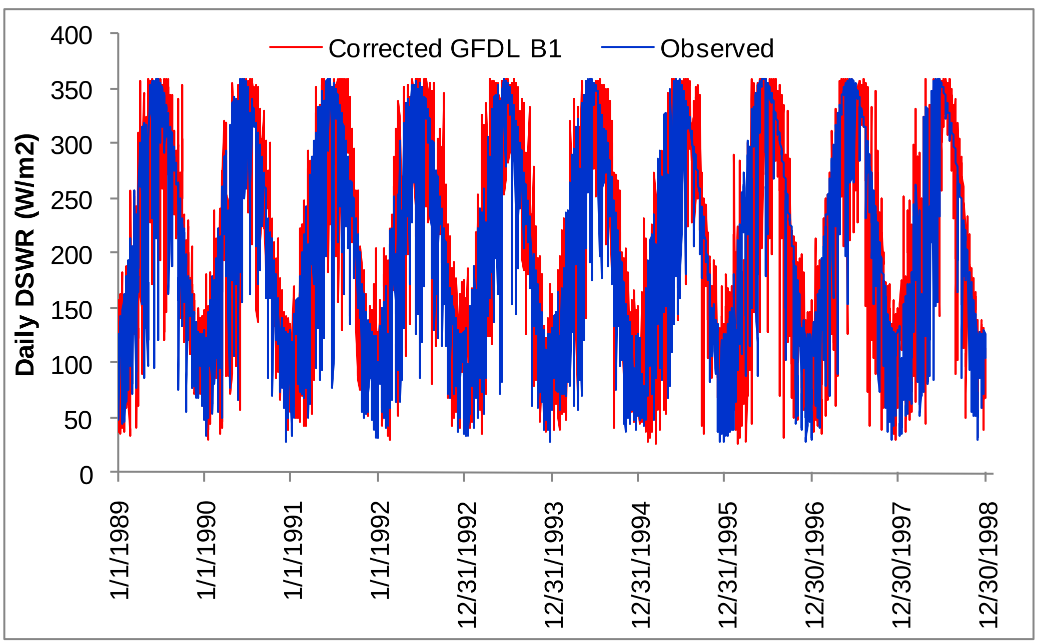

Figure 9-5. Bias-corrected GFDL B1 DWSR and observed records at SLTA.

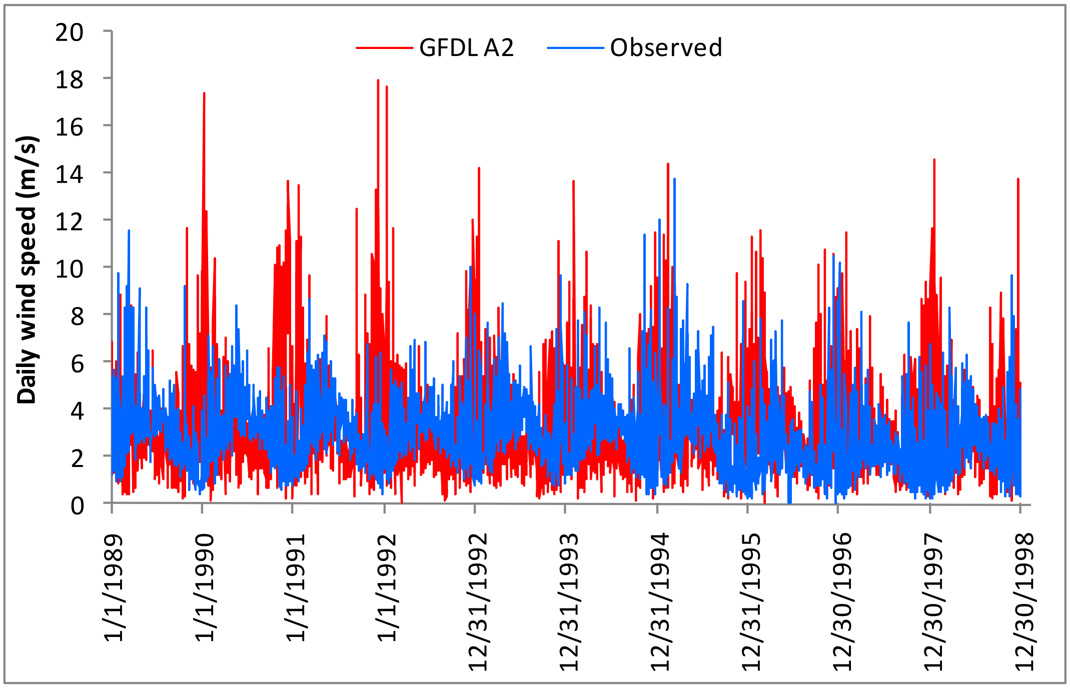

Figure 9-6. Comparison of daily downscaled wind speed with measured records.

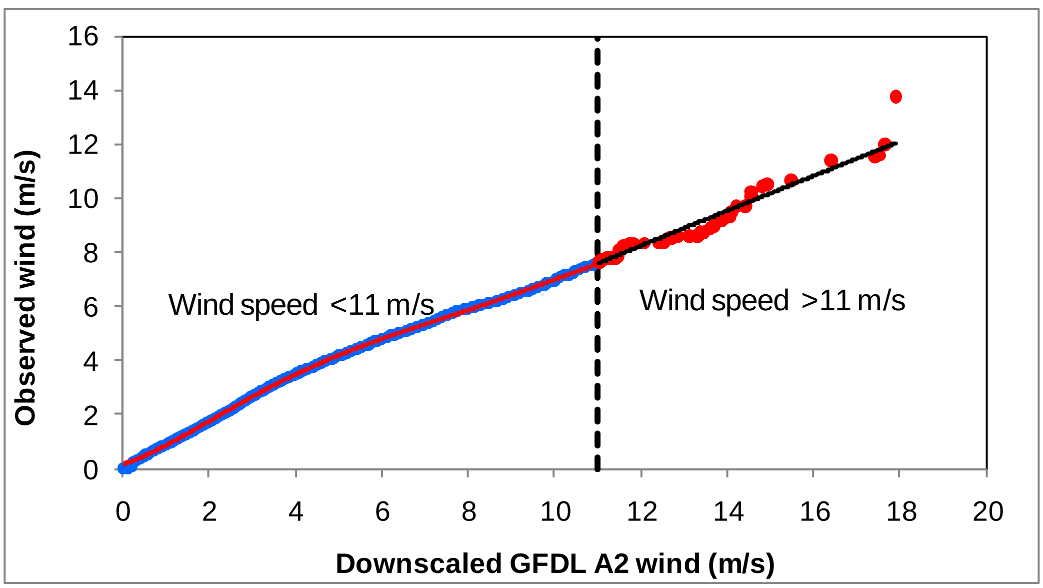

Figure 9-7. Non-linear relation between rank-ordered GFDL A2 wind speed and rank-ordered observed records. Solid lines represent 6th order polynomial trend line for wind speed less than 11 m/s and a power regression trend line for wind speed > 11 m/s. The regression coefficients are presented in Table 9-5.

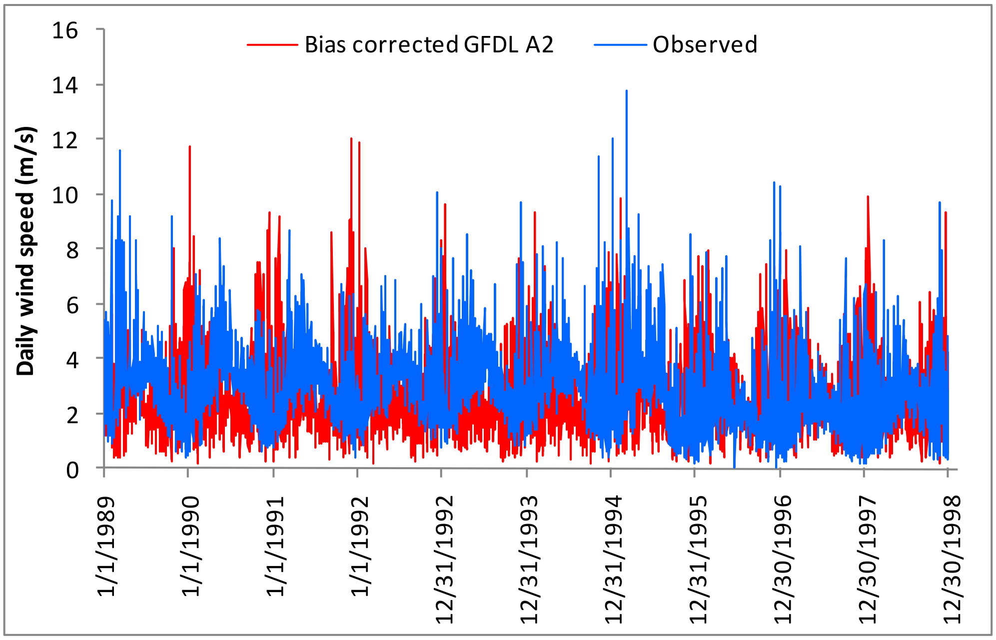

Figure 9-8. Bias-corrected GFDL A2 wind speed and observed records at SLTA.

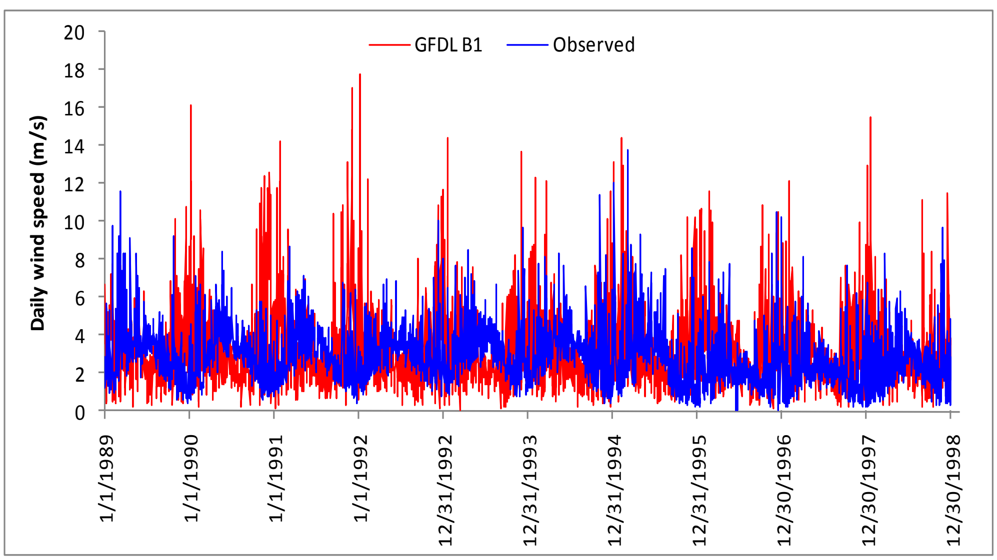

Figure 9-9. Comparison of daily downscaled wind speed with observed records.

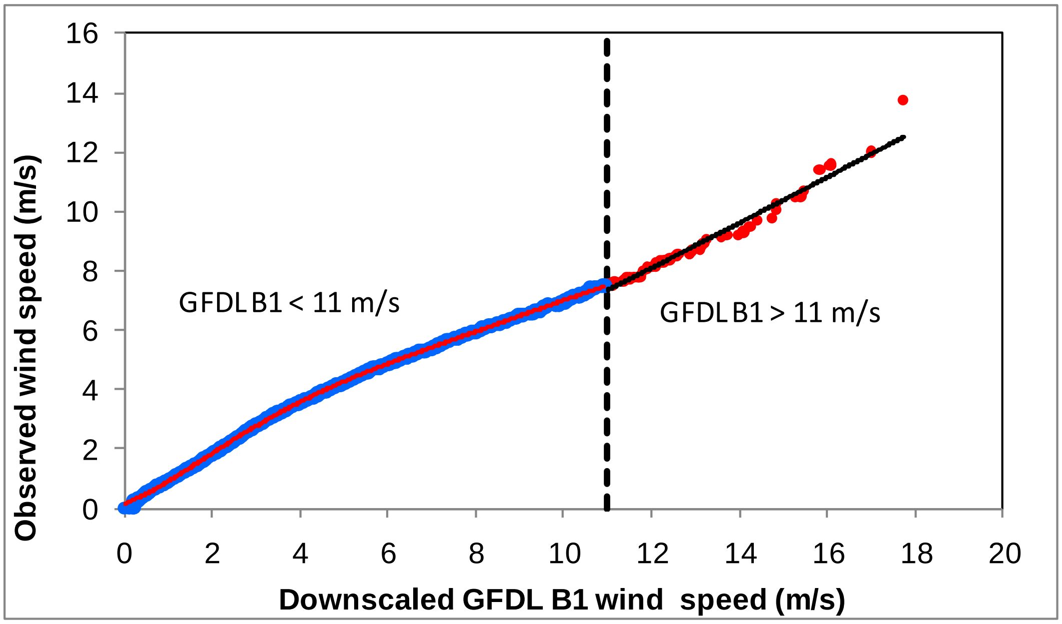

Figure 9-10. Non-linear relations between rank-ordered GFDL B1 wind speed and rank-ordered observed records. Solid lines represent 6th order polynomial trend line for wind speed less than 11 m/s and a power regression trend line for wind speed > 11 m/s. The regression coefficients are presented in Table 9.6.

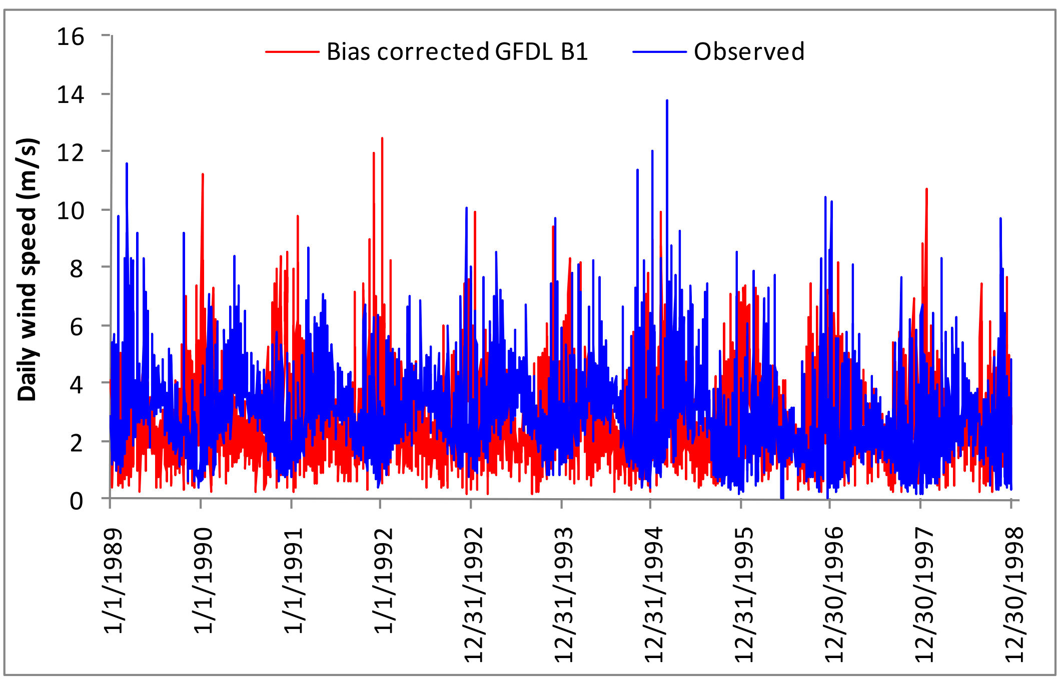

Figure 9-11. Bias-corrected GFDLB1 wind speed and observed records at SLTA.

APPENDIX 2 - Bias-correction of 7.5 arc minute resolution daily GCM precipitation, by quantile mapping to station observations in the vicinity of Lake Tahoe, California.

Author: Mariza Costa-Cabral Ph.D.

Bias-correction of 7.5 arc minute resolution daily GCM precipitation, by quantile mapping to station observations in the vicinity of Lake Tahoe, California.

Mariza Costa-Cabral
Hydrology Futures, LLC
cabral@hydrologyfutures.com
September, 2009

Table of Contents

Description of the contents of all output files produced by the Fortran program in the attachment.

Attachment (electronic file)

Fortran program implementing the bias correction for all stations. All input data files and all output data files are provided also, in Zip files. The output data files include the bias-corrected time series for every station and for the 2 GCMs and 2 emissions scenarios (the desired products from this work).

Objectives

The objective of this study is to downscale, using quantile-mapping, the daily time series of precipitation simulated by the global climate models GFDL and PCM for grid cells, to the point locations of observation stations. "Quantile mapping" refers to the empirical transformation of Panofsky and Brier (1968) in which each value from a distribution to be transformed is converted (or "mapped") into the value from the reference distribution which has the same cumulative frequency as the transformed value. The simulated time series entering this project had already been previously subjected to downscaling, from the coarser model grid, to the 1/8°-degree (7.5 arc minutes, circa 12 km) delivered as input to the project. This prior downscaling is described in Hidalgo *et al.* (2008).

GFDL simulations were provided for the period 1950-2100, with year 2000 missing. PCM simulations were provided for 1950-2099. Station observations are available for 1950-2006, but only 1950-1999 was considered as the "historical period", while 2000-2100 was designated the "future period".

Brief analysis of the original simulated datasets

The simulated precipitation time series entering this project are designated the "incoming" or "original" time series. Those produced in this project are designated the "final" time series. The incoming time series had been subjected to downscaling (from the models' coarse grid to a 1/8o resolution) prior to entering this project, using the method of constructed analogues and based on the historical climatology put together by Maurer *et al.* (2002). This is described in Hidalgo *et al.* (2008).

The incoming precipitation time series include simulations by two global climate models (GCMs): the Geophysical Fluid Dynamics Laboratory Model (GFDL2.1; *http://www.gfdl.noaa.gov/research/climate*) and the Parallel Climate Model (PCM, Barnett *et al.*, 2004; *http://www.cgf.ucar.edu/pcm*). For each model, and consistently with several recent climate change studies in California, two SRES greenhouse emission scenarios are included: A2 and B1.

In this project, quantile mapping was applied to the incoming time series, to produce, for each station location, final time series with the statistical properties characteristic of each station (and which, for the historical period, closely resemble those of the observed time series).

Figure 1 shows the relative locations of the precipitation observation stations and of the model grid cell centers. Figure 2 shows, for all 12 cells, the historical mean monthly precipitation, as simulated by the two downscaled GCMs and as recorded by the nearest precipitation station. The mean monthly values for the two GCMs are almost identical, hence the red plotted line (GFDL) is only rarely visible from behind the green plotted line (PCM). No doubt this reflects the downscaling procedure performed on the two simulated time series before entering this project. Agreement with station observations is fair presumably for similar reasons, although considerable deviations are seen in the wet season for cells 5, 9 and 21 (over-estimation by the models) and cells 15 and 16 (under-estimation by the models).

While the mean monthly precipitation values (Figure 2) gives a first impression of good agreement between model simulations and station observations, this agreement is illusory. This can be seen in Figure 3 where we compute the means for the event days only (i.e., the monthly totals are divided by the number of precipitation days in the month, rather than in Figure 2 where it was divided by the total number of days in the month). In Figure 3 we see that for every cell and for (nearly) every month, the model results under-estimate the mean daily precipitation amounts in days with precipitation. In the case of cell 15, the under-estimation exceeds a factor of 2 in some of the winter months.

Comparing Figures 2 and 3, one concludes that the downscaled model simulations must over-estimate the number of event days. Indeed this is the case, for every cell and every month, as shown in Figure 4. The large differences in Figure 3 between simulated and observed mean precipitation in event days immediately lead us to suspect that this is not a case of many spurious precipitation days representing so-called "model mist", as it does not seem that small precipitation values would add up to such large differences.

Indeed, when we plot the cumulative frequency of daily precipitation[1] for each month (Figure 5, for cell 4 used as an example), we confirm that whatever model mist might have been present has been removed during the downscaling processing of the incoming datasets (prior to entering this project). In fact, the distributions for summer months show a lack (rather than an excess) of low-precipitation days in the simulated time series, when compared to the observed distribution (possibly as a result of a mist-removal step). The distributions for winter months show nice agreement with the observed distributions, except for an approximately multiplicative factor (a shift to the left along the logarithmic-scale *x* axis).

It therefore appears (Figure 4) that the simulated and observed distributions of daily precipitation for a given month are mostly similar in shape in the case of the winter months when most of the precipitation falls (although significant shape differences are found in the drier months), but that the models over-sample from this distribution. The models have an excess of event days of all magnitudes, i.e., a probability of precipitation (POP) in any given day that is too high.

In this report, most of the plots refer to the example of Echo Peak station and its closest model grid cell, cell 4. Similar plots and analyses can be carried out for all other stations using the results produced by the Fortran program in attachment. Temporal trends in precipitation in the incoming time series were tested for each month for cell 4, using the Mann-Kendall test. Neither of the two historical (1950-1999) simulated precipitation time series has any statistically-significant trend. The PCM projections had just one statistically-significant trend, namely a declining trend for the month of February under scenario B1

---

[1] If we assume that, for each given month, daily precipitation values in the historical period (1950-1999) are drawn from a stationary distribution, it follows that the cumulative frequency plotted in Figure 2 represents a sample approximation of the probability of non-exceedance for that distribution. Hence, it represents an *empirical* cumulative distribution function, denoted eCDF.

(estimated Sen's slope of -0.855 mm/a, α=0.05). The GFDL projections for both scenarios A2 and B1 had a few statistically-significant declining trends. For GFDL A2, a declining trend for April (-0.32 mm/a, α=0.05), and high-confidence declining trends for May (-0.307 mm/a, α=0.01) and October (-0.472 mm/a, α=0.01). For GFDL B1, a declining trend for December (-0.871 mm/a, α=0.05) and a highly-significant declining trend for January (-1.119 mm/a, α=0.01).

Bias-correction methodology

The methodology used was developed by Hydrology Futures, LLC, for the purposes of this project, and represents a modification of the original quantile-mapping method of Wood *et al.* (2002) and Wood *et al.* (2004). The steps involved in the methodology of Wood *et al.* are described in http://gdo-dcp.ucllnl.org/downscaled_cmip3_projections/#About (press the tab "Methodology"). The reasons for the modifications, and the nature of the modifications, are summarized below.

The present downscaling effort must achieve a reduction of event days, but not by eliminating the lowest-precipitation days. Not only is there no "model mist" to be removed (see the previous section), but also we would have to eliminate days with precipitation totals up to more than 3 mm/day in winter months in order to achieve the desired reduction in number of events. We are led to conclude that the sensible way of reducing the number of event days in this case is to randomly select the precipitation events to be removed, among all events in a month, regardless of event length or precipitation total. This is equivalent to resampling the events from what are essentially correct simulated distributions.

Once the simulated historical time series has been resampled so as to have the same number of events as the observed time series (see Figure 6), these two distributions then contain precipitation values with the exact same cumulative frequency. Resampling of the future simulated time series is performed under the assumption that each model produces, for any given month, a consistent proportion of excess number of precipitation days, regardless of a climate warming trend. Thus, the same percentage of precipitation days is removed for the 100 months of September (e.g.) in a future simulated time series, as the percentage removed for the 50 months of September in the historical time period for the same model. (September was cited as an example. The same applies to all 12 months.)

Computation of the plotting position[2] of a precipitation value is a function of its rank among all values, and of the total number of values (which, after correction, is the same in both distributions). "Quantile mapping" consists in replacing the values in a simulated time series with the observed values that have the same plotting position. Thus, for a given model (GFDL or PCM), the observed distribution and the model's historical distribution (resampled so as to have the same number of event days as the observed distribution) forms a pair that represents something akin to a dictionary from which we can translate values simulated by that model into values in agreement with observation. This dictionary can be used to translate

[2] Plotting positions are sampled approximations of non-exceedance probabilities, which they approach for large sample sizes.

simulated values for future time periods as well as historical periods. When translating future simulations, it is not the simulated future distribution that is used to form the dictionary. We again use the simulated historical distribution and the observed distribution as our dictionary (or lookup table). See Figures 7 and 8.

Plotting positions are calculated in this study using the Cunnane formula, which offers advantages over the Weibull plotting positions when computing exceedance probabilities (see Cunnane, 1978). Cunnane plotting positions are used widely in water resources statistics applications, and we used the parameters recommended by Helsel and Hirsch (2002):

$$F(x) = (i-0.4) / (N_p+0.2)$$

Where $F(x)$ is the sampled cumulative frequency (plotting position), i is the rank of each given daily precipitation value, and N_p is the number of precipitation days in the month in question.

The method used in this study has the following 3 steps:

1. For the simulated historical time series, randomly select precipitation events for removal, so as to achieve, for each of the 12 months, the same number of event days as in the observed time series. Following the suggestion by Goloka Behari Sahoo and John Reuter (team members of the Lake Tahoe project), we randomly selected and eliminated precipitation events, regardless of event length or magnitude. In the case of the future simulated time series, we randomly select precipitation events for removal so that the percentage of event days removed, for each of the 12 months, is the same as for the historical period.

2. Each value x (precipitation amount) in each simulated historical distribution (GFDL and PCM) is replaced by the observed value x' (observed in the same month as x) having the same plotting position as x.

3. This step uses GFDL as an example. A similar step is performed for PCM. For each value y in a GFDL simulated future time series we check whether an identical value $x=y$ exists in the GFDL simulated historical time series corresponding to that same month. If x exists, then the value y is replaced by the observed value x' having the same plotting position as x. If x does not exist (which is most often the case), there are 3 possible cases:

   a) The most common case is when y falls within the range of the GFDL historical distribution for that month. In this case, the two closest values, x_1 (slightly lower than y, at a positive distance d_1 from y) and x_2 (slightly higher than y, at a positive distance d_2 from y) are identified. The observed values x_1' and x_2' having the same plotting positions as x_1 and x_2 are identified. Value y in the GFDL future distribution is replaced by an inverse-distance weighted average value $\alpha x_1'+(1-\alpha)x_2'$ where $\alpha=d_2/(d_1+d_2)<1$.

b) In the case where *y* is larger than any value in the GFDL historical time series of that month, we use a fitted theoretical distribution to extend the range of the GFDL simulated historical distribution beyond its higher end. We use another fitted theoretical distribution to extend the range of the observed distribution for that month. We experimented with several theoretical distributions (an example is shown in Figure 9), and found that the Weibull, Generalized Pareto and Exponential distributions provided the best fit. Given its computational simplicity, the Exponential distribution was chosen. See also figures 10 and 11. The Exponential distribution's expression is used to calculate the cumulative frequency *F(x)* of precipitation value *y* in the GFDL simulated historical distribution. A similar expression, fitted to the observed distribution is then used to calculate the precipitation value *x'* corresponding to *F(x)*. Value *y* is replaced with *x'* in the GFDL future simulation time series. Given the Exponential distribution's general expression $F(x) = 1-\exp\{(\mu_x-\sigma_x-x)/\sigma_x\}$, it is fairly simple to show that the value *x'* that replaces *y* by quantile mapping is given by: $x'=\mu_{obs}-\sigma_{obs}*(1+(\mu_{hist}-\sigma_{hist}-y)/\sigma_{hist})$.

c) If *y* is smaller than any value in the GFDL historical distribution, we use a simple linear scaling, replacing *y* with a value $x'=y * \mu_{obs}/\mu$, where μ_{obs} is the mean of the observed values and μ is the mean of the future simulated values for the given month. Instead, a theoretical distribution (such as the Weibull distribution used by Wood *et al*., 2002) could have been used. However, given that precipitation totals at the lowest extreme (close to zero) are of minimal importance in this study, the additional effort was considered unjustified for this application.

The following is a summary of differences and similarities between the above-described methodology developed for this study and that of Wood *et al.* (2002) and Wood *et al.* (2004); and also described in http://gdo-dcp.ucllnl.org/downscaled_cmip3_projections/#About (press the "Methodology" tab).

1. The method of Wood *et al.* uses quantile mapping at the monthly time scale (attending to that daily time series are most often not available, or not considered to be realistic), while the present method uses quantile mapping at the daily time scale. As we will see, we found that mapping at the daily time scale resulted in monthly distributions in good agreement with observations for the winter months (i.e., the main precipitation months), and in annual distributions in remarkably good agreement with observations.

2. The method of Wood *et al.* achieved agreement between the number of historical simulated and observed precipitation days in each of the 12 months by removing the event days with the lowest daily totals. This is appropriate when the model has generated an excess of "mist" days. Examination of the simulated precipitation time series in this project (see previous section) revealed that there is no excess of spurious, model-generated "mist" days (event days with low daily totals). There is, however, a consistent excess of precipitation days of all magnitudes in every month of the year. Upon suggestion from Goloka Behari Sahoo and John Reuter (team members of the larger Lake Tahoe project), we randomly selected and eliminated precipitation events, regardless of event length or magnitude. Elimination of randomly selected events was performed until the number of precipitation days in each month matched the observed one. E.g., in the final resampled simulated time series, the total number of precipitation days in all historical-period October (e.g.) months pooled together (50 October months) will equal the total number of precipitation days in all 50 observed October months.

3. Similarly to Wood *et al.* (2002), a theoretical distribution is fitted to the upper (high-value) end of the historical eCDF for each month. This is done for the observed eCDF and the historical eCDF simulated by each model. This ensures that, should values higher than the historical (observed or simulated) be projected by the future simulations, they too can undergo quantile mapping. Wood *et al.* used a Gumbel distribution. Sampled datasets from the present study were better fitted by the Exponential, Weibull or Generalized Pareto distributions, and we used the Exponential distribution for its simplicity.

4. Wood *et al.* (2002) used the Weibull distribution to extend the historical (observed and simulated) distributions to values below the minimum (observed or simulated). Given that precipitation totals at the lowest extreme (close to zero) are of minimal importance in this study, the additional effort of fitting a distribution to extend the distributions at their lower end was considered unjustified for this application, and a simple scaling was used (see above).

5. We used Cunnane plotting positions (see above) rather than Weibull plotting positions.

Example Results

Again, most of the results plotted use the case of station Echo Peak, and its closest cell, cell 4. GFDL A2 is the most commonly plotted case. These are used as examples. Similar plots can be created for any of the stations, cells, models and scenarios.
Some of the results, plotted as examples, are shown in Figures 13-21. Figures 13, 14 and 15 show examples of simulated daily precipitation distributions at their 3 stages: A) As they entered the project (top panels in Figures 13-15), B) After resampling (center panels), and C) As they leave the project, i.e., after resampling and quantile mapping (bottom panels). The future period is represented by three 30-year subperiods: 2011-2040, 2041-2070, and 2071-2100. Figure 16 shows details, for example months, of the effect of resampling on the positioning of the eCDFs. The original and final time series are plotted, aggregated to the monthly time scale, in Figure 17.

Figure 18 shows the distribution of event lengths, for Echo Peak and its closest cell, cell 4, plotted as an example. The distribution in the original simulated precipitation time series (red line) is maintained after downscaling (light blue line). This is explained by that the resampling procedure gives equal likelihood to removing excess simulated events of all lengths. Given that the frequency distribution of event length in the original historical simulations (by both GFDL and PCM) is relatively close to the observed distribution, it follows that it is a favorable feature of the event-based resampling that it retains this distribution.

Figure 19 shows the frequency distribution of annual precipitation totals. We see that for both GFDL and PCM, the downscaled simulated distribution agrees remarkably well with observations. This good agreement is not forced by construct, and is a welcomed result. Figure 20 shows the frequency distribution of monthly precipitation totals. Agreement with observations is good in all of the wet months, though less good in drier months – especially April, May, June and September – which are of lesser import to this study. Again, this good agreement is not forced by construct. Had the annual or monthly agreement with observations been poor, it would have been necessary to consider quantile-mapping at higher scales of aggregation. The good agreement at monthly and annual scales obtained by daily-scale quantile-mapping was a welcomed result that simplified the project's effort.

The distribution of annual maxima (Figure 21) is well represented in the downscaled time series for the annual 1-day maxima, but under-represents the highest values of 3-day annual maxima (for both GFDL and PCM). This is tentatively attributed to a lower degree of temporal correlation in the simulated time series during heavy storms, as compared to observations.

A final remark regarding linear trends, which were tested for each month for cell 4 using the Mann-Kendall test for trends. The downscaling procedure described here preserved quite well, for cell 4, the highly-significant linear trends detected in the incoming time series. For GFDL A2, the highly significant trend for May (estimated Sen's slope -0.307 mm/a, α=0.01

for the incoming time series) resulted in a similar trend with even higher significance in the final time series (-0.319 mm/a, α = 0.001); and for October, the incoming trend (-0.472 mm/a, α=0.01) was somewhat accentuated in the final time series (-0.769 mm/a, α=0.01). For GFDL B1, the incoming January trend (-1.119 mm/a, α=0.01) was slightly lowered in the final time series (-0.905), where it did not show statistical significance for α=0.1.

Many additional plots can be prepared using the various files outputted by the program *downscale_Tahoe_event_based.f*. The contents of each of those files is described in the Appendix (at the end below).

Literature References

Cunnane, C. (1978): Unbiased plotting positions – a review. *J. Hydrology* **37** (3-4): 205-222. doi: 10.1016/0022-1694(78)90017-3.

Helsel, D.R., and R.M. Hirsch (2002): Statistical Methods in Water Resources. Chapter 3 in *Hydrologic Analysis and Interpretation*. U.S. Geological Survey. Publication available at: http://water.usgs.gov/pubs/twri/twri4a3

Hidalgo, H.G., M.D. Dettinger, and D.R. Cayan (2008): Downscaling with constructed analogues: Daily precipitation and temperature fields over the United States. Pier Final Project Report, California Energy Commission (CEC) report no. CEC-500-2008-123. Publication available at: http://www.energy.ca.gov/2007publications/CEC-500-2007-123/CEC-500-2007-123.PDF

Maurer. E.P., A.W. Wood, J.C. Adam, D.P. Lettenmaier, and B. Nijssen (2002): A long-term hydrologically based data set of land surface fluxes and states for the conterminous United States. *J. Climate* **15**: 3237-3251.

Panofsky, H.A., and G.W. Brier (1968): Some applications of statistics to meteorology. The Pennsylvania State University, University Park. 224 p.

Wood, A.W., E.P. Maurer, Arun Kumar, and D.P. Lettenmaier (2002): Long-range experimental hydrologic forecasting for the eastern United States. *J. Geophysical Research* **107** (D20), 4429, doi: 10.1029/2001JD000659.

Wood, A.E., R.L. Leung, V. Sridhar, and D.P. Lettenmaier (2004): Hydrologic implications of dynamical and statistical approaches to downscaling climate model outputs. *Climatic Change* **62**: 189-216.

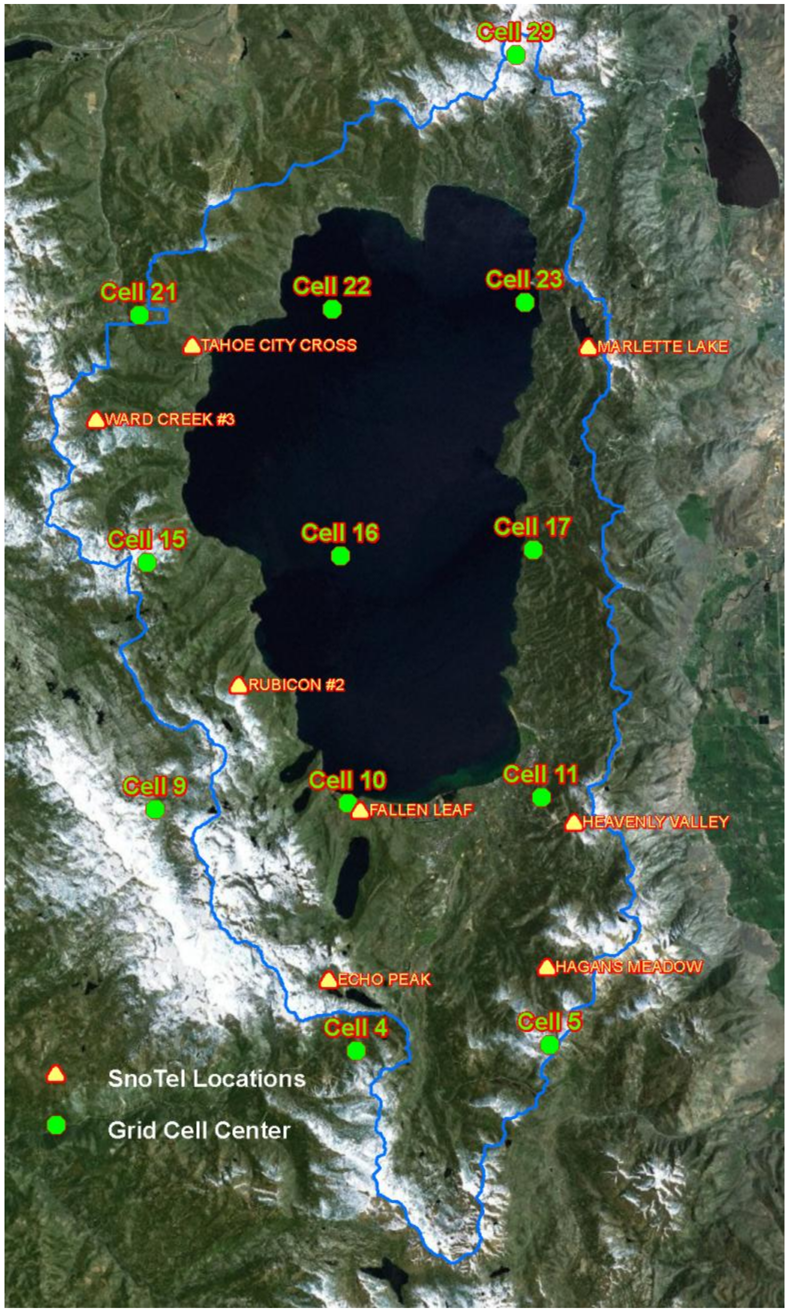

Figure 1: Relative location of the SnoTel precipitation observation stations (orange triangles) and of the model grid cell centers (green circles). Figure prepared by Brent Wolfe (Northwest Hydraulic Consultants, Inc).

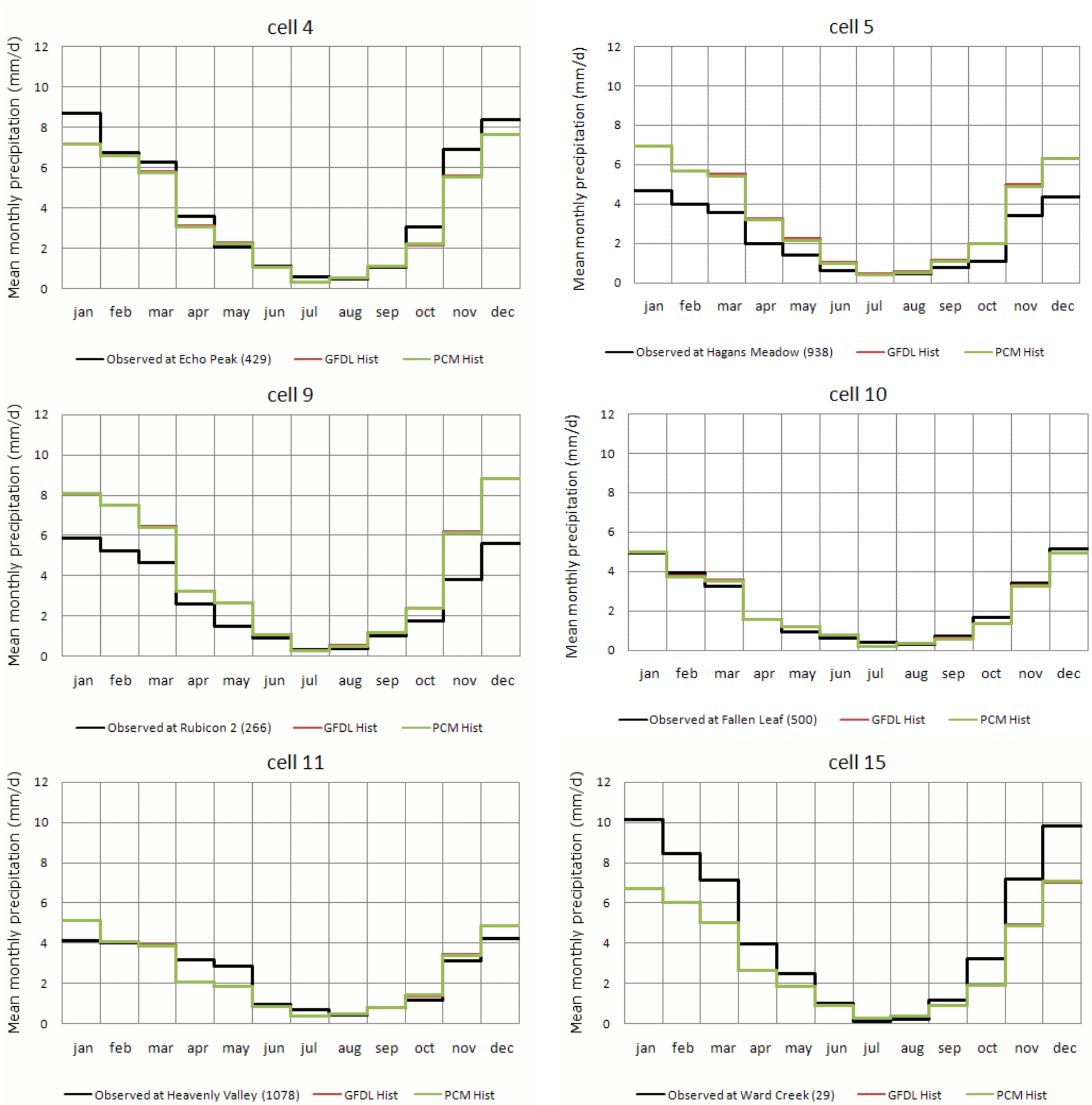

Figure 2: Historical (1950-1999) mean monthly precipitation simulated at each cell by PCM (green) GFDL (red – rarely visible behind the green lines), and observed values at the closest recording station (black). For example, for January, values are computed by taking the total precipitation observed in all January days in the historical period (i.e., the sum of the 50 January totals) and dividing it by the total number of January days (31x50=1550 days). Values for GFDL and PCM and very similar, reflecting the previous processing of the original data (as described in Hidalgo *et al.*, 2008). Agreement with station observations is very good, presumably for similar reasons. *(Figure continues.)*

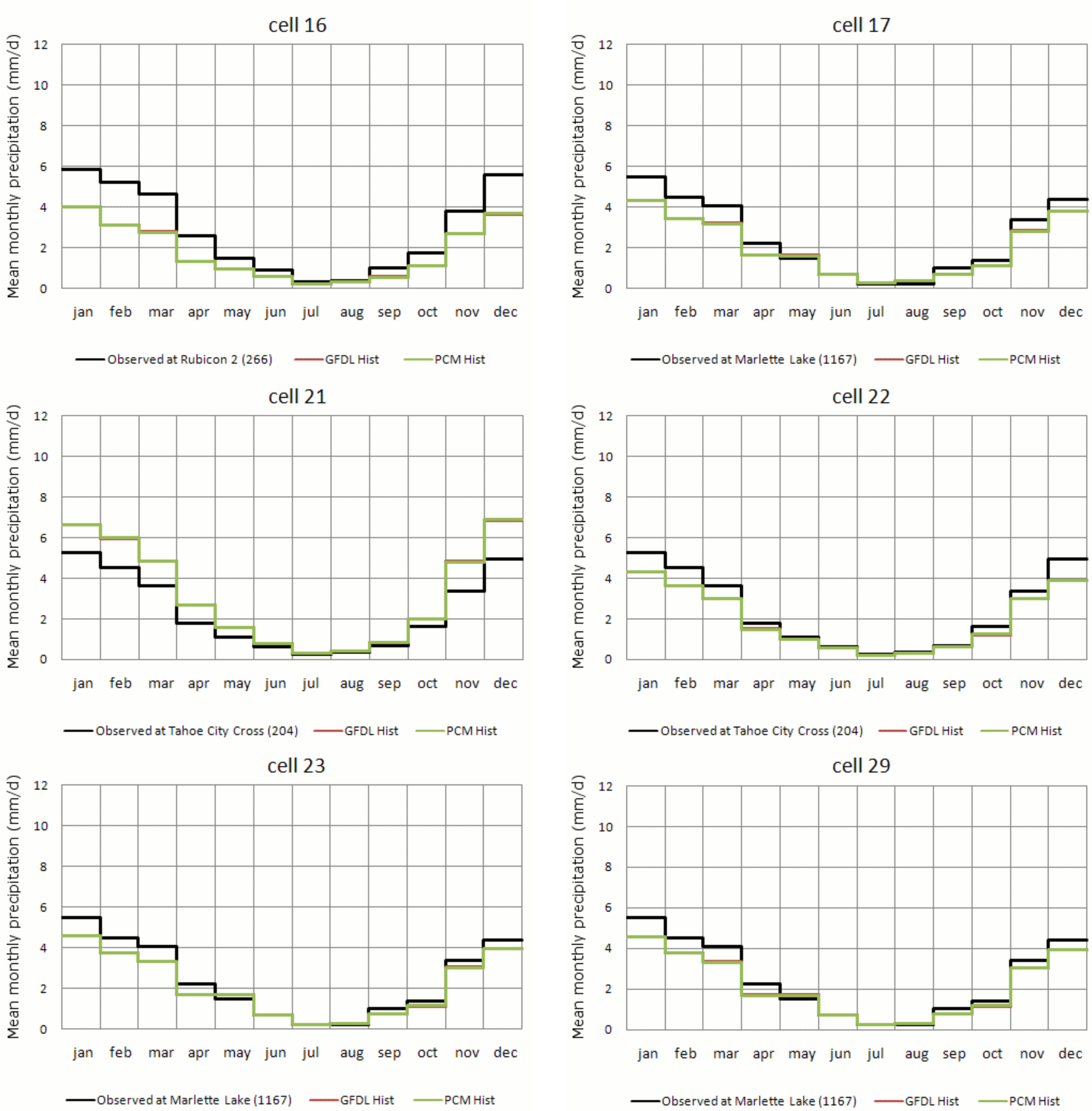

Figure 2, continued.

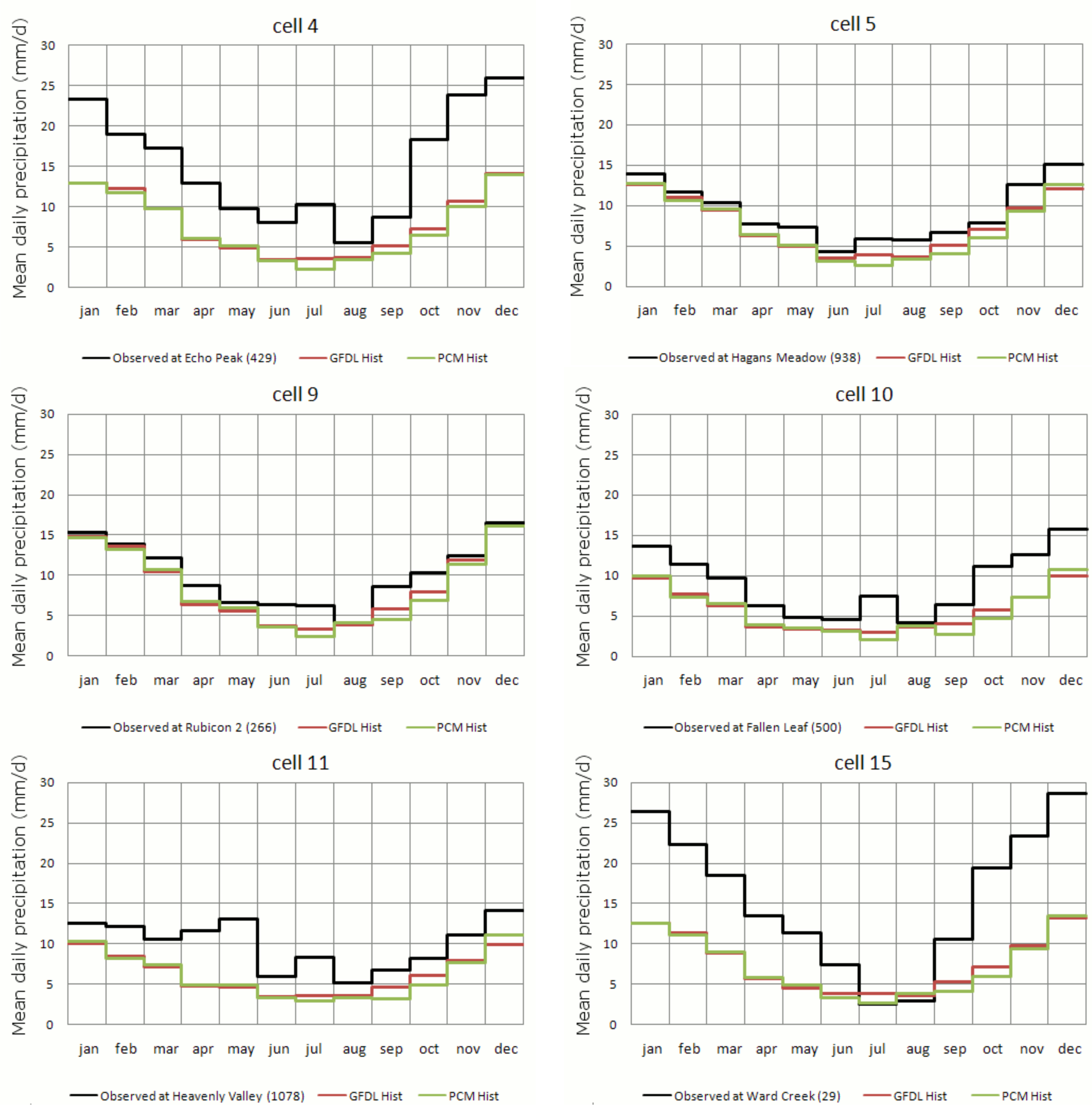

Figure 3: Historical (1950-1999) monthly mean daily precipitation in event days (i.e., in days with precipitation) simulated at each cell by GFDL (red) and PCM (green), and observed values at the closest recording station (black). For example, for January, values are computed by taking the total precipitation observed in all January days in the historical period (i.e., the sum of the 50 January totals) and dividing it by the number of precipitation January days in the 50-year period. *(Figure continues.)*

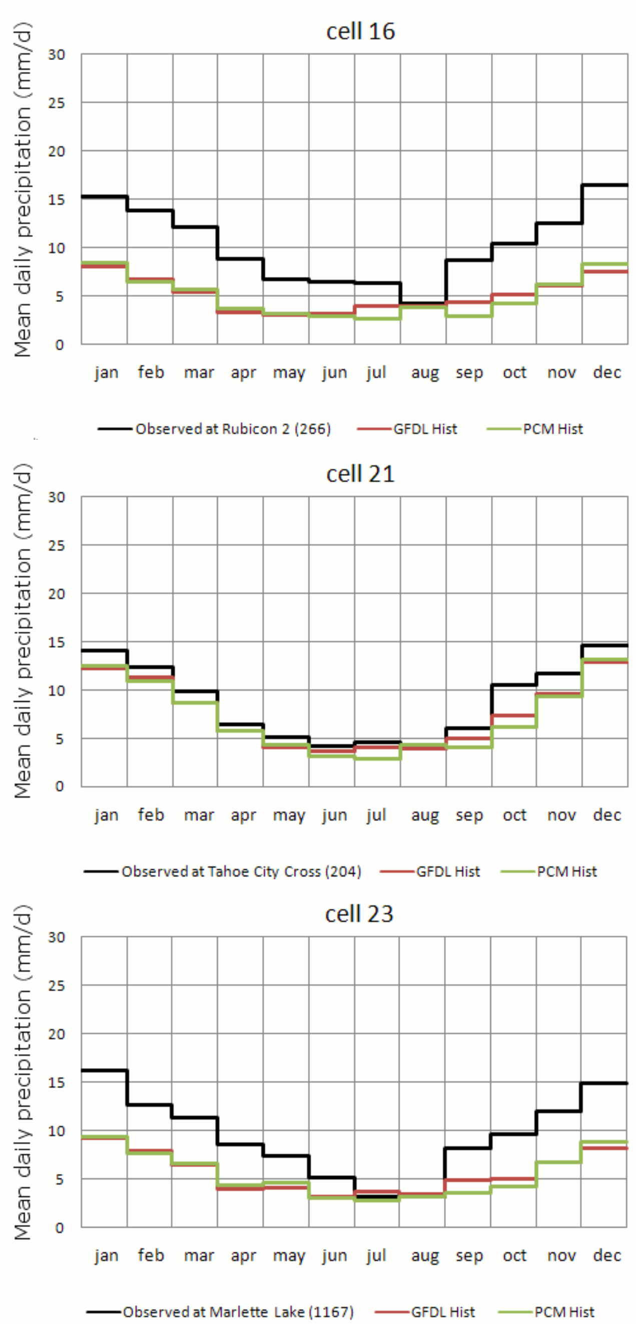

Figure 3, continued.

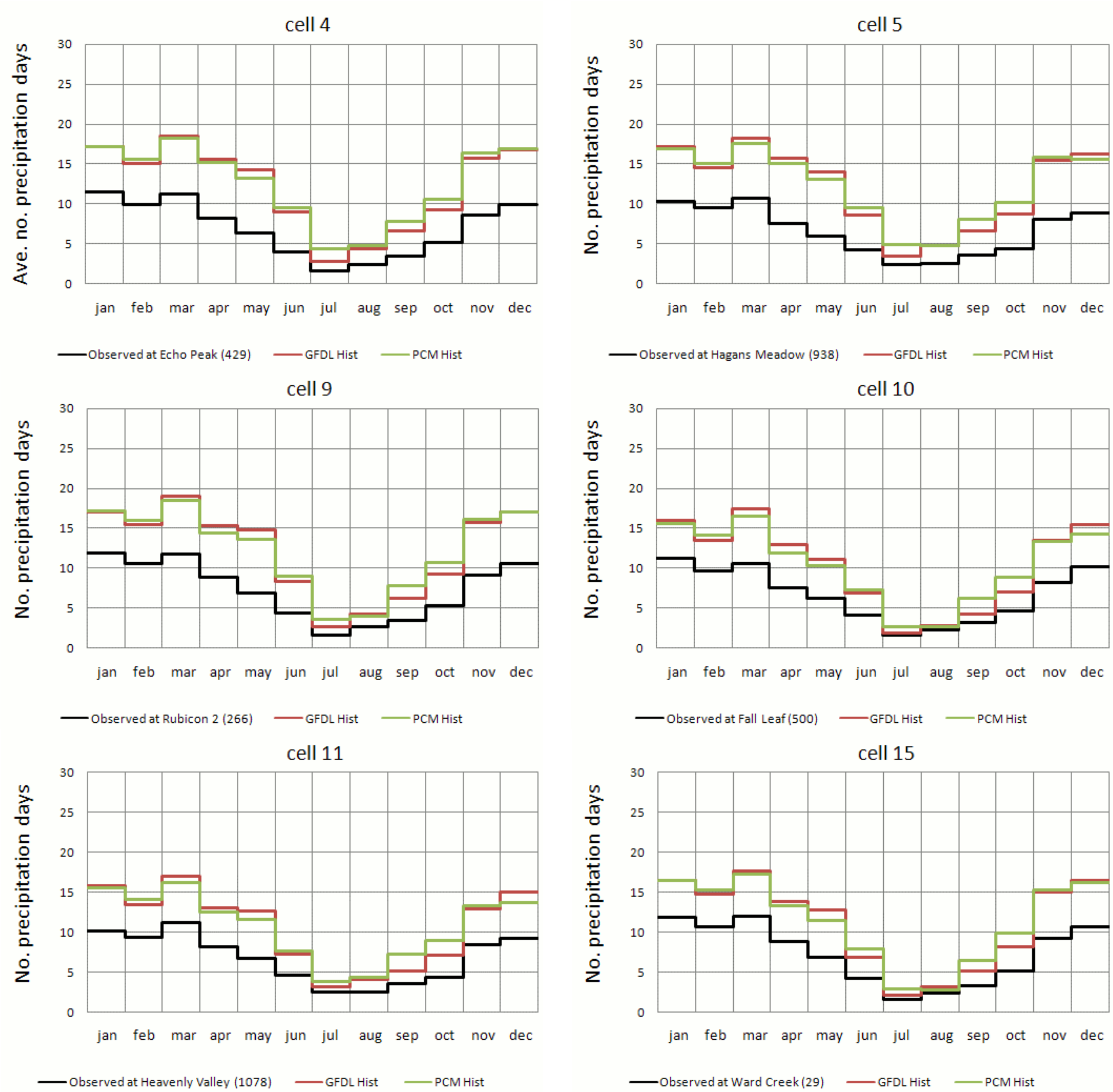

Figure 4: Historical (1950-1999) average number of precipitation days in each month of the year simulated at each cell by GFDL (red) and PCM (green), and observed values at the closest recording station (black). For example, for January, values are computed by taking the total number of precipitation days in all 50 months of January, and dividing it by the total number of January days (i.e., dividing it by 31x50=1550 days). *(Figure continues.)*

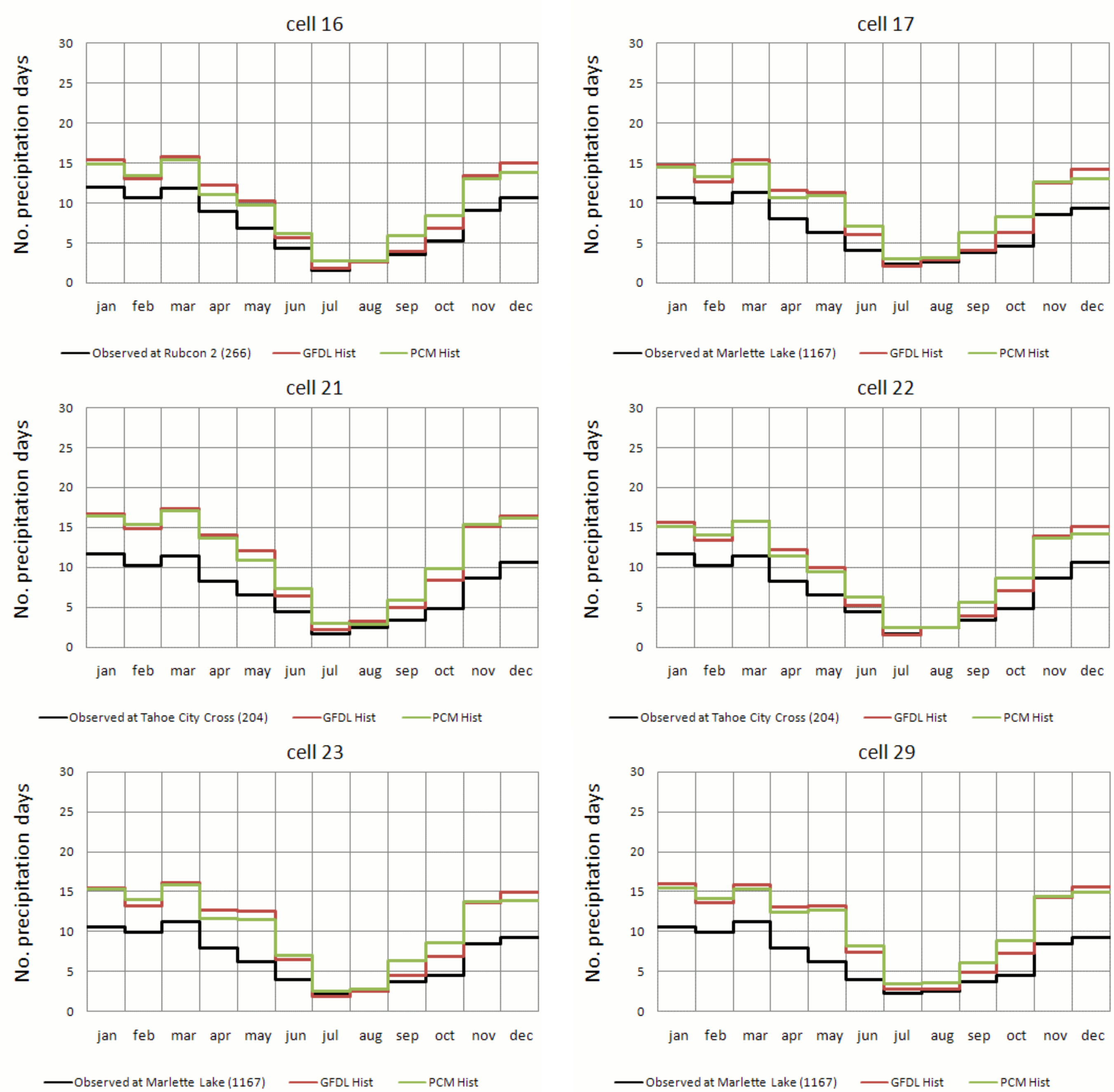

Figure 4, continued

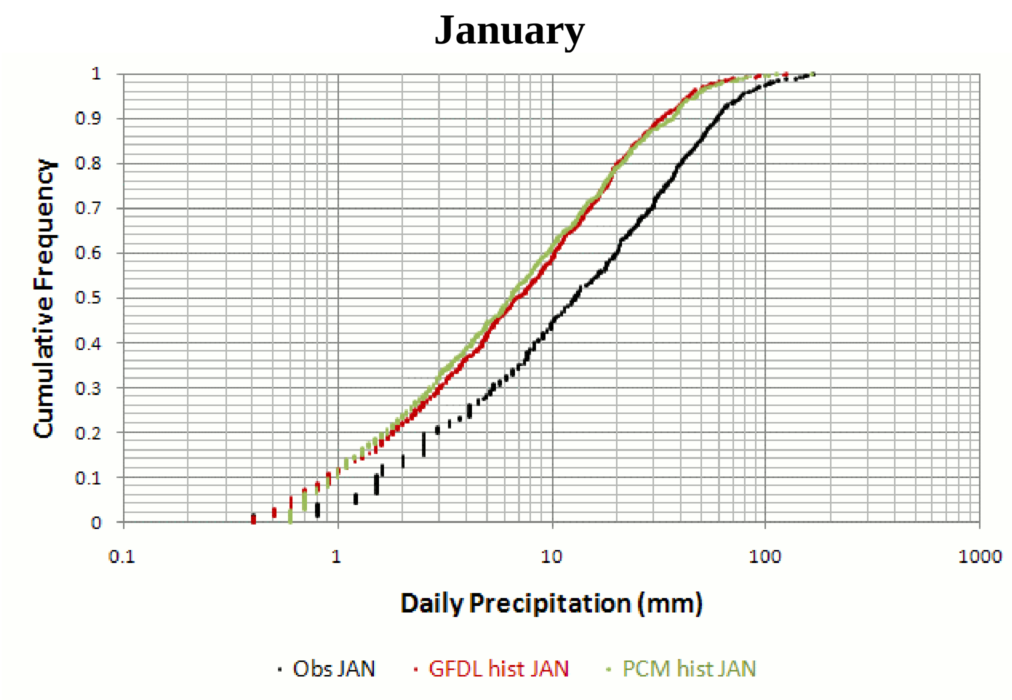

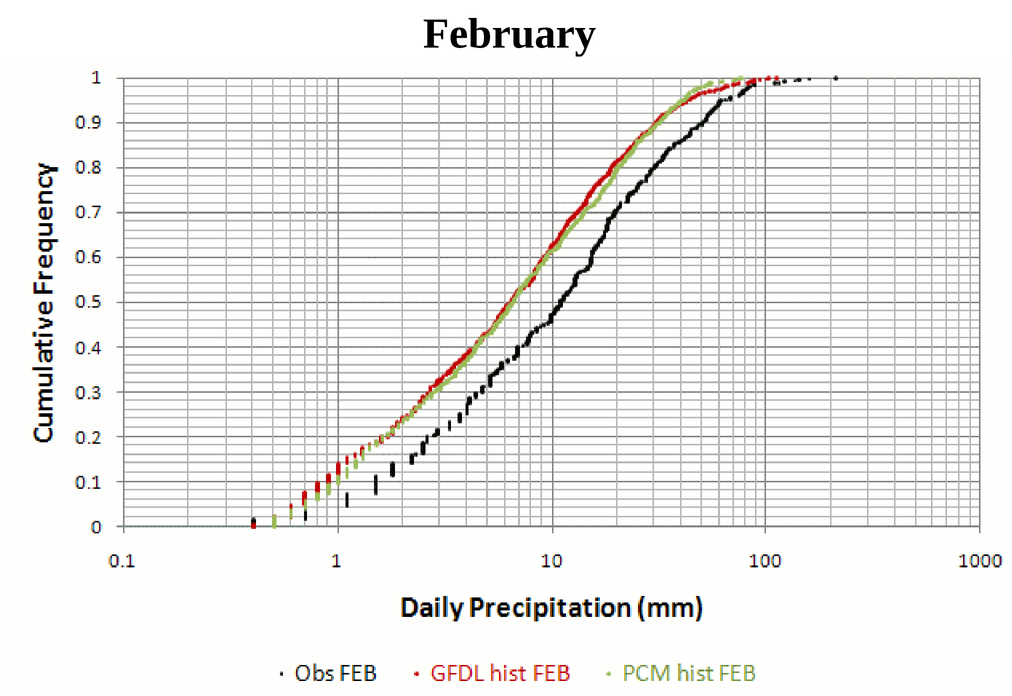

Figure 5: Monthly distributions of daily precipitation in the historical period (1950-1999) for cell#4 (shown as an example), for the observed time series (black), the GFDL simulations (red), and the PCM simulations (green). *(Figure continues.)*

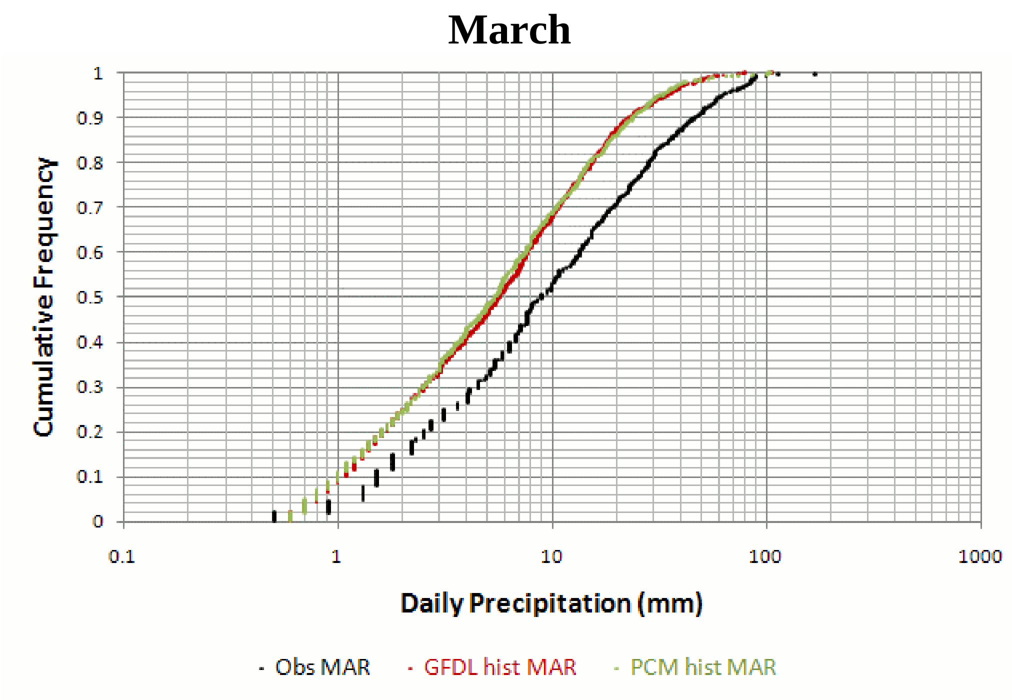

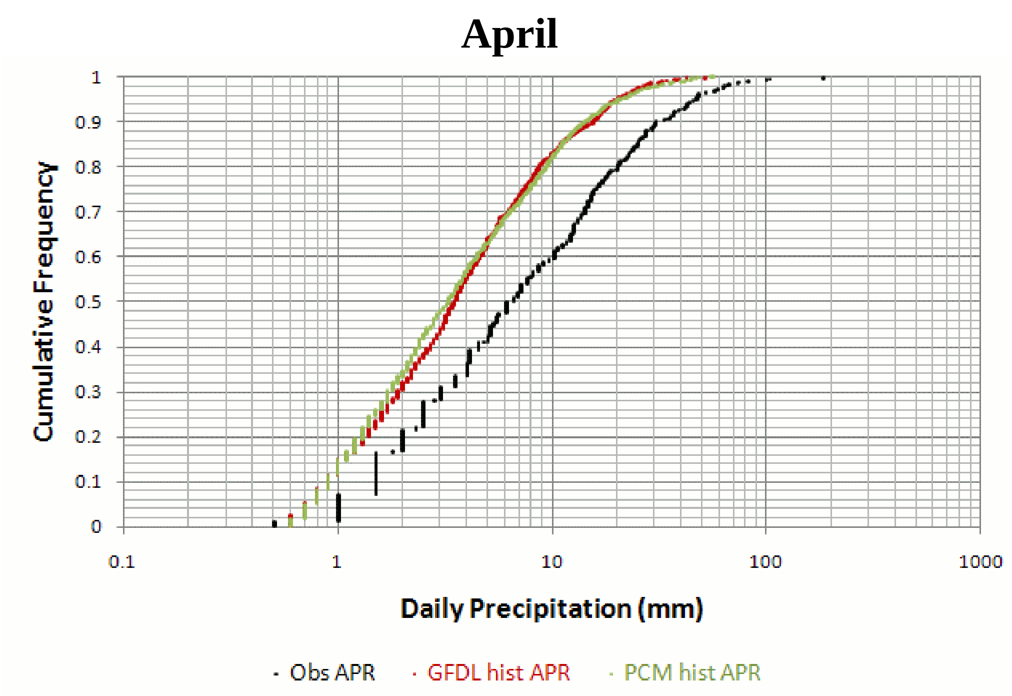

Figure 5, continued.

May

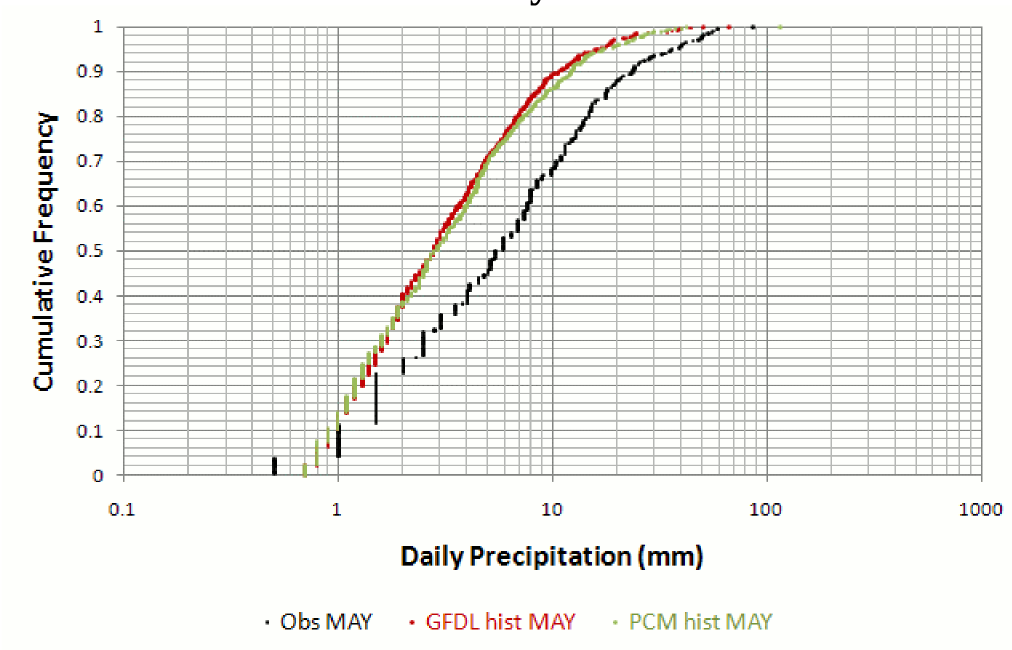

June

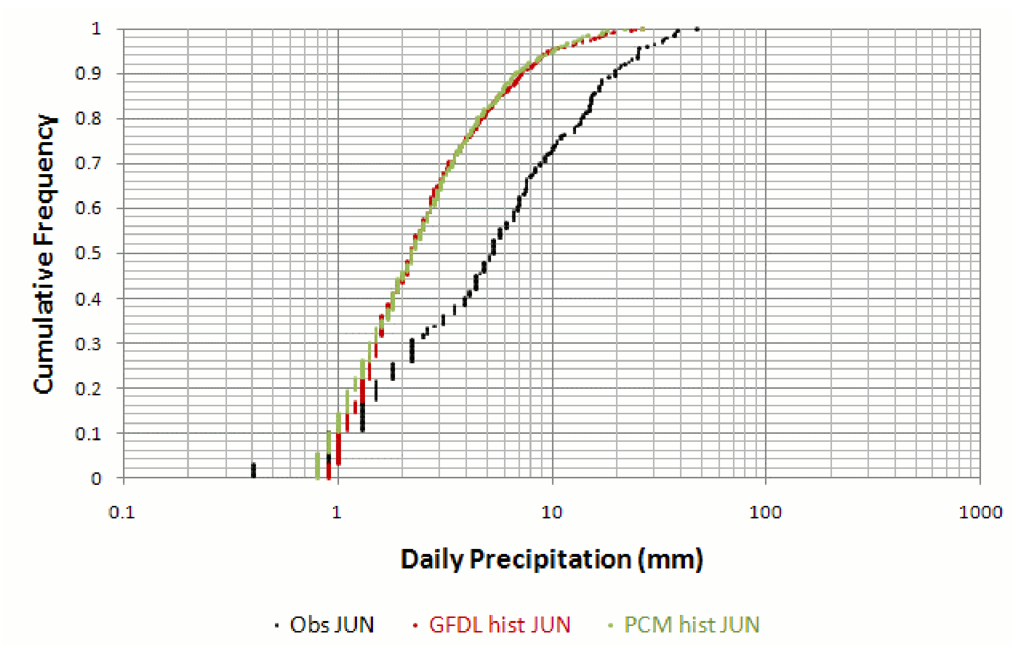

Figure 5, continued.

July

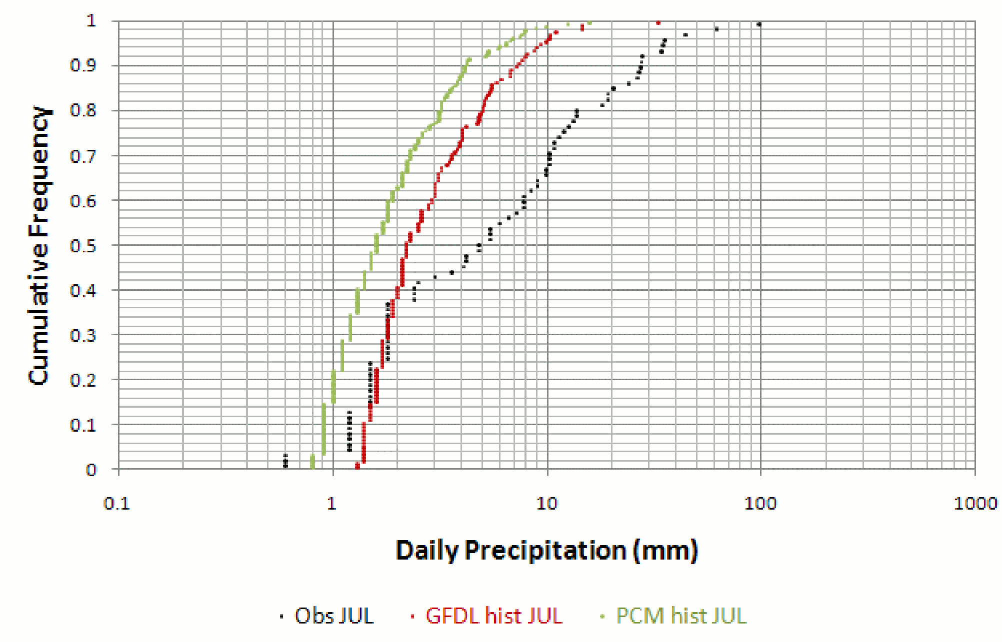

August

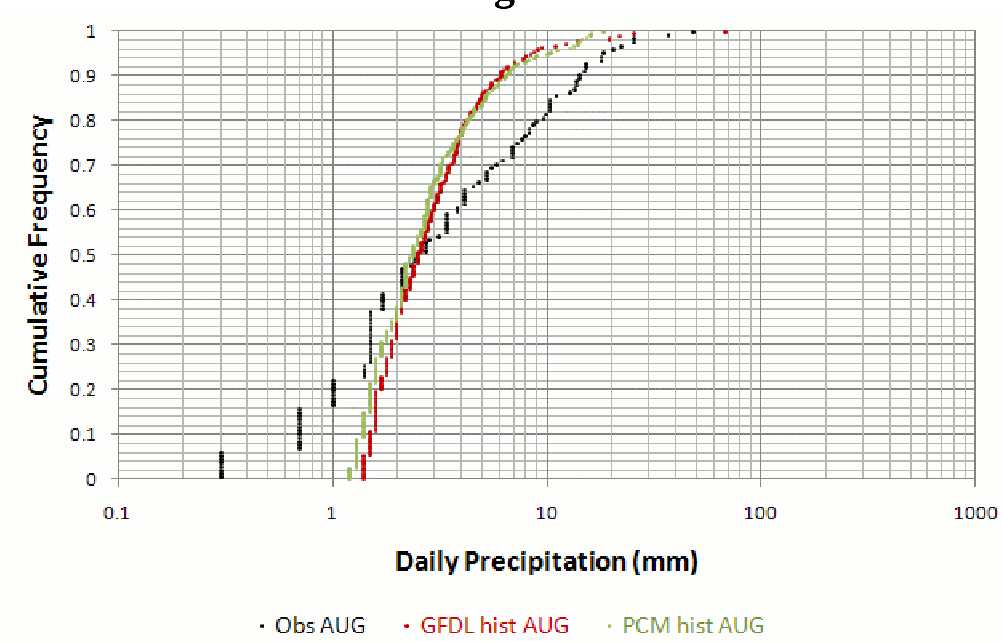

Figure 5, continued.

September

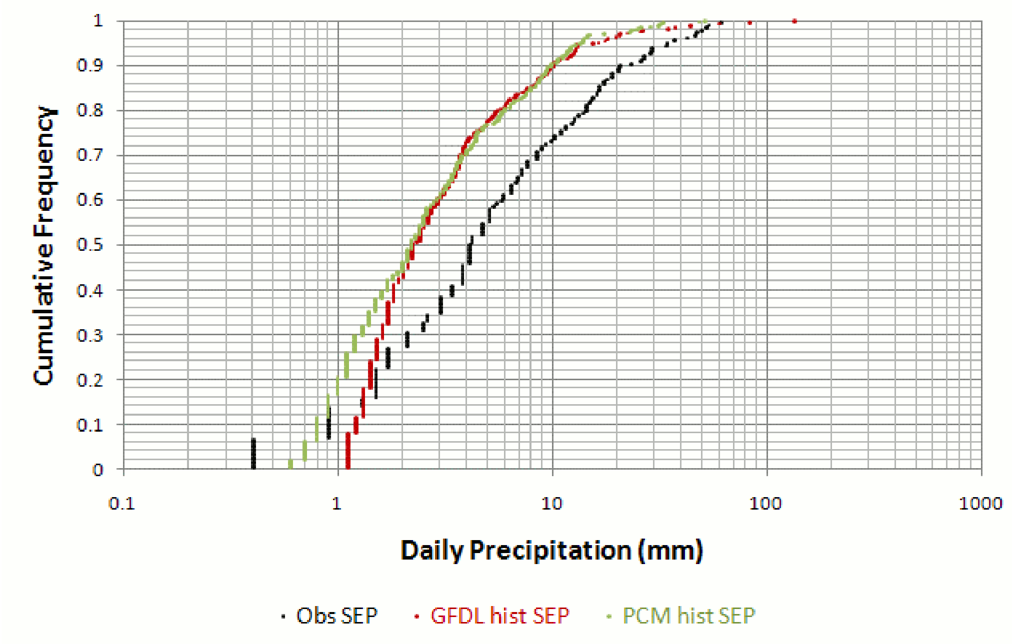

October

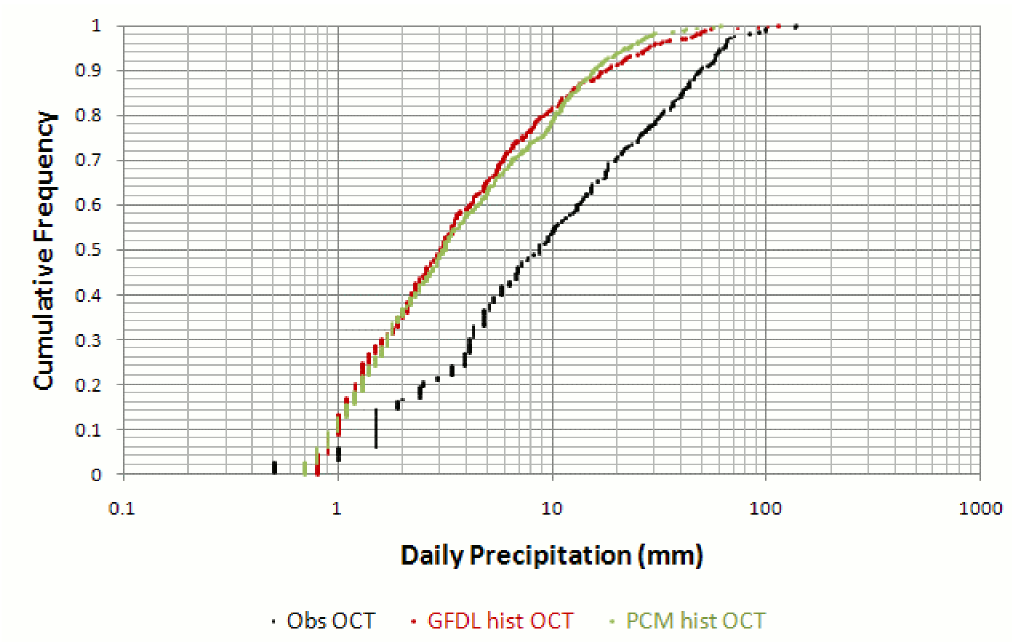

Figure 5, continued.

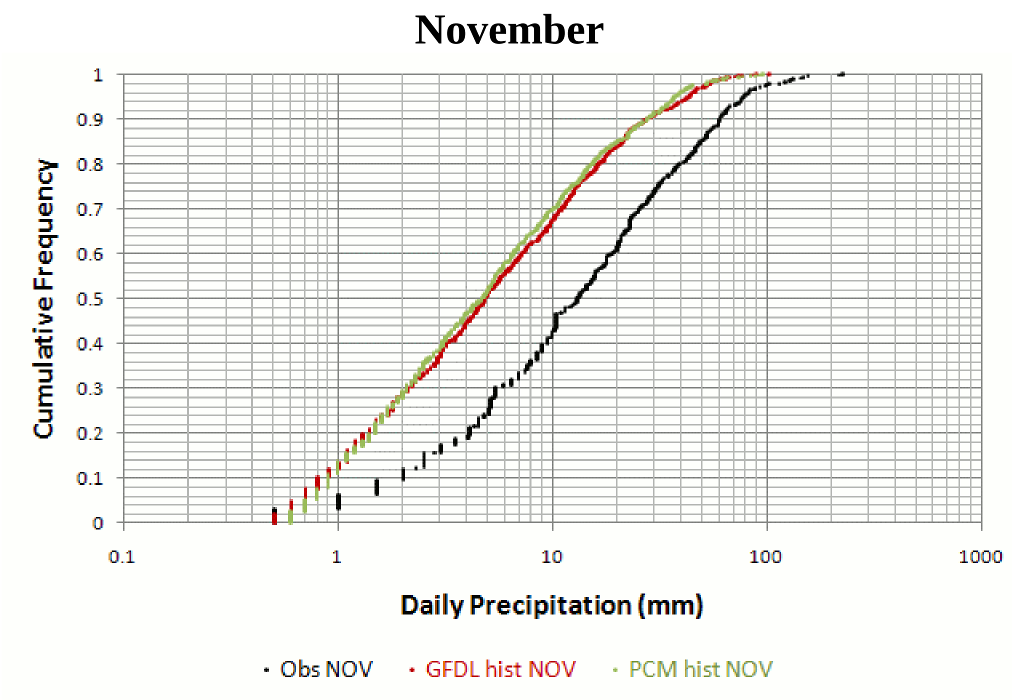

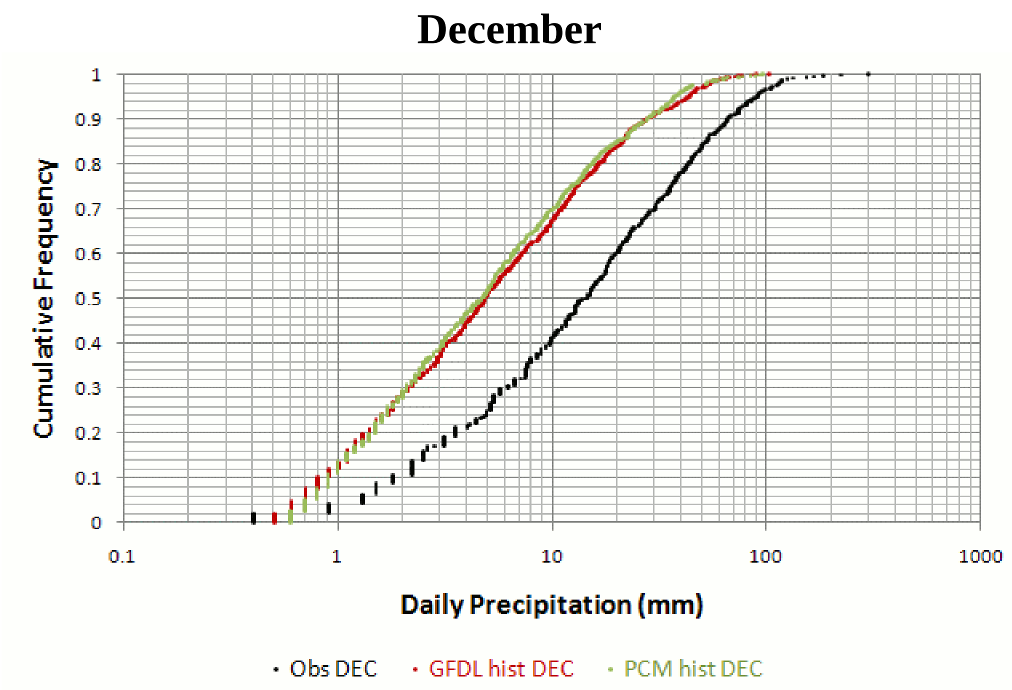

Figure 5, continued.

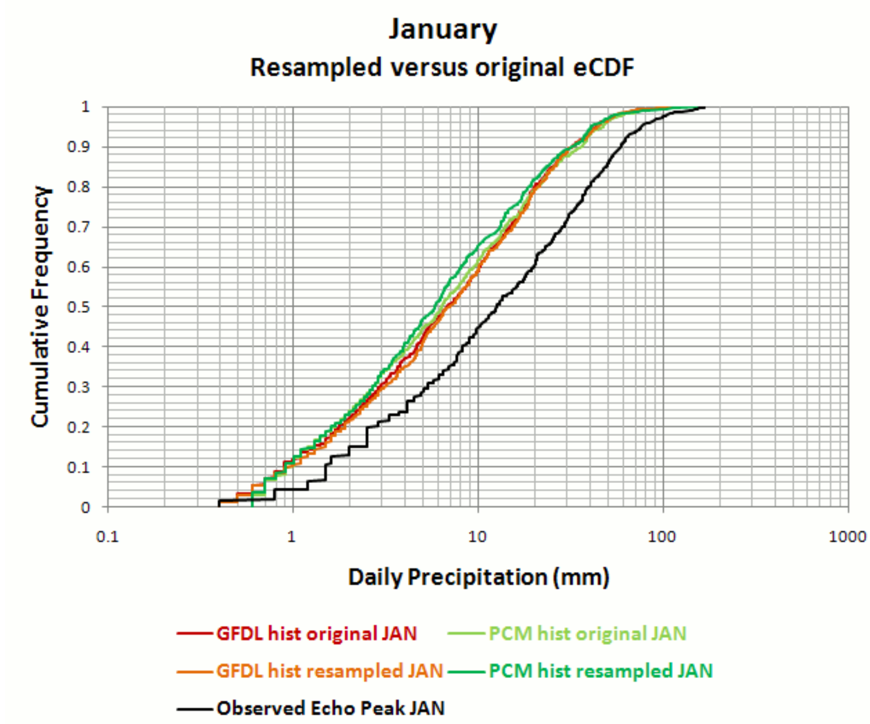

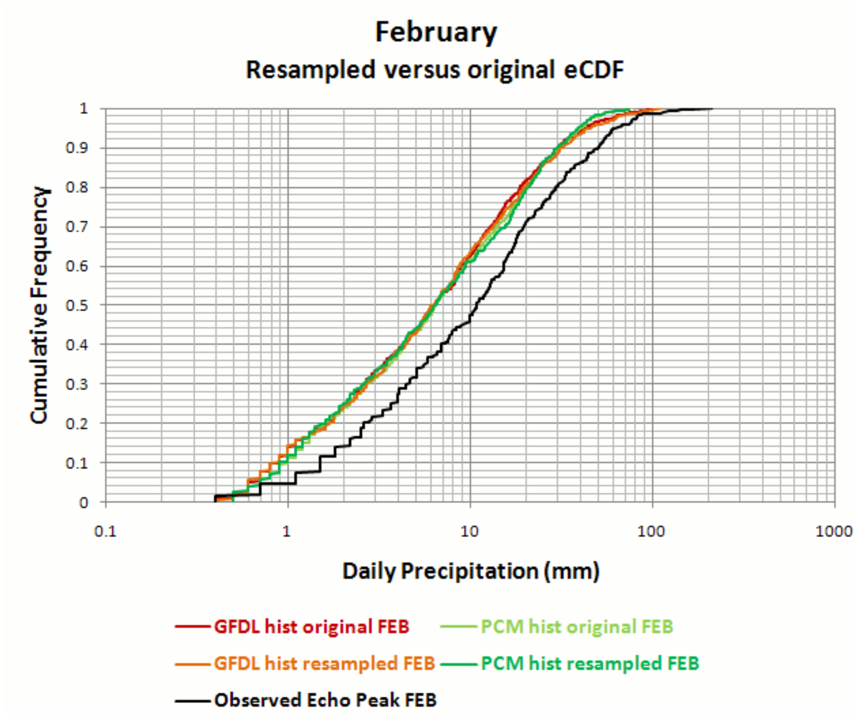

Figure 6: Similar to Figure 5, but also showing the simulated historical distributions after they have been re-sampled in order to match, for each month, the number of observed precipitation events (see text). The original distributions (from Figure 5) are also shown, for comparison. Note that the resampled distributions differ somewhat from the original ones in some of the months. *(Figure continues.)*

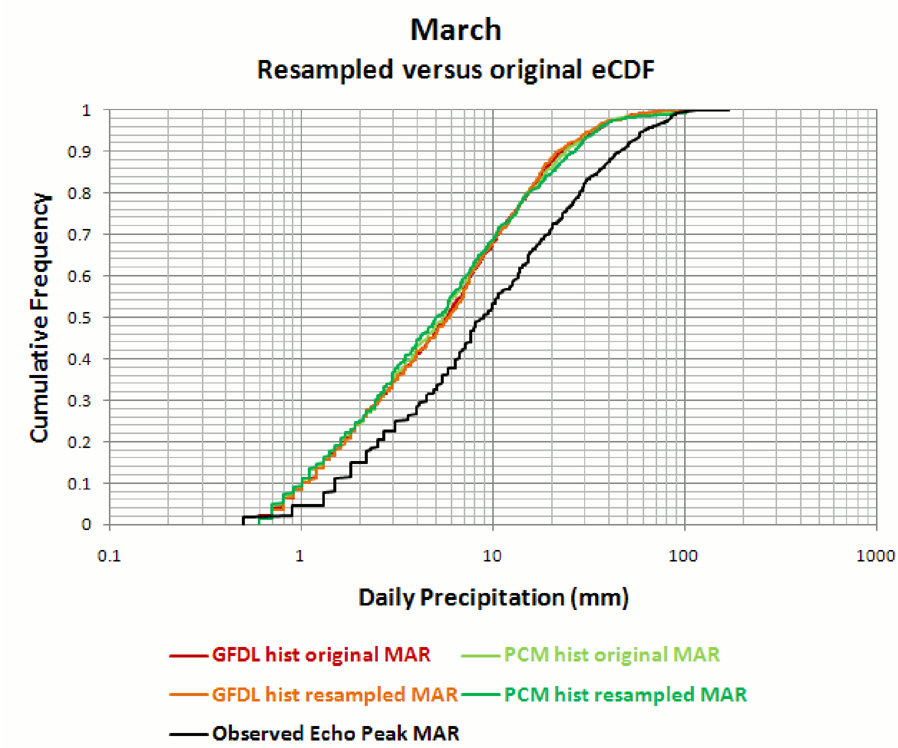

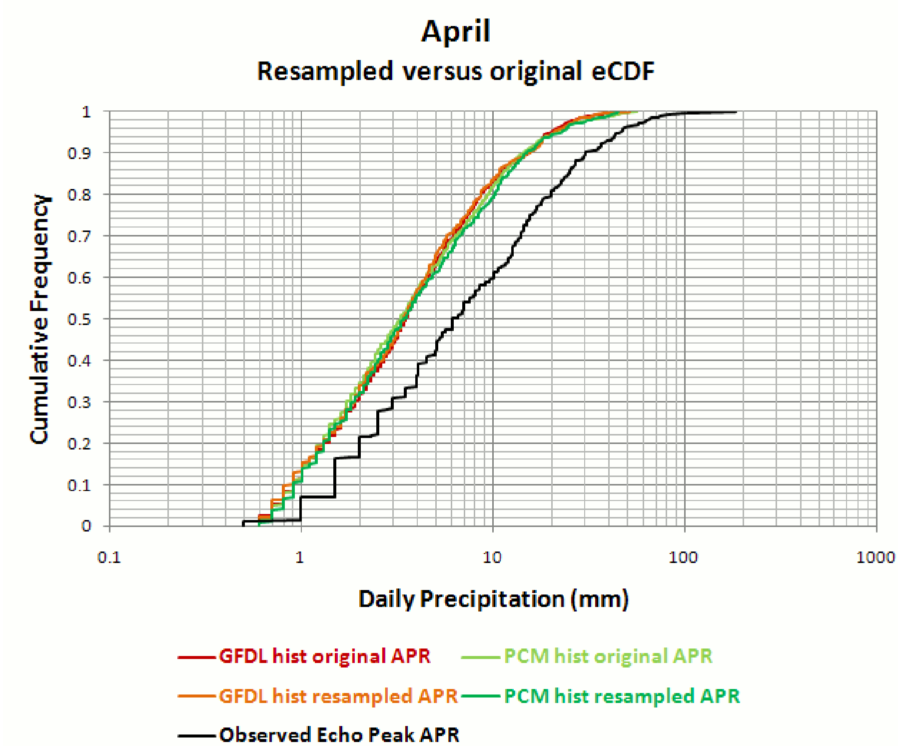

Figure 6, continued.

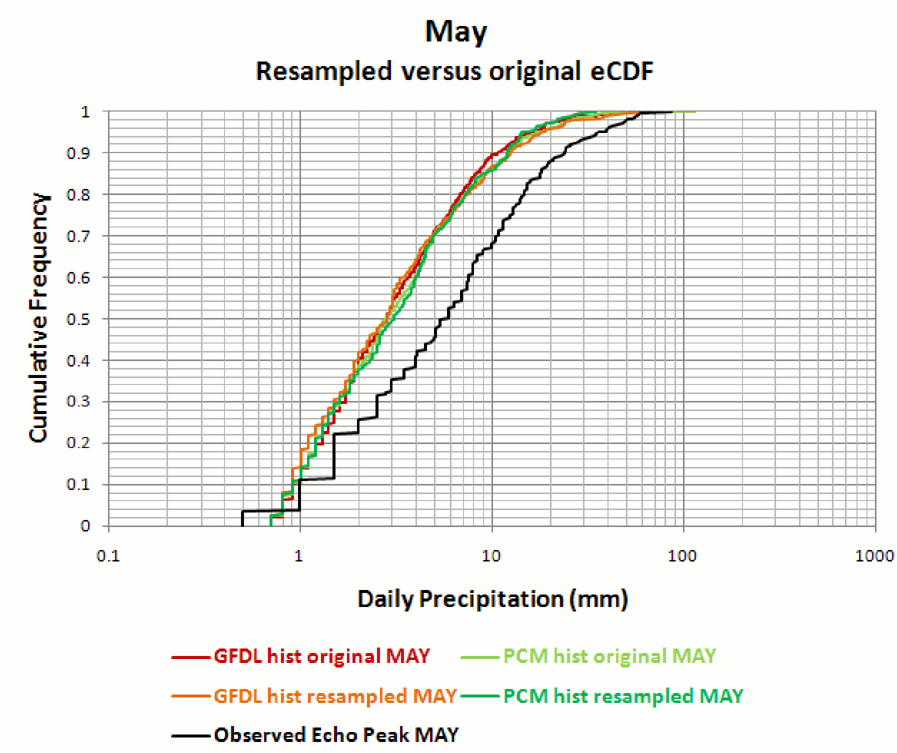

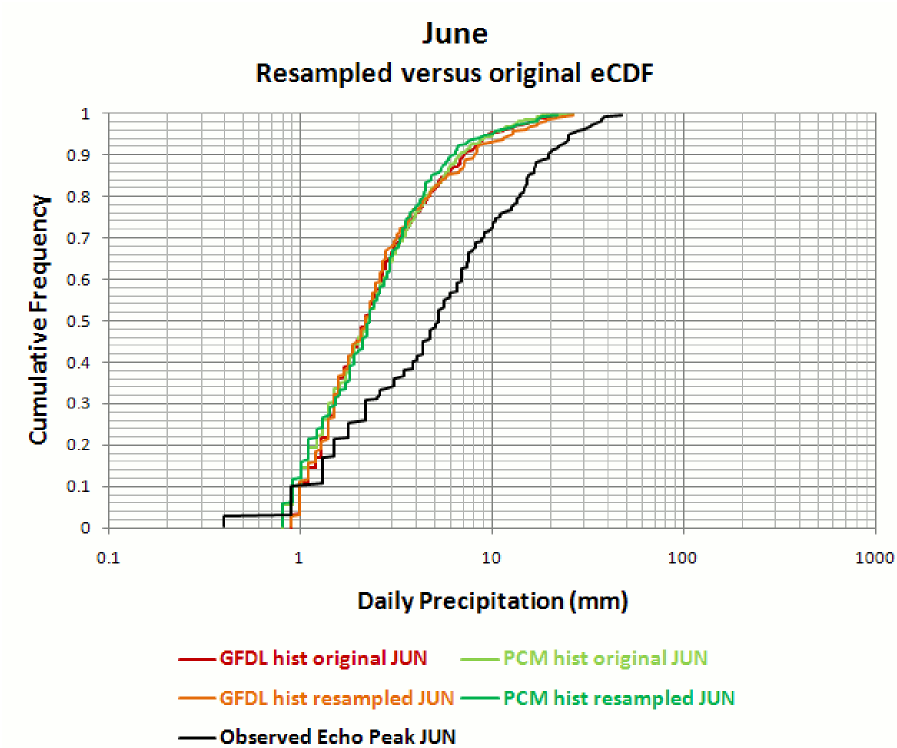

Figure 6, continued.

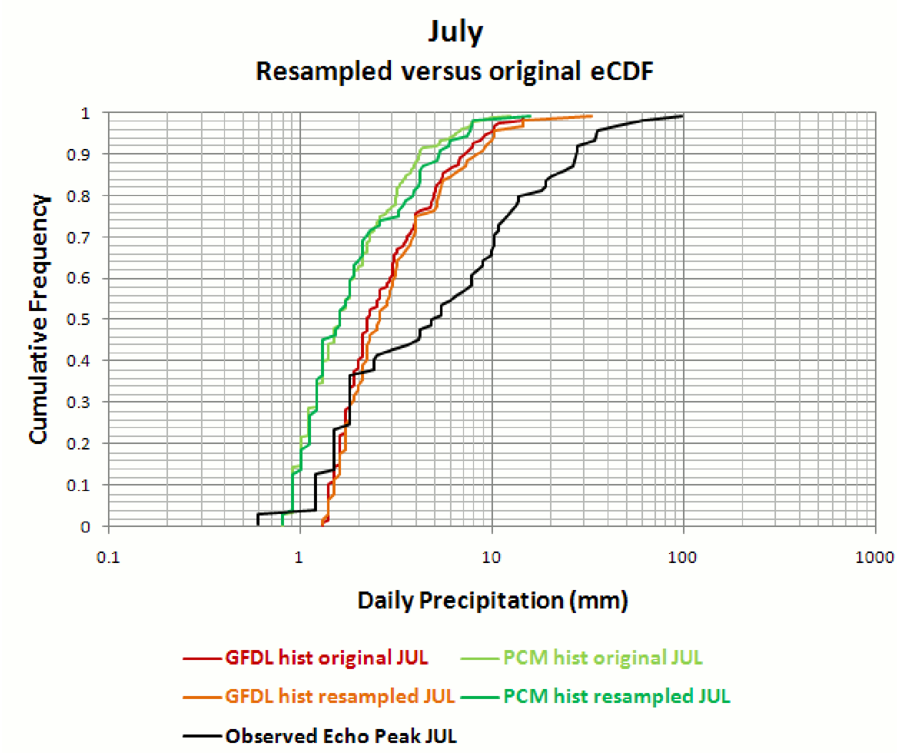

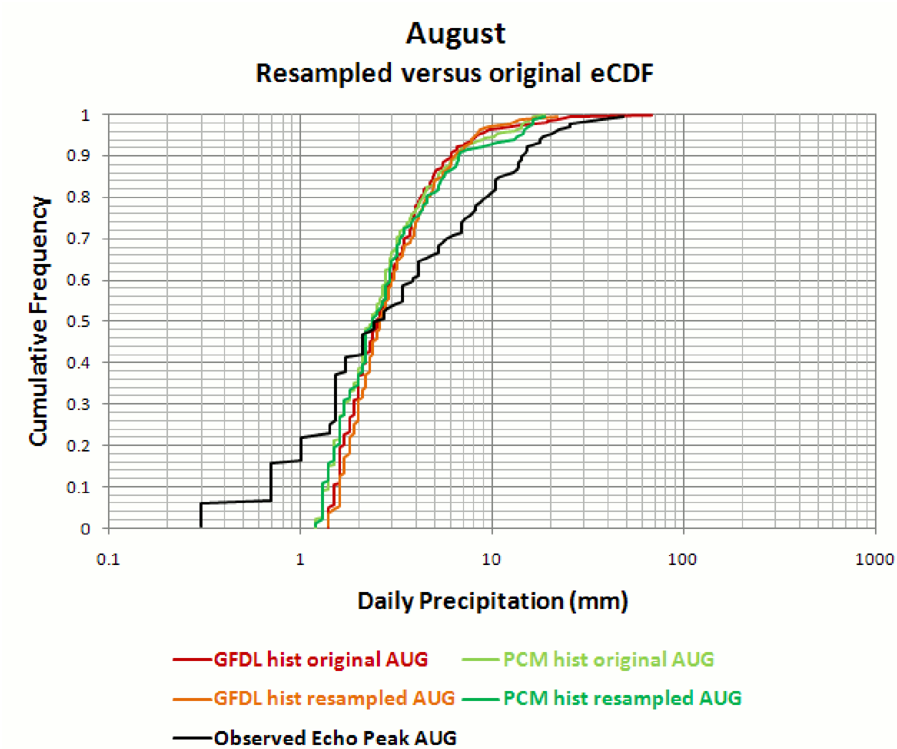

Figure 6, continued.

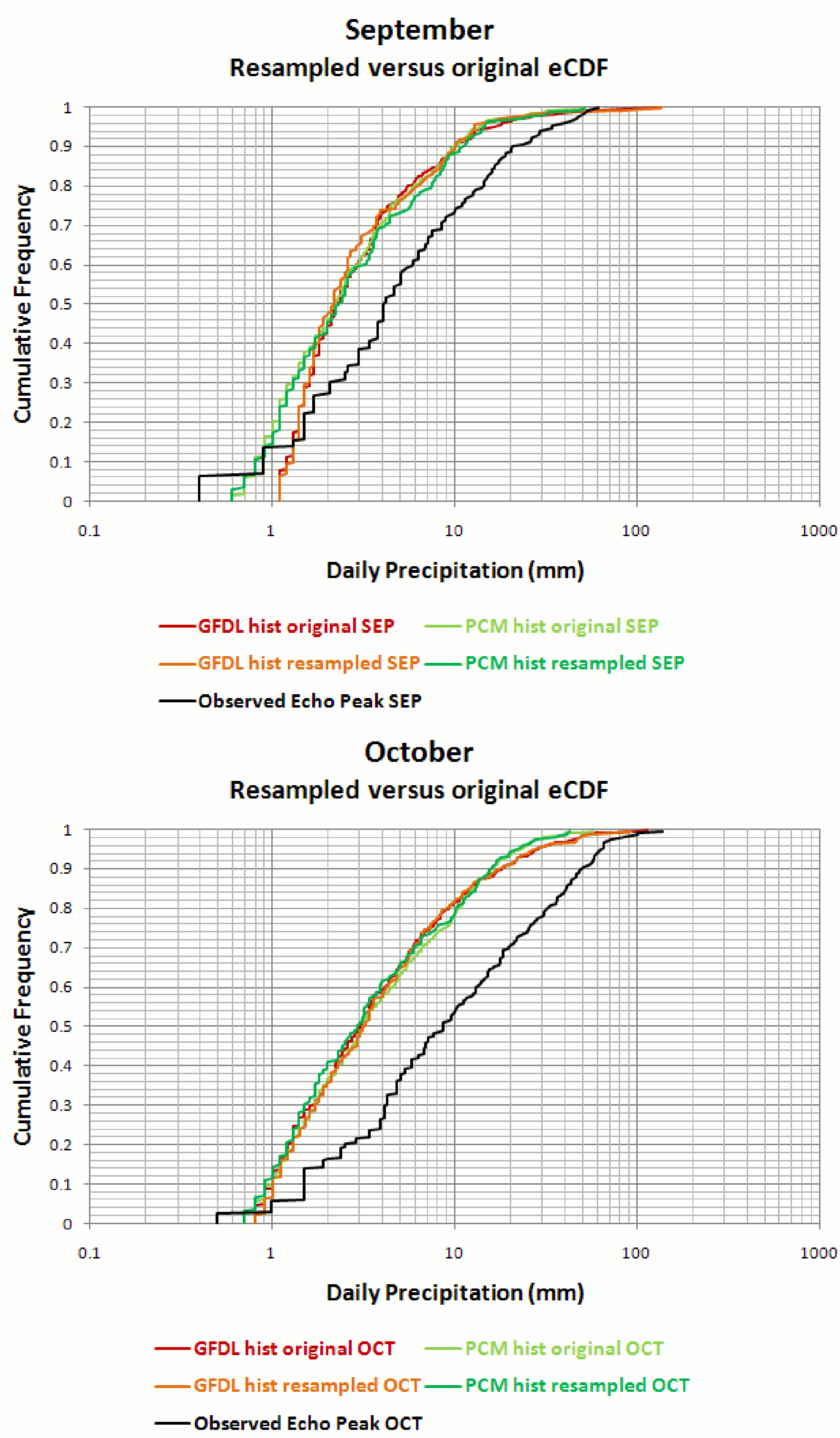

Figure 6, continued.

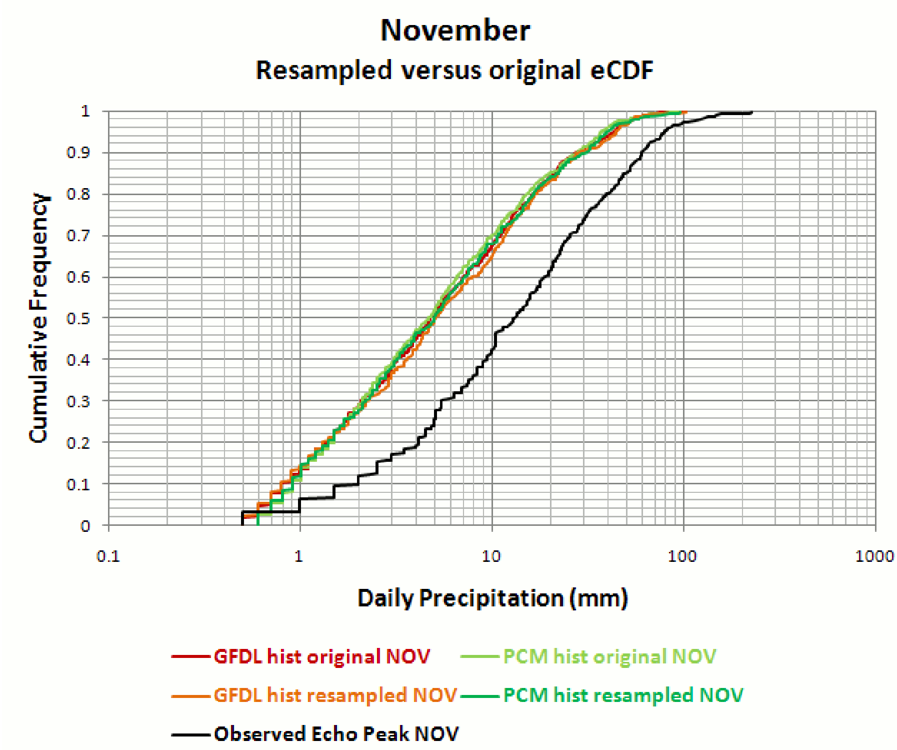

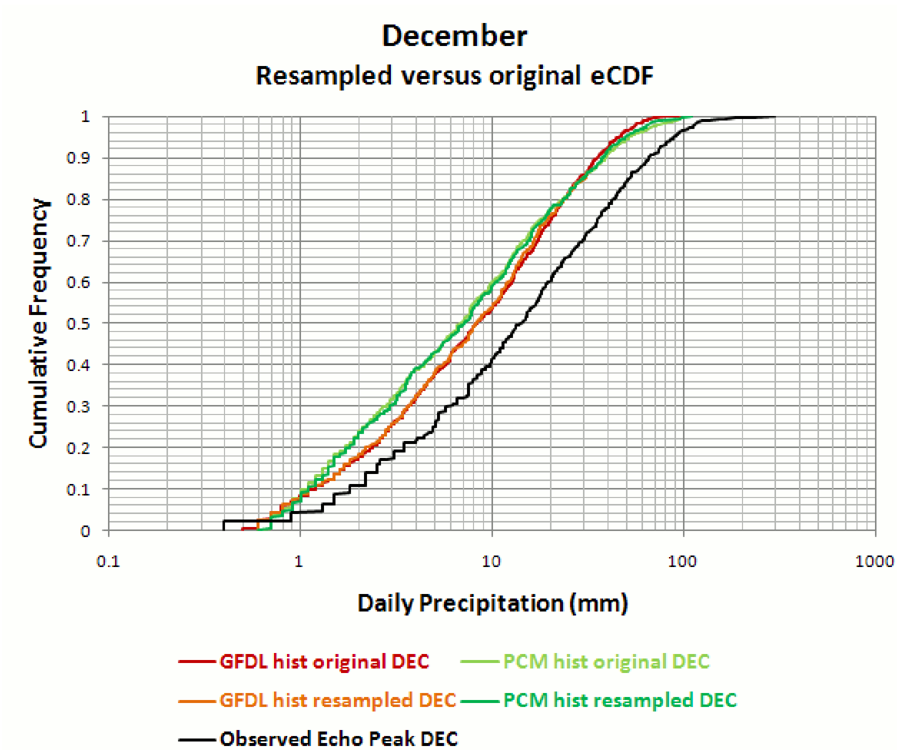

Figure 6, continued.

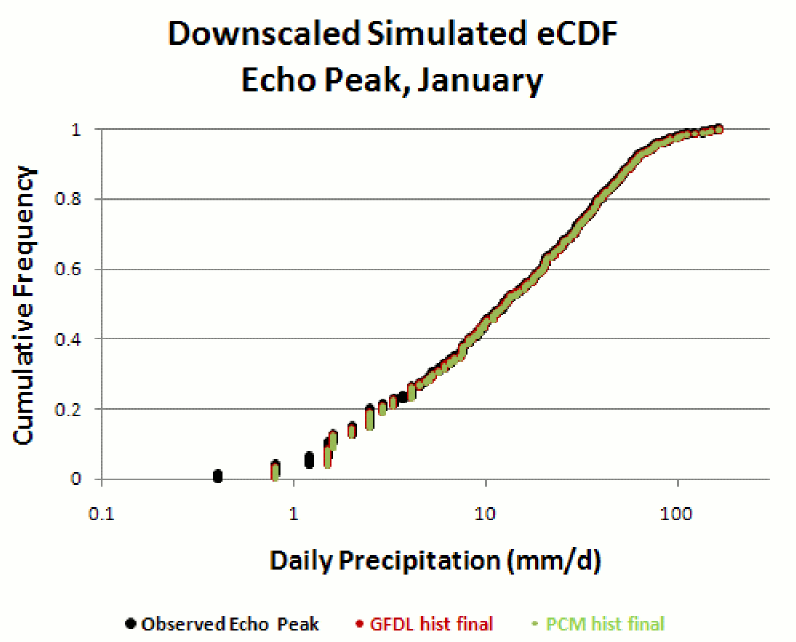

Figure 7: Similar to Figures 5 and 6, for cell 4 and for January, but after the two simulated historical time series have undergone quantile mapping. As a result, the two simulated distributions overlap with the observed distribution.

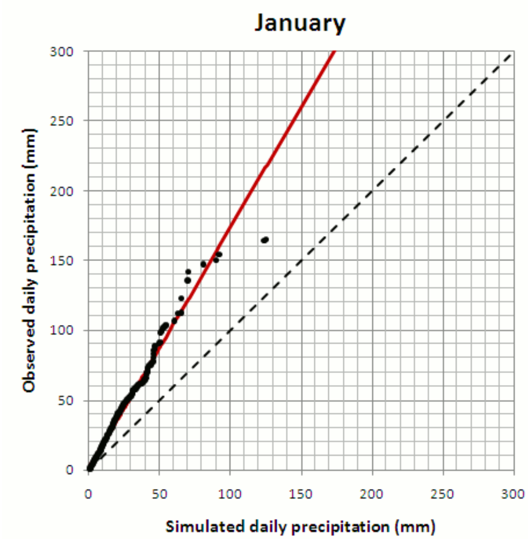

Slope = $\sigma_{obs}/\sigma_{GFDLhist}$ = 1.77

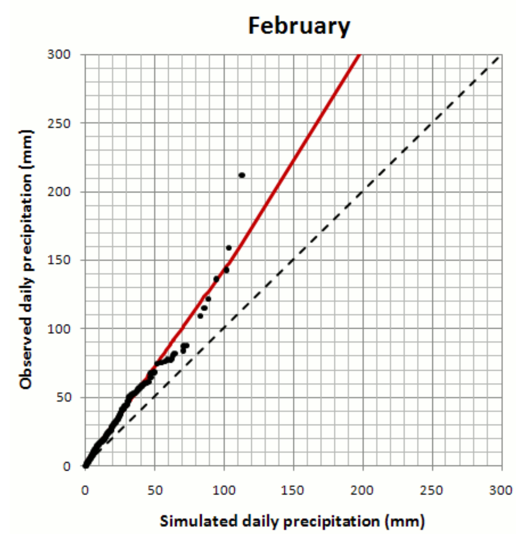

Slope = $\sigma_{obs}/\sigma_{GFDLhist}$ = 1.42

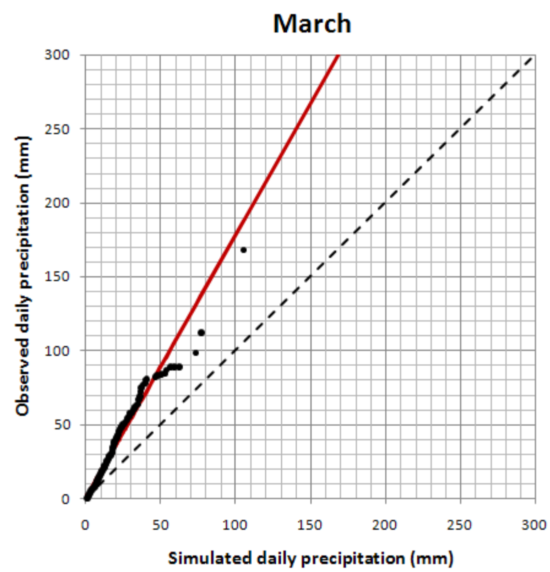

Slope = $\sigma_{obs}/\sigma_{GFDLhist}$ = 1.78

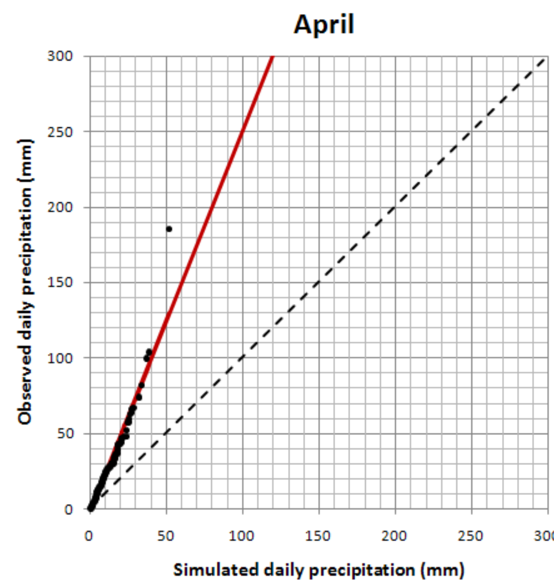

Slope = $\sigma_{obs}/\sigma_{GFDLhist}$ = 2.53

Figure 8: "Dictionary" relationship for Echo Peak and its closest model grid cell, cell 4, between observed daily precipitation values and the GFDL-simulated values (in each of the 12 months). Any simulated value can be located on the xx axis and, by interpolating between the sampled points, it can be mapped onto the yy axis. This corresponds to quantile mapping, since each point identifies a pair of (x, y) values having the same plotting positions (or cumulative frequency). Values simulated by GFDL for future climate scenarios, can similarly be read from the xx axis of these figures and mapped onto the yy axis. Values that fall above the range of the simulations for the historical period are mapped using the red fitted line, which corresponds to an exponential approximation of the simulated and the observed distributions. Given the Exponential distribution's general expression $F(x) = 1\text{-}\exp\{(\mu_x\text{-}\sigma_x\text{-}x)/\sigma_x\}$, it is fairly simple to show that the value x' in the yy axis corresponding to a value x in the xx axis is given by: $x' = \mu_{obs}\text{-}\sigma_{obs}*(1+(\mu_{hist}\text{-}\sigma_{hist}\text{-}x)/\sigma_{hist})$. Thus, the slope of the red line is given by the ratio between the standard deviations of the two distributions, $\sigma_{GFDLhist}/\sigma_{obs}$. *Figure continues.*

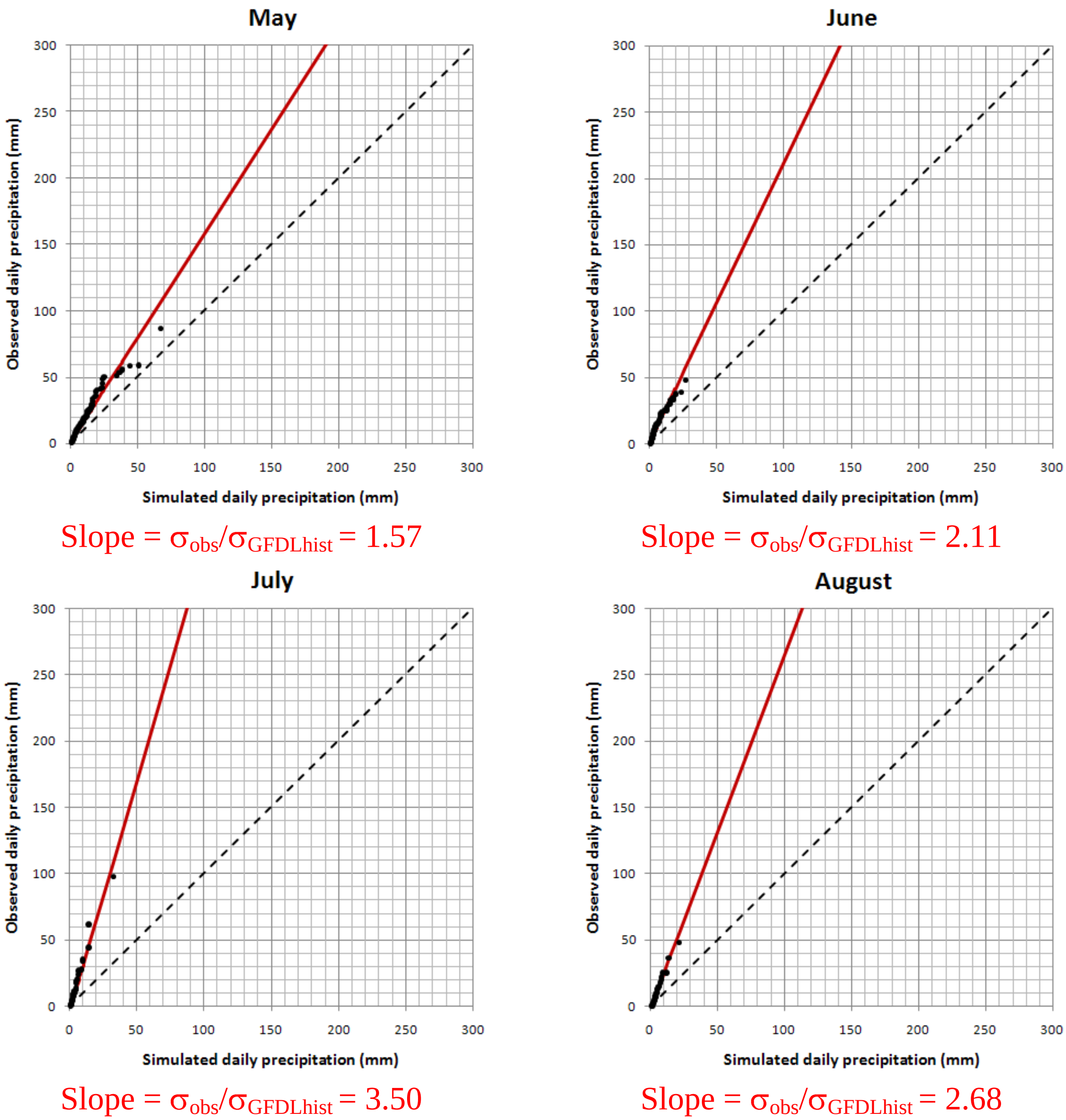

Figure 8, continued.

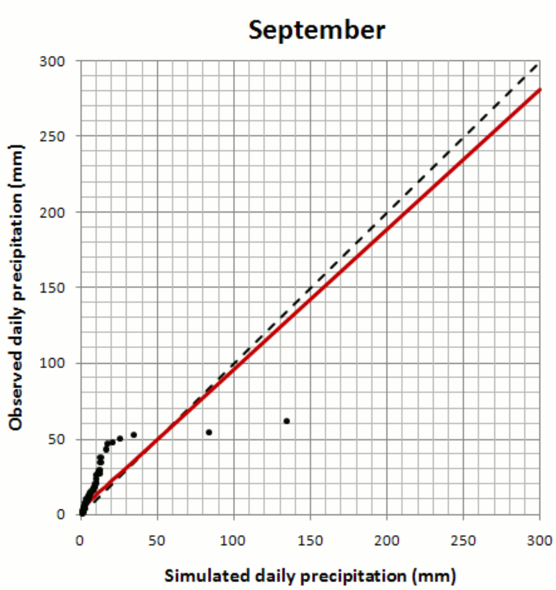

Slope = $\sigma_{obs}/\sigma_{GFDLhist}$ = 0.92

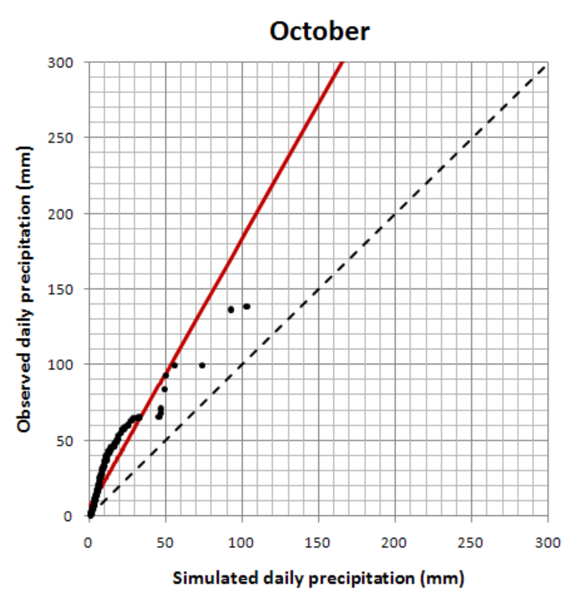

Slope = $\sigma_{obs}/\sigma_{GFDLhist}$ = 1.78

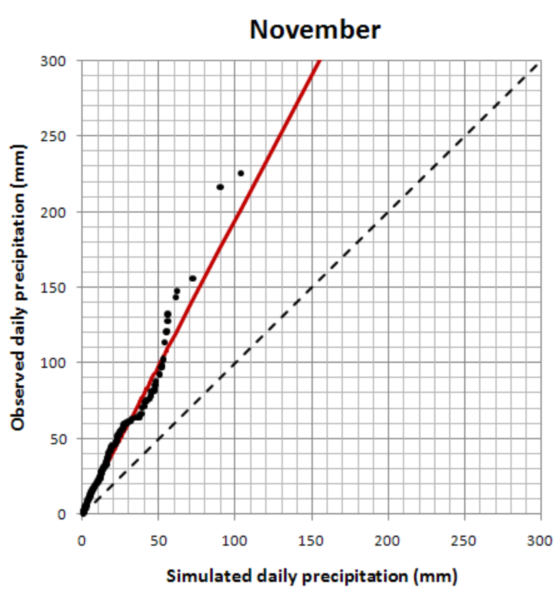

Slope = $\sigma_{obs}/\sigma_{GFDLhist}$ = 2.06

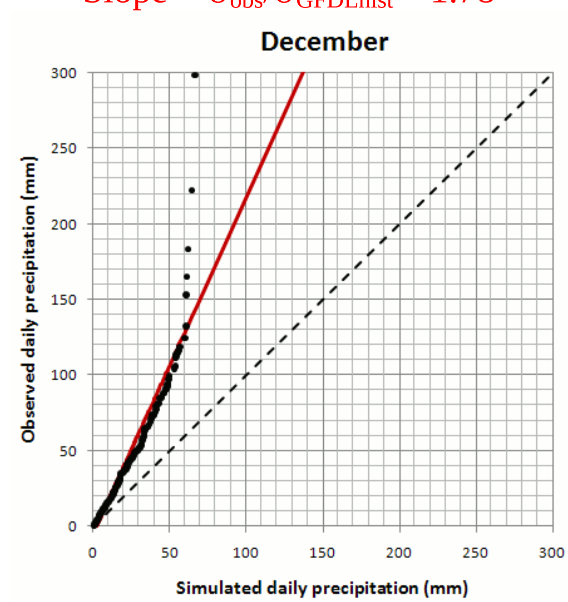

Slope = $\sigma_{obs}/\sigma_{GFDLhist}$ = 2.24

Figure 8, continued.

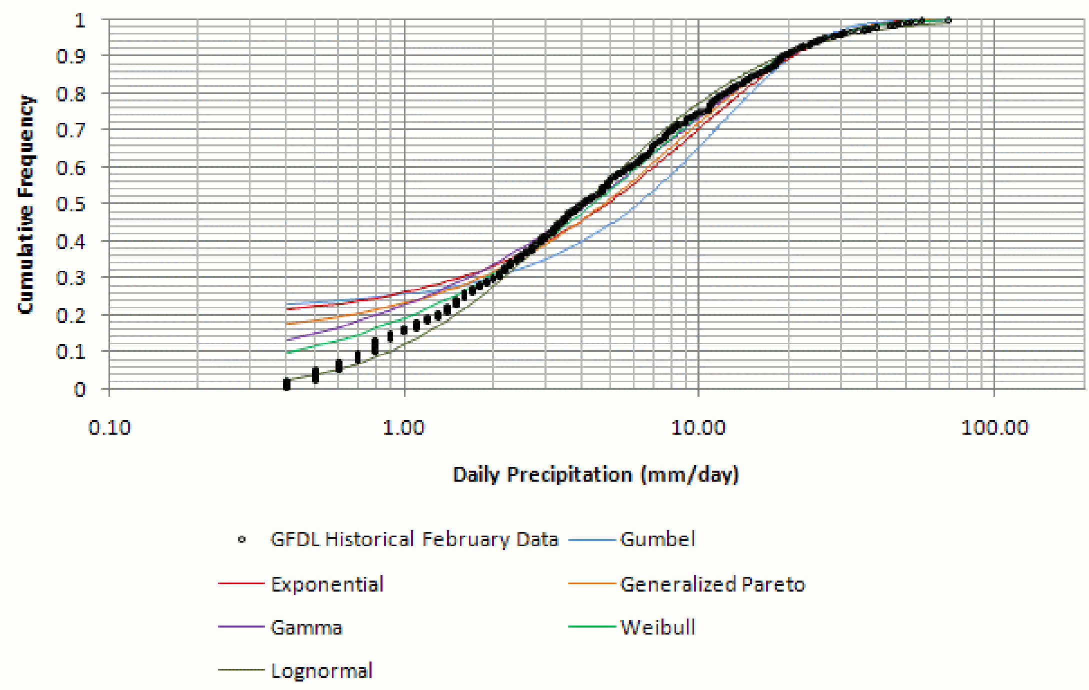

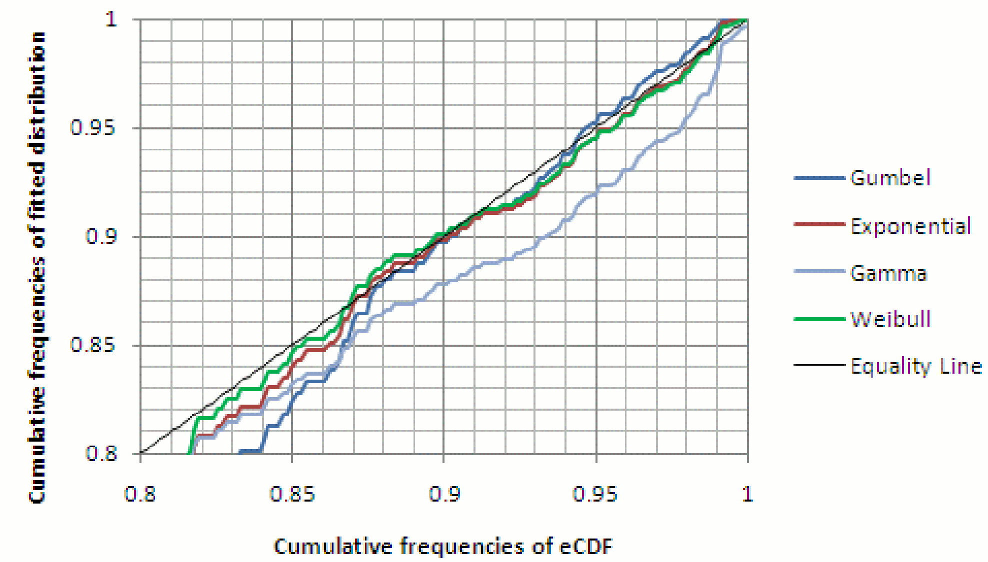

Figure 9: Different theoretical distributions fitted to the GFDL historical eCDF by the method of moments. **Top panel:** Whole-distribution fit to GFDL historical eCDF for February (used as an example). Only the lognormal distribution is capable of reproducing the distributions shape over the entire range of values. However, local deviations are considerable even for the lognormal distribution. **Bottom panel:** Cunnane plotting positions of the eCDF versus the Cunnane plotting positions of the fitted theoretical distribution (for GFDL historical, February), zoomed in to the top corner of the graph (only values above the 0.8 cumulative frequency are shown, since the goal is to use the fitted distribution to extend the eCDF beyond its maximum value). The Weibull, Generalized Pareto, Exponential and Lognormal distributions perform well at this upper range. The Exponential was chosen for its simplicity.

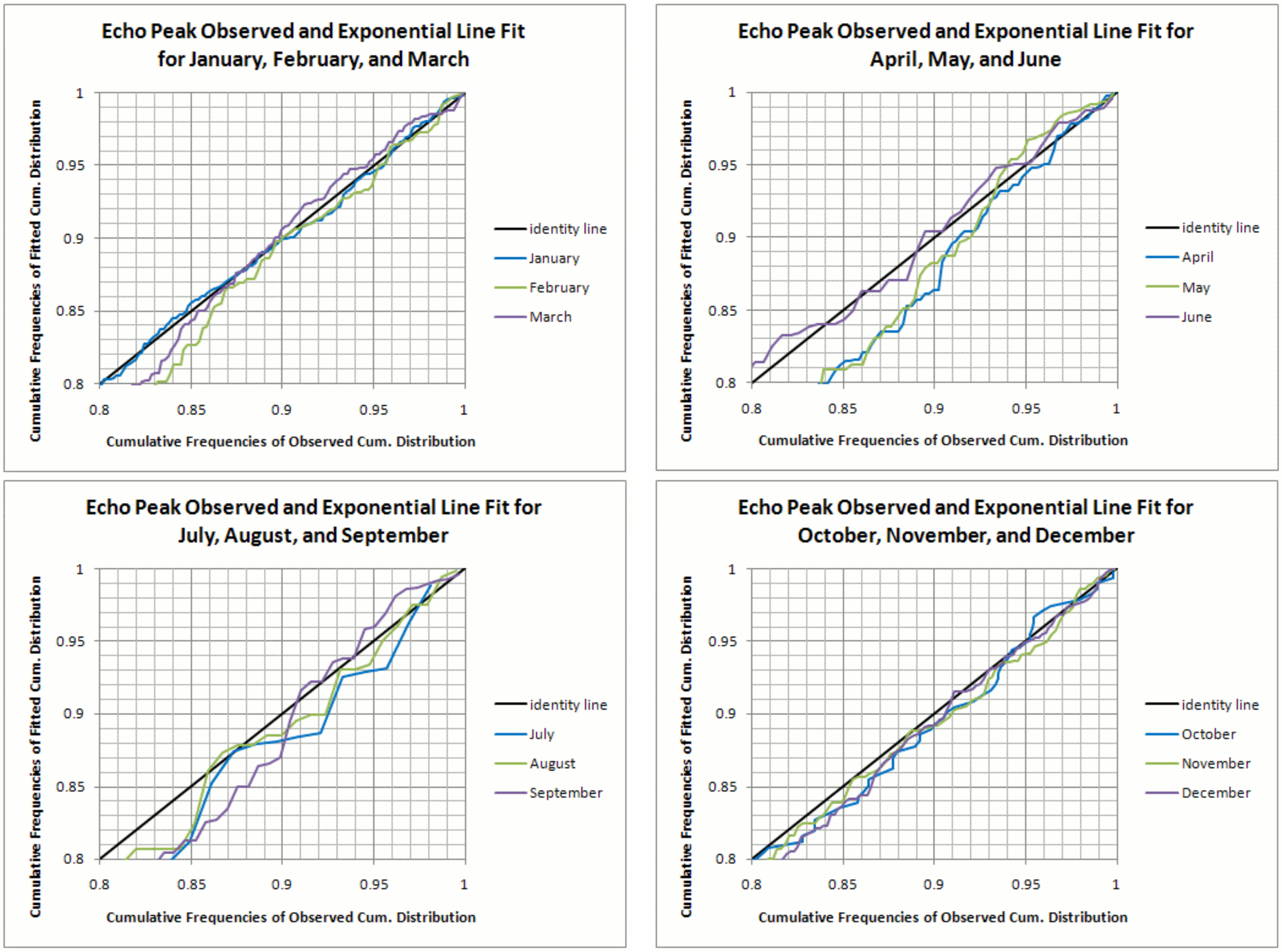

Figure 10: Quality of the fit of the exponential distribution at the higher-value end: Cunnane plotting positions of the observed eCDF are plotted against the Cunnane plotting positions of the fitted theoretical distribution, zoomed in to the top corner of the graph (only values above the 0.8 cumulative frequency are shown, since the goal is to use the fitted distribution to extend the eCDF beyond its maximum value). Echo Peak is used as an example.

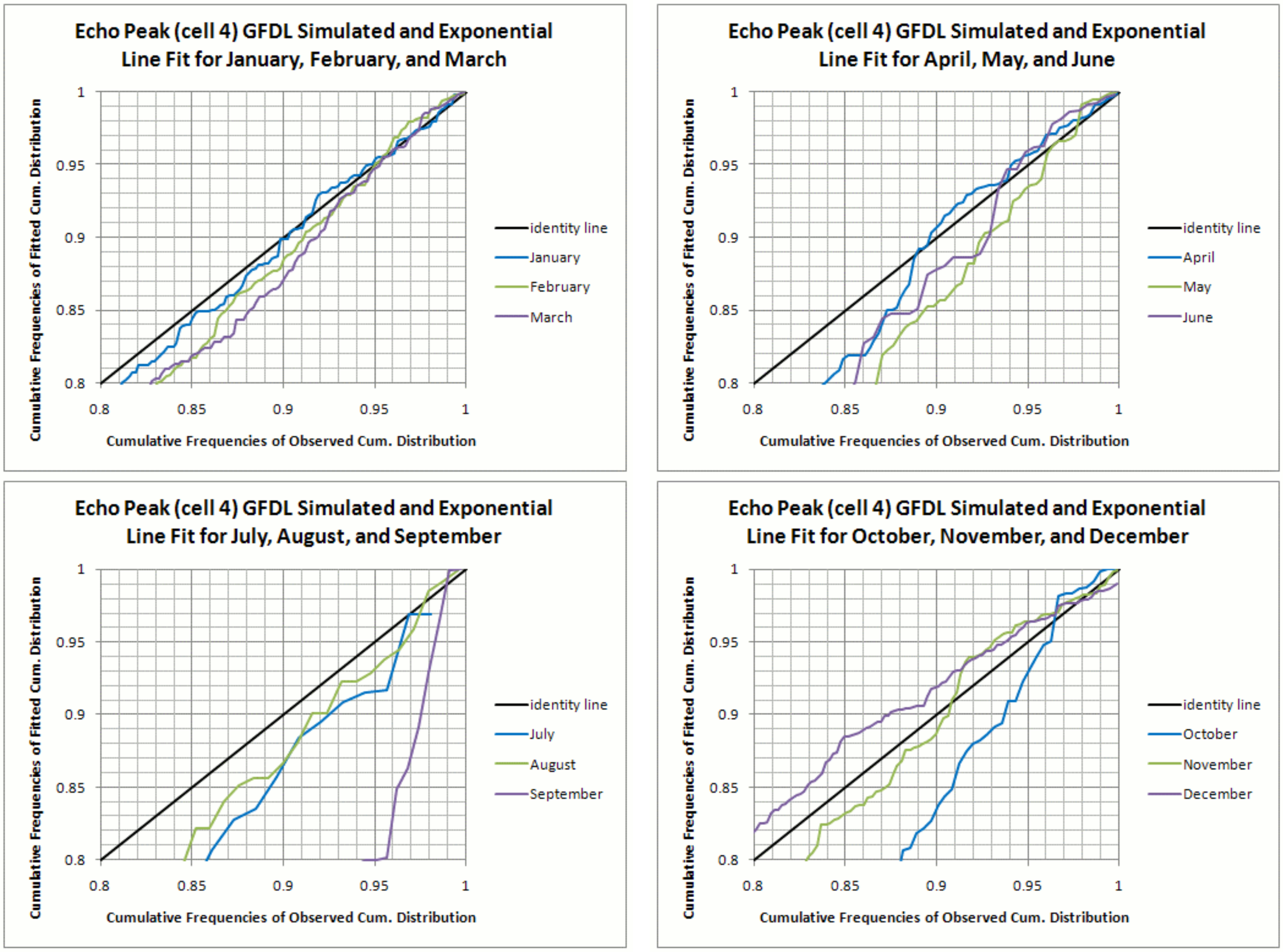

Figure 11: Similar to Figure 10, but for the GFDL simulated eCDF. Cell 4 (the cell closest to Echo Peak) is used as an example.

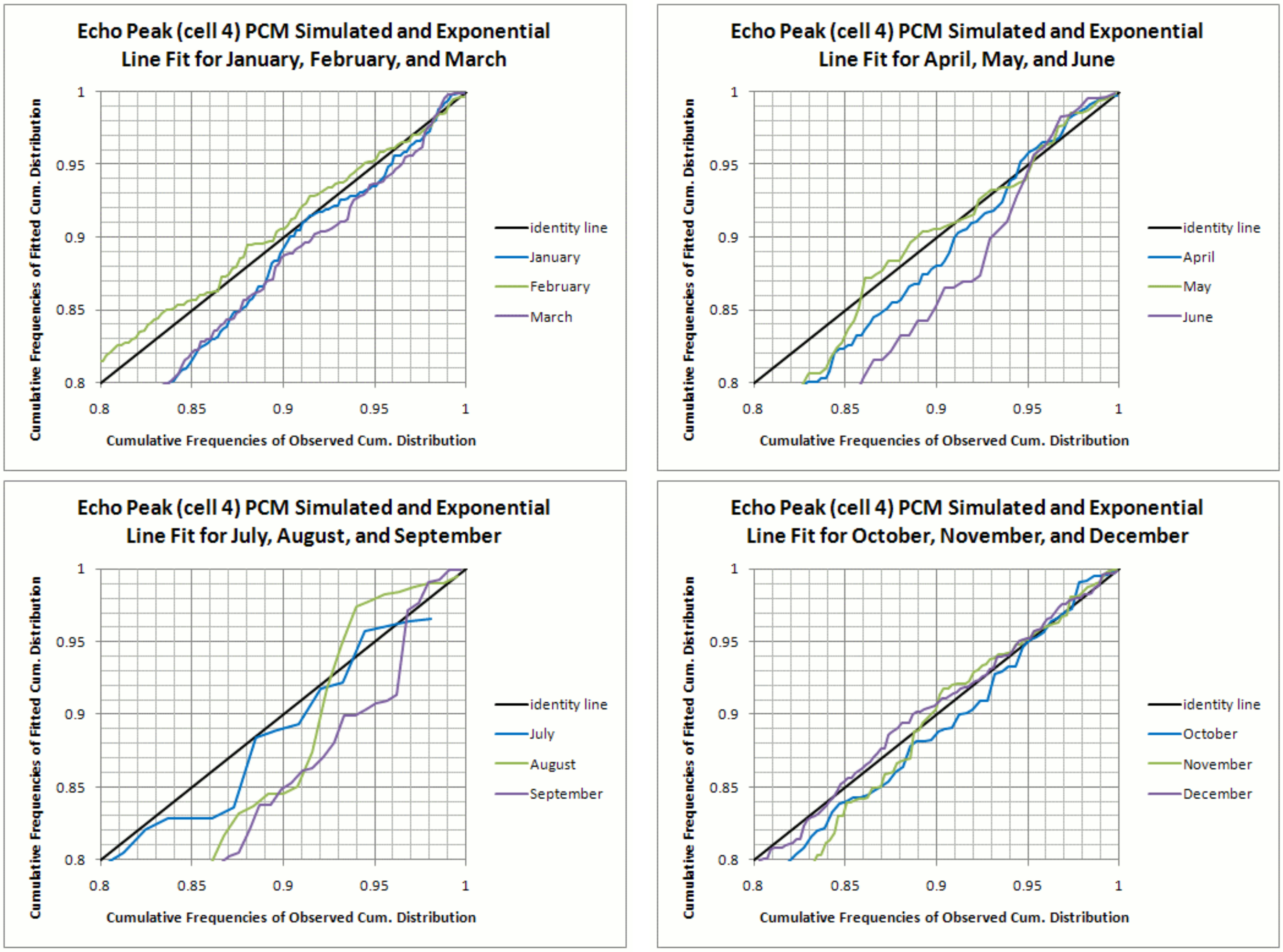

Figure 12: Similar to Figures 10 and 11, but for the PCM simulated eCDF. Cell 4 (the cell closest to Echo Peak) is used as an example.

Original eCDFs:

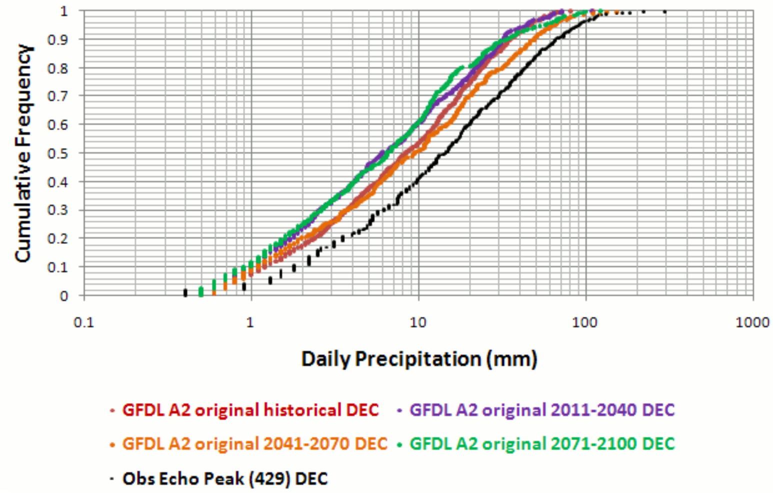

Resampled eCDFs:

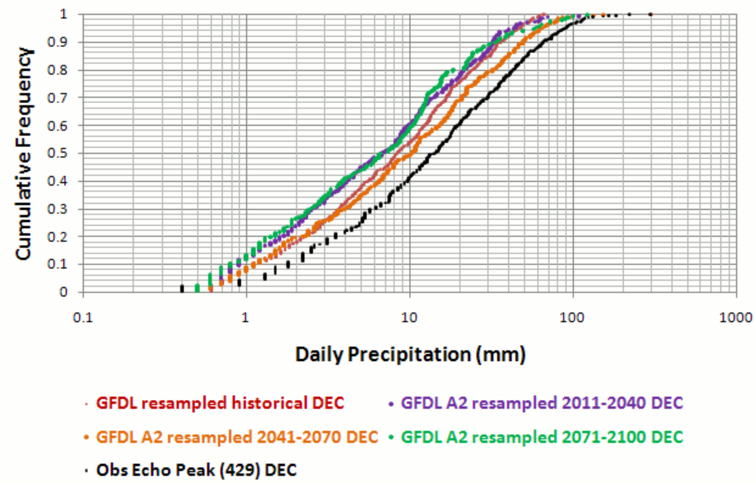

Final eCDFs:

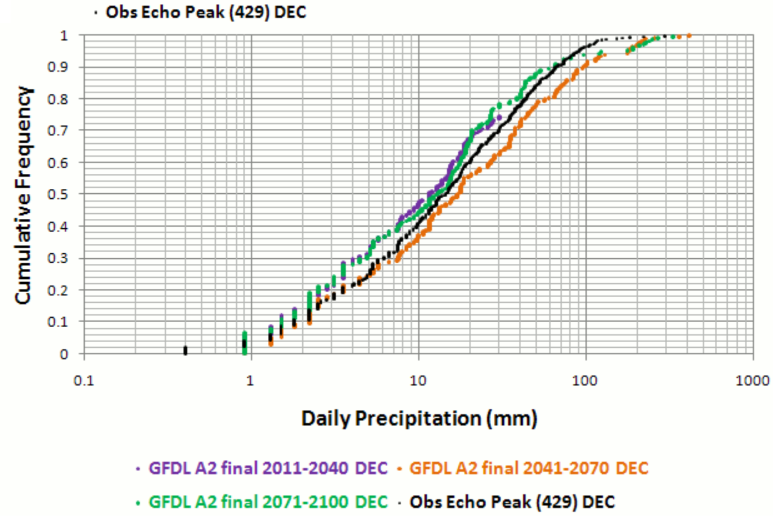

Figure 13: Monthly distributions of daily precipitation for GFDL, cell 4, December (used as an example). **Top panel:** Original distributions. **Center panel:** Original distributions after resampling (random removal of precipitation events – see text). **Bottom panel:** Final distributions produced in this project for station Echo Peak (429) (for which cell 4 is the closest cell). The final historical GFDL distribution is not shown, as it overlaps with the observations curve (as in the case shown in Figure 7). In the case of this month, the different curves maintain their positions relative to each other after resampling. This is not always the case. See Figures 14-16.

Original eCDFs:

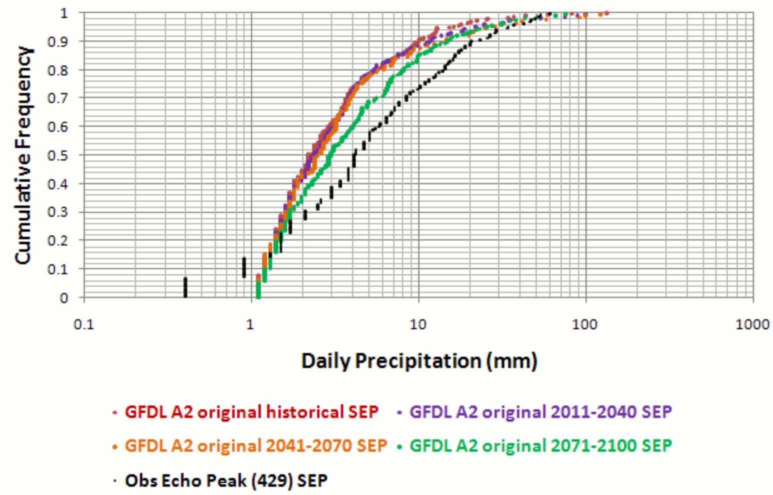

Resampled eCDFs:

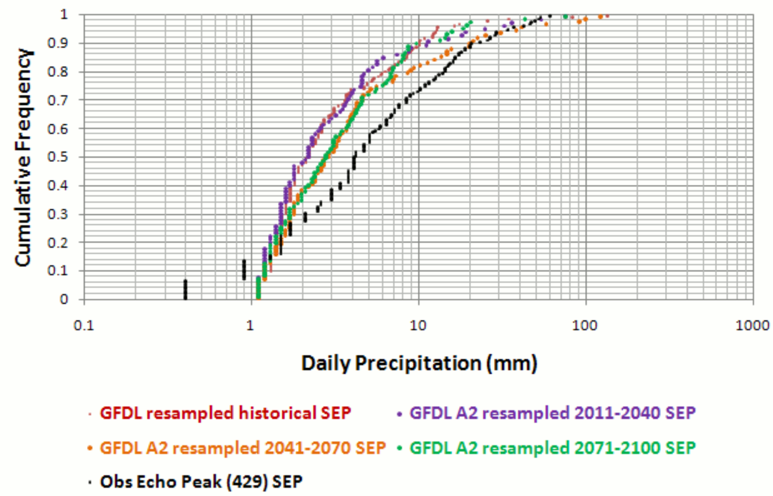

Final eCDFs:

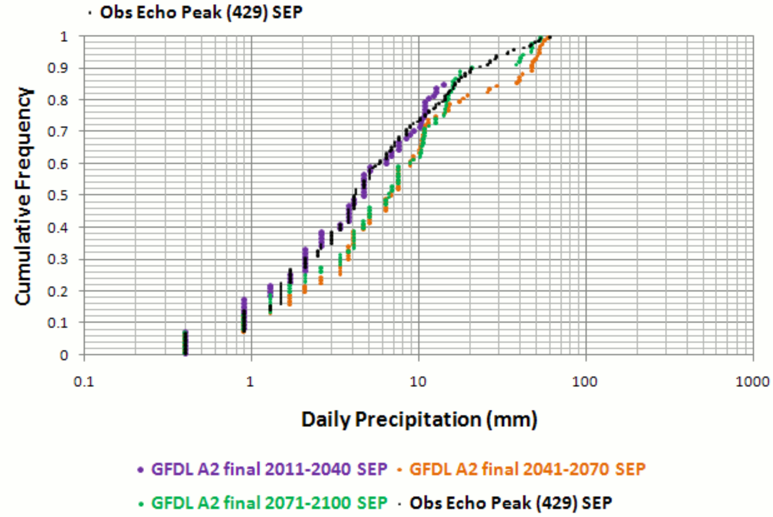

Figure 14: Similar to Figure 13, but for September. In this case, the relative positions of the curves change (near the higher end of the curves) as a result of the resampling step. See also Figure 16, September panel.

Original eCDFs:

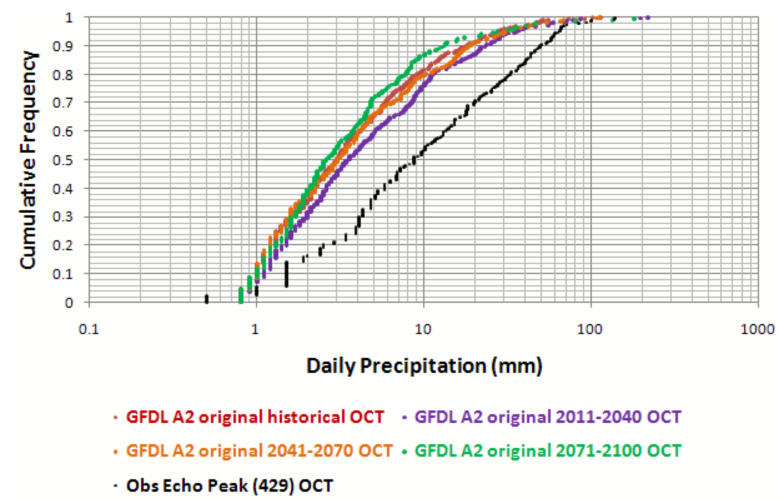

Resampled eCDFs:

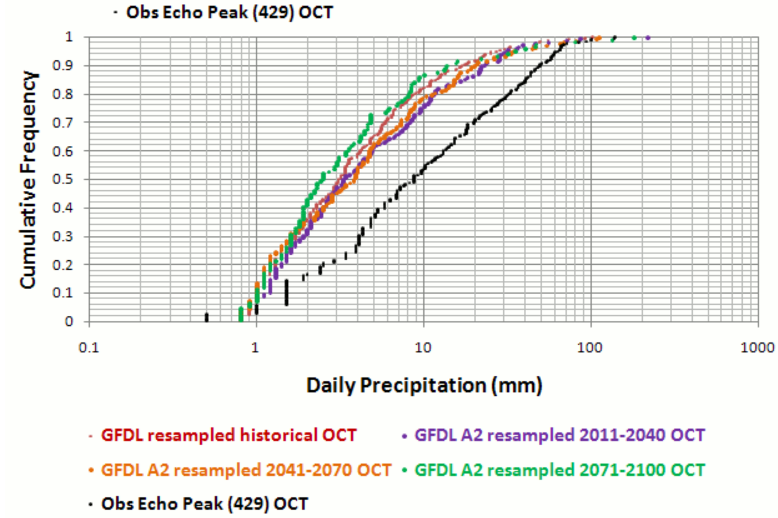

Final eCDFs:

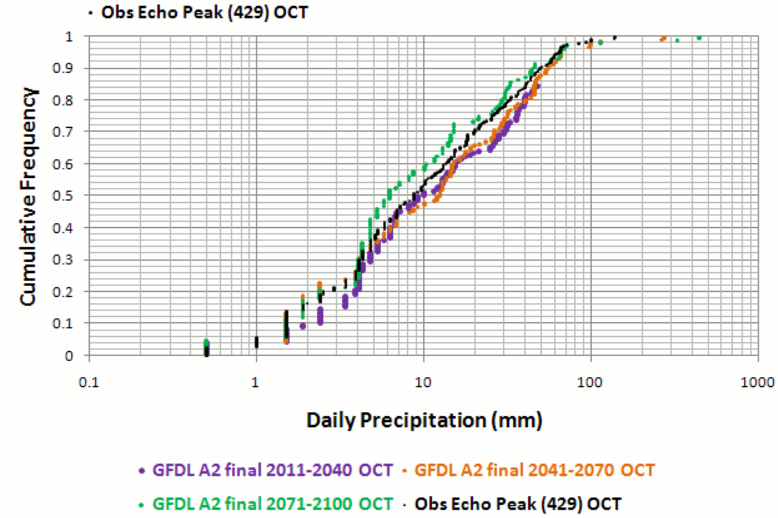

Figure 15: Similar to Figures 13 and 14, but for October. In this case, the eCDFs of periods 2011-2040 and 2041-2070 (purple and orange lines, respectively) are brought closer together as a result of the resampling step. See also Figure 16, October panel.

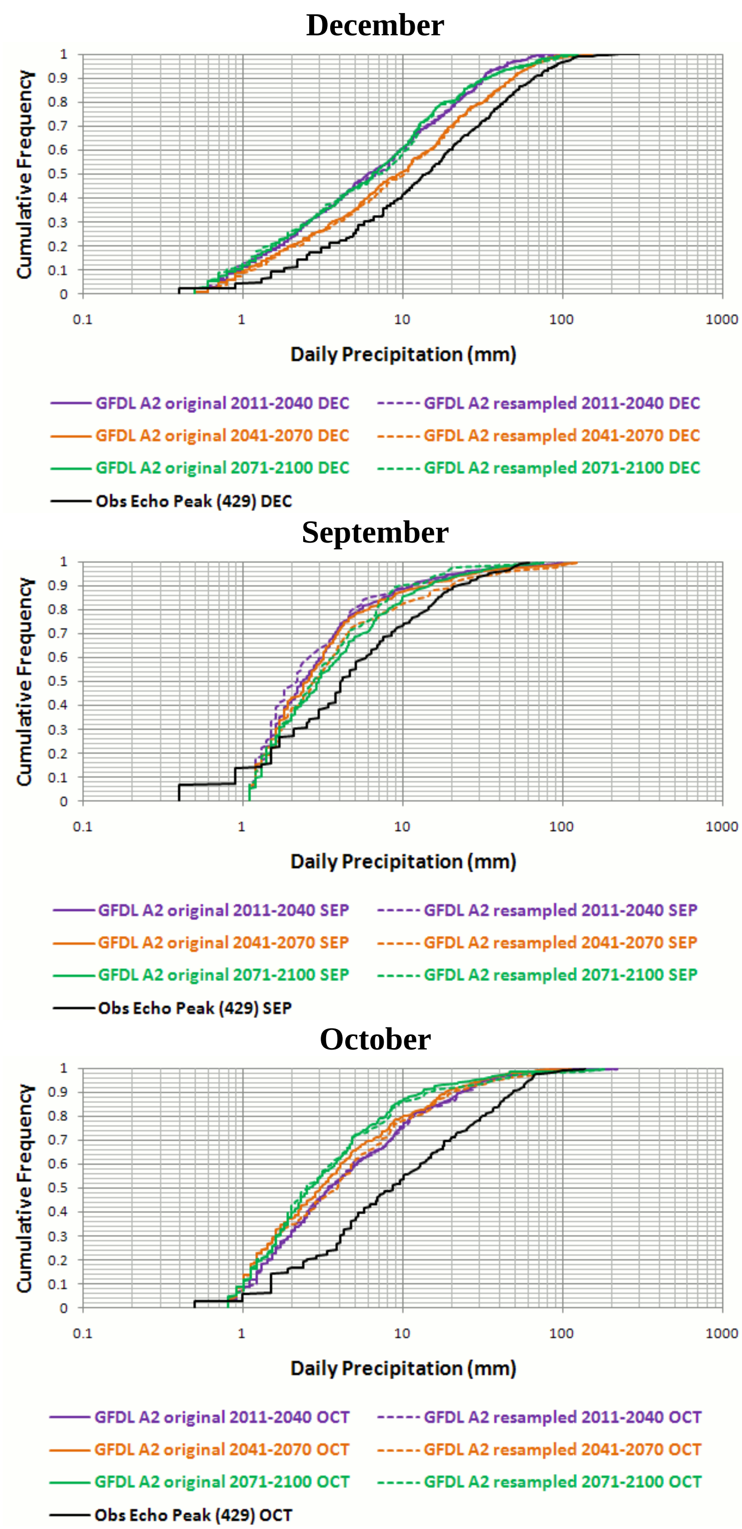

Figure 16: Original (solid lines) and resampled (dashed lines) distributions for GFDL A2, cell 4, for three example months. Lines are used rather than isolated points (used e.g. in Figure 13) for maximum clarity. See the related Figures 13-15 for these three months.

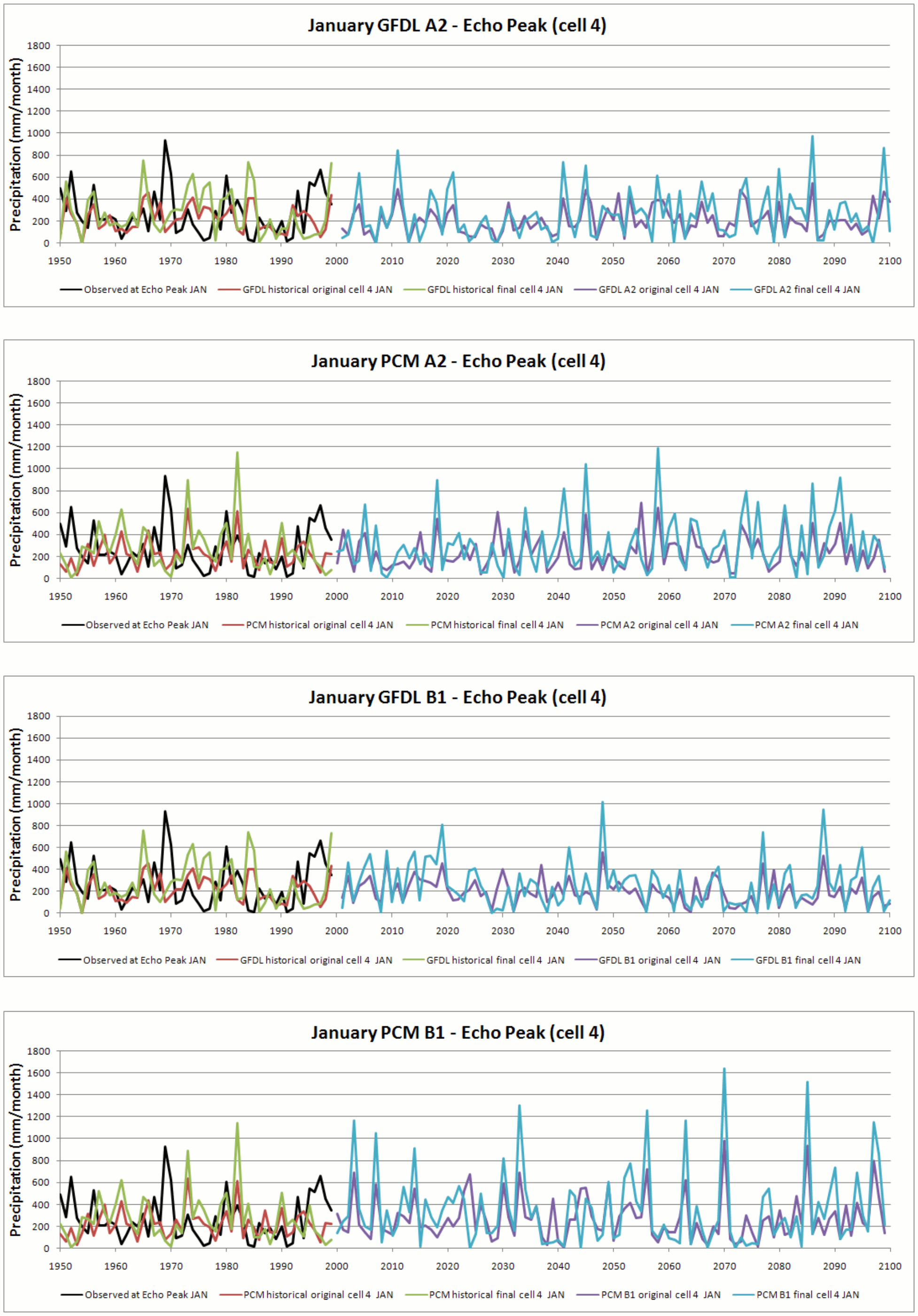

Figure 17: Example monthly time series derived from the daily time series that were input to this project (labeled "original") and output of this project (labeled "final"). Plots are for Echo Peak (cell 4) and for both GFDL and PCM. After quantile mapping, most monthly precipitation totals become higher than the original values, given that the observed daily distribution had higher values than the simulated historical (for either model). However, some points in the monthly time series become lowered, as a result of the random removal of precipitation days (re-sampling) described in the text. *(Figure continues.)*

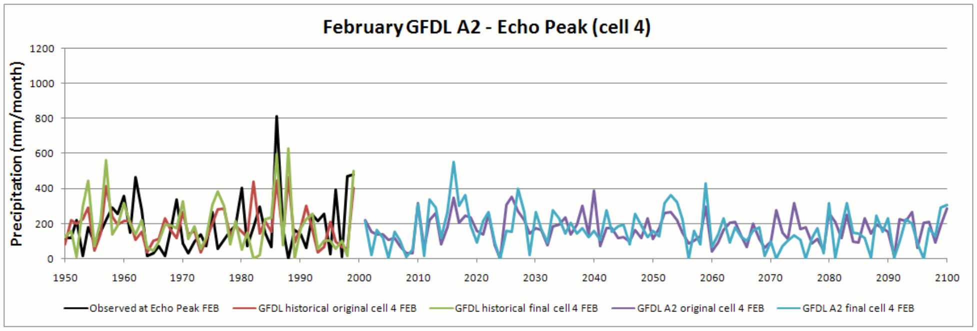

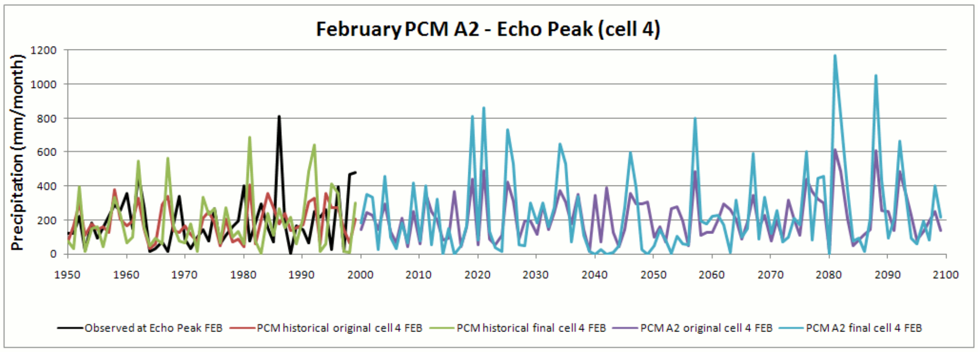

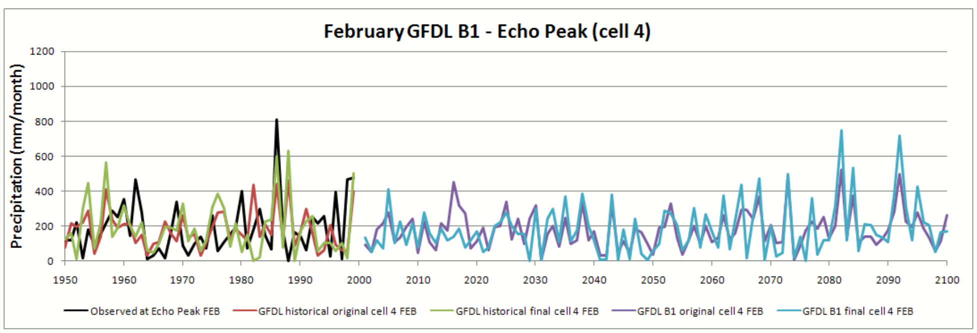

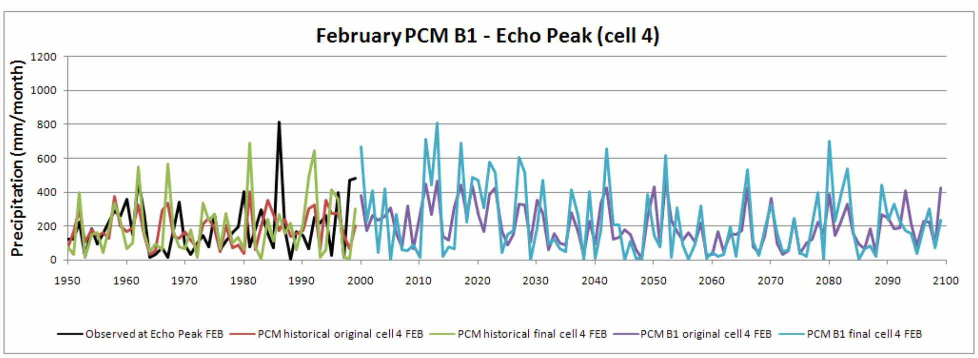

Figure 17, continued.

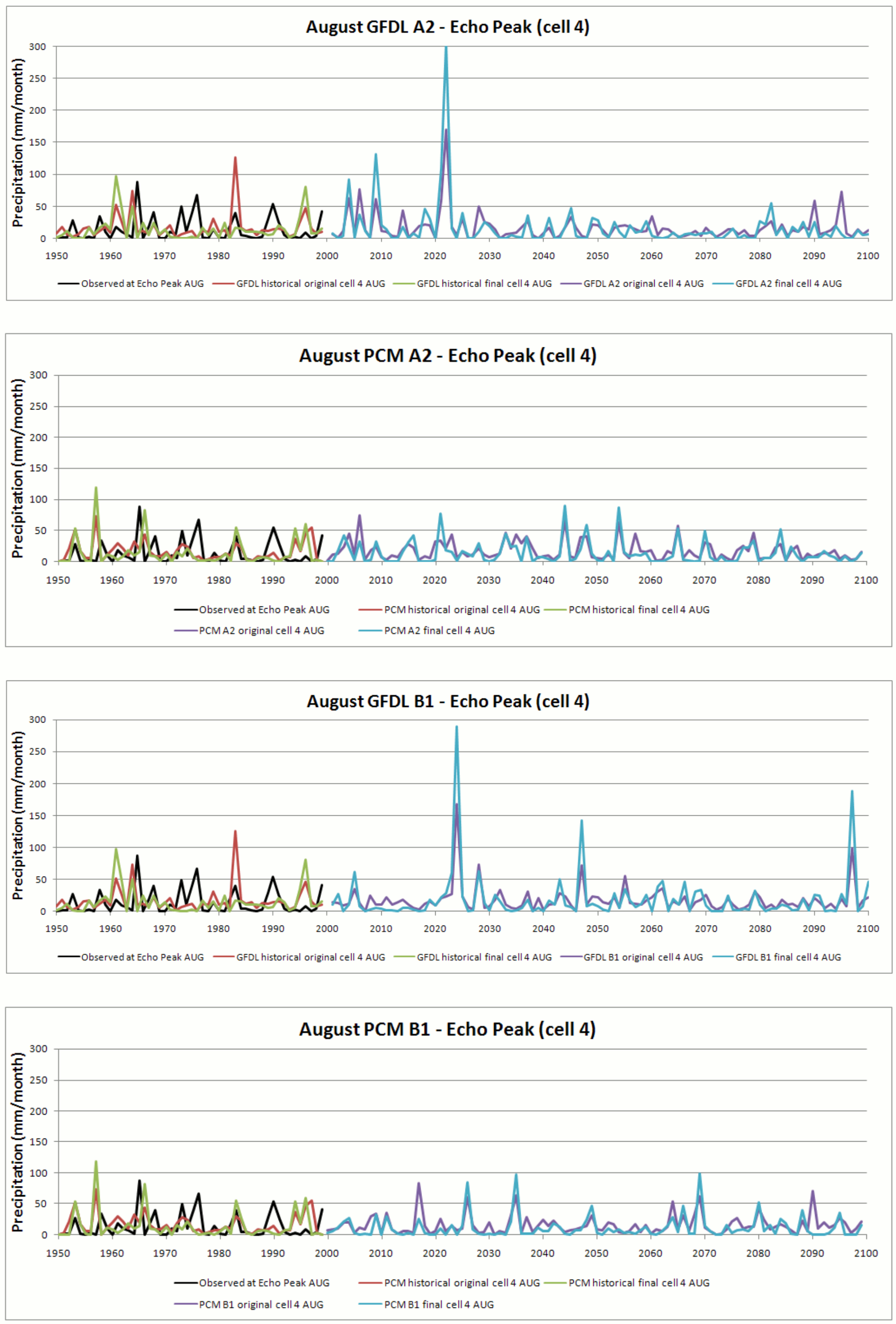

Figure 17, continued.

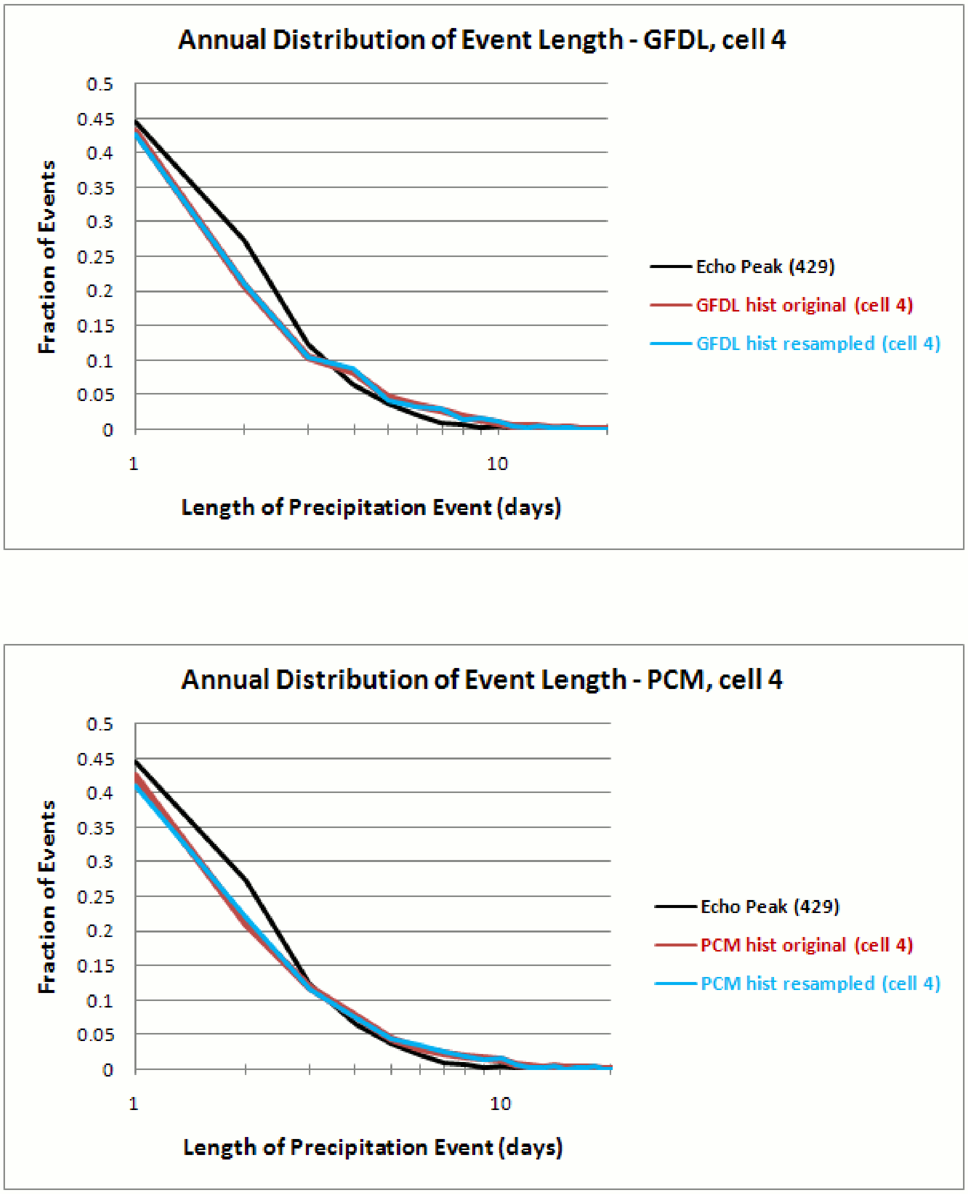

Figure 18: Annual distribution of event length for Echo Peak and its closest grid cell, cell 4. The original simulated values (red lines), for both GFDL and PCM, agreed well with observations (black lines). The simulated distributions are preserved after resampling because removal of excess precipitation events assigns equal likelihood of removal to events of any length.

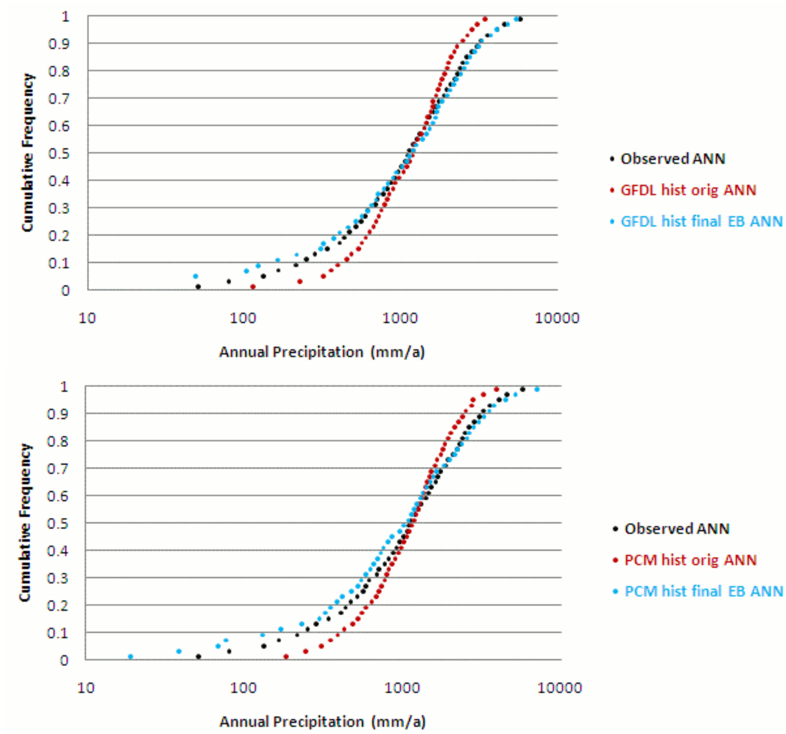

Figure 19: Comparison of the distributions of annual precipitation totals. The downscaled simulated distributions of annual values (blue) match the observed distribution (black) more closely than the original simulated distribution (red), both in the case of GFDL (top) and PCM (bottom).

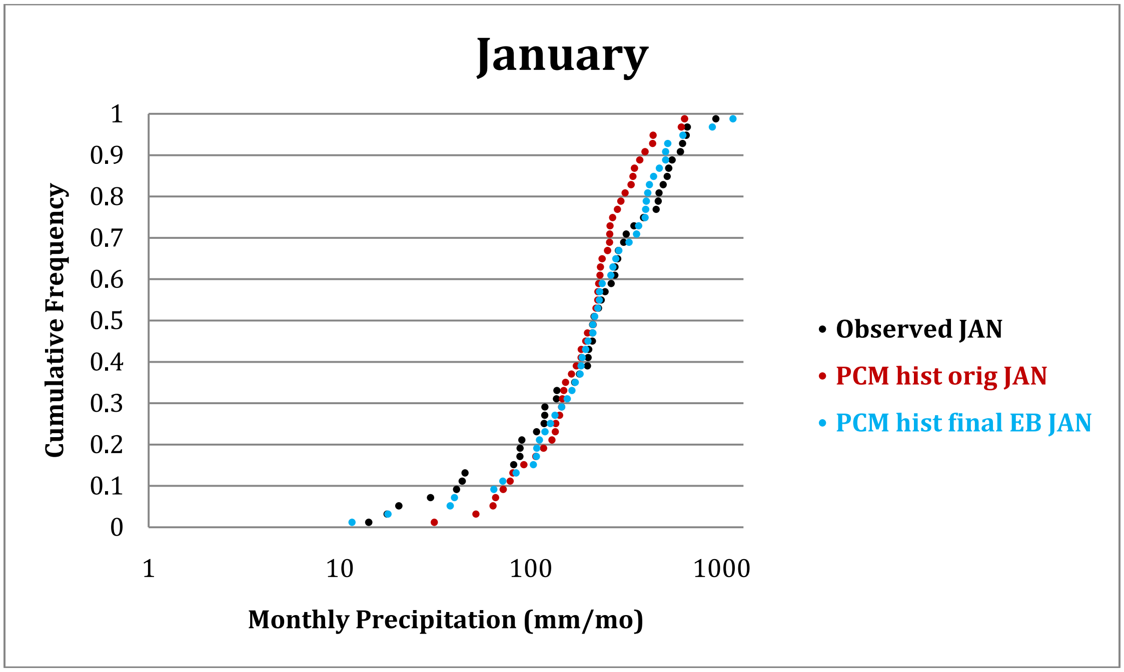

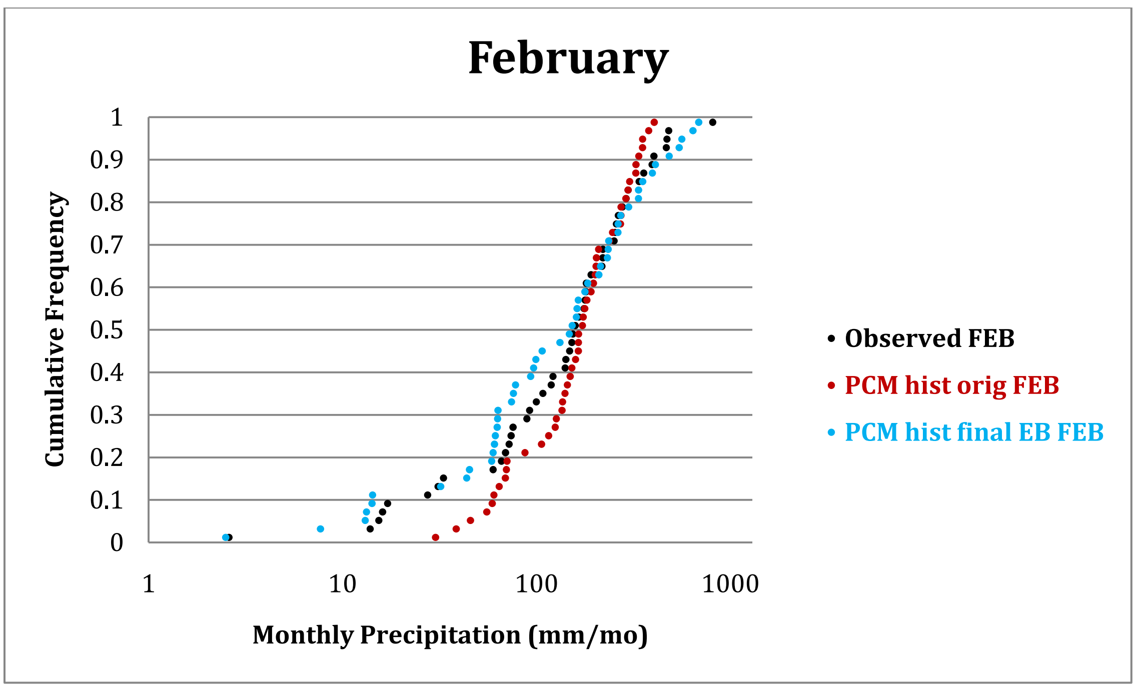

Figure 20: Monthly eCDFs for Echo Peak and its closest cell, cell 4. Simulations are by PCM. *(Figure continues.)*

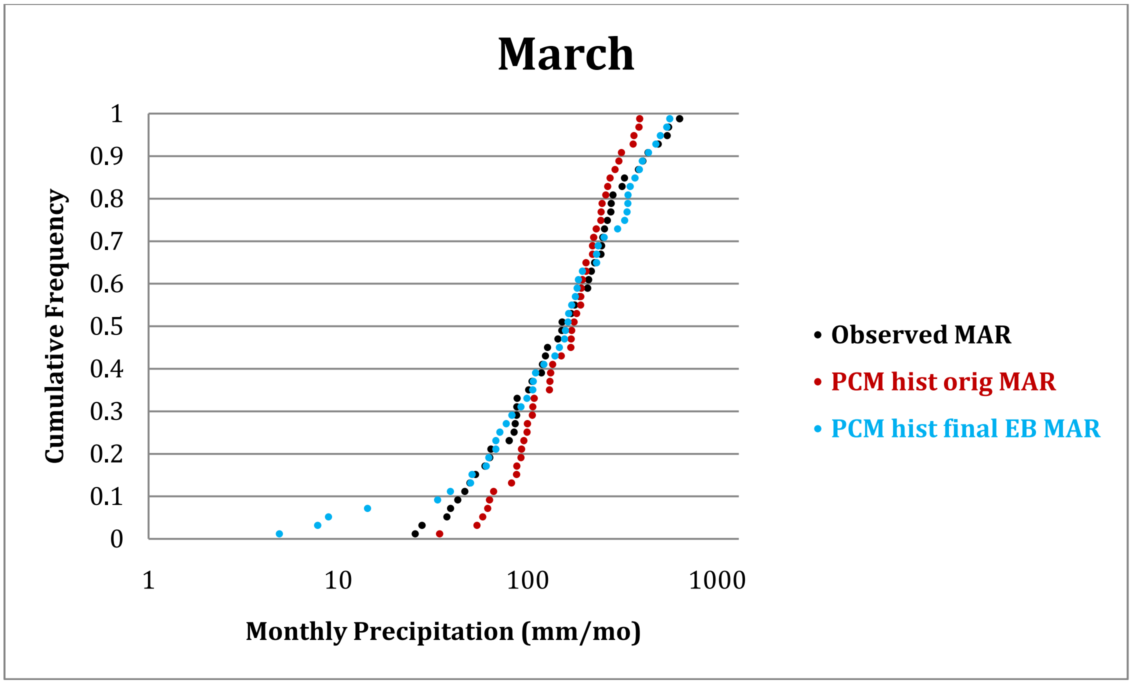

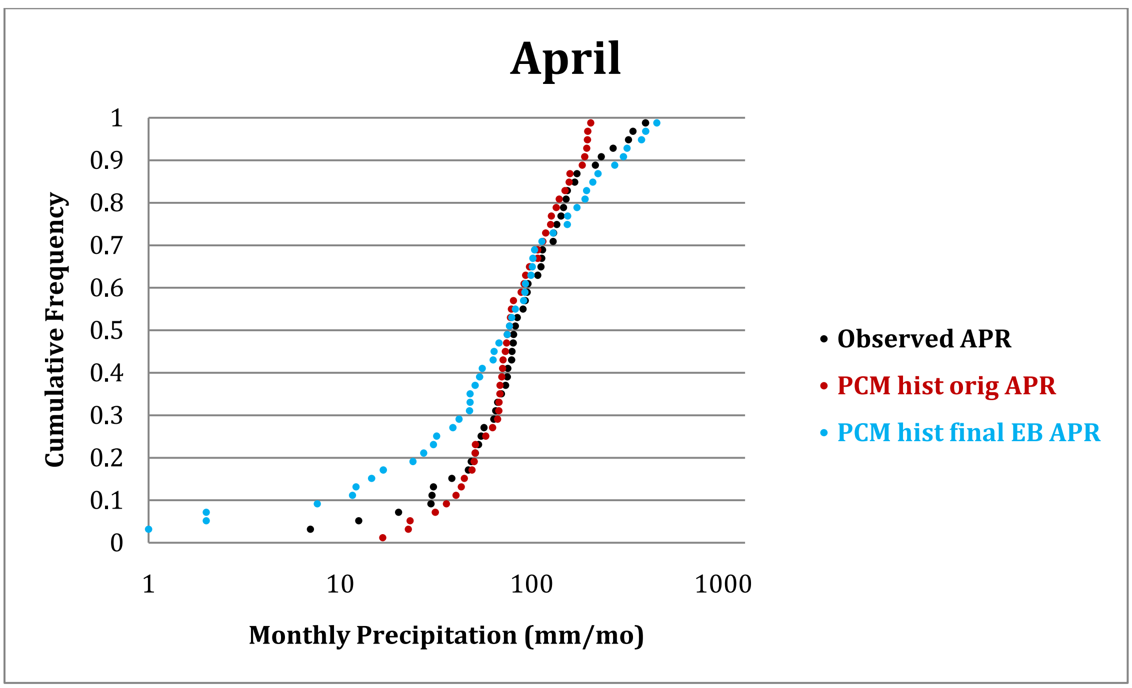

Figure 20, continued.

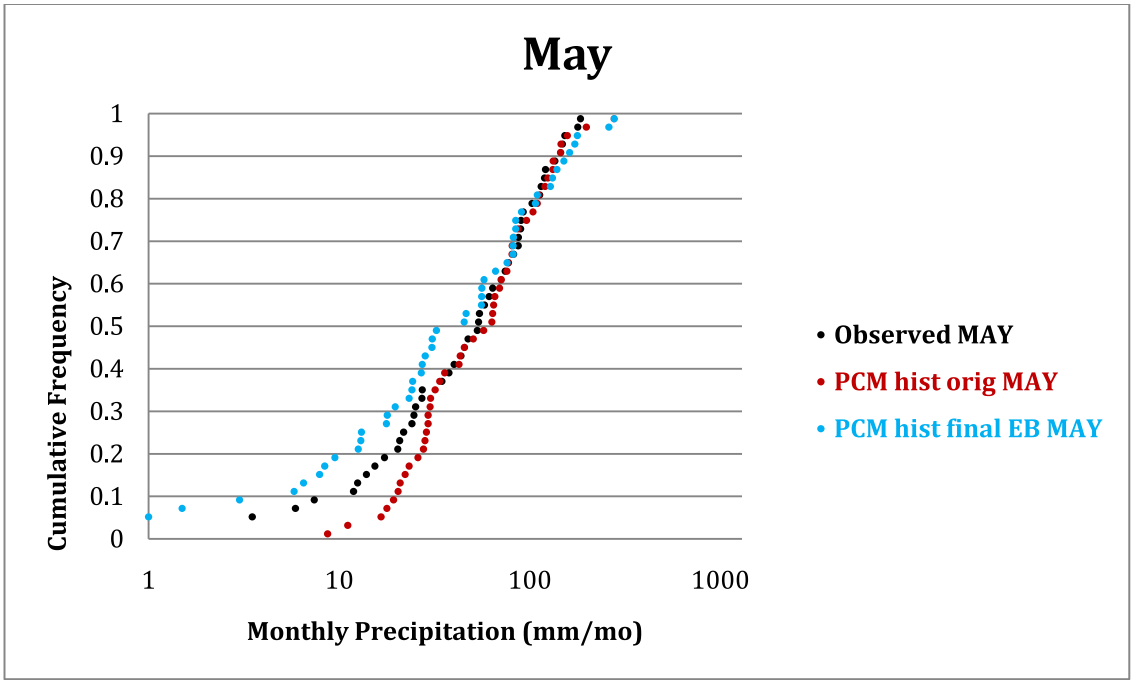

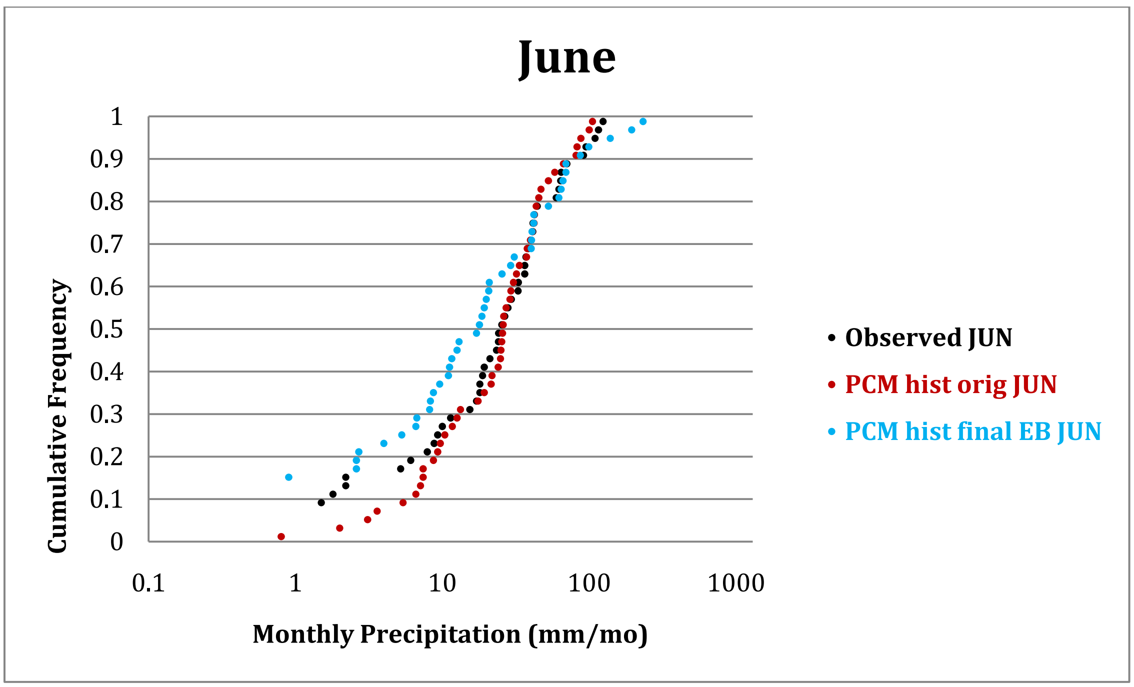

Figure 20, continued.

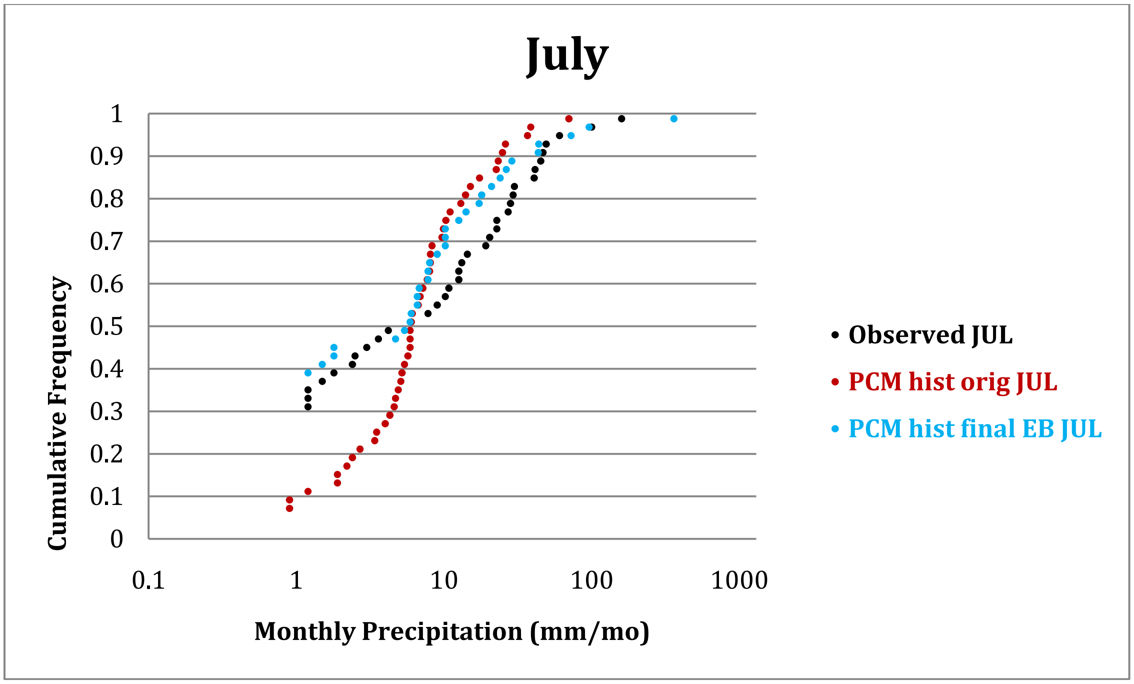

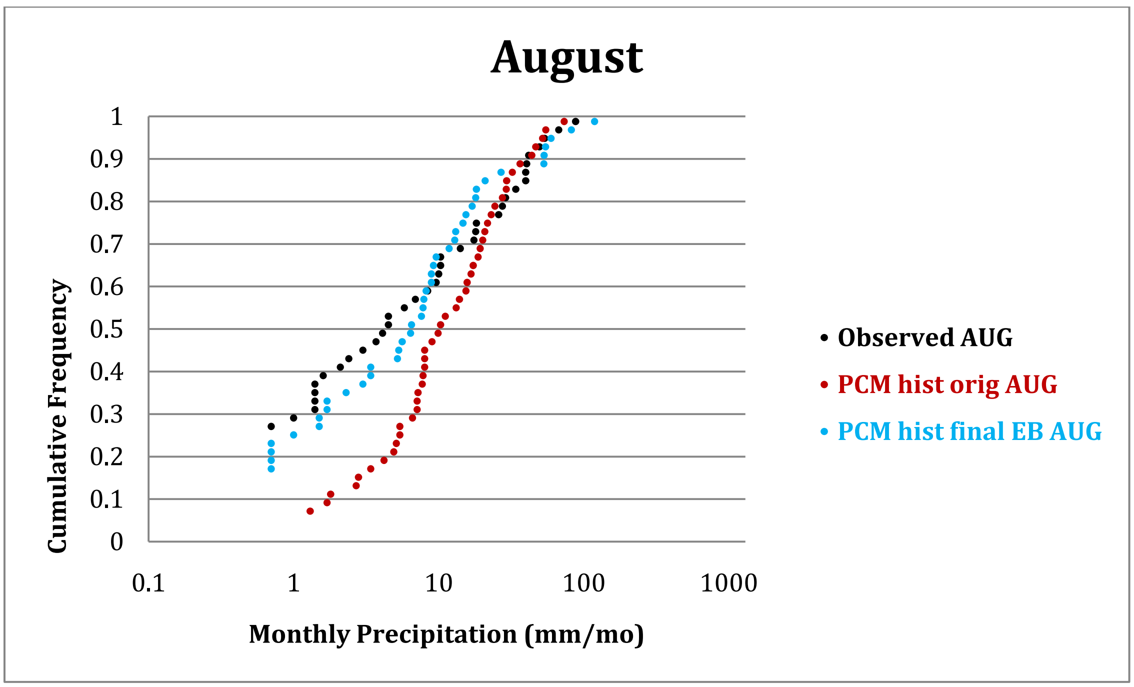

Figure 20, continued.

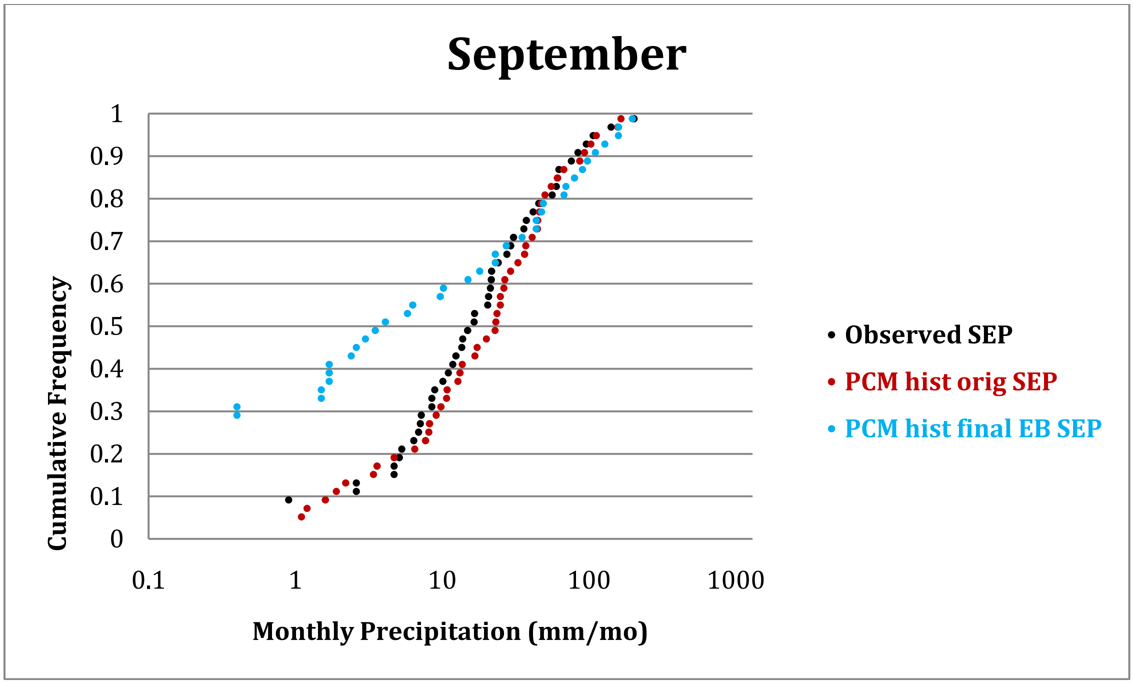

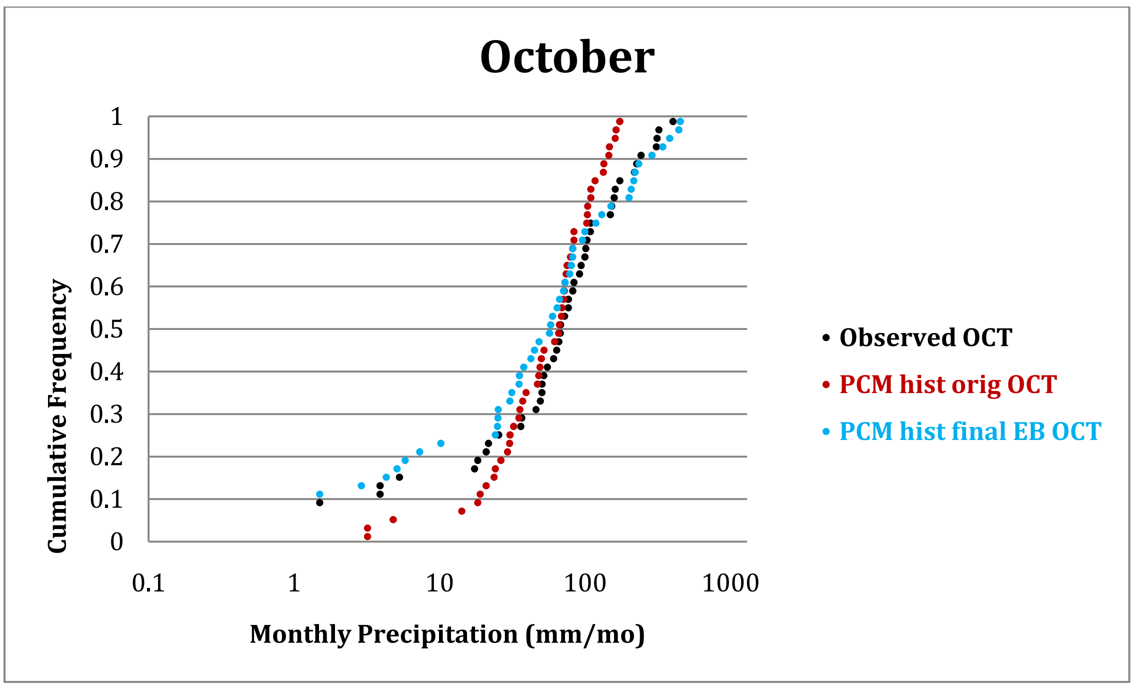

Figure 20, continued.

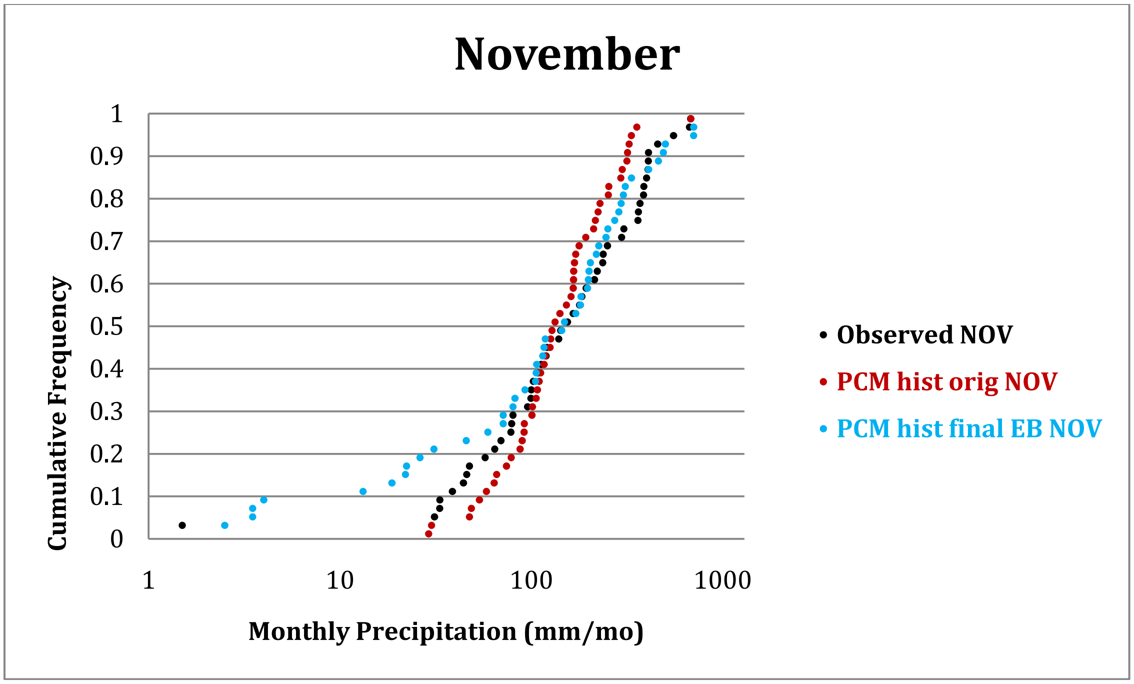

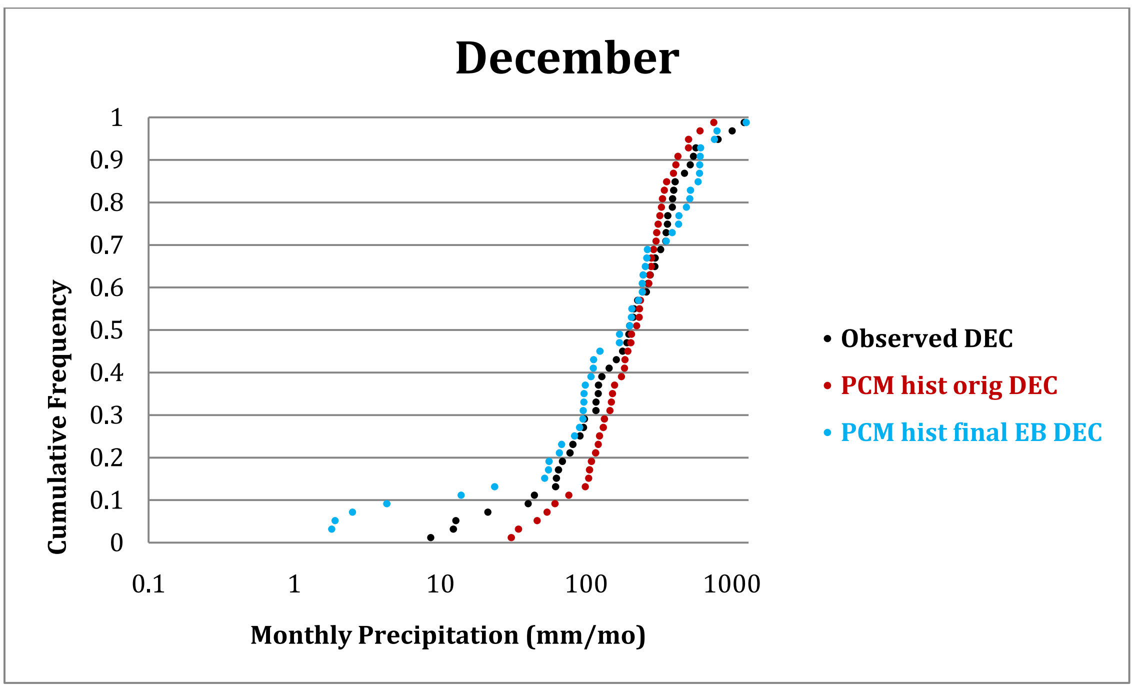

Figure 20, continued.

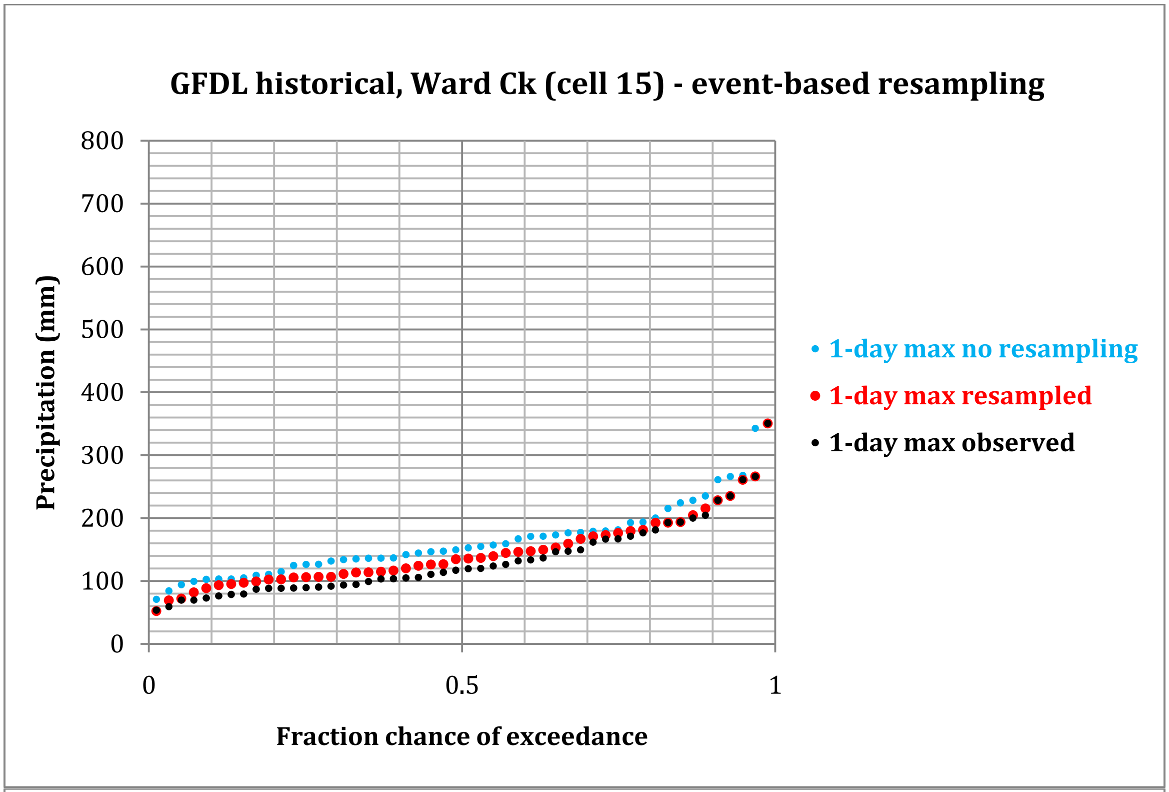

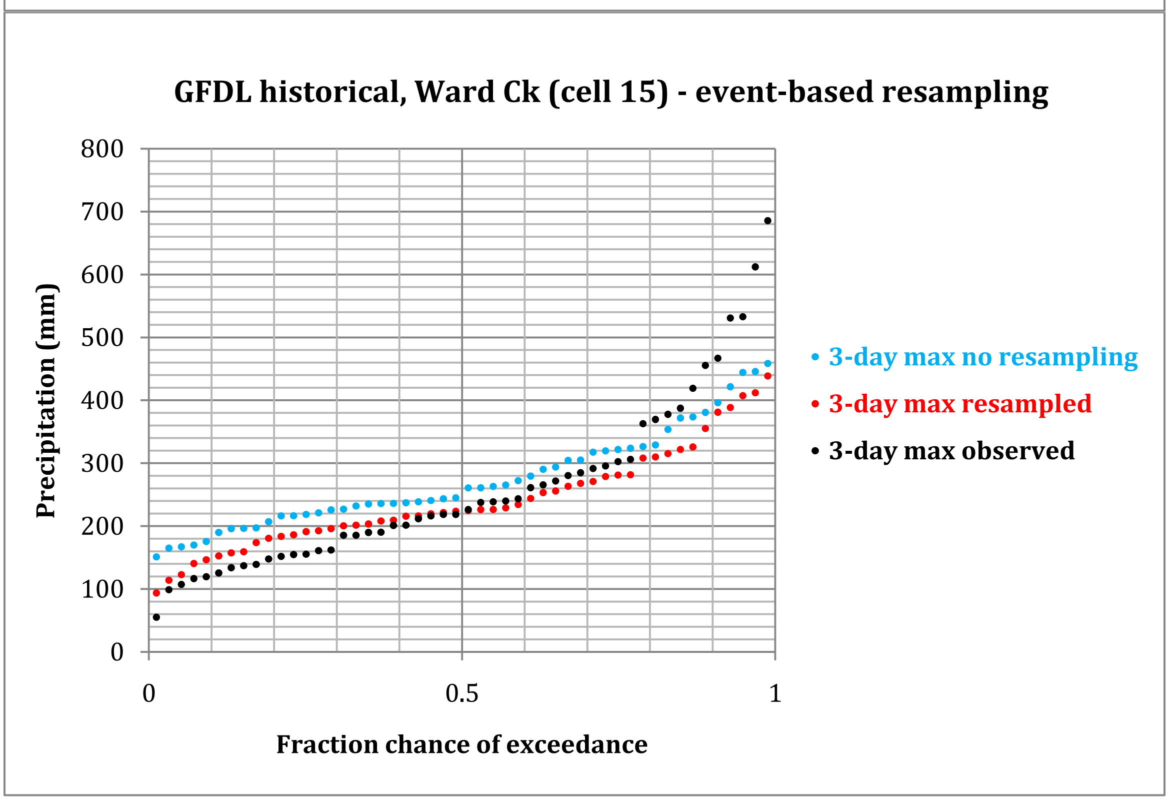

Figure 21: Empirical distributions of 1-day and 3-day annual maximum precipitation.

Description of the contents of all output files produced by the Fortran program *downscale_Tahoe_event_based.f* in the Attachment.

Files describing the statistics of the original datasets entering this project

mean_obs.txt

This file contains, for each of the 10 stations, the average monthly precipitation (in units of mm/d) for each of the 12 months. The average is taken over the entire period of observation (1950-1999). There are 10 rows (each for a station) and 12 columns (each for a month). The values are reproduced in the table below.

	1	2	3	4	5	6	7	8	9	10	11	12
Glenbrook (NCDC) *(not downscaled)*	8.84	7.27	6.33	4.17	4.45	3.74	3.66	4.22	5.37	4.93	7.49	8.70
Tahoe City (NCDC) *(not downscaled)*	15.59	14.01	10.92	7.00	5.08	4.74	4.50	4.44	5.54	10.67	12.77	15.61
Ward Creek (29)	26.41	22.26	18.49	13.51	11.37	7.37	2.48	2.88	10.52	19.35	23.32	28.64
Tahoe City (204)	14.07	12.40	9.84	6.49	5.11	4.21	4.60	4.35	6.12	10.50	11.69	14.65
Rubicon #2 (266)	15.25	13.83	12.14	8.75	6.67	6.43	6.29	4.20	8.62	10.34	12.46	16.46
Echo Peak (429)	23.36	19.06	17.31	12.99	9.82	8.12	10.39	5.59	8.81	18.4	23.93	26.00
Fallen Leaf (500)	13.58	11.38	9.61	6.19	4.76	4.57	7.44	4.14	6.41	11.06	12.51	15.73
Hagans Meadow (938)	13.96	11.68	10.31	7.77	7.29	4.29	5.90	5.74	6.67	7.78	12.58	15.08
Heavenly Valley (1978)	12.54	12.15	10.65	11.64	13.09	6.06	8.33	5.23	6.83	8.31	11.11	14.17
Marlette Lake (1167)	16.16	12.59	11.26	8.48	7.50	5.08	3.16	3.15	8.15	9.65	11.97	14.85

stdev_obs.txt

Similar to file mean_obs.txt, but contains the values of standard deviation.

nprecipdays_obs.txt

Similar to file mean_obs.txt, but contains the number of precipitation days (days with precipitation values greater than zero).

distrib_WardCreek_29.txt
distrib_TahoeCityCross_204.txt
distrib_Rubicon2_266.txt
distrib_EchoPeak_429.txt
distrib_FallenLeaf_500.txt
distrib_HagansMeadow_938.txt
distrib_HeavenlyValley_1078.txt
distrib_MarletteLake_1167.txt

These files contain the observed daily precipitation values (mm/day) for each of the named stations, in ranked order, i.e., from small to large. Zero values have been excluded.
There are 24 columns. The first column has the value of the Cunnane plotting position for January. The Cunnane plotting position is given by the following formula: $F(x) = (i-0.4)/(N_p+0.2)$, where i is the rank in the series and N_p is the number of precipitation days in the monthly series. The smallest precipitation value has rank i = 1, and the largest has rank i = N_p. The 2nd column has the (ranked) values of daily precipitation in January. The 3rd and 4th columns have the Cunnane plotting positions and ranked precipitation values for February. And so on for all months. The number of rows in the file equals the maximum number of days belonging to a give month in 1950-1999, equal to 50 years x 31 days/year = 1,550 days. However, only the first N_p rows contain results, while the remainder rows (which have the value zero in the precipitation column) are to be discarded.

These files are useful for plotting the cumulative frequency for each month. For example for January, we would plot the 1st column (*xx* axis) against the 2nd column (*yy* axis), using only the rows that correspond to precipitation days, i.e., excluding any last rows that contain zeroes.

monthly_timeseries_obs_GlenbrookNCDC.txt,
monthly_ timeseries _obs_TahoeCityNCDC.txt,
monthly_ timeseries_obs_WardCreek29.txt,
monthly_ timeseries_obs_TahoeCityCross204.txt,
monthly_ timeseries_obs_Rubicon266.txt,
monthly_ timeseries_obs_EchoPeak429.txt,
monthly_ timeseries_obs_FallenLeaf500.txt,
monthly_timeseries_obs_HagansMeadow938.txt,
monthly_timeseries_obs_Heavenly Valley1078.txt,
monthly_timeseries_obs_MarletteLake1167.txt

Time series of monthly total precipitation (in units of mm/month) for the observations at each of the 10 stations named. There are 13 columns. The first column in each file specifies the year, and the remainder 12 columns correspond to the 12 months. There are 50 rows, one for each year (1950-1999).

mean_GFDL_hist_original.txt

This file contains, for each of the 12 model cells, the average monthly precipitation (in units of mm/d) of the original simulated by GFDL for the historical period (1950-1999), for each of the 12 months. By “original” is meant the simulations that entered this project (at 1/8° resolution). The average is taken over the entire period of observation (or “historical period”) (1950-1999). There are 12 rows (each for a cell) and 12 columns (each for a month). The values are reproduced in the table below.

	1	2	3	4	5	6	7	8	9	10	11	12
Cell 4	12.92	12.22	9.74	5.95	4.90	3.45	3.58	3.75	5.12	7.29	10.65	14.10
Cell 5	12.54	10.93	9.34	6.17	4.86	3.46	3.82	3.54	5.09	7.01	9.65	12.07
Cell 9	14.79	13.66	10.53	6.38	5.63	3.84	3.39	3.90	5.83	8.03	11.85	16.10
Cell 10	9.66	7.78	6.31	3.64	3.39	3.30	3.03	3.67	4.07	5.77	7.31	9.93
Cell 11	10.07	8.45	7.10	4.76	4.56	3.41	3.56	3.55	4.59	6.04	7.99	10.00
Cell 15	12.59	11.46	8.84	5.73	4.48	3.80	3.85	3.54	5.28	7.15	9.77	13.26
Cell 16	8.10	6.71	5.48	3.32	3.01	3.12	4.01	4.00	4.37	5.22	6.09	7.62
Cell 17	9.11	7.67	6.46	4.26	4.51	3.54	4.04	3.94	5.04	5.43	6.81	8.33
Cell 21	12.34	11.31	8.71	5.70	4.06	3.61	4.02	3.85	4.97	7.3	9.67	12.94
Cell 22	8.54	7.51	5.93	3.69	3.15	3.29	4.05	4.18	4.68	5.42	6.52	8.00
Cell 23	9.18	7.91	6.42	4.00	4.17	3.22	3.71	3.44	4.89	5.09	6.73	8.14
Cell 29	11.64	10.25	7.77	5.21	5.19	3.35	3.44	3.28	4.88	6.21	9.35	11.80

If we wish to compare the simulated values in the above table to the observed ones in the table for mean_obs.txt, we compare each cell against its closest station. In accordance with Figure 1, the following table gives the closest station:

Cell:	Closest Station	
	Station #:	Station Name:
Cell 4	6	Echo Peak (429)
Cell 5	8	Hagans Meadow (938)
Cell 9	5	Rubicon #2 (266)
Cell 10	7	Fallen Leaf (500)
Cell 11	9	Heavenly Valley (1078)
Cell 15	3	Ward Creek (29)
Cell 16	5	Rubicon #2 (266)
Cell 17	10	Marlette Lake (1167)
Cell 21	4	Tahoe City Cross (204)
Cell 22	4	Tahoe City Cross (204)
Cell 23	10	Marlette Lake (1167)
Cell 29	10	Marlette Lake (1167)

stdev_GFDL_hist_original.txt
Similar to file mean_gfdl_hist_original.txt, but contains the values of standard deviation.

nprecipdays_GFDL_hist_original.txt
Similar to file mean_gfdl_hist_original.txt, but contains the number of precipitation days (days with precipitation values greater than zero).

mean_PCM_hist_original.txt,
stdev_PCM_hist_original.txt, and
nprecipdays_PCM_hist_original.txt
Similar to the files listed above for model GFDL with similar names, but for the model PCM.

mean_GFDL_A2_original.txt
Similar to mean_gfdl_hist_original.txt above, but for the GFDL simulations for the 21st century (2001-2100), under the SRES-A2 scenario of greenhouse emissions. The average is taken over the entire period 2001-1999, designated the “future” period.

stdev_GFDL_A2_original.txt
Similar to file mean_gfdl_A2_original, but contains the values of standard deviation.

nprecipdays_GFDL_A2_original.txt
Similar to file mean_gfdl_A2_original, but contains the number of precipitation days (days with precipitation values greater than zero).

mean_PCM_A2_original.txt,
stdev_PCM_A2_original.txt, and
nprecipdays_PCM_A2_original.txt

Similar to the files listed above for model GFDL with similar names, but for the model PCM.

mean_GFDL_B1_original.txt,
stdev_GFDL_B1_original.txt,
nprecipdays_GFDL_B1_original.txt,
mean_PCM_B1_original.txt,
stdev_PCM_B1_original.txt,
nprecipdays_PCM_B1_original.txt

Similar to the files listed above for scenario A2 with similar names, but for scenario B1.

distrib_GFDL_hist_original_cell_4.txt,
distrib_GFDL_hist_original_cell_5.txt,
distrib_GFDL_hist_original_cell_9.txt,
distrib_GFDL_hist_original_cell_10.txt,
distrib_GFDL_hist_original_cell_11.txt,
distrib_GFDL_hist_original_cell_15.txt,
distrib_GFDL_hist_original_cell_16.txt,
distrib_GFDL_hist_original_cell_17.txt,
distrib_GFDL_hist_original_cell_21.txt,
distrib_GFDL_hist_original_cell_22.txt,
distrib_GFDL_hist_original_cell_23.txt,
distrib_GFDL_hist_original_cell_29.txt,
distrib_PCM_hist_original_cell_4.txt,
distrib_PCM_hist_original_cell_5.txt,
distrib_PCM_hist_original_cell_9.txt,
distrib_PCM_hist_original_cell_10.txt,
distrib_PCM_hist_original_cell_11.txt,
distrib_PCM_hist_original_cell_15.txt,
distrib_PCM_hist_original_cell_16.txt,
distrib_PCM_hist_original_cell_17.txt,
distrib_PCM_hist_original_cell_21.txt,
distrib_PCM_hist_original_cell_22.txt,
distrib_PCM_hist_original_cell_23.txt,
distrib_PCM_hist_original_cell_29.txt

These files contain the simulated daily precipitation values that originally entered this project for the named model and for the historical period (1950-1999), in units of mm/day, for each of the named cells, in ranked order, i.e., from small to large. Zero values have been excluded. There are 24 columns. The first column has the value of the Cunnane plotting position for January. The Cunnane plotting position is given by the following formula: $F(x) = (i-0.4)/(N_p+0.2)$, where i is the rank in the series and N_p is the number of precipitation days in the monthly series. The smallest precipitation value has rank $i = 1$, and the largest has rank $i = N_p$. The 2nd column has the (ranked) values of daily precipitation in January. The 3rd and 4th columns have the Cunnane plotting positions and ranked precipitation values for February. And so on for all months. The number of rows in the file equals the maximum number of days belonging to a give month in 1950-1999, equal to 50 years x 31 days/year = 1,550 days.

However, only the first N_p rows contain results, while the remainder rows (which have the value zero in the precipitation column) are to be discarded.

These files are useful for plotting the cumulative frequency for each month. For example for January, we would plot the 1st column (*xx* axis) against the 2nd column (*yy* axis), using only the rows that correspond to precipitation days, i.e., excluding any last rows that contain zeroes.

monthly_timeseries_GFDL_hist_orig_cell_4.txt,
monthly_timeseries_GFDL_hist_orig_cell_5.txt,
monthly_timeseries_GFDL_hist_orig_cell_9.txt,
monthly_timeseries_GFDL_hist_orig_cell_10.txt,
monthly_timeseries_GFDL_hist_orig_cell_11.txt,
monthly_timeseries_GFDL_hist_orig_cell_15.txt,
monthly_timeseries_GFDL_hist_orig_cell_16.txt,
monthly_timeseries_GFDL_hist_orig_cell_17.txt,
monthly_timeseries_GFDL_hist_orig_cell_21.txt,
monthly_timeseries_GFDL_hist_orig_cell_22.txt,
monthly_timeseries_GFDL_hist_orig_cell_23.txt,
monthly_timeseries_GFDL_hist_orig_cell_29.txt

Time series of monthly total precipitation (in units of mm/month) for the GFDL historical simulations at each of the 12 model cells named. The inclusion of "orig" in the file's name signifies that these are the simulations that entered this project (at 1/8° resolution). There are 13 columns. The first column in each file specifies the year, and the remainder 12 columns correspond to the 12 months. There are 50 rows, one for each year (1950-1999).

monthly_timeseries_PCM_hist_orig_cell_4.txt,
monthly_timeseries_PCM_hist_orig_cell_5.txt,
monthly_timeseries_PCM_hist_orig_cell_9.txt,
monthly_timeseries_PCM_hist_orig_cell_10.txt,
monthly_timeseries_PCM_hist_orig_cell_11.txt,
monthly_timeseries_PCM_hist_orig_cell_15.txt,
monthly_timeseries_PCM_hist_orig_cell_16.txt,
monthly_timeseries_PCM_hist_orig_cell_17.txt,
monthly_timeseries_PCM_hist_orig_cell_21.txt,
monthly_timeseries_PCM_hist_orig_cell_22.txt,
monthly_timeseries_PCM_hist_orig_cell_23.txt,
monthly_timeseries_PCM_hist_orig_cell_29.txt

Similar to the files listed for GFDL with similar names, but for PCM.

monthly_timeseries_GFDL_A2_orig_cell_4.txt,
monthly_timeseries_GFDL_A2_orig_cell_5.txt,
monthly_timeseries_GFDL_A2_orig_cell_9.txt,
monthly_timeseries_GFDL_A2_orig_cell_10.txt,
monthly_timeseries_GFDL_A2_orig_cell_11.txt,
monthly_timeseries_GFDL_A2_orig_cell_15.txt,
monthly_timeseries_GFDL_A2_orig_cell_16.txt,

monthly_timeseries_GFDL_A2_orig_cell_17.txt,
monthly_timeseries_GFDL_A2_orig_cell_21.txt,
monthly_timeseries_GFDL_A2_orig_cell_22.txt,
monthly_timeseries_GFDL_A2_orig_cell_23.txt,
monthly_timeseries_GFDL_A2_orig_cell_29.txt

Similar to the files listed for the GFDL historical period ("GFDL_hist") with similar names, but for the period 2001-2100, designated the "future" period, and for the SRES-A2 scenario of greenhouse emissions.

monthly_timeseries_PCM_A2_orig_cell_4.txt,
monthly_timeseries_PCM_A2_orig_cell_5.txt,
monthly_timeseries_PCM_A2_orig_cell_9.txt,
monthly_timeseries_PCM_A2_orig_cell_10.txt,
monthly_timeseries_PCM_A2_orig_cell_11.txt,
monthly_timeseries_PCM_A2_orig_cell_15.txt,
monthly_timeseries_PCM_A2_orig_cell_16.txt,
monthly_timeseries_PCM_A2_orig_cell_17.txt,
monthly_timeseries_PCM_A2_orig_cell_21.txt,
monthly_timeseries_PCM_A2_orig_cell_22.txt,
monthly_timeseries_PCM_A2_orig_cell_23.txt,
monthly_timeseries_PCM_A2_orig_cell_29.txt

Similar to the files listed for GFDL with similar names, but for PCM.

monthly_timeseries_GFDL_B1_orig_cell_4.txt,
monthly_timeseries_GFDL_B1_orig_cell_5.txt,
monthly_timeseries_GFDL_B1_orig_cell_9.txt,
monthly_timeseries_GFDL_B1_orig_cell_10.txt,
monthly_timeseries_GFDL_B1_orig_cell_11.txt,
monthly_timeseries_GFDL_B1_orig_cell_15.txt,
monthly_timeseries_GFDL_B1_orig_cell_16.txt,
monthly_timeseries_GFDL_B1_orig_cell_17.txt,
monthly_timeseries_GFDL_B1_orig_cell_21.txt,
monthly_timeseries_GFDL_B1_orig_cell_22.txt,
monthly_timeseries_GFDL_B1_orig_cell_23.txt,
monthly_timeseries_GFDL_B1_orig_cell_29.txt

Similar to the files listed for the SRES-A2 scenario of greenhouse emissions, with similar names, but for the B1 scenario.

monthly_timeseries_PCM_A2_orig_cell_4.txt,
monthly_timeseries_PCM_A2_orig_cell_5.txt,
monthly_timeseries_PCM_A2_orig_cell_9.txt,
monthly_timeseries_PCM_A2_orig_cell_10.txt,
monthly_timeseries_PCM_A2_orig_cell_11.txt,
monthly_timeseries_PCM_A2_orig_cell_15.txt,
monthly_timeseries_PCM_A2_orig_cell_16.txt,
monthly_timeseries_PCM_A2_orig_cell_17.txt,
monthly_timeseries_PCM_A2_orig_cell_21.txt,
monthly_timeseries_PCM_A2_orig_cell_22.txt,

monthly_timeseries_PCM_A2_orig_cell_23.txt,
monthly_timeseries_PCM_A2_orig_cell_29.txt

Similar to the files listed for the SRES-A2 scenario of greenhouse emissions, with similar names, but for the B1 scenario.

Files recording the statistics of interim datasets, i.e., datasets that are neither original inputs entering the project or final output of the project. They are useful for checking the soundness of the Fortran code, and for plotting to aid understanding of the methodology

distrib_GFDL_hist_resampled_cell_4.txt,
distrib_GFDL_hist_resampled_cell_5.txt,
distrib_GFDL_hist_resampled_cell_9.txt,
distrib_GFDL_hist_resampled_cell_10.txt,
distrib_GFDL_hist_resampled_cell_11.txt,
distrib_GFDL_hist_resampled_cell_15.txt,
distrib_GFDL_hist_resampled_cell_16.txt,
distrib_GFDL_hist_resampled_cell_17.txt,
distrib_GFDL_hist_resampled_cell_21.txt,
distrib_GFDL_hist_resampled_cell_22.txt,
distrib_GFDL_hist_resampled_cell_23.txt,
distrib_GFDL_hist_resampled_cell_29.txt,
distrib_PCM_hist_resampled_cell_4.txt,
distrib_PCM_hist_resampled_cell_5.txt,
distrib_PCM_hist_resampled_cell_9.txt,
distrib_PCM_hist_resampled_cell_10.txt,
distrib_PCM_hist_resampled_cell_11.txt,
distrib_PCM_hist_resampled_cell_15.txt,
distrib_PCM_hist_resampled_cell_16.txt,
distrib_PCM_hist_resampled_cell_17.txt,
distrib_PCM_hist_resampled_cell_21.txt,
distrib_PCM_hist_resampled_cell_22.txt,
distrib_PCM_hist_resampled_cell_23.txt,
distrib_PCM_hist_resampled_cell_29.txt,

Most months in the original simulated time series that entered this project had more precipitation days than the number recorded at the closest station. The excess precipitation days occurred not only near the lowest values of the range, but across all values. For this reason, the precipitation days simulated for the historical period were randomly resampled so as to match the number of precipitation days belonging to a given month recorded at the closest station (given in file nprecipdays_obs.txt). The re-sampling consists of randomly choosing precipitation days for removal, assigning equal likelihood to any day belonging to a given month. For example, when removing a precipitation day from January, any of the 1,550 January days (= 31 days x 50 years) has equal likelihood of being chosen, so long as it had a precipitation value greater than zero.

These files named above contain the simulated daily precipitation values after re-sampling. They are not final output datasets of this project because following re-sampling we still need to perform quantile mapping to produce the final datasets. They are interim datasets useful for checking whether the random removal technique has worked properly, i.e., has not affected the overall shape of the cumulative frequency distribution (eCDF).

The contents of the file are analogous to those described for files with similar names, but containing the word "original" or "final", instead of "resampled".

These files are useful for plotting the cumulative frequency of the resampled datasets for each month, and comparing them against the original datasets. For example for January, we would plot the 1st column (*xx* axis) against the 2nd column (*yy* axis), using only the rows that correspond to precipitation days, i.e., excluding any last rows that contain zeroes.

Files describing the statistics of the datasets produced as final output within this project

mean_GFDL_hist_final.txt,
stdev_GFDL_hist_final.txt,
nprecipdays_GFDL_hist_final.txt,
mean_PCM_hist_final.txt,
stdev_PCM_hist_final.txt,
nprecipdays_PCM_hist_final.txt,
mean_GFDL_A2_final.txt,
stdev_GFDL_A2_final.txt,
nprecipdays_GFDL_A2_final.txt,
mean_PCM_A2_final.txt,
stdev_PCM_A2_final.txt,
nprecipdays_PCM_A2_final.txt,
mean_GFDL_B1_final.txt,
stdev_GFDL_B1_final.txt,
nprecipdays_GFDL_B1_final.txt,
mean_PCM_B1_final.txt,
stdev_PCM_B1_final.txt,
nprecipdays_PCM_B1_final.txt

GFDL_hist_final_timeseries.txt

This file contains the final downscaled time series of daily precipitation values (in units of mm/day) produced in this project, for the historical period (1950-1999) and for each station using a nearby cell. The file has 12 columns, each for one of the 12 cells. The order of the cells from the 1st to the last column is: cell 4, 5, 9, 10, 11, 15, 16, 17, 21, 22, 23, and 29. There are as many rows as there are days in the historical period, i.e., 18,250 rows (= 50 years x 365 days/year).

To find the downscaled time series for a specific station, we look at the column of its closest cell. For example, the closest cell to Echo Peak (429) station is cell 4. Therefore, the time series in the first column represents the downscaled GFDL historical time series for Echo Peak (429).

PCM_hist_final_timeseries.txt

Similar to the file listed above for model GFDL with a similar name, but for the model PCM.

GFDL_A2_final_timeseries.txt

Similar to the files listed above for the historical period (“hist_final” instead of “A2_final” in the file name) but for the “future” period (2001-2100).

PCM_A2_final_timeseries.txt

Similar to the file listed above for model GFDL with a similar name, but for the model PCM.

GFDL_B1_final_timeseries.tx

Similar to the file listed above for scenario A2 with a similar name (“A2” instead of “B1” in the file name), but for scenario B1.

PCM_B1_final_timeseries.tx

Similar to the file listed above for model GFDL with a similar name, but for the model PCM.

distrib_GFDL_hist_final_cell_4.txt
distrib_GFDL_hist_final_cell_5.txt,
distrib_GFDL_hist_final_cell_9.txt,
distrib_GFDL_hist_final_cell_10.txt,
distrib_GFDL_hist_final_cell_11.txt,
distrib_GFDL_hist_final_cell_15.txt,
distrib_GFDL_hist_final_cell_16.txt,
distrib_GFDL_hist_final_cell_17.txt,
distrib_GFDL_hist_final_cell_21.txt,
distrib_GFDL_hist_final_cell_22.txt,
distrib_GFDL_hist_final_cell_23.txt,
distrib_GFDL_hist_final_cell_29.txt,
distrib_PCM_hist_final_cell_4.txt,
distrib_PCM_hist_final_cell_5.txt,
distrib_PCM_hist_final_cell_9.txt,
distrib_PCM_hist_final_cell_10.txt,
distrib_PCM_hist_final_cell_11.txt,
distrib_PCM_hist_final_cell_15.txt,
distrib_PCM_hist_final_cell_16.txt,
distrib_PCM_hist_final_cell_17.txt,
distrib_PCM_hist_final_cell_21.txt,
distrib_PCM_hist_final_cell_22.txt,
distrib_PCM_hist_final_cell_23.txt,
distrib_PCM_hist_final_cell_29.txt

Even though these files are named for model cells, what they in fact contain is downscaled precipitation values for the station closest to that cell, based on the model simulations for at that cell.

These files contain the downscaled simulated daily precipitation values produced during this project for the named model and for the historical period (1950-1999), in units of mm/day, for the station closest to each of the named cells. The precipitation values are in ranked order, i.e., from small to large. Zero values have been excluded. There are 24 columns. The first column has the value of the Cunnane plotting position for January. The Cunnane plotting position is given by the following formula: $F(x) = (i-0.4)/(N_p+0.2)$, where i is the rank in the series and N_p is the number of precipitation days in the monthly series. The smallest precipitation value has rank $i = 1$, and the largest has rank $i = N_p$. The 2nd column has the (ranked) values of daily precipitation in January. The 3rd and 4th columns have the Cunnane plotting positions and ranked precipitation values for February. And so on for all months. The number of rows in the file equals the maximum number of days belonging to a give month in 1950-1999, equal to 50 years x 31 days/year = 1,550 days. However, only the first N_p rows contain results, while the remainder rows (which have the value zero in the precipitation column) are to be discarded.

These files are useful for plotting the cumulative frequency for each month. For example for January, we would plot the 1st column (*xx* axis) against the 2nd column (*yy* axis), using only the rows that correspond to precipitation days, i.e., excluding any last rows that contain zeroes.

Note that, as a result of the quantile-mapping in the downscaling methodology, the contents of the above files, which are for the historical period, ought to approximately match the contents of the corresponding files for the closest station. For example, the contents of files **distrib_GFDL_hist_final_cell_4.txt** and **distrib_PCM_hist_final_cell_4.txt** ought to roughly match that of file **distrib_EchoPeak_429.txt.**

monthly_timeseries_GFDL_hist_final_cell_4.txt,
monthly_timeseries_GFDL_hist_final_cell_5.txt,
monthly_timeseries_GFDL_hist_final_cell_9.txt,
monthly_timeseries_GFDL_hist_final_cell_10.txt,
monthly_timeseries_GFDL_hist_final_cell_11.txt,
monthly_timeseries_GFDL_hist_final_cell_15.txt,
monthly_timeseries_GFDL_hist_final_cell_16.txt,
monthly_timeseries_GFDL_hist_final_cell_17.txt,
monthly_timeseries_GFDL_hist_final_cell_21.txt,
monthly_timeseries_GFDL_hist_final_cell_22.txt,
monthly_timeseries_GFDL_hist_final_cell_23.txt,
monthly_timeseries_GFDL_hist_final_cell_29.txt,
monthly_timeseries_PCM_hist_final_cell_4.txt,
monthly_timeseries_PCM_hist_final_cell_5.txt,
monthly_timeseries_PCM_hist_final_cell_9.txt,
monthly_timeseries_PCM_hist_final_cell_10.txt,
monthly_timeseries_PCM_hist_final_cell_11.txt,
monthly_timeseries_PCM_hist_final_cell_15.txt,
monthly_timeseries_PCM_hist_final_cell_16.txt,
monthly_timeseries_PCM_hist_final_cell_17.txt,

monthly_timeseries_PCM_hist_final_cell_21.txt,
monthly_timeseries_PCM_hist_final_cell_22.txt,
monthly_timeseries_PCM_hist_final_cell_23.txt,
monthly_timeseries_PCM_hist_final_cell_29.txt,
monthly_timeseries_GFDL_A2_final_cell_4.txt,
monthly_timeseries_GFDL_A2_final_cell_5.txt,
monthly_timeseries_GFDL_A2_final_cell_9.txt,
monthly_timeseries_GFDL_A2_final_cell_10.txt,
monthly_timeseries_GFDL_A2_final_cell_11.txt,
monthly_timeseries_GFDL_A2_final_cell_15.txt,
monthly_timeseries_GFDL_A2_final_cell_16.txt,
monthly_timeseries_GFDL_A2_final_cell_17.txt,
monthly_timeseries_GFDL_A2_final_cell_21.txt,
monthly_timeseries_GFDL_A2_final_cell_22.txt,
monthly_timeseries_GFDL_A2_final_cell_23.txt,
monthly_timeseries_GFDL_A2_final_cell_29.txt,
monthly_timeseries_PCM_A2_final_cell_4.txt,
monthly_timeseries_PCM_A2_final_cell_5.txt,
monthly_timeseries_PCM_A2_final_cell_9.txt,
monthly_timeseries_PCM_A2_final_cell_10.txt,
monthly_timeseries_PCM_A2_final_cell_11.txt,
monthly_timeseries_PCM_A2_final_cell_15.txt,
monthly_timeseries_PCM_A2_final_cell_16.txt,
monthly_timeseries_PCM_A2_final_cell_17.txt,
monthly_timeseries_PCM_A2_final_cell_21.txt,
monthly_timeseries_PCM_A2_final_cell_22.txt,
monthly_timeseries_PCM_A2_final_cell_23.txt,
monthly_timeseries_PCM_A2_final_cell_29.txt,
monthly_timeseries_GFDL_B1_final_cell_4.txt,
monthly_timeseries_GFDL_B1_final_cell_5.txt,
monthly_timeseries_GFDL_B1_final_cell_9.txt,
monthly_timeseries_GFDL_B1_final_cell_10.txt,
monthly_timeseries_GFDL_B1_final_cell_11.txt,
monthly_timeseries_GFDL_B1_final_cell_15.txt,
monthly_timeseries_GFDL_B1_final_cell_16.txt,
monthly_timeseries_GFDL_B1_final_cell_17.txt,
monthly_timeseries_GFDL_B1_final_cell_21.txt,
monthly_timeseries_GFDL_B1_final_cell_22.txt,
monthly_timeseries_GFDL_B1_final_cell_23.txt,
monthly_timeseries_GFDL_B1_final_cell_29.txt,
monthly_timeseries_PCM_A2_final_cell_4.txt,
monthly_timeseries_PCM_A2_final_cell_5.txt,
monthly_timeseries_PCM_A2_final_cell_9.txt,
monthly_timeseries_PCM_A2_final_cell_10.txt,
monthly_timeseries_PCM_A2_final_cell_11.txt,
monthly_timeseries_PCM_A2_final_cell_15.txt,

monthly_timeseries_PCM_A2_final_cell_16.txt,
monthly_timeseries_PCM_A2_final_cell_17.txt,
monthly_timeseries_PCM_A2_final_cell_21.txt,
monthly_timeseries_PCM_A2_final_cell_22.txt,
monthly_timeseries_PCM_A2_final_cell_23.txt,
monthly_timeseries_PCM_A2_final_cell_29.txt

Time series of monthly total precipitation (in units of mm/month) after downscaling (indicated by the inclusion of "final" in the file names). Each file's name indicates the time period ("hist" for the historical period, 1950-1999, and "A2" or "B1" for the time period 2001-2100 using SRES greenhouse emission scenarios A2 or B1), model used (GFDL or PCM) and the cell whose simulations were used in the downscaling. There are 13 columns. The first column in each file specifies the year, and the remainder 12 columns correspond to the 12 months. There are 50 rows, one for each year (1950-1999).

Once again, to find the downscaled monthly time series for a specific station, we look at the file of its closest cell. For example, the closest cell to Echo Peak (429) station is cell 4. Therefore, the downscaled monthly time series for Echo Peak (429) station are found in the files:

monthly_timeseries_GFDL_hist_final_cell_4.txt,
monthly_timeseries_PCM_hist_final_cell_4.txt,
monthly_timeseries_GFDL_A2_final_cell_4.txt,
monthly_timeseries_PCM_A2_final_cell_4.txt,
monthly_timeseries_GFDL_B1_final_cell_4.txt, and
monthly_timeseries_PCM_B1_final_cell_4.txt.